Characterisation of buried conjugated polymer interfaces by off specular neutron scattering.

James, David William

Swansea University
Prifysgol Abertawe

Characterisation of Buried Conjugated Polymer Interfaces by Off Specular Neutron Scattering

David William James
MEng, MRes

Submitted to Swansea University in the fulfilment of the requirements for the degree of Doctor of Philosophy

2011

Declaration

This work has not previously been accepted in substance for any degree and is not being concurrently submitted in candidature for any degree.

Signed ..... (candidate)

Date 10/4/12

Statement 1

This thesis is the result of my own investigations, except where otherwise stated.Other sources are acknowledged giving explicit references. A bibliography is appended.

Signed ..... (candidate)

Date 10/4/12

Statement 2

I hereby give consent for my thesis, if accepted, to be available for photocopying and for inter-library loan, and for the title and summary to be made available to outside organisations.

Signed ... (candidate)

Date 10/4/12

Certificate of Originality

This thesis is submitted to Swansea University under the supervision of Dr. A. M. Higgins and Prof. P. Rees in the Multidisciplinary Nanotechnology Centre in Swansea University in candidature for the degree of Doctor of Philosophy. The material in this thesis is the original work of the author except where acknowledgment to other authors is expressed.

Signed .....

Dated .....

David William James

(Candidate)

Signed .....

Dated .....

Dr. A. M. Higgins

(Supervisor)

Signed .....

Dated .....

Prof. P. Rees

(Supervisor)

Acknowledgments

Deepest thanks go to Dr Anthony Higgins for his excellent supervision during the course of this work. I greatly appreciate the thought and time he has given to all the problems I have encountered, his company on experiments and his reading and re-reading of this thesis and his encouragement.

I thank Professor Paul Rees for his supervision and his help in understanding the theory.

I would like to thank Dr Rowan Brown as has always been available to chat through problems and give useful advice and pick me up with a cup of tea when I have felt that this work is too much for me.

Gratitude goes to my predecessor Dr. Samson Chang for all his help in the early days, teaching me how to prepare samples and use AFM and for his company on experiments. I'd like to thank my successor Dyfrig Mon for his help with the work on P3HT/PCBM.

Thanks go to Dr R. Daniels, Dr A. Neate and Prof N. Jacob for assistance with solving my integrals!

I would like to thank Dr M. Geoghegan for believing in this work and for staying up changing samples late at night during experiments!!

Thanks go to instrument scientists Dr R. Dalgliesh, Dr T. Charlton and Dr R. Cubbitt for all there help during my times conducting experiments at neutron scattering facilities.

Many thanks go to Tami James, Georgy Markin, Emma Savory, Rhian Haden, Marina Udy and David Lewis for proof reading this thesis.

Thank you to my parents and brother for their love and support.

The biggest thanks must go to my wonderful wife Tami. I do not think that any of this work would have been possible without her help. She has spent many hours picking me up, motivating and encouraging me with no complaint. She has never stopped believing in me or loving me. I am truly blessed.

Thank you to God for the peace, hope and grace that is made known through the Lord Jesus Christ.

No one can comprehend what goes on under the sun. Despite all their efforts to search it out, no one can discover its meaning. Even if the wise claim they know, they cannot really comprehend it. Ecclesiastes 8:17

Your word is a lamp for my feet, a light on my path. Psalm 119:105

Abstract

Neutron reflectivity offers the opportunity for non-destructive characterisation of buried polymer interfaces. Specular neutron reflectivity is commonly used to characterise the structure of conjugated polymer interfaces found in organic electronic devices. However, detecting specularly reflected neutrons only allows the measurement of the root-mean-square (RMS) roughness of the interface averaged over a macroscopic lateral distance. There are two contributions to the RMS roughness of a polymer/polymer interface; i) the so-called 'intrinsic interfacial width' due to mixing of the polymers at a molecular level and ii) lateral roughness due to deviations of the interface position from the plane of the substrate.

In this work a numerical model is developed to analyse experimental off specular reflectivity. The model is based on the distorted wave Born approximation (DWBA). Specular and off specular neutron reflectivity data is collected from a model conjugated polymer/amorphous polymer interface (poly(9,9-dioctylfluorene) (F8) on deuterated PMMA) and a conjugated polymer/fullerene interface (poly(3-hexylthiophene) (P3HT) polymer on [6,6]-phenyl C61-butyric acid methylester (PCBM)). This allows probing of the structure in the plane of the interfaces to distinguish the intrinsic interfacial width from the lateral roughness. The structure of the F8/dPMMA interface is studied by systematically varying the film thickness, which strongly impacts on the amplitude of the lateral interface roughness, and allows more complete analysis of the relative contributions of intrinsic mixing and lateral roughness. For comparison off specular measurements on amorphous/amorphous polymer (PMMA/polystyrene) interfaces are performed, which have been studied previously using specular neutron reflectivity and self consistent field theory.

Fitting specular reflectivity using standard techniques and off specular reflectivity data using the model developed allow intrinsic and lateral roughness contributions for the F8/ dPMMA system to be separated by direct measurement. The P3HT/PCBM interface exhibits no lateral roughness as the materials are found to be miscible.

Contents

List of Figures

List of Tables

Nomenclature

m	Mass
v	Velocity
$\hbar$	Planks constant
θ_i	Angle of incidence
θ_f	Angle of reflection
λ	Neutron wavelength
k_i	Incident wavevector
k_f	Reflected wavevector
$\mathbf{q}$	Momentum transfer
q_z	Momentum transfer in z direction
q_x	Momentum transfer in x direction
q_y	Momentum transfer in y direction
r	Reflectance coefficient
t	Transmittance coefficient
R	Reflectivity coefficient
T	Transmittivity coefficient
SLD	Scattering length density
Nb	Scattering length density
σ	Interfacial roughness
σ_{tot}	Total interfacial roughness
σ_{lat}	Lateral roughness
σ_{int}	Intrinsic roughness
h	Hurst parameter
ξ_{lat}	Lateral correlation length
ξ_{int}	Interface to interface correlation length
d	Thickness of a film
z	Height of an interface
χ	Flory Huggins interaction parameter
$\langle R_{ee}^2 \rangle$	Mean square end to end distance of a polymer molecule
R_g	Radius of gyration of a polymer molecule
b	Segment length of a polymer molecule
a	Monomer length of a polymer molecule
M_n	Number average molar mass
M_w	Weight average molar mass
RMS	Root mean square
FWHM	Full width half maximum

Chapter 1

Introduction

The study of interfaces between adjacent polymer thin films by neutron reflectivity is well established. Most neutron reflectivity experiments use specular reflectivity where the angle of reflection of a neutron beam from a sample is equal to the angle of incidence. Specular reflectivity can only give information about the structure of an interface perpendicular to its plane. Off specular neutron reflectivity where the angle of incidence is not necessarily equal to the angle of reflection can provide information about the in plane structure of the interface. Off specular reflectivity is not widely used due to difficulties with both experimental procedures and data analysis. Due to the low number of neutrons reflected in off specular directions, off specular experiments require far longer count times and are much more sensitive to background neutron radiation.

The main aim of this work is to develop techniques to gather and analyse off specular neutron reflectivity data from thin film polymer bilayer systems to characterise the interface. Two bilayer systems have been chosen to study. The first is poly(9,9-dioctylfluorene) (F8) on deuterated poly(methyl methacrylate) (dPMMA), which is a polymer pair with well known interfacial mixing characteristics when annealed to reach thermodynamic equilibrium conditions. The F8/ PMMA system has been used in organic field effect transistors. The second system is poly(3-hexylthiophene) (P3HT) polymer on [6,6]-phenyl C61-butyric acid methylester(PCBM) a fullerene derivative. This system is of interest because these materials have been used to make the most efficient organic solar cells made to date.

It has been shown that the interfacial properties affect device performance. Groups studying organic electronic devices such as organic photo voltaics (PV) cells and organic field effect transistors (oFETs) have shown that the device performance is affected by interfacial roughness. It is thought that there are two contributions to the total roughness of a polymer/polymer interface; i) an intrinsic roughness caused by mixing of polymer chains from the different species across the interface at a molecular level and ii) a lateral roughness caused by thermal fluctuations of the interface from the mean position, which results in a spectrum of capillary waves. Efforts have been made to separate these two contributions by measuring the total roughness and inferring the contributions either by theory [84] or by spectroscopic measurements [37]. To date no attempt has been made to separate out these contributions by direct measurement.

Specular neutron reflectivity is sensitive only to the total root mean square (RMS) roughness of the interface. Off specular neutron reflectivity is sensitive to the lateral roughness and the total (RMS) roughness. Using off specular reflectivity the two contributions can be separated out by direct measurement. By separating out the roughness contributions the effect each

contribution has on device performance could be analysed. This could contribute to improved device performance. A greater understanding of the physics of polymers at interfaces could also be obtained.

The analysis of off specular reflectivity data is a quantum mechanical problem. The theory to model an off specular reflectivity experiment for both x-ray and neutron experiments for thin films was first derived by Sinha et al [88] from the distorted wave Born approximation (DWBA) theory and subsequently built upon by other authors [43] [42]. The DWBA theory is derived in reciprocal space. There is a fairly large body of work in the literature using DWBA based models to fit to thin films for off specular x-ray experiments. There are few examples of off specular experiments and analysis in the literature using neutrons [97] [24] and no examples of fitting of off specular reflectivity from polymer bilayers. The main reasons for this being that x-ray experiments have far higher flux than neutron experiments and off specular x-ray reflectivity can easily be converted into reciprocal space due to the instrumental geometry. However due to the way neutrons interact with matter they can give information about the structure of interfaces between organic materials that cannot be obtained using x-rays. Recent advances in neutron sources and instruments mean greater fluxes and capability to measure off specular scattering. Although the experimental techniques have developed the measured neutron reflectivity still cannot be easily converted into reciprocal space and analysis of off specular neutron data is still very much in its infancy.

In this work experimental specular and off specular neutron reflectivity data is collected from the samples described above. The specular reflectivity data is fitted using standard models. A numerical model is developed based upon the DWBA theory to fit off specular reflectivity data in real space, so that experimental data does not have to be transformed into reciprocal space. The experimental reflectivity data is successfully fitted using the model and an evolutionary fitting algorithm. From fitting the experimental data, parameters describing the interface between thin polymer films are obtained, the two roughness contributions are separated out.

This thesis is structured as follows:

Chapter 2 Description of neutron scattering. The theory of specular neutron scattering and the theory of off specular scattering for scattering from rough thin films in multilayer stacks is described. Neutron reflectivity experimental techniques are outlined and the experimental instruments used in this work are described.

Chapter 3 Theory of polymers at interfaces is summarised. The theory of capillary wave fluctuations at interfaces is also summarised.

Chapter 4 Describes the experimental work carried out in the course of this work. Optimisation and data reduction techniques are documented, with examples of experimental results. Atomic force microscope work is documented with results and sample preparation techniques are described.

Chapter 5 Development of the model based upon the DWBA in order to fit the experimental off specular neutron scattering data is described, including problems that were encountered and how they were overcome.

Chapter 6 A study of the F8/ dPMMA polymer system for samples with varying thickness dPMMA films is carried out. Data is analysed using well known specular analysis techniques and the model described in chapter 5 is used to fit the off specular data and extract parameters to characterise the interfacial structure.

Chapter 7 A preliminary study of the P3HT/PCBM system is carried out analysing the specular neutron reflectivity data.

Chapter 8 Conclusions from the work presented.

In summary this work combines experimental work and numerical modelling. The majority of the time and effort was spent developing the model, understanding the theory, and fitting the experimental data with the model.

Chapter 2

Neutron Scattering

2.1 Neutron scattering introduction

Neutrons are normally considered as a particle. However due to their small size they have wave properties associated with them. Understanding a neutrons interaction with matter is therefore a quantum mechanical problem. It is the wave properties of neutrons that make them useful as a technique to look at structures on a small length scale.

Neutron scattering is a probing technique using the deflection of neutron radiation to study properties of a solid or liquid structure. Probing techniques using radiation generally require the wavelength of the radiation to be similar to the length scale of the structure of interest. For instance x-ray radiation is used to probe the structure of crystalline solids as the wavelength of x-rays is similar to the distance between atoms. Neutrons can also be used to probe the structure of crystalline solids. Neutrons have a wavelength related to their mass and velocity, which is given by the de Broglie formula

$$\lambda = \frac{h}{mv} \tag{2.1}$$

where h is Planks constant, m is the mass of the neutron and v is the velocity of the neutron. Neutrons used in scattering experiments generally have a wavelength in the order of Angstroms. The wavelength of the neutron is controlled by controlling the velocity of the neutrons as explained in section 2.4.1.

Compared with equivalent power x-ray facilities the flux of neutrons from a neutron source is about 14 orders of magnitude lower than the flux of photons [69]. Production of neutrons requires specialist facilities which are expensive to build and run.

Why then use neutrons as a probing technique? The main reason for using neutrons is how they interact with atoms. Unlike other probing techniques which use electromagnetic radiation (such as x-ray scattering) and interact with the electron cloud surrounding an atom, neutrons interact with the nucleus of an atom. Because of this the sample appears far less dense to a neutron beam than to an x-ray beam. This allows far greater penetration depth, so neutrons can probe deeper into samples. As a comparison the decrease in intensity of a neutron beam in aluminium is 1% per mm for a neutron beam compared with 99% per mm for an x-ray beam.

X-rays are scattered more strongly as the atomic number of the atoms in the scattering medium increases. For neutrons the strength of scattering is independent of atomic number. The

strength of scattering for neutrons can vary for different isotopes of the same type of atom. This is particularly useful in studies on soft condensed matter, as labelling molecules by changing the isotope of one of the elements in the material is far less obtrusive to the chemical properties than labelling with another element. Figure 2.1 shows the relative strengths of scattering from different elements for x rays and neutrons. It can be seen that the scattering for the ^{2}H isotope of hydrogen is much larger than the ^{1}H isotope.

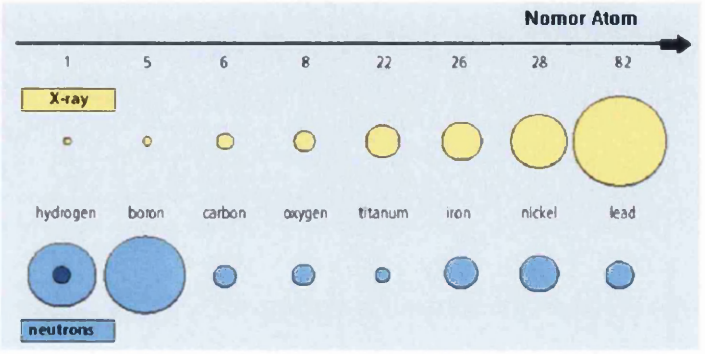

Figure 2.1: Relative strengths of scattering for different elements for x rays and neutrons. H shows the scattering from isotopes ^{1}H (darker circle)and ^{2}H (lighter circle) (taken from reference [44])

2.2 Basic principles of neutron scattering

The basic geometry of a neutron scattering experiment is shown in figure 2.2

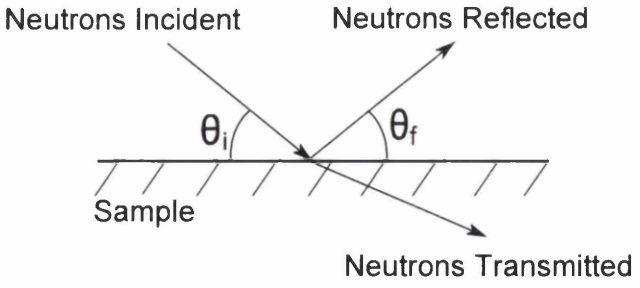

Figure 2.2: Basic Scattering experiment geometry

Neutrons impinging on a sample are either reflected from the sample or transmitted through the sample. The diffracted neutrons are then measured by a detector to give information about

the structure of the sample.

2.2.1 Elastic and inelastic Scattering

Scattering may be elastic or inelastic. Elastic scattering neutrons scattered from a nucleus retain all their initial energy and momentum. In inelastic scattering the neutron can lose or gain energy in the interaction with the nucleus, changing the energy of the nucleus also, as the energy of the system must be maintained. The momentum of the neutron is changed. Inelastic scattering can be used to look at the dynamics of small structures. In this work only elastic scattering is used, so all theoretical discussions from this point on shall refer to elastic scattering.

2.2.2 Braggs law

Braggs law is an example of how information about the structure of a crystalline material can be found using wave like properties from scattering experiments. The diffraction of neutrons from atoms in two different crystalline planes separated by a distance d is shown in figure 2.3.

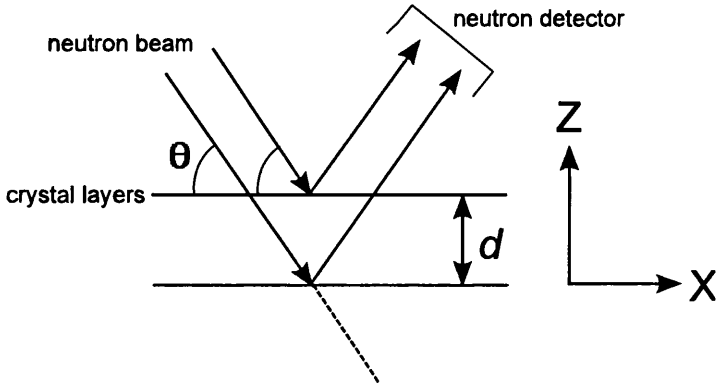

Figure 2.3: Diffraction of neutrons from two crystalline layers

For constructive interference the conditions of equation 2.2 must be fulfilled.

$$n\lambda = 2d\sin\theta \tag{2.2}$$

where n is an integer and θ is the angle of incidence. This is known as Bragg's law. Immediately

information about the spacing of atoms in the sample is found in terms of the wavelength λ and the angle of incidence. The scattering can be represented in terms of wave vectors for the incoming and outgoing waves. If neutrons with a range of different wavelengths or different angles of incidence are scattered from the sample, then much stronger reflection will be given for those that fulfill Braggs law, as these neutrons will all interfere constructively, allowing the inter atomic spacing to be probed.

2.3 Scattering from surfaces and interfaces

Neutrons can be used to probe structures much larger than their wavelength. By making the incident angle small, neutrons can be used to probe structures in the order of up to hundreds of microns. If the angle of incidence is small enough then the scattering medium will appear continuous to the neutrons. In thin film samples, such as the ones used in this work, neutrons will mostly pass through the bulk materials and diffraction will be dominated by contrast in the scattering strength between media either side of interfaces present in the sample. The scattering length density is a measure of strength scattering from a material and will be discussed further in section 2.6. The larger the contrast in scattering strength the greater the scattering. By controlling the scattering strength of the films then the reflectivity from interfaces of interest can be made dominant.

Neutrons can probe the surface structure of surfaces and interfaces. Pynn [69] describes neutron waves as probe waves with effective wavelength λ_{probe} which is given by

$$\lambda_{probe} = \frac{\lambda}{2\sin\theta} \tag{2.3}$$

This is effectively the same as Braggs law but for non atomic spacing. Probe waves of effective wavelength λ_{probe} will find if there are features on the interface that are spaced a distance apart d where $d = \lambda_{probe}$. If these features are present then constructive interference will occur. Spacing of features on the surface or interface in the z direction and the x, y plane can be measured, as will be shown in the next two subsections.

2.3.1 Momentum transfer

The neutron wave vector has magnitude $2\pi/\lambda$, and points in the direction of the neutron momentum. Neutrons incident on the sample and scattered by the sample shall be denoted by $\mathbf{k_i}$ and $\mathbf{k_f}$ respectively. The wavevectors $\mathbf{k_i}$ and $\mathbf{k}_f$ have components in the x, y and z directions denoted k_x, k_y and k_z, where x and y are in plane coordinates and z is perpendicular to the scattering sample surface. For the wavevector $\mathbf{k}_i$ the components in each direction are given by

$$\mathbf{k}_i = (k_{ix}, k_{iy}, k_{iz}) = \frac{2\pi}{\lambda}(\cos\theta_i \cos\varphi_i, \cos\theta_i \sin\varphi_i, \sin\theta_i) \tag{2.4}$$

where θ_i is the angle the incident beam makes with the surface, φ_i is the azimuth angle and λ is the de Broglie wavelength of the incident neutron. Similarly the diffracted beam is defined by

$$\mathbf{k}_f = (k_{fx}, k_{fy}, k_{fz}) = \frac{2\pi}{\lambda}(\cos\theta_f \cos\varphi_f, \cos\theta_f \sin\varphi_f, \sin\theta_f) \tag{2.5}$$

assuming λ is constant. The wavevectors $\mathbf{k}_i$ and $\mathbf{k_f}$ for a scattering experiment are shown in figure 2.4

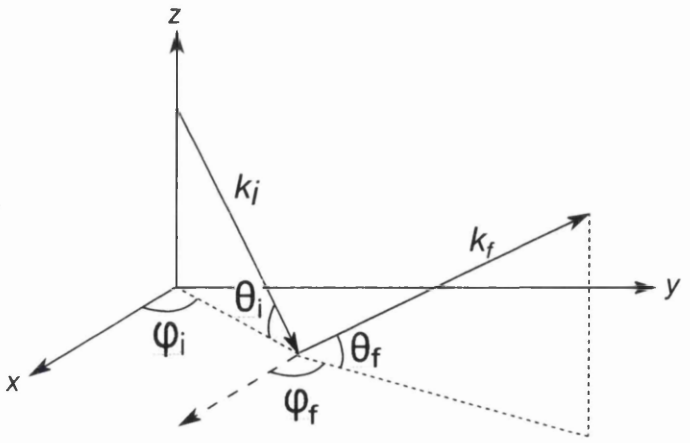

Figure 2.4: $\mathbf{k}$ vectors showing the angles of scattering

The difference in $\mathbf{k}_i$ and $\mathbf{k}_f$ is called $\mathbf{q}$ where

$$\mathbf{q} = \mathbf{k}_f - \mathbf{k}_i \tag{2.6}$$

The parameter $\mathbf{q}$ is known as the reflectivity vector and also the momentum transfer. From equation 2.1 it can be seen that $mv = h/\lambda = hk/2\pi = \hbar k$. The change in momentum of a neutron from a scattering process is then $\hbar\mathbf{q}$ and the momentum transfer in x, y and z directions are q_x, q_y and q_z respectively, where $q_x = \mathbf{k_{fx}} - \mathbf{k_{ix}}$ etc.

For neutron reflectivity experiments (as used in this work and discussed in section 2.4) it is common to use a ribbon beam that is highly collimated in the x direction and broad in the y direction as shown in figure 2.5.

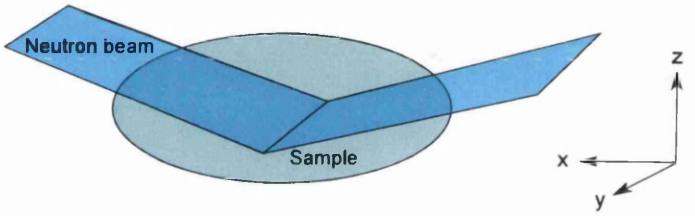

Figure 2.5: Ribbon beam highly collimated in the x direction

For this experimental configuration the beam intensity is integrated over q_y and the scattering is a function of q_x and q_z only. The scattering vectors q_z and q_x are given by

$$q_z = k_{iz} + k_{fz} = \frac{2\pi}{\lambda}(sin\theta_i + sin\theta_f) \tag{2.7}$$

$$q_x = k_{fx} - k_{ix} = \frac{2\pi}{\lambda}(cos\theta_f - cos\theta_i) \tag{2.8}$$

In a reflectivity experiment the intensity is measured as a function of θ_r and λ for a fixed value of θ_i. For small values of θ_i and θ_r equations 2.7 and 2.8 can be written

$$q_z = \frac{2\pi}{\lambda}(\theta_i + \theta_f) \tag{2.9}$$

$$q_x = \frac{2\pi}{\lambda}\left(\frac{\theta_f^2 - \theta_i^2}{2}\right) \tag{2.10}$$

From equations 2.9 and 2.10 it is evident that the relationship between q_x, q_z space and θ, λ space is non-linear. Figures 2.6 and 2.7 show how q_z and q_x vary with $\theta_r - \theta_i$ and λ.

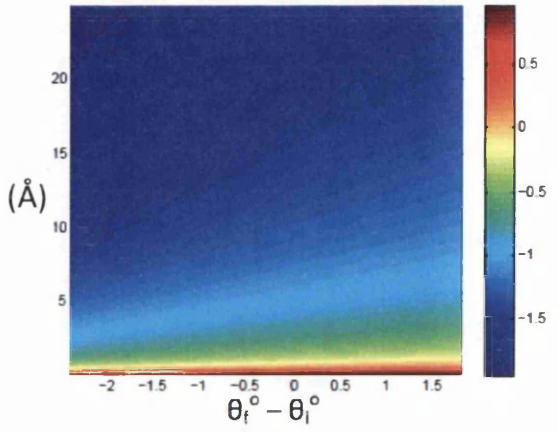

Figure 2.6: q_z contours in λ, θ_f space. Scale bar is in units of Å on a log scale

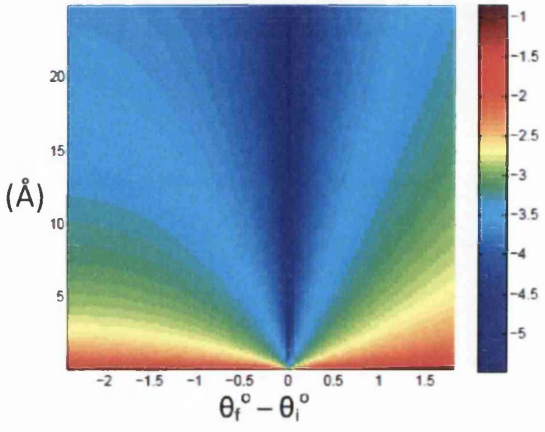

Figure 2.7: q_x contours in λ, θ_f space. Scale bar is in units of Å on a log scale

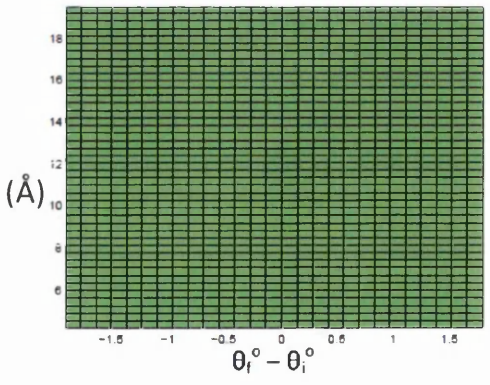

Figure 2.8: Grid in θ, λ space

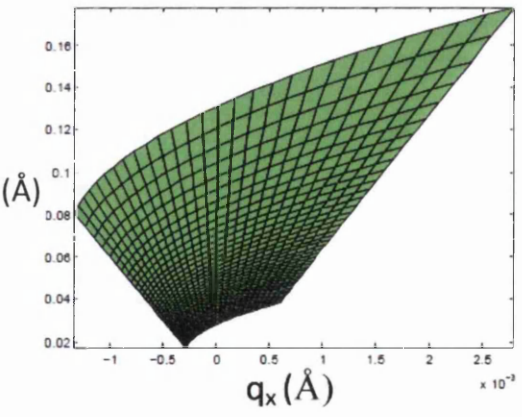

Figure 2.9: Grid transformed into q space

In figure 2.6 contour lines of constant q_z point toward $-\theta_i$. In figure 2.7 contour lines of constant q_x curl out from $q_x = 0$ ($\theta_r - \theta_i = 0$). This results in difficulties when transforming experimental data from q space to θ, λ space or vice versa. Transforming pixels from θ, λ space to q space is shown in figures 2.8 and 2.9. It can be seen that the pixels in q space are non Cartesian. For this reason all experimental data presented in this thesis is presented in θ, λ space.

2.3.2 Specular and off specular scattering

For a given neutron of wavelength λ, $\mathbf{q}$ is dependent on the angle of incidence θ_i and the angle of reflection θ_f. If $\theta_i = \theta_f$ then this is specular scattering with q_z being the only non zero component. If $\theta_i \neq \theta_f$ then this is off specular scattering. Considering the interface between two continuous homogeneous media off specular scattering occurs if the interface has roughness or lateral structure (ie if the interface z position changes as a function of x). Scattering from a perfectly smooth ideal surface will have no off specular component. Wavevector diagrams for specular and off specular scattering are shown in figures 2.10 and 2.11 respectively.

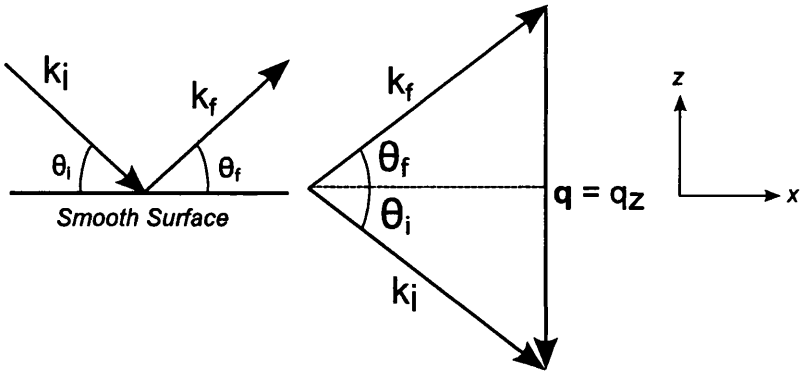

Figure 2.10: $\mathbf{q}$ for specular scattering ($\theta_i + \theta_f = 2\theta_i$)

For the specular case (figure 2.10) it can be seen that

$$\mathbf{q} = q_z = \frac{4\pi}{\lambda} \sin 2\theta_i \tag{2.11}$$

For the off specular case (figure 2.11) it can be seen

$$q_z = \frac{2\pi}{\lambda}(\sin\theta_i + \sin\theta_f) \tag{2.12}$$

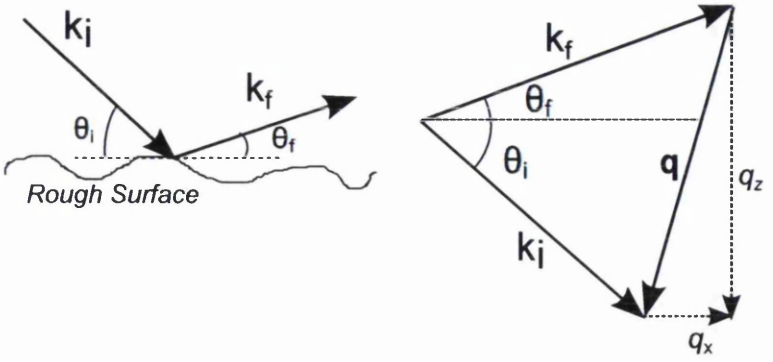

Figure 2.11: q for off specular scattering ($\theta_i \neq \theta_f$)

$$q_x = \frac{2\pi}{\lambda}(\cos\theta_f - \cos\theta_i) \tag{2.13}$$

The specular scattering can give information about structures in the z direction, for example the thickness of uniform thin films. Because $q_x = q_y = 0$ no information is found from specular scattering about the in plane features of the sample. Information about the in plane structure of the sample can be found from off specular scattering, where $\theta_i \neq \theta_f$. Generally the off specular scattering is orders of magnitude lower intensity than the specular scattering and presents a far greater challenge in data acquisition and data analysis.

Since the reflectivity is a function of $\mathbf{q}$, which is reciprocal to the wavelength, the size of the features that correspond to scattering at a certain value of $\mathbf{q}$ are in the x, and z planes $\frac{2\pi}{q_x}$ and $\frac{2\pi}{q_z}$ respectively.

2.4 Experimental neutron scattering techniques

In this section the basic principles of neutron reflectivity experiments shall be reviewed, including details of production and detection of neutrons and specific instruments used in this work.

All neutron scattering experiments consist of three basic elements:

1. A source of neutrons directed at a sample
2. Scattering of neutrons from the sample
3. Detectors to detect the direction and/or energy of scattered neutrons

as shown in figure. This work deals with reflectivity experiments. The basic geometry of a neutron reflectivity experiment is shown in figure 2.12

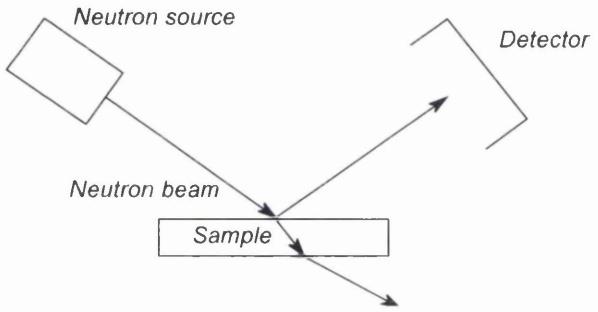

Figure 2.12: Basic geometry of a neutron reflectivity experiment

The reflectivity is the ratio of the number of neutrons reflected from the sample to the number of incident neutrons. If all incident neutrons at a particular wavelength are reflected at the same angle then the reflectivity at that wavelength and angle of reflection is 1. To measure the reflectivity as a function of neutron wavelength the energy of neutrons hitting the sample needs to be known to a high degree of accuracy.

2.4.1 Neutron sources

There are two main types of neutron sources, reactor sources and spallation sources. In a reactor neutrons are produced by nuclear fission using uranium fuel. In a spallation source high

energy protons are fired at a metal target (typically tungsten or uranium) which 'dislodges' neutrons. Reactor sources produce continuous beams of neutrons, whereas spallation sources produce pulses of neutrons. Generally the energy of neutrons directly from these sources is high and therefore the wavelength of the neutrons is too small to be used in the investigation of materials on atomic lengthscales. The energy of the neutrons is reduced to a usable level by passing the neutrons through a moderator. This moderator usually consists of a large volume of liquid with high scattering length density. Collisions with atoms in the moderator quickly reduce the energy of the neutrons to a level similar to that of the atoms in the moderator. The energy of the neutrons leaving the moderator can be controlled by its temperature, and the neutrons are referred to as thermal neutrons. Typical energy distributions for neutrons from each source type are shown in figure 2.13 [69]

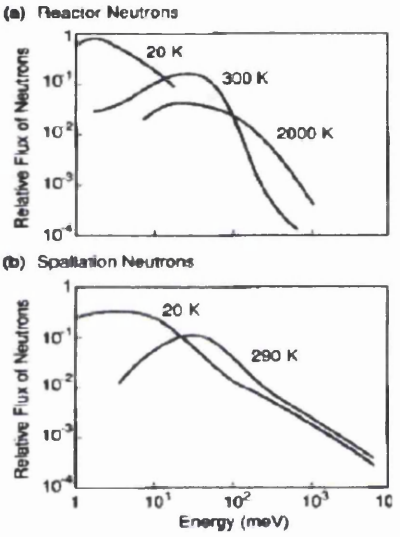

Figure 2.13: Relative flux of neutrons at a) ILL reactor Grenoble, b) LANSCE spallation source Los Alamos (taken from reference [69])

After passing through the moderators neutrons are guided to a variety of instruments. For neutron reflectivity neutrons reflected from the sample are measured at the detector. There are two choices of experimental modes to measure reflectivity for neutrons over a range of $\mathbf{q}$, time of flight (TOF) mode and monochromatic mode.

2.4.2 Neutron detectors

The detection of a neutron involves its absorption by a suitable nuclei followed by detection of charged particles from the absorption event. ^{3}He gas is most commonly used as the absorption medium. The efficiency of the detector is determined by how quickly it can respond to consecutive neutrons arriving. The time before the detector is ready to detect another neutron is known as dead time. There are two types of neutron detectors. A single detector collects data at a specified angle and will consist of a single pixel. An area detector can measure a wide range of angles at the same time, so off specular reflectivity data from neutrons scattered at different angles can be collected simultaneously. The area detector is made up of an array of pixels.

2.4.3 Monochromatic mode

In a monochromatic experiment neutrons of a single wavelength are incident on the sample. In order to measure reflectivity over a range of $\mathbf{q}$ the angle of incidence on the sample is varied throughout the experiment. The angle of the detector should be varied with the sample in order to keep q_x at zero in order to gather specular data. Off specular data is collected using a rocking scan. The angle of the detector is kept constant, but the angle of the sample is varied. When the angle of incidence is small, by keeping the sum of the angle of incidence and angle of reflection to be constant then off specular reflectivity for a range of q_x can be measured at constant q_z. The footprint of the beam on the sample will change with angle of incidence and this must be taken into account when fitting reflectivity data.

2.4.4 Time of flight mode

In TOF experiments neutrons of a range of wavelengths are incident on the sample in pulses. By knowing the path length of the neutrons, the time of a pulse of neutrons leaving the source and measuring the time each neutron reaches the detector the wavelength of the neutrons can be determined. The range of wavelengths means that reflectivity for the entire $\mathbf{q}$ range is collected simultaneously. Due to the use of pulses of neutrons, TOF scattering lends itself to use in spallation sources. Reactor sources can be used by including choppers between the neutron source and the instrument. A chopper consists of a rotating disc with a small segment cutout from it. The chopper blocks the neutron beam except when the cutout segment passes in front

of it, allowing neutrons through for a short time period. This effectively pulses the neutron beam. The chopper speed can be varied to change the pulse timing. Spallation sources can also use choppers to better define the pulses of neutrons. A TOF experiment must include a method to prevent frame overlap where slow neutrons from one pulse arrive at the detector at the same time as fast neutrons from the next pulse.

2.4.5 Coherence length

The coherence length is the maximum in plane length on a sample surface over which neutrons will coherently interfere at the detector and will determine the maximum in plane lengthscale over which an instrument can probe a sample. Different neutrons in the beam are not coherent so each neutron interferes with itself [7]. Using the uncertainty principle and considering the energy spread $\Delta\lambda$ and the angular spread Δk of the neutron source then the distance on the surface over which a neutron can interfere with itself can be determined geometrically. For further discussion the reader is referred to reference [75]. The coherence length on the reflectometers used in this work is of the order of tens of microns.

2.4.6 Resolution

There are several factors which affect the resolution of the instrument. There are wavelength and angular resolution effects. Wavelength resolution is caused by the length of time a neutron pulse for TOF and by the distribution of wavelengths in monochromatic experiments. For a TOF experiment wavelength resolution is given by [75]

$$\frac{\Delta t}{t} = \frac{\Delta\lambda}{\lambda} \tag{2.14}$$

where Δt is the length of time of a pulse of neutrons (how long the chopper is opened for to allow neutrons through) and t is the TOF of a neutron (the time taken for a neutron to get from the chopper to the detector). The wavelength resolution is $\frac{\Delta\lambda}{\lambda}$. It can be improved by using two choppers and increasing the offset of the openings between them, at the expense of neutron flux. For monochromatic experiments the wavelength resolution is given by the full width half maximum (FWHM) of the distribution.

Angular resolution $\frac{d\theta}{\theta}$ is dominated by the divergence of the beam. Efforts are made to keep

the beam well collimated to minimise the resolution. In general there will be several sets of collimators along the path of the beam, with the final collimation taking place just before the sample by passing the beam through a pair of cadmium slits as shown in figure 2.14. The angular resolution $\frac{d\theta}{\theta}$ is dominated by the spacing of these slits. Better resolution comes at the expense of reduced flux.

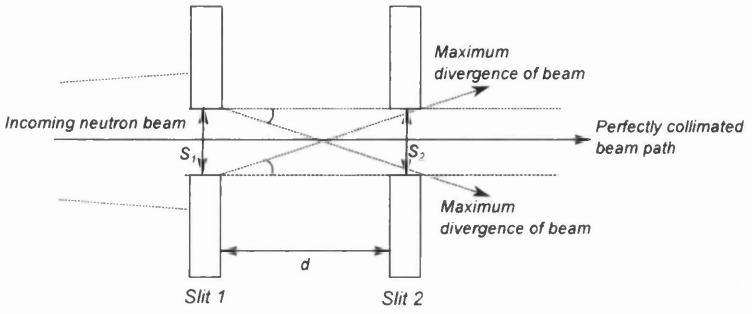

Figure 2.14: Slit geometry of neutron scattering experiment

The divergence of the beam where $d\theta$, the angular divergence of the beam is given by

$$d\theta = \tan^{-1}\left(\frac{s_1 + s_2}{2d}\right) \tag{2.15}$$

where s_1 and s_2 are the opening of the first and second slits respectively and d is the slit spacing. There are also resolution effects from the pixel size of the detector, however these are normally small when compared with the effects of the slit geometry.

2.4.7 Reflectometers

Experiments in this work were neutron reflectivity experiments, using neutron reflectometers D17, CRISP and Offspec.

2.4.8 D17

The D17 instrument is located at the Institute Laue Langevin (ILL) in Grenoble France, which is a reactor source providing a constant beam of neutrons. Since the variation in flux is minimal it is assumed to be constant in time. It can operate in either TOF or monochromatic modes.

Samples are mounted vertically on the instrument and the neutron beam is collimated to give a ribbon beam, which gives good resolution in q_x and q_z. The q_y direction is integrated over. Figure 2.15 shows diagrams of D17 in TOF and monochromatic modes.

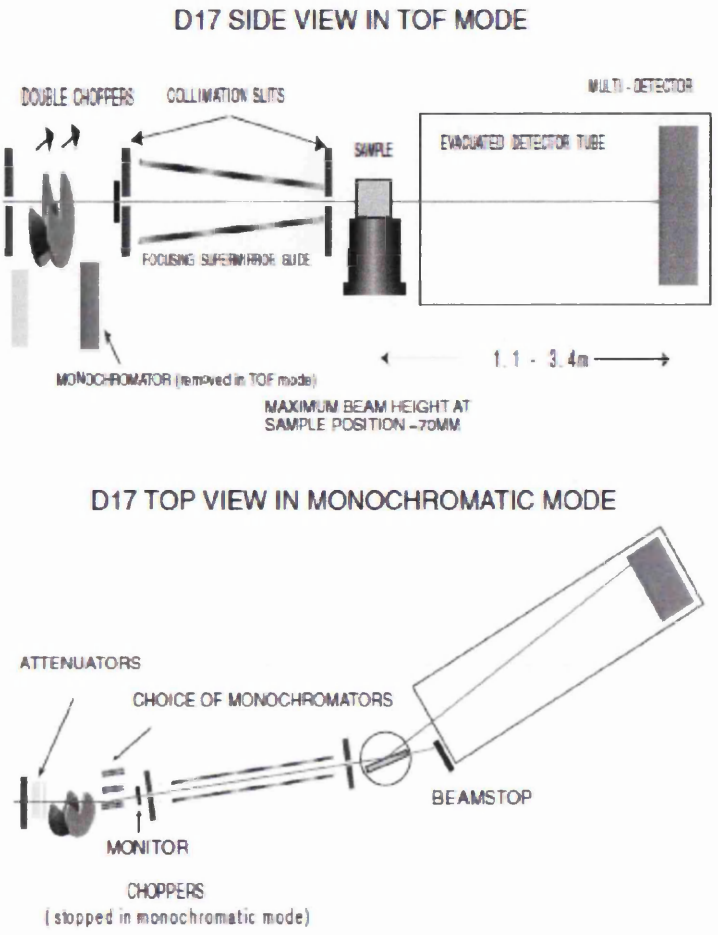

Figure 2.15: Schematic of D17 in TOF and monochromatic modes taken from reference ([19])

The detector is an area detector with pixel size of 1.04mm and a low dead time of 350nanoseconds. In both modes there are two collimation slits in front of the sample. There is a small air filled section to the flight path where the sample is placed, though a vacuum chamber with quartz windows can be placed over the sample to further reduce the flight path in air to a few mm. To take into account difference in efficiency of the detector pixels the neutron beam is diffracted using a water cell which scatters the neutrons evenly at all possible angles measured by the

detector. Experimental data is then divided through by the result of this run.

D17 TOF mode

In TOF mode D17 uses two choppers spaced 87mm apart to pulse the neutrons. The opening in the choppers can be offset to give higher flux at the expense of resolution. The chopper period is set to the TOF of the slowest neutrons in the instruments useful range which have a wavelength 30 Å. A neutron mirror is used to prevent frame overlap which reflects neutrons of longer wavelength out of the beam. The wavelength resolution of the instrument is given by

$$\frac{d\lambda}{\lambda}(q) = \frac{dT}{T}(q) = \frac{C}{D} + \frac{\phi}{2\pi}(\frac{q}{q_{min}}) \tag{2.16}$$

where dT is the time of a pulse, T is the time of flight of a neutron, C is the distance between the choppers, D is the TOF distance, ϕ is the angular offset between the choppers in radians, q is magnitude of $\mathbf{q}$ and q_{min} is the minimum q measurable at a given angle. If $\phi = 0$ then the wavelength resolution has no q dependence [19]. The wavelength resolution varies between 0.1% and 20%.

The distribution of neutron wavelengths in the beam is taken into account by measuring the incident beam directly on the detector using the slit settings to be used in the experiment. Experimental reflectivity data is then divided through by the direct beam run. A q_z range of between 0.002Å^{-1} and $2\ \text{Å}^{-1}$ can in principle be measured, however the background of the instrument is of an order of between 10^{-7} and 10^{-6} and limits the useful q_z range to $\sim 0.2\text{Å}^{-1}$.

D17 monochromatic mode

In monochromatic mode the choppers are set to an open position and a monochromator which blocks all other wavelengths of neutrons is placed in front of the beam. The wavelength of the neutrons is chosen to be the peak wavelength flux of the reactor and is $5.4\ \text{Å}^{-1}$, with a fixed wavelength resolution of 5%. An attenuator is placed in front of the beam to reduce the flux so that the detector does not become saturated. A q range of 0.005Å^{-1} to 1.5Å^{-1} can be measured. Again this is limited to $\sim 0.2\text{Å}^{-1}$ due to background.

2.4.9 CRISP

CRISP is located at ISIS in the UK which is a spallation source. It is a TOF instrument and has the option of a linear detector or a single detector. Samples are mounted horizontally. The single detector can be used for specular experiments and in combination with extra slits after the sample gives lower background. Like D17 the neutron beam is collimated into a ribbon beam and integrates over q_y. Figure 2.16 shows the geometry of CRISP. Slits 3 and 4 are removed when using the linear detector.

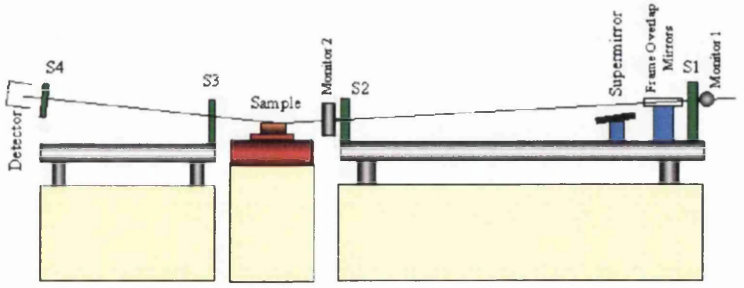

Figure 2.16: Schematic of CRISP taken from reference [16]

The neutrons are pulsed by the source, with the zero time for a pulse set by the initial pulse of protons hitting the target. Choppers are used in order to limit the wavelength range between 0.5 Å and 6.5 Å. This gives a measurable q range of 0.006Å-1 to 1.0Å-1. The useful q range is limited to $\sim$ 0.2 Å-1 by the reflectivity being dominated by background neutron radiation [16]. The resolution of the instrument is determined by the pulse time and the slit geometry. The angular resolution is dominant and the wavelength resolution is negligible.

2.4.10 Offspec

Offspec is a recently commissioned instrument using the new target station 2 at ISIS. It is specifically designed to have low background. It is is capable of probing smaller in plane length scales than standard reflectometers by using spin echo scattering, though this feature was not used in this work [22]. It has a wavelength range of 1.5 Å to 14.5 Å and uses choppers to limit the range. The resolution in q_z is 2.5% and is dominated by the slit geometry.

2.5 Scattering theory

In this section the basic ideas of scattering theory will be developed and expressions for scattering in the Born approximation (BA) and the distorted wave Born approximation (DWBA) will be stated. For the complete derivation of these expressions please refer to appendix A and quantum mechanics text books by Schiff [78], Sakurai [76] or Messiah [60]

Scattering theory is an important branch of classical and quantum physics. Almost all knowledge of nuclear physics and atomic structure has been gained from scattering experiments. In a scattering experiment a wave or particle is fired from a known direction at a target and its direction of scatter after the scattering event is measured.

The simplest type of scattering experiment to analyse is of a wave or particle interacting with a single fixed point potential. Clearly this situation is unrealistic in actual physical systems, nevertheless it forms the basis of analysis of more realistic systems.

2.5.1 Differential cross section

Scattering experiments are characterised by scattering cross section σ. A scattering experiment involves detecting the number of particles per unit time N, scattered into the solid angle $d\Omega$ in the direction (θ, ϕ). The number of particles entering $d\Omega$ is $Nd\Omega$ and is proportional to the incident flux per unit time crossing a unit area per unit time normal to the beam j_i. The scattering is analysed in terms of differential scattering cross section which gives the number of particles scattered into direction (θ, ϕ) per unit time per unit solid angle over the incident flux.

$$\frac{d\sigma}{d\Omega} = \frac{N}{j_i} \tag{2.17}$$

The total scattering cross section σ is obtained by integrating over all the differential scattering cross sections, giving $4\pi b^2$, the solid angle of a sphere multiplied by the scattering potential. It is related to the differential scattering angles $d\theta$ and $d\phi$ by

$$\sigma = \int \frac{d\sigma}{d\Omega} d\Omega = \int_0^{2\pi} d\phi \int_0^{\pi} d\theta sin\theta \frac{d\sigma}{d\Omega} \tag{2.18}$$

For a single fixed central potential where $b(\theta)$ represents the strength of the interaction between

the scattering particle and the potential, dependent on the distance between them. The number of particles scattered into the solid angle $d\Omega$ between the scattering angles θ and $\theta d\theta$ per unit time is equal to the number of particles passing the potential experienced by the particle between b and $b + db$. This is shown is figure 2.17.

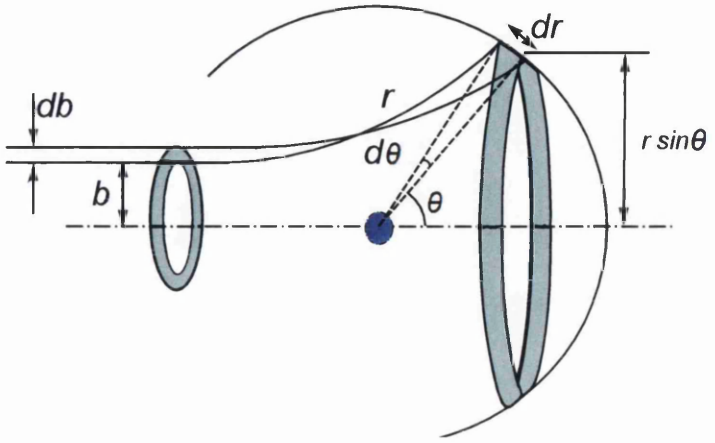

Figure 2.17: Differential scattering Cross section showing the scattering of a particle from a potential b into solid angle $d\Omega$ between θ and $\theta d\theta$

2.5.2 Quantum mechanical derivation

In quantum mechanics the incoming particles are represented by a wave function. Strictly speaking the scattering is found by solving the time dependent Schrödinger equation for the system, at a time before the scattering event and a time after the event. However if the compatible observables of energy and momentum of the particle are well defined, the wave packet is many wavelengths long and due to the uncertainty principle the position of the particle is not well defined. The wave packet can then be approximated by a plane wave $e^{i\mathbf{kr}}$. Since the potential does not change there is no time dependence and the system can be solved using the time independent Schrödinger equation (TISE). All that can be detected is the scattered particle wave function far from the scattering event. The scattered wave from a central potential will be a spherical wave whose amplitude decays with distance from its source. The wave function for a scattering event far from the potential is

$$\psi_k(\mathbf{r}) \cong e^{i\mathbf{kr}} + f(\theta, \phi)\frac{e^{ikr}}{r} \tag{2.19}$$

with the first and second terms on the right hand side representing the particle before the

scattering event and the scattered particle. The term $f(\theta, \phi)$ represents the amplitude of the scattered wave. In the case of scattering total normalisation is not required as it is the relative fraction of the incident beam scattered in each direction, or into a solid angle $d\Omega$ in direction (θ, ϕ) which is measured. As in the case of the classical system the flux of beam scattered into $d\Omega$ is equivalent to the flux of the beam passing through a small area $d\sigma(\theta, \phi)$. The relative probability of the wave being scattered into $d\Omega$ is found by squaring the wave function $\psi_k(\mathbf{r})$ giving $C|f(\theta, \phi)|^2 d\Omega$, where C is a constant. Relating this to $d\sigma$ gives the differential scattering cross section

$$\frac{d\sigma}{d\Omega} = \frac{|f(\theta, \phi)|^2}{(4\pi)^2} \tag{2.20}$$

where the $(4\pi)^2$ denominator is given by the square of solid angle of the sphere surrounding the scattering centre and the normalisation constant is disregarded. The probability of scattering into a state after collision is characterised by $f(\theta, \phi)$.

2.5.3 Born approximation

The expression for $f(\theta, \phi)$ can be expanded out in the form of an perturbation series. For derivation of the series please see appendix A. The Born approximation is a first order perturbation, taking the first term of the series. The result is

$$f_{BA} = -\frac{m}{2\pi\hbar} \int d^3r \phi_{\mathbf{k}_f} V \phi_{\mathbf{k}_i} \tag{2.21}$$

where $\phi_{\mathbf{k}_i}$ and $\phi_{\mathbf{k}_f}$ are the wavefunctions of the incident and scattered neutrons respectively, represented by plane waves and V is the scattering potential. $\phi_{\mathbf{k}_i} = e^{i\mathbf{k}_i\mathbf{r}}$ $\phi_{\mathbf{k}_f} = e^{i\mathbf{k}_f\mathbf{r}}$. The integral is over all r.

This first Born approximation is equivalent to Fermi's Golden rule, which maps the probability of a system in one state acted on by an operator transforming into any of a continuum of states. The Born approximation does not take into account diffraction, or multiple scattering.

2.5.4 Distorted wave Born approximation

The DWBA seperates the scattering potential in two potentials V_1 and V_2. The potential V_1 is the potential for an exactly solvable system and V_2 is a correcting term acting on it. The DWBA works well when the correcting term is small enough to be regarded as a perturbation. The expression for $f(\theta, \phi)$ in the first order DWBA is

$$f_{DWBA} \approx \int d^3r \psi^-_{\mathbf{k_f}} V_1 \phi_{\mathbf{k}_i} + \int d^3r \psi^-_{\mathbf{k_f}_i} V_2 \psi^+_{1\mathbf{k}_i} \tag{2.22}$$

where $\psi^-_{\mathbf{k_f}}$ is the time reversed ideal wave function for a neutron with wave number $\mathbf{k}_f$, $\psi^-_{\mathbf{k_i}}$ is ideal wave function for a neutron with wave number $\mathbf{k}_i$ and $\phi_{\mathbf{k}_i}$ is the ideal incoming plane wave $e^{i\mathbf{k}_i\mathbf{r}}$. For details or derivation of these terms including the time reversed states please refer to appendix A. When applying the DWBA to thin films V_1 is used to describe a perfectly flat ideal film and the V_2 describes the roughness, which is the perturbation of the morphology of the film from the ideal film. This is discussed in detail in section 2.9.

2.6 Interactions between neutrons and assemblies of atoms

This section looks at how neutrons interact with an assembly of atoms, as found in any material. The basic concepts are explained. For a fuller derivation of the terms please refer to appendix B and Higgins and Benoit chapter four [41].

The scattering amplitude f of a neutron scattered by a potential V is described by the Born approximation (see appendix A.1.1, equation 2.21). It can be written as an integral equation in terms of $\mathbf{q}$ the momentum transfer as $\mathbf{q} = \mathbf{k}_i - \mathbf{k}_f$ where $\mathbf{k}_i$ and $\mathbf{k}_f$ are the wave numbers of the incoming and outgoing neutrons respectively. Solving for a single neutron impinging on a nucleus results in a term b which is a measure of the strength of scattering from the nucleus and is called the scattering length of the nucleus. The total scattering potential for an assembly of nuclei $V(r)$, as found in any medium is given by the summation of the potential of each individual nucleus. Using Fermi pseudo potential [60] and the Born approximation (see equation 2.21) the potential can be shown to be

$$V(\mathbf{r}) = \frac{2\pi\hbar}{m} \sum_j b_j \delta(\mathbf{r} - \mathbf{r_j}) \tag{2.23}$$

and the differential scattering cross section is shown to be [41]

$$\frac{d\sigma}{d\Omega} = N\langle b^2 \rangle + \langle b \rangle^2 \sum_{j \neq k}^{N} \langle e^{i\mathbf{q}\cdot(\mathbf{r_k} - \mathbf{r_j})} \rangle \tag{2.24}$$

where N is the number of nuclei and j, k are labels numbering each atom. For a fuller derivation of equation 2.24 please refer to appendix B.1. The scattering cross section can be split into coherent and incoherent parts. The first term on the right hand side defines the incoherent scattering. The incoherent scattering is caused by different isotopes in the scattering medium and the different spin states of the neutrons (see appendix B.1.1). It gives no information about the structure of the scattering medium, as it has no dependence on the relative position of the nuclei. In an isotopically pure scattering medium, scattering neutrons with a single spin state would have no incoherent scattering. The coherent scattering is dependent on the relative positioning of the nuclei and therefore can give information about the scattering medium's structure.

2.6.1 Coherent scattering

The remainder of this section shall look at solely at coherent scattering and b shall refer to the coherent scattering length. When scattering is at a small angle each molecule can be described as a point in space $\mathbf{r}$, rather than an assembly of nuclei. The scattering length b for a molecule at point $\mathbf{r}$ is the sum of all the scattering lengths from the individual atoms of the molecule.

The coherent scattering can be written

$$\left(\frac{d\sigma}{d\Omega}\right)_{coh} = b^2 \sum_{j=1}^{N}\sum_{k=1}^{N}\langle e^{i\mathbf{q}\cdot(\mathbf{r_j}-\mathbf{r_k})}\rangle \tag{2.25}$$

The summation equation can be changed into a integral over the volume of the scattering medium using a Dirac delta function. Defining the local density of molecules by

$$n(\mathbf{r}) = \sum_{j=1}^{N}\delta(\mathbf{r}-\mathbf{r}_j) \tag{2.26}$$

The expression $\int_V f(\mathbf{r})\delta(\mathbf{r}-\mathbf{r}_k)d\mathbf{r} = f(\mathbf{r}_k)n(\mathbf{r})$ gives the density of molecules at any point $\mathbf{r_k}$. Therefore the summation over one of the exponential terms can be written

$$\sum_{k=1}^{N} e^{i\mathbf{q}\cdot\mathbf{r_k}} = \int_V \sum_{k=1}^{N} e^{i\mathbf{q}\cdot\mathbf{r_k}}\delta(\mathbf{r}-\mathbf{r}_k)d\mathbf{r} = \int_V n(\mathbf{r})e^{i\mathbf{q}\cdot\mathbf{r}}d\mathbf{r} \tag{2.27}$$

From this result the coherent differential cross section can be written

$$\left(\frac{d\sigma}{d\Omega}\right)_{coh} = b^2 \left\langle \int_V n(\mathbf{r})e^{-i\mathbf{q}\cdot\mathbf{r}}d\mathbf{r}\int_V n(\mathbf{r}')e^{i\mathbf{q}\cdot\mathbf{r}'}d\mathbf{r}'\right\rangle \tag{2.28}$$

which can then be written

$$\left(\frac{d\sigma}{d\Omega}\right)_{coh} = b^2 \int_V\int_{V'} e^{-i\mathbf{q}\cdot(\mathbf{r}-\mathbf{r}')}\langle n(\mathbf{r})n(\mathbf{r}')\rangle d\mathbf{r}d\mathbf{r}' \tag{2.29}$$

Assuming that there is no correlation between the molecular density of the scattering medium then $\langle n(\mathbf{r})n(\mathbf{r}')\rangle$ is simply the square average density N^2 per unit volume. Equation 2.29 becomes

$$\left(\frac{d\sigma}{d\Omega}\right)_{coh} = N^2 b^2 \int_V \int_{V'} e^{-i\mathbf{q}\cdot(\mathbf{r}-\mathbf{r}')} d\mathbf{r} d\mathbf{r}' \tag{2.30}$$

This is the expression derived by van Hove [100] for neutrons scattered by an assembly of atoms. Nb is called the scattering length density and is tabulated for many mediums. The strength of the scattering is therefore the product of the squares of the scattering length of the scattering centres and the density of the scattering centres.

2.7 Specular scattering from thin films

In specular scattering the angle of reflection is equal to the angle of incidence and $q_x = q_y = 0$. Specular reflectivity can probe the scattering length density (SLD) profile of a sample in the z direction, perpendicular to the sample surface. The composition of the sample may vary continuously or can be in discrete layers. A continuous system can be modeled as a stack of many discrete thin layers. No information can be found about the lateral structure of the surface. The theory employed in analysing specular reflectivity is somewhat analogous to classical refraction through a medium. The medium has a refractive index n, as in classical optics, which is a measure of the wave number of the neutron in the medium compared with its wavenumber in air. It is dependent on the scattering length density, mentioned in section 2.6. The angle of reflection and transmission through the medium is dependent on the angle of incidence and the refractive index. Fresnel coefficients can be found which determine the ratio of neutrons transmitted and reflected by the sample by solving the Helmholtz wave equation [83].

2.7.1 Refractive index

The refractive index of a material n is the ratio between the wave number on the medium and the wave number in a vacuum. It is given by

$$n = \sqrt{1 - \frac{V(r)}{E}} = \sqrt{1 - \frac{\lambda^2 \rho(r)}{\pi}} \tag{2.31}$$

where $V(r)$ is the potential of the medium impeding the neutrons, E is the energy of the neutrons, λ is the de Broglie wavelength of the neutrons and ρ is the scattering length density of the medium. If the wavelength of the neutrons is of the order of Angstroms then n differs from unity by a factor of 10^{-5} and n can be approximated by

$$n \approx 1 - \frac{\lambda^2 \rho(r)}{2\pi} \tag{2.32}$$

If ρ is positive then $n < 1$ and neutrons can be totally externally reflected at small enough angles of incidence.

2.7.2 Helmholtz equation

The interaction of neutrons with matter is described by the time independent Schrödinger equation where the potential of the scattering medium is constant in time. The Schrödinger equation can be recast in the form of the three dimensional Helmholtz equation which describes the propagation of a wave through a medium.

$$\nabla^2\psi(\mathbf{r}) + \chi^2\psi(\mathbf{r}) = 0 \tag{2.33}$$

where $\chi = \sqrt{\frac{2m(E-V)}{\hbar^2}}$ and E is the energy of incident neutrons. The potential χ can be written equivalently as

$$\chi = \sqrt{k^2 - 4\pi\rho(r)} \tag{2.34}$$

where $k = \sqrt{\frac{2mE}{\hbar^2}}$ the wave number of the neutron in a vacuum. Therefore χ is the wave number of a neutron in the medium. In order to solve equation 2.33 across an interface between two mediums of different ρ, the wavefunction and the derivative of the wavefunction must be continuous at the interface. For specular reflectivity the z component of the wave number k is of interest, denoted k_z. Therefore only the 1D Helmholtz equation is required. The magnitude of k_z is given by

$$k_z = k\sin\theta = \frac{2\pi}{\lambda}sin\theta \tag{2.35}$$

The z component of the wave number in vacuum will be denoted $k_{z,0}$ and the wave number in the medium $k_{z,m}$.

From equation 2.34 in the z direction the k_z component of the neutron inside the medium is given by

$$k_{z,m} = \sqrt{k_{z,0}^2 - 4\pi\rho_m} \tag{2.36}$$

The critical wave number $k_{z,c}$ is given by $\sqrt{4\pi\rho_m}$. For neutrons with wave numbers below the critical wave number total reflection occurs.

We must now define the equation for neutrons in a vacuum (or air) and in the medium, and use the boundary conditions described above to solve them. The 1D Helmholtz equations for neutrons in a vacuum and in the medium are

$$\psi''(z) + k_{z,0}\psi(z) = 0 \text{ for } z \geq 0 \text{ (vacuum)} \tag{2.37}$$

$$\psi''(z) + k_{z,m}\psi(z) = 0 \text{ for } z \leq 0 \text{ (medium)} \tag{2.38}$$

The problem then becomes a 1D potential barrier problem as shown in figure 2.18.

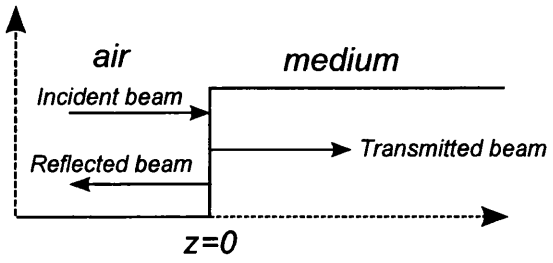

Figure 2.18: Specular scattering experiment showing incident, reflected beam and transmitted neutron beam

The solutions to the 1D wave equations are

$$\psi(z) = e^{ik_{z,0}z} + re^{-ik_{z,0}z} \text{ for } z \geq 0 \tag{2.39}$$

$$\psi(z) = te^{ik_{z,m}z} \text{ for } z \leq 0 \tag{2.40}$$

The first term on the right of equation 2.39 represents the incident wave and the second term the reflected wave. The sign in front of the exponent represents the direction the wave is traveling in, plus represents the direction of the incident beam and minus the direction of the reflected beam. The r coefficient in the second term is the complex Fresnel reflectivity coefficient, which is the amplitude of the wave. Equation 2.40 represents the wave transmitted into the medium, where t is the Fresnel transmission coefficient. From the boundary conditions at $z = 0$ it can be shown

$$1 + r = t \tag{2.41}$$

$$k_{z,0}(1 - r) = k_{z,m}t \tag{2.42}$$

Solving these equations for t and r give

$$r = \frac{k_{z,0} - k_{z,m}}{k_{z,0} + k_{z,m}} \tag{2.43}$$

$$t = \frac{2k_{z,0}}{k_{z,0} + k_{z,m}} \tag{2.44}$$

The reflectivity of the interface R is the ratio of incident neutrons reflected and is given by $|r^2|$.

2.7.3 Multiple layers

The above result gives the reflectivity for a single interface. Specular reflectivity from systems with multiple layers of media (multilayers) will now be described. An example of such a system containing two interfaces is illustrated in figure 2.19. It assumes a perfectly flat medium of thickness d on a perfectly flat substrate. It can be seen from figure 2.19 that there are now extra reflection and transmission terms. The two main exact methods of finding reflectivity from multilayers will be described. For the two layer system the Helmholtz equations are given by

$$\psi''(z) + k_{z,0}\psi(z) = 0 \text{ for } z \leq 0 \text{ (vacuum)} \tag{2.45}$$

$$\psi''(z) + k_{z,m}\psi(z) = 0 \text{ for } 0 \leq z \leq d \text{ (medium)} \tag{2.46}$$

$$\psi''(z) + k_{z,s}\psi(z) = 0 \text{ for z} \geq \text{d (substrate)} \tag{2.47}$$

and the solutions to these equations are

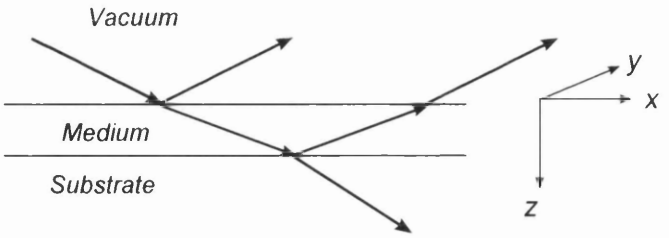

Figure 2.19: Specular scattering experiment. i is the incident neutron beam, r is the reflected beam and t is the neutron beam transmitted into the sample

$$\psi(z) = e^{ik_{z,0}z} + r_0 e^{-ik_{z,0}z} \text{ for z} \leq 0 \tag{2.48}$$

$$\psi(z) = t_m e^{ik_{z,0}z} + r_m e^{-ik_{z,0}z} \text{ for } 0 \leq z \leq d \text{ (medium)} \tag{2.49}$$

$$\psi(z) = t_s e^{ik_{z,m}z} \text{ for } z \geq d \text{ (substrate)} \tag{2.50}$$

where r_s, t_s and r_m, t_m are the Fresnel reflection and transmission coefficients for the substrate and the medium respectively.

2.7.4 Transfer matrix

To solve for reflectivity and transmission again the boundary conditions have to be applied at the interfaces between the vacuum and medium and the medium and substrate.

Assuming that $A_{v,t}$ is the amplitude of the initial wave in the vacuum, $A_{v,r}$ is the amplitude of the wave reflected into the vacuum, $A_{m,r}$ is the wave reflected into the medium and $A_{m,t}$ is the wave transmitted into the medium at $z = 0$ the boundary conditions are satisfied by [61]

$$A_{v,t} + A_{v,r} = A_{m,t} + A_{m,r} \tag{2.51}$$

$$k_{z,v}A_{v,t} - k_{z,v}A_{v,r} = k_{z,m}A_{m,t} - k_{z,m}A_{m,r} \tag{2.52}$$

This result can be expressed in the matrix form as

$$p^v \cdot \vec{A}^v(0) = p^m \cdot \vec{A}^m(0) \tag{2.53}$$

where the vector $\vec{A}^v$ gives the amplitudes of the waves (in the vacuum) given by

$$\vec{A}^v(0) = \begin{bmatrix} A_{v,t} \\ A_{v,r} \end{bmatrix} \tag{2.54}$$

and p^v is (at $z = 0$ in this case) given by

$$p^v = \begin{bmatrix} 1 & 1 \\ k_{z,v} & -k_{z,v} \end{bmatrix} \tag{2.55}$$

The amplitude of the waves in the vacuum are related to those in the medium by

$$\vec{A}^v(0) = (p^v)^{-1}p^m \cdot \vec{A}^m(0) \tag{2.56}$$

and the inverse of the vector of amplitudes for the vacuum is given by

$$p^v = \frac{1}{2k_{z,v}} \begin{bmatrix} k_{z,v} & 1 \\ -k_{z,v} & 1 \end{bmatrix} \tag{2.57}$$

$(p^v)^{-1}p^m$ which will be called the boundary matrix can be written in terms of the Fresnel coefficients for the medium

$$(p^v)^{-1}p^m = \frac{1}{t_m} \begin{bmatrix} 1 & r_m \\ r_m & 1 \end{bmatrix} \tag{2.58}$$

It can be seen from these expressions that the Fresnel reflection coefficient is the ratio of the amplitudes of the initial wave and that reflected from the medium

$$r_m = \left(\frac{A_{v,r}}{A_{v,t}}\right) \tag{2.59}$$

and the transmission coefficient the ratio of the amplitudes of the initial and transmitted waves

$$t_m = \left(\frac{A_{m,t}}{A_{v,t}}\right) \tag{2.60}$$

Solving for the second interface requires changing the coorindate system to z'. Then when $z = d$ $z' = 0$. The results for the amplitude vectors and the boundary matrix at the interface between the medium and the substrate are the same, just replacing the the subscript v with m and m with s and remembering the change in coordinates. In order to solve for the reflectivity and transmission of the whole system the change in coordinates need to be taken into account. There will be a change in phase of the wave transmitted into the medium between the two interfaces. In the original coordinate system the wave amplitude vector for the wave in the medium at any point z is given by

$$\vec{A}^m(z) = \begin{bmatrix} A_{m,t}e^{ik_{z,m}z} \\ A_{s,r}e^{-ik_{z,m}z} \end{bmatrix} \tag{2.61}$$

the exponential terms can be separated into a phase matrix

$$Q^m(z) = \begin{bmatrix} e^{ik_{z,m}z} & 0 \\ 0 & e^{ik_{z,m}z} \end{bmatrix} \tag{2.62}$$

so

$$\vec{A}^m(z) = Q^m(z) \cdot \vec{A}^m(0) \tag{2.63}$$

The reflection coefficient (the ratio total amplitude of the reflected wave in the vacuum which includes contributions from the reflectivity of the medium and of the substrate and the amplitude of the initial wave) and transmission coefficient (the ratio total amplitude of the wave transmitted into the substrate and the initial wave) for the whole system can be found by multiplying the boundary matrix of the first interface by the phase matrix across the medium by

the boundary matrix of the second interface as shown in equation 2.64. These reflection and transmission coefficients for a multilayer replace the Fresnel coefficients for a single interface.

$$A^v(0) = (p^v)^{-1} p^m Q^m(d)(p^m)^{-1} p^s A^s(d) \tag{2.64}$$

If the elements of the matrix $(p^v)^{-1} p^m Q^m(d)(p^m)^{-1} p^s$ are given by

$$\begin{bmatrix} M_{11} & M_{12} \\ M_{21} & M_{22} \end{bmatrix} \tag{2.65}$$

The reflection coefficient is then

$$r = \left(\frac{M_{21}}{M_{11}}\right) \tag{2.66}$$

and the transmission coefficient is given by

$$t = \left(\frac{1}{M_{11}}\right) \tag{2.67}$$

The reflectivity R and the transmittivity T are given by $|r|^2$ and $|t|^2$ respectively. Clearly this formulation can be applied to a system of any number of interfaces by finding the phase and boundary matrices at each interface of the system. The final interface (generally the substrate) is considered semi infinite so there are no further interfaces for reflection to take place.

2.7.5 Parratt formalism

An alternative formulation to calculate the reflectivity and transmittivity of a multilayer stack is the Parratt recursion formulation derived by L.G. Parratt [66] in 1954. Starting from the substrate which is assumed semi-infinite the reflection coefficient r in each preceding layer is found by the formula [90]

$$r_{(j-1,j)} = \frac{f_{r(j-1,j)} + r_{j,j+1} e^{-iq_z^{j,j+1} d_{j+1}}}{1 + f_{r(j-1,j)} r_{j,j+1} e^{-iq_z^{j,j+1} d_{j+1}}} \tag{2.68}$$

where j is a index of a layer. To denote the interfaces $j-1, j$ represents the interface between layer j and $j-1$, r is the reflection coefficient of the an interface, f_r is the reflection coefficient

of an interface (from equation 2.43), d_j is the thickness of layer j and q_z is the momentum transfer in the z direction. $q_z = 2k_z$ for specular reflectivity. An illustration of a multilayer is shown in figure 2.20

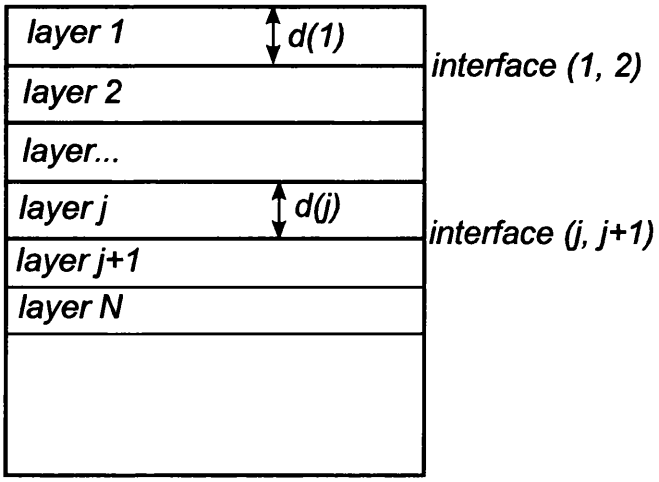

Figure 2.20: Multilayer stack geometry

The transfer matrix and Parratt formalism are two different iterative ways of calculating the total reflectivity from a multilayer, although the order in which the reflectances from each interface are calculated are the opposite of each other. This results in different reflection and transmission coefficients for the layers within the stack but the reflection and transmission coefficients of the top interface and therefore the total reflectivity and transmittivity are the same for the two schemes. The consequences of this will be discussed in the next section.

2.7.6 Features of the specular reflectivity

The specular reflectivity is a function of the scattering length density and the thickness of the layers in the multilayer and k_z of the incoming neutrons. The value of k_z is a function of the angle of incidence and the wavelength. Generally reflectivity is plotted as a function of q_z, with the y axis on a log scale. Figure 2.21 shows a typical reflectivity plot for a single interface.

It can be seen for low q_z that $R = 1$, and as q_z increases $R = 1$ up to a given point when R decreases rapidly with q_z. The region where $R = 1$ is called the critical edge. The point at which R starts to fall corresponds to the critical q_z which is equal to $2k_{z,c}$ value. Since the reflectivity is the ratio of the reflected to the incident wave then a reflectivity of 1 shows that all

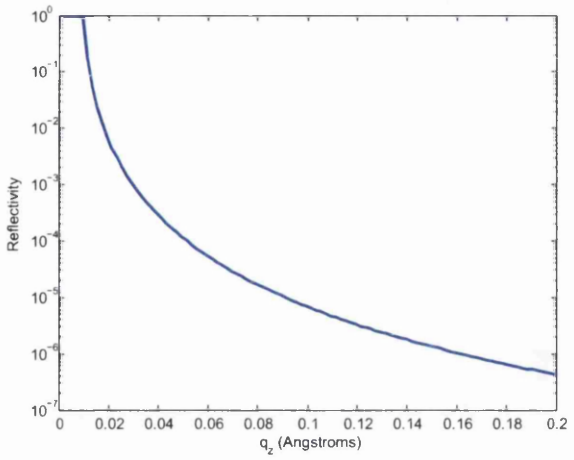

Figure 2.21: Calculated reflectivity from silicon with $\rho = 2.073e\text{-}6$

neutrons are reflected from the sample. For any q_z corresponding to a k_z lower than $k_{z,c}$ then all neutrons are reflected. At large values of q_z, R can be approximated by $R \approx (\pi\rho_m)^2 \frac{1}{k_{z,0}^4}$. This is known as Porod's Q^{-4} law.

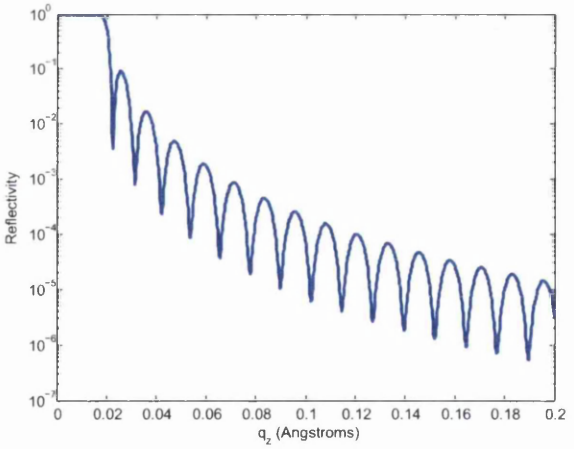

Figure 2.22: Calculated reflectivity from 50nm film on a silicon substrate with $\rho = 6.8e\text{-}6\text{Å}^{-1}$ (eg a deuterated polymer) on Si with $\rho = 2.073e\text{-}6\text{Å}^{-1}$

Figure 2.22 shows the reflectivity as a function of q_z from a system with two interfaces. The most notable feature of the two layer system is the appearance of fringes in the reflectivity. These are called Kiessig fringes. Their period is related to the thickness of the medium on the substrate and comes from the exponential terms in the Parratt formalisation and the phase

matrix in the transfer matrix. The distance between adjacent interfaces is the thickness of the films. The period of the fringes is given by $2\pi/t$. Maximums occur when the length of the path through the medium corresponds with an integer multiple of the wavelength of the neutron in the medium. The waves reflected from the vacuum/ medium interface and the medium/substrate interface then interfere constructively. By fitting experimental data with either of the above theories the thickness of the film can be determined. If further films are added to the create a multilayer, then fringes from these films can also be seen in the data. The strength of the contribution of reflectivity from a film to the total reflectivity is dependent on the SLD. This is shown in the 3 layer system in figure 2.23 which is the same as the system in 2.22 with another film with a lower scattering length density added on top. The fringes of the bottom layer are dominant, but the effect of interference from scattering from the other layer can be seen.

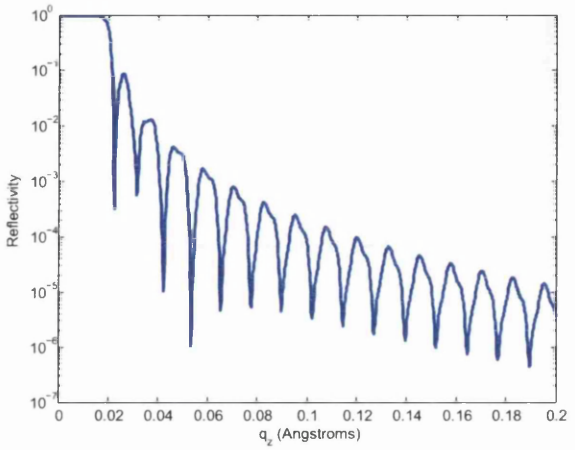

Figure 2.23: Reflectivity from 2 layer multilayer on Si substrate ρ_1 = 1e-6Å^{-1} ρ_2 = 6.8e-6Å^{-1}ρ_3 = 2.03e-6Å^{-1}

Parratt and transfer matrix calculation schemes

Figure 2.24 shows the reflectivity for each interface using Parratt formalism and figure 2.25 shows the reflectivity at each interface using the transfer matrix scheme, both for the multilayer described above. The red line on each plot is the final reflectivity, which is the same for both calculation schemes. The blue line corresponds to the calculation of reflectivity for the first interface for each scheme. The Parratt formalisation starts with the reflectivity from the silicon substrate, using the k_z values in the bottom layer, whereas the transfer matrix scheme

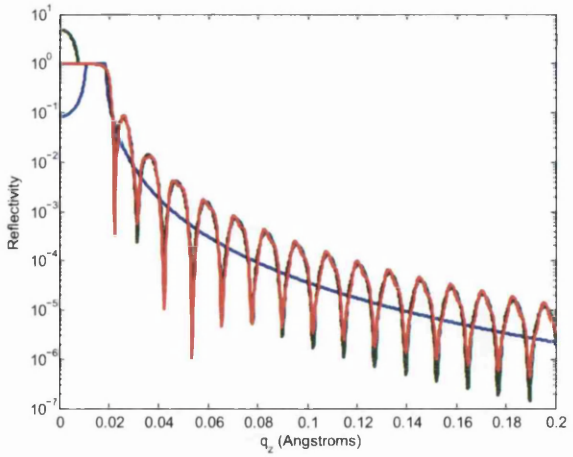

Figure 2.24: Reflectivity from 3 layer multilayer on Si substrate $\rho_1 = 1e\text{-}6\text{Å}^{-1}\rho_2 = 6.8e\text{-}6\text{Å}^{-1}\rho_3 = 2.03e\text{-}6\text{Å}^{-1}$ calculated using Parratt formalism. Blue line shows the reflectivity from the substrate, green line reflectivity from the substrate and the interface above it and the red line shows the total reflectivity

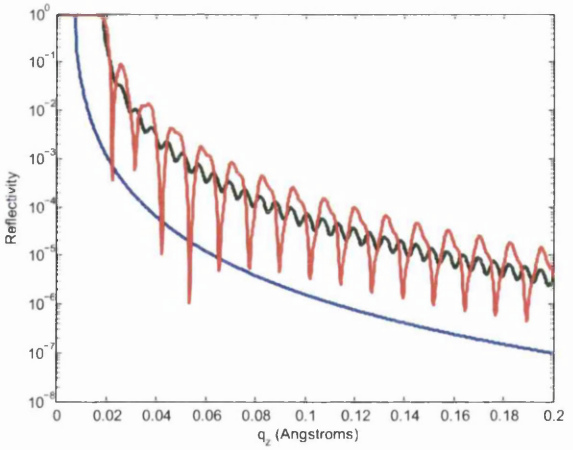

Figure 2.25: Reflectivity from 3 layer multilayer on Si substrate $\rho_1 = 1e\text{-}6\text{Å}^{-1}\rho_2 = 6.8e\text{-}6\text{Å}^{-1}\rho_3 = 2.03e\text{-}6\text{Å}^{-1}$ calculated using Transfer Matrix. Blue line shows reflectivity from the top interface, green line shows the reflectivity from the top interface and the interface below it and the red line shows the total reflectivity

starts at the air/film interface using the k_z values in air. The scattering length density of the substrate is greater than that of the first film, so the reflectivity of the blue curve of the Parratt formalism is seen to be higher. The green line shows the second stage of calculation. The fringes on the Parratt reflectivity plot show the interference between the film/film interface and the film/substrate interface across the bottom film, which are the main fringes in the total reflectivity. The fringes on the transfer matrix plot show the interference between the air/film interface and the film/film interface or across the top film. The fringes are smaller due to the scattering length density being smaller and spaced closer together as the top layer is thicker than the bottom layer. The consequences of the different ways the two schemes calculate the reflectivity is important in the DWBA model and is discussed in section 5.3.1

2.7.7 Surface roughness

Surface roughness on the interfaces of the multilayer cause the experimental specular reflectivity to be damped. This is due to neutrons being scattered in off specular directions, so the overall intensity of the specular reflectivity is reduced. Nevot and Croce [65], [18] introduce an exponential damping factor so that the Fresnel coefficient is replaced by

$$r_d = r_{Fresnel} e^{-2k_{z,0}k_{z,m}\sigma^2} \tag{2.69}$$

where σ^2 is the variance of a Gaussian height distribution (see section 2.8). Nevot's description of the surface is shown in figure 2.26

The RMS roughness of a surface is given by σ, the square root of the variance. The Fresnel reflection coefficients that appear in the Parratt formalism and the boundary matrix in the transfer matrix are replaced by the expression in equation 2.69. Figure 2.27 shows the effect of roughness on the reflectivity of a single layer on a substrate using the Parratt formalism.

It can be seen that as the samples increase in roughness the fringes die away at a greater rate with increasing q_z.

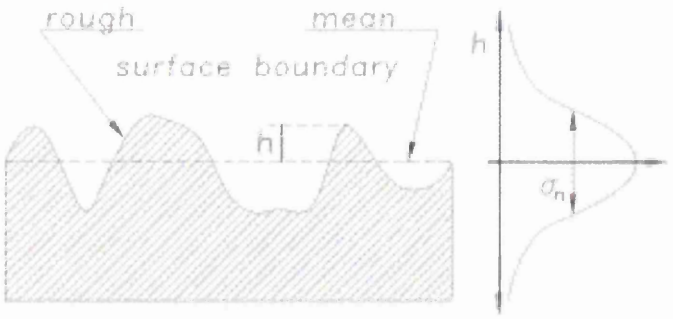

Figure 2.26: Interface roughness according to Nevot and Croce [65]. The distribution of peaks and valleys on a mean interface level is described using the Gaussian function and its σ parameter. (Image from reference [65])

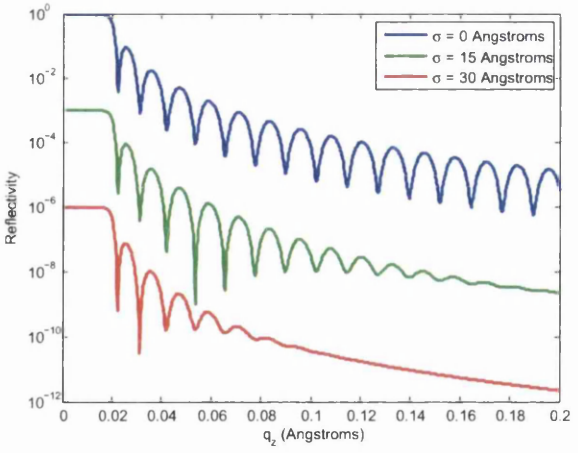

Figure 2.27: Reflecivity from single medium on a substrate with different roughness (curves shifted by 10^{-3} for clarity)

2.7.8 Resolution

The experimental reflectivity is affected by the resolution of the instrument. This is most noticeable at the minima between fringes, where destructive interference occurs. A Gaussian convolution of the reflectivity function is usually used to smear the theoretical reflectivity curve, where the full width half maximum (FWHM) of the Gaussian corresponds to the resolution of the instrument. The effect of finite instrument resolution is to reduce the sharpness and depth of the minima on the reflectivity curve as shown in figure 2.28

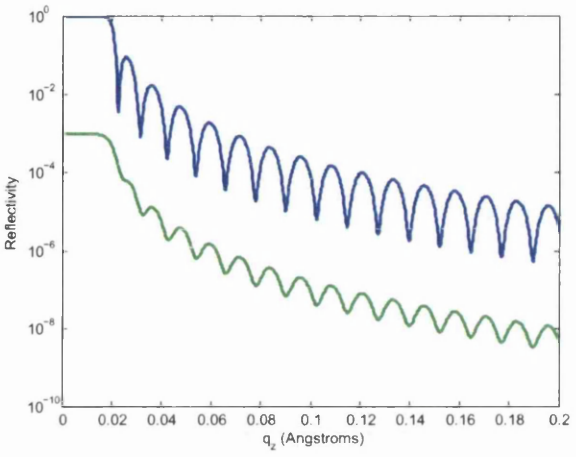

Figure 2.28: Reflecivity without and with Gaussian convolution smoothing (curves shifted by 10^{-3} for clarity)

2.8 Height to height correlation functions

To model the off specular reflectivity of a rough surface the surface needs to be defined statistically. This is done using a height to height correlation function, which describes the strength of correlation between any two points on the rough surface in terms of the distance they are separated.

2.8.1 Height to height correlations for single layers

A rough surface is defined in terms of its height z at any lateral coordinate (x, y). Roughness can be modelled as perturbations from an ideal smooth flat surface of height $z(x, y) = z$. A perturbation U is a function of the lateral coordinates, $U(x, y)$, where $\langle U(x, y) \rangle = 0$ as shown in figure 2.29.

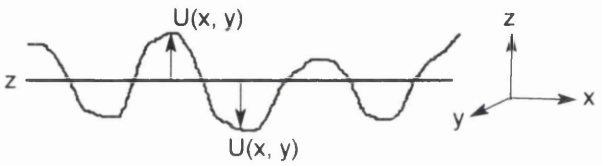

Figure 2.29: 2D cut through rough surface showing the ideal smooth surface and the deviations caused by the roughness

If the surface roughness is isotropic x, y can be written as $\mathbf{r}_{||}$, where $||$ denotes that $\mathbf{r}_{||}$ is parallel to the ideal surface.

$$z(\mathbf{r}_{||}) = z + U(\mathbf{r}_{||}) \tag{2.70}$$

The heights $z(\mathbf{r})$ at every point on the surface can be described statistically in terms of a probability distribution function. A single point distribution function $w(U)$ describes the probability of a displacement U from the ideal surface independent of lateral position. It is given by

$$w(U) = \frac{1}{S} \int dU \delta(U(\mathbf{r}_{||}) - \overline{U}) \tag{2.71}$$

where δ is the Dirac delta function and S is the area of the surface. The RMS roughness σ is a measure of the average displacement of the surface which is given by

$$\sigma = \sqrt{\langle U(\mathbf{r}_{||})\rangle^2} = \sqrt{\int dU w(U) U^2} \tag{2.72}$$

It has been shown that a Gaussian distribution function $w(U)$ can adequately represent a variety of surfaces [68].

$$w(U) = \frac{1}{\sqrt{2\pi}\sigma} e^{\frac{U^2}{2\sigma^2}} \tag{2.73}$$

The FWHM is given by $2\sigma\sqrt{2ln2}$. The two point probability distribution function $w(U, U')$ [55] describes the probability of a specific height difference between any two points on the surface. This results in a complicated function which contains a correlation coefficient $K(\mathbf{r}_{||} - \mathbf{r'}_{||})$. This term is a measure of how well correlated U and U' are, when separated by a distance $(\mathbf{r}_{||} - \mathbf{r'}_{||}) = R$. The correlation coefficient $K(\mathbf{r}_{||} - \mathbf{r'}_{||})$ is given by

$$K(\mathbf{r}_{||} - \mathbf{r'}_{||}) = \frac{1}{\sigma^2}\langle U(\mathbf{r}_{||}) U'(\mathbf{r'}_{||})\rangle \tag{2.74}$$

where

$$c(R) = \langle U(\mathbf{r}_{||}) U(\mathbf{r'}_{||})\rangle \tag{2.75}$$

The quantity $c(R)$ is the height to height correlation function as defined by Sinha [88]. The correlation coefficient $K(\mathbf{r}_{||} - \mathbf{r'}_{||})$ must be unity when $(\mathbf{r}_{||} - \mathbf{r'}_{||}) = 0$ (perfectly correlated heights) and zero as $(\mathbf{r}_{||} - \mathbf{r'}_{||}) \to \infty$ (uncorrelated surface). If $R = 0$ then $c(R)$ must be equal to the mean squared roughness as $\langle U(\mathbf{0}_{||}) U'(\mathbf{0}_{||})\rangle = \sigma^2$. A function that is often used for $c(R)$ which has been shown to adequately represent many surfaces and satisfies these conditions is found from fractal geometry for a self affine surface [56]

$$c(R) = \sigma^2 e^{-\left(\frac{R}{\xi}\right)^{2h}} \tag{2.76}$$

where the exponent h is called the Hurst parameter and varies between 0 and 1. It describes how smooth or jagged the interface is. The expression includes a correlation length ξ which limits the strength of the correlation over large distances.

2.8.2 Correlations between interfaces

For systems with multiple layers the scattering will be affected by the distance between the surfaces or interfaces. A two point probability function can be used to statistically describe the probability of finding a displacement of U_j given a displacement of U_k for two points on interfaces j and k respectively, independent of lateral position. This can be defined by an interface to interface correlation function. The interface to interface correlation function is similar to the height to height correlation function in equation 2.75 and is given by

$$c_{j,j+1}(R) = \sigma_j \sigma_k K_{j,k}(\mathbf{r}_{||} - \mathbf{r'}_{||}) = \langle U_j(\mathbf{r}_{||}) U_k(\mathbf{r'}_{||}) \rangle \tag{2.77}$$

In the scattering there will be interference effects caused by the thickness of the layers of medium, ie the distance between interfaces j and k. If the surfaces are rough then the thickness is a local quantity and dependent of the correlation of the interfaces and their individual roughnesses. The three possible cases for the correlation of the interfaces are shown in figure 2.31; A) the interfaces are perfectly correlated, the thickness is constant. B) there is partial correlation of the interfaces, the thickness has some dependence on $c_{j,k}$. C) uncorrelated interfaces. This is shown graphically in figure 2.30.

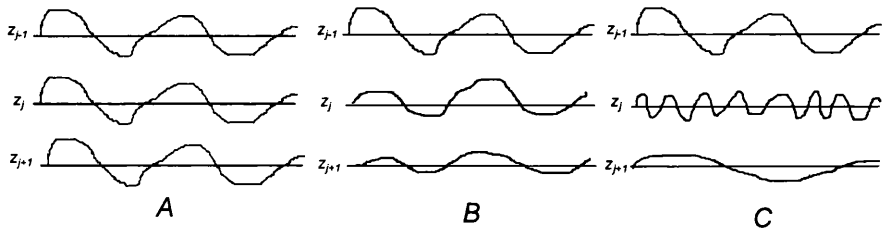

Figure 2.30: Possible interfacial correlations between layers A) perfectly correlated, B) partially correlated C) uncorrelated

The thickness of a layer t_j at lateral position $\mathbf{r}_{||}$ is given by

$$t_j(\mathbf{r}_{||}) = z_j(\mathbf{r}_{||}) - z_k(\mathbf{r}_{||}) = t_j + U_j(\mathbf{r}_{||}) - U_k(\mathbf{r}_{||}) \tag{2.78}$$

where t_j is the thickness of the medium between ideal layers j and $j-1$. This is shown in figure 2.31

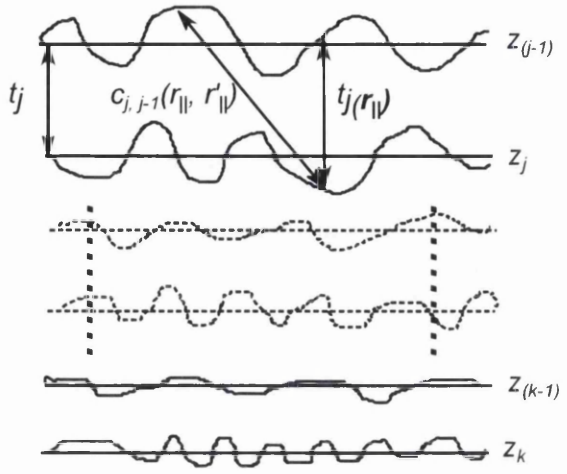

Figure 2.31: Thickness and height to height correlation of between layers

The RMS thickness is given by

$$\langle \delta t_j^2 \rangle = \langle (t_j - \langle t_j \rangle)^2 \rangle = \langle (U_j - U_{j-1})^2 \rangle = \sigma_j^2 + \sigma_{j-1}^2 - 2c_{j,j-1}(0) \tag{2.79}$$

This is the variance of thickness of layer j. When there is no correlation between the layers $\langle \delta t_j^2 \rangle = \sigma_j^2 + \sigma_{j-1}^2$.

The expression for interface to interface correlation functions 2.77 are subject to the same conditions as the height to height correlation functions (defined in the previous section) and additionally Schlomka et al [79] state that $c_{j,k}(R)$ must also satisfy

$$|c_{jk}(\mathbf{R})|^2 \leq c_j(0)c_k(0) \tag{2.80a}$$

$$|c_{jk}(\mathbf{R})|^2 \leq \frac{1}{2}[c_j(0) + c_k(0)] \tag{2.80b}$$

The following interface correlation function is suggested which satisfies all these conditions and

expresses $c_{jk}(\mathbf{R})$ in terms of the individual height to height correlation functions of layers j and k.

$$c_{jk}(\mathbf{R}) = \frac{1}{2}\left[\frac{\sigma_j}{\sigma_k}c_j(\mathbf{R}) + \frac{\sigma_k}{\sigma_j}c_k(\mathbf{R})\right] e^{-|z_j - z_k|/\xi_{\perp j,k}} \tag{2.81}$$

$\xi_{\perp j,k}$ is a cut off parameter determining the distance that the correlation between the layers is effective for, in the z direction. When $\xi_{\perp j,k} = 0$, $c_{jk}(\mathbf{R}) = 0$ and $\langle \delta t_j^2 \rangle = \sigma_j^2 + \sigma_{j-1}^2$ as stated above.

This section has focused on correlation functions for rough interfaces and between rough interfaces as these are used to characterise interfaces within the Born approximation and the distorted wave Born approximation. The lengthscale of features that scattering experiments probe is dependent on the wavelength of the incident radiation. If there are features on the sample that are separated by a distance equal to the probe wavelength, then coherent scattering occurs, increasing the intensity of scattering seen into the corresponding q values. Remembering R gives the distance between features on a surface, then c_j is a measure of the likelihood of two features on the surface separated by R having the same height z. This means the larger the correlation function for a separation distance R the greater the scattering into the corresponding q values. As R is increased the likelihood decreases, so c_j decreases. The interface to interface correlation function $c_{j,k}$ then gives the likelihood of the thickness $t_j(R)$ being t_j, the thickness of the layer between two ideal interfaces at the mean positions of interface j and k.

2.9 Off Specular Scattering from thin films

2.9.1 Scattering from a single interface in the Born approximation

At small scattering angles it can be assumed that the neutrons will see a medium as homogeneous except at its surfaces. This means that there will only be significant refraction events at the interfaces between different mediums. The atomic structure can be ignored and the structure of the surfaces can be probed. This allows the study of interfaces between films, polymer films in the case of this work [88]. The volume integral expression 2.30 for scattering in the Born approximation (see section 2.5.3) can be transformed into a surface integral by considering a rough surface that is parallel to an ideal flat surface. Considering a sample with a rough film with its interfaces parallel to the z direction of the ideal surface, so that its lateral coordinates are x and y and integrating over z gives

$$\frac{d\sigma}{d\Omega} = \frac{N^2b^2}{q_z^2}\int\int_{S_0} dxdy \int\int_{S_0} dx'dy' exp(-iq_z(z(x,y)-z(x',y')))exp(-i(q_x(x-x')+q_y(y-y')) \tag{2.82}$$

where S_0 surface area of the interface the beam is incident on. Now assume that $(z(x',y') - z(x,y))$ is a random variable with Gaussian distribution which is dependent on the relative coordinates $(X,Y) = ((x'-x),(y'-y))$ on the sample. The square of the average difference in z between any two points separated by (X,Y) can be defined as

$$\langle [z(x',y') - z(x,y)]^2 \rangle = g(X,Y) \tag{2.83}$$

Substituting 2.83 into 2.82 for an incident surface area (the footprint of the beam on the sample) L_xL_y gives

$$\frac{d\sigma}{d\Omega} = \frac{N^2b^2}{q_z^2} L_xL_y \int\int_{S_0} dXdY e^{-q_z^2 g(X,Y)/2} e^{-iq_xXq_yY} \tag{2.84}$$

This is the Fourier transform of $g(X,Y)$. For many isotropic surfaces the following form of $g(X,Y)$ is satisfactory [88]

$$g(X,Y) = AR^{2h}, \;\; 0 < h < 1 \tag{2.85}$$

where $R \equiv (X^2+Y^2)^2$. However it can be seen that this function diverges as $R \to \infty$, showing that the roughness of the surface is completely dependent on the area measured. For real surfaces the roughness often saturates above a cutoff length ξ. A form suggested for $g(X,Y)$ with a cutoff is

$$g(R) = 2\sigma^2(1 - e^{(\frac{R}{\xi})^{2h}}) \tag{2.86}$$

where σ^2 is the mean squared roughness, ζ is the cut off length and h is the Hurst parameter which varies between 0 and 1 and is a measure of the 'jaggedness' of a surface (see reference [56] for further details). Writing

$$g(X,Y) = 2\langle z^2 \rangle - 2\langle z(X,Y)z(0,0) \rangle \tag{2.87}$$

where $\langle z^2 \rangle = \sigma^2$ the mean squared roughness then we can obtain $g(X,Y)$ in terms of the height to height correlation function (see section 2.8) and σ

$$c(X,Y) = \langle z(X,Y)z(0,0) \rangle = \sigma^2 - g(X,Y)/2 \tag{2.88}$$

Putting this expression for g(X, Y) into equation 2.84 gives

$$\frac{d\sigma}{d\Omega} = \frac{N^2b^2}{q_z^2} L_x L_y e^{-q_z^2\sigma^2} \int\int_{S_0} dXdY e^{q_z^2 g(X,Y)} e^{-i(q_x X + q_y Y)} \tag{2.89}$$

It can be seen that using expression 2.86 for the $g(R)$, that $c(R)$ is given by $e^{(\frac{R}{\xi})^{2h}}$ which is the same as expression 2.76 for the self affine fractal height to height correlation function in section 2.8.

Figures 2.32 and 2.33 show typical forms of the functions $g(R)$ and $c(R)$ with cutoff ξ as defined above.

2.9.2 Separating specular and off specular scattering

From figure 2.33 it can be seen that as $R \to \infty$ then $c(X,Y) \to 0$ and the q_z dependent exponential in the integral of equation 2.89 goes to 1. There is no dependence on X,Y as

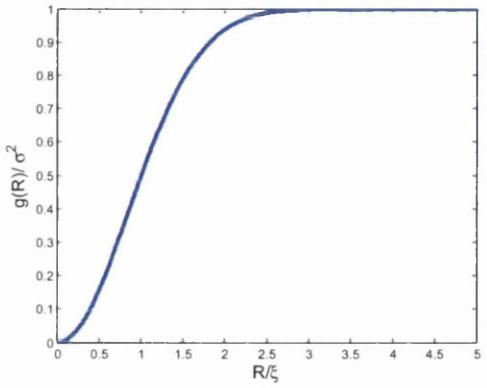

Figure 2.32: g(R)/ σ^2 vs R/ξ for h = 0.7

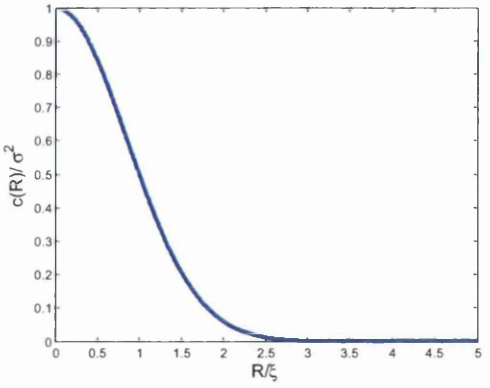

Figure 2.33: c(R)/ σ^2 vs R/ξ for h = 0.7

$c(X,Y)$ tends to zero. As there is no dependence on the in plane structure as $R \to \infty$ this region of the height to height correlation function corresponds to the specular scattering. Therefore specular and off specular scattering can be separated out, so the scattering is of the form $\left(\frac{d\sigma}{d\Omega}\right) = \left(\frac{d\sigma}{d\Omega}\right)_{\text{spec}} + \left(\frac{d\sigma}{d\Omega}\right)_{\text{offspec}}$. Equation 2.89 can then be written

$$\frac{d\sigma}{d\Omega} = \frac{N^2b^2}{q_z^2} L_x L_y e^{-q_z^2\sigma^2} \int\int_{S_0} dX dY (e^{q_z^2 c(X,Y)} - e^{q_z^2 c(X,Y)_{(c\to 0)}} + e^{q_z^2 c(X,Y)_{(c\to 0)}}) e^{-i(q_x X + q_y Y)} \tag{2.90}$$

where $e^{q_z^2 c(X,Y)_{(c\to 0)}} = 1$. The specular part can then be written

$$\left(\frac{d\sigma}{d\Omega}\right)_{\text{spec}} = \frac{N^2b^2}{q_z^2} L_x L_y e^{-q_z^2\sigma^2} \int\int_{S_0} dX dY e^{-i(q_x X + q_y Y)} = \frac{N^2b^2}{q_z} L_x L_y \frac{4\pi^2}{q_z^2} e^{-q_z^2\sigma^2} \delta(q_x)\delta(q_y) \tag{2.91}$$

which can be shown to be equal to $|R|^2 e^{-q_z^2\sigma^2}$ which is similar to the expression given by Nevot and Croce [65] (see section 2.7 equation 2.69 for reflectivity from a rough surface). The off specular part is

$$\left(\frac{d\sigma}{d\Omega}\right)_{\text{offspec}} = \frac{N^2b^2}{q_z^2} L_x L_y e^{-q_z^2\sigma^2} \int\int_{S_0} dX dY al (e^{q_z^2 c(X,Y)} - 1) e^{-i(q_x X + q_y Y)} \tag{2.92}$$

The integer 1 in equation 2.92 effectively subtracts the specular scattering from the off specular scattering. The separation of the specular and off specular scattering is dependent on there being a cut off length so that σ^2 saturates. If there is no cutoff then $g(X,Y)$ is divergent

and there is no X, Y independence in $c(X, Y)$ and hence no true specular component to the scattering.

2.9.3 Scattering from a single interface in the distorted wave Born approximation

The Born approximation breaks down as R tends toward one as multiple reflectivities are neglected.

The DWBA derived by Sinha et al [88] for an interface describes the rough surface as a perturbation on an ideal smooth surface. For further discussion and derivation of the DWBA see appendix A. The height of the ideal surface is at $z = 0$. The potential V_1 in the first order DWBA (see section 2.5 equation 2.22 is the potential of an ideal smooth surface which is given by

$$V_1 = \begin{cases} k_0^2(1 - n^2), & z < 0 \\ 0 & z > 0 \end{cases} \tag{2.93}$$

where k_0 is the incident wave and n is the neutron refractive index of the medium (see section 2.7). The pertubating potential V_2 represents the scattering potential of a rough surface, with mean height $z = 0$ and is dependent on whether $z(x, y)$ on the rough interface is above or below $z = 0$.

$$V_2 = \begin{cases} k_0^2(1 - n^2), \text{ for } 0 < z < z(x, y) & \text{if } z(x, y) > 0 \\ -k_0^2(1 - n^2), \text{ for } z(x, y) < z < 0 & \text{if } z(x, y) < 0 \\ 0 & \text{elsewhere.} \end{cases} \tag{2.94}$$

The surface is considered to have x and y dimensions L_x and L_y with periodic boundary conditions and the medium is semi infinite in the z direction. The situation for a smooth surface where $z(x, y) = z = 0$ can be solved exactly using Fresnel reflectivity equations (see section 2.7). The exact eigenstate for the smooth surface is

$$\psi_1(\mathbf{r}) = \begin{cases} C[e^{i\mathbf{k}_1\cdot\mathbf{r}} + R(\mathbf{k}_1)e^{i\mathbf{k'}_1\cdot\mathbf{r}}], & z > 0 \\ CT(\mathbf{k}_1)e^{i\mathbf{k^t}_1\cdot\mathbf{r}} & z < 0 \end{cases} \tag{2.95}$$

where $\mathbf{k'}_1$ is the specularly reflected beam and $\mathbf{k^t}_1$ is the beam transmitted into the medium, C is a normalisation constant to normalise the beam to unit flux and $T(\mathbf{k}_1)$ and $R(\mathbf{k_1})$ are the complex Fresnel transmission and reflection coefficients resepctively (see section 2.7). Restating equation 2.22

$$\langle \mathbf{k_f}|T|\mathbf{k}\rangle \approx \langle \psi^-_{\mathbf{kf}}|V_1|\phi_{\mathbf{k}}\rangle + \langle \psi^-_{\mathbf{kf}}|V_2|\psi^+_{1\mathbf{k}}\rangle \tag{2.22}$$

Sinha [88] puts the eigenstate $\psi^+_{1\mathbf{k}}$ equal to $\psi_1(\mathbf{r})$ which has just been defined. The time reversed eigenstates from equation 2.22 are defined for a smooth surface with incident wave vector $-\mathbf{k_2}$ by

$$\psi^-_{\mathbf{k_f}} = \tilde{\psi}_2(\mathbf{r}) = \begin{cases} C[e^{i\mathbf{k}_2\cdot\mathbf{r}} + R^*(\mathbf{k}_2)e^{i\mathbf{k'}_2\cdot\mathbf{r}}], & z > 0 \\ CT^*(\mathbf{k}_2)e^{i\mathbf{k^t}_2\cdot\mathbf{r}} & z < 0 \end{cases} \tag{2.96}$$

$\mathbf{k_2}$ is now the specular reflection of the incident wave $\mathbf{k'_2}$ and $\mathbf{k^t_2}$ is the wave in the medium propagating up to the surface and combining with $\mathbf{k'_2}$ to produce $\mathbf{k_2}$. These waves are time reversed. This is shown in figure 2.34

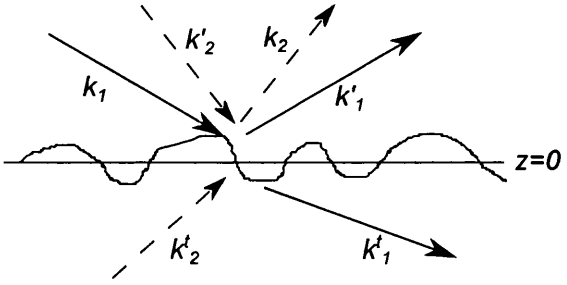

Figure 2.34: Rough surface which is a perturbation of the smooth surface (horizontal line at $z = 0$) with the wave vectors of the DWBA for a thin film shown

Now defining the plane wave $\phi_{\mathbf{k}}$ which will be called $\phi_1(\mathbf{r})$ by

$$\phi_1(\mathbf{r}) = Ce^{i\mathbf{k}_1 \cdot \mathbf{r}} \tag{2.97}$$

The T matrix element for scattering of neutrons (or x-rays) with initial wave vector $\mathbf{k}_1$ into a state $\mathbf{k}_2$ scattering from a surface film approximated by the DWBA may be written as the sum of two matrix elements

$$\langle 2|T|1\rangle = \langle \widetilde{\psi}_2|V_1|\phi_1\rangle + \langle \widetilde{\psi}_2|V_2|\psi_1\rangle \tag{2.98}$$

The differential scattering cross section is given in terms of the T matrix element

$$\frac{d\sigma}{d\Omega} = \frac{|\langle 2|T|1\rangle|^2}{16\pi^2|C|^4} = \frac{1}{16\pi^2|C|^4}\left(|\langle \widetilde{\psi}_2|V_1|\phi_1\rangle + \langle \widetilde{\psi}_2|V_2|\psi_1\rangle|^2\right) \tag{2.99}$$

To find the differential scattering cross section the T matrix element needs to be averaged over for the rough surface. The averaging is over all possible heights on the surface $z(X,Y)$ for an incoming eigenstate 1 and an outgoing eigenstate 2 (see equation 2.98). The averaged differential scattering cross section can be split into a specular and off specular part as shown for the Born approximation in section 2.9.2.

$$\frac{d\sigma}{d\Omega} = \frac{d\sigma}{d\Omega}_{\text{spec}} + \frac{d\sigma}{d\Omega}_{\text{offspec}} \tag{2.100}$$

The first matrix element from the DWBA expression $\langle \widetilde{\psi}_2|V_1|\phi_1\rangle$ contains only the ideal potential V_1 and so all reflection is specular. It can be shown that the differential scattering cross section for the first matrix element of the T matrix (when $V_2 = 0$) is [78], [88]

$$\frac{d\sigma}{d\Omega}_{(V_2=0)} = (L_x L_y)k_0^2 sin^2\theta_1 |R(k_1)|^2 \delta(q_x)\delta(q_y) \tag{2.101}$$

where θ_1 is the angle of incidence. The delta functions are conditions for specular reflectivity. The second matrix element $\langle \widetilde{\psi}_2|V_2|\psi_1\rangle$ when averaged contains both a specular and off specular part. Remembering for the first matrix element z is fixed at 0 and for the 2nd z is fluctuating and writing the first matrix element as $V^{(1)}$ and the second as $V^{(2)}$ the averaged specular and off specular differential scattering cross sections are given respectively by

$$\frac{d\sigma}{d\Omega}_{\text{spec}} = |V^{(1)} + \langle V^{(2)} \rangle|^2 \tag{2.102}$$

$$\frac{d\sigma}{d\Omega}_{\text{offspec}} = \langle V^{(2)} V^{(2)*} \rangle - |\langle V^{(2)} \rangle|^2 \tag{2.103}$$

Now the $V^{(2)}$ needs to be solved. Using equations 2.95 and 2.96 the following expression is derived

$$V^{(2)} = |C|^2 k_0^2 (1-n^2)[F_+(q)+R(\mathbf{k'}_2)F_+(\mathbf{q}_1)+R(\mathbf{k}_1)F_+(\mathbf{q}_2)R(\mathbf{k'}_2)R(\mathbf{k}_1)F_+(\mathbf{q}_3)+T(\mathbf{k}_2)T(\mathbf{k}_1)F_-(\mathbf{q}_t)] \tag{2.104}$$

where F_+ is the term given by the products of the wavefunctions above the rough surface after integrating the z component between $z(x,y) > 0$ and 0. It is given by

$$F_+(\mathbf{q}_{nz}) = \frac{i}{\mathbf{q}_n} \int\int_{S_0 z(x,y)>0} dxdy(e^{-\mathbf{q}_{nz}(z(x,y))} - 1)e^{-i(\mathbf{q}_{nx}x+\mathbf{q}_{ny}y)} \tag{2.105}$$

and F_- is given by the products of the wavefunctions below the rough surface integrating the z component between $z(x,y) < 0$ and 0. The expression for F_- is

$$F_-(\mathbf{q}_{nz}) = \frac{i}{\mathbf{q}_n} \int\int_{S_0 z(x,y)<0} dxdy(e^{-\mathbf{q}_{nz}(z(x,y))} - 1)e^{-i(\mathbf{q}_{nx}x+\mathbf{q}_{ny}y)} \tag{2.106}$$

q_n defines the five different possible wavevectors from the various summations of $\mathbf{k}_n$ in the exponential

$$\begin{aligned} \mathbf{q}_0 &= \mathbf{k}_2 - \mathbf{k}_1 \\ \mathbf{q}_1 &= \mathbf{k}'_2 - \mathbf{k}_1 \\ \mathbf{q}_2 &= \mathbf{k}_2 - \mathbf{k}'_1 \\ \mathbf{q}_3 &= \mathbf{k}'_2 - \mathbf{k}'_1 \\ \mathbf{q}_t &= \mathbf{k}^t_2 - \mathbf{k}^t_1 \end{aligned} \tag{2.107}$$

The wavevector q_t is the momentum transfer in the medium. It can be seen that $q_{2z} = -q_{1z}, q_{3z} = -q_{0z}$ and under specular conditions all $q(x,y) = 0$ and $q_{2z} = -q_{1z} = 0$. Returning to equation 2.102 Sinha [88] shows if the distribution of $(z(x',y') - z(x,y))$ for a surface is Gaussian then $\langle V^{(2)} \rangle$ subtracts from the ideal smooth surface reflectivity $\langle V^{(1)} \rangle$. The averaged matrix element $\langle V^{(2)} \rangle$ represents a decrease in the measured intensity at $q_x = 0$, caused by the rough surface. This gives a result for the specular component of the scattering that is consistent with the Nevot and Croce result, mentioned in section 2.7.7, to order q_z^2 if $q_c\sigma$ is not large (q_c is the critical wave vector value for total external reflection).

Sinha et al [88] simplifies the derivation for the off specular scattering by noting that the wave function and its derivative must be continuous across the the interface. The terms for $z > 0$ are replaced by the terms for $z < 0$ in the wavefunctions ψ_1 and $\widetilde{\psi_2}$. The expression for the second matrix element simplifies greatly to

$$\langle \widetilde{\psi}_2 | V_2 | \psi_1 \rangle = T(\mathbf{k}_1) T(\mathbf{k}_2) | k_0^2 (1 - n^2) | F(\mathbf{q_t}) \tag{2.108}$$

where

$$F(\mathbf{q_t}) = \frac{i}{\mathbf{q}_t} \int \int_{S_0} dx dy (e^{-i\mathbf{q}_z^t (z(x,y))} - 1) e^{-i(\mathbf{q}_x^t x + \mathbf{q}_y^t y)} \tag{2.109}$$

where the t denotes that it is the wave vector transmitted into the layer. From expression 2.103 the $V^{(2)}$ matrix is squared and then averaged giving the following expression

$$|\langle \widetilde{\psi}_2 | V_2 | \psi_1 \rangle|^2 = |C|^4 |T(\mathbf{k}_1)|^2 |T(\mathbf{k}_2)|^2 |k_0^2 (1 - n^2)|^2 [\langle F(\mathbf{q}_t) F(\mathbf{q}_t) * \rangle - \langle F(\mathbf{q}_t) \rangle \langle F * (\mathbf{q}_t) \rangle] \tag{2.110}$$

where

$$\langle F(\mathbf{q}_t) F(\mathbf{q}_t)^* \rangle = \frac{1}{\mathbf{q}_t^2} \int \int_{S_0} dx dy \int \int_{S_0} dx' dy' \langle (e^{-i\mathbf{q}_z^t (z(x,y))} - 1)(e^{i\mathbf{q}_z^t (z(x',y'))} - 1) \rangle e^{-i(\mathbf{q}_{x-x'}^t x + \mathbf{q}_{y-y'}^t y)} \tag{2.111}$$

$\langle F(\mathbf{q}_t) \rangle \langle F * (\mathbf{q}_t) \rangle = 0$ when z is evenly distributed around 0. The off specular differential scattering cross section is given by

$$\frac{d\sigma}{d\Omega}_{\text{offspec}} = (L_x L_y) \frac{|k_0^2 (1 - n)^2|^2}{16\pi^2} |T(\mathbf{k}_1)|^2 |T(\mathbf{k}_2)|^2 S(\mathbf{q}_t) \tag{2.112}$$

where

$$S(\mathbf{q}_t) = \frac{1}{|q_z^t|^2} e^{-((q_z^t)^2+(q_z^t*)^2\sigma^2/2)} \int\int_{S_0} dXdY(e^{|q_z^t|^2 c(X,Y)} - 1)e^{i(q_x X + q_y Y)} \tag{2.113}$$

The height to height correlation function $c(X,Y)$ is now present within the DWBA expression for off specular scattering from a single surface. The justification for this can be seen by referring to the derivation of expression 2.92, the expression for off specular scattering in the BA derived earlier in this chapter. Expressions 2.112 and 2.113 are almost identical to expression 2.92 for the off specular scattering in the Born approximation, except for now q_z^t is used instead of q_z and the Fresnel transmission coefficients T are in the coefficient. These T coefficients give rise to maxima for scattering at the critical angle, which corresponds to Yoneda scattering [105] seen in experimental work. This can be seen in figure 2.35 comparing the BA and DWBA reflectivity calculation for a single layer with the same parameters. For high q_z $|T|^2 \approx 1$ and $q_z^t \approx q_z$ and this expression reduces to the Born approximation expression. The height to height correlation $c(X,Y)$ used in section 2.9.1 can be used in the DWBA model.

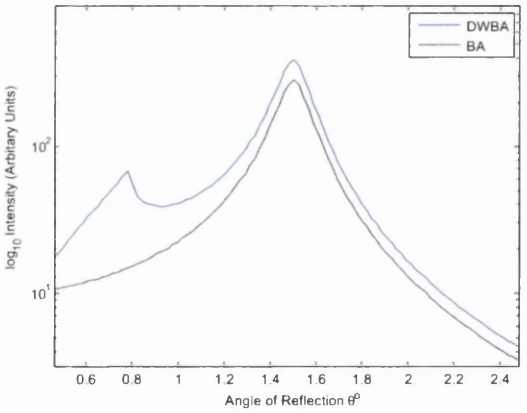

Figure 2.35: Comparison of BA and DWBA for single layer with $\lambda = 8$, $NB = 9.407e-6$, $\theta_i = 1.5$, $h = 0.4$ and $\xi = 7000$. The DWBA shows Yoneda scattering

Isotropic surfaces in the DWBA

In time of flight experiments the resolution is usually relaxed in the q_y direction and good in the q_x, so that the scattering is a function of q_x only [70]. If the sample is isotropic it is expected the scattering from q_x and q_y will give the same results for the surface height distribution of the surface. Therefore in the expression for $S(\mathbf{q}_t)$ (2.113) the y direction is integrated over, giving

$$S(\mathbf{q}_t) = \frac{1}{|q_z^t|^2} e^{-((q_z^t)^2+(q_z^{t*})^2\sigma^2/2)} \int_x dX (e^{|q_z^t|^2 c(X)} - 1) e^{i(q_x X)} \tag{2.114}$$

which is a function of x only in the lateral plane. Putting in the self affine expression for $c(X,Y)$ 2.76

$$S(\mathbf{q}_t) = \frac{1}{|q_z^t|^2} e^{-((q_z^t)^2+(q_z^{t*})^2\sigma^2/2)} \int_x dX (e^{|q_z^t|^2\sigma^2 e^{-(|X|/\xi)^{2h}}} - 1) e^{i(q_x X)} \tag{2.115}$$

This expression is in general not analytically solvable and numerical methods have to be employed.

2.10 Scattering from multiple interfaces

Pynn [70] extends Sinha et als [88] DWBA formalisation to a two layer system and Holy and Baumbach [43] extend it to systems containing multiple layers. In their initial work Holy and Baumbach assume there are no interference effects between layers and the total reflectivity is the sum of the reflectivity from each of the individual layers. The wavefunctions are defined for each individual layer and are given by

$$\psi_1(\mathbf{r}) = C[T^*(\mathbf{k}_1^j) e^{i\mathbf{k}_1^j \cdot \mathbf{r}} + R^*(\mathbf{k'}_1^j) e^{i\mathbf{k'}_1^j \cdot \mathbf{r}}] \tag{2.116}$$

$$\widetilde{\psi}_2(\mathbf{r}) = C[T^*(\mathbf{k}_2^j) e^{i\mathbf{k}_2^j \cdot \mathbf{r}} + R^*(\mathbf{k'}_2^j) e^{i\mathbf{k'}_2^j \cdot \mathbf{r}}] \tag{2.117}$$

where j is the index of the layer. The transmission and reflection coefficients for each layer are dependent on the medium. This sis shown in figure 2.36

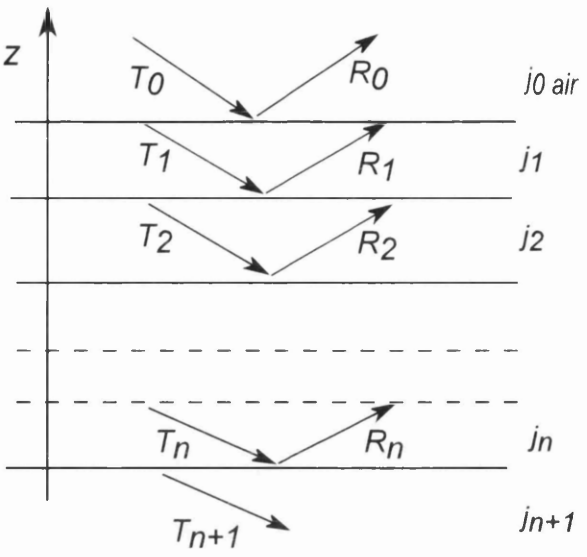

Figure 2.36: Transmission and reflection coefficients in a multi layer

It can be seen that this is the same as Sinha's wave functions as $T = 1$ for a vacuum or air and $R = 0$ in a semi infinite medium. The assumption of continuity across the interface is still made, however the wavefunctions above the interface for each layer are used, in contrast to Sinha et al [88] who uses the wavefunctions below the interface. There is now no advantage in using the wave function from below the surface as they now both contain the same number of terms, either choice is equally valid. Putting $T(\mathbf{k}_2^j) = T_1^j$ and $R(\mathbf{k}_2^j) = R_1^j$ and ignoring the constant coefficients which just scale the scattering.

The 2nd matrix element becomes

$$\langle\widetilde{\psi}_2|V_2|\psi_1\rangle = k_0^2(n_j^2 - n_{j+1}^2)\sum_{j=1}^{N}(T_1^jT_2^jF(\mathbf{q}_0^j) + T_1^jR_2^jF(\mathbf{q}_1^j) + R_1^jT_2^jF(\mathbf{q}_2^j) + R_1^jR_2^jF(\mathbf{q}_3^j)) \quad (2.118)$$

where $F(\mathbf{q}_n^j)) = F_+(\mathbf{q}_n))$ defined in equation 2.105 and N is the number of layers. The summation is over all the layers. Initially it is assumed that only terms from the same layers interact so $\langle\widetilde{\psi}_2|V_2|\psi_1\rangle_j\langle\widetilde{\psi}_2|V_2|\psi_1\rangle_k = 0$ when $(j \neq k)$. Multiplying expression 2.118 by its complex conjugate in order to find $d\sigma/d\Omega$ results in four combinations of the k_{zi}^j and k_{zf}^j vectors to produce q_z^j type vectors in the exponentials. These q_z^j type vectors come from the addition of q_z^j vectors when the exponential terms of expression 2.118 and is complex conjugate are multiplied. These are given by

$$\begin{aligned}
\mathbf{q}^j_{0z} &= \mathbf{k}_{z1} + \mathbf{k}_{z2} \\
\mathbf{q}^j_{1z} &= -(\mathbf{k}_{z1} + \mathbf{k}_{z2}) \\
\mathbf{q}^j_{2z} &= (\mathbf{k}_{z1} - \mathbf{k}_{z2}) \\
\mathbf{q}^j_{3z} &= -(\mathbf{k}_{z1} - \mathbf{k}_{z2})
\end{aligned} \tag{2.119}$$

where $\mathbf{q}^j_{0z} = -\mathbf{q}^j_{1z}$ and $\mathbf{q}^j_{2z} = -\mathbf{q}^j_{3z}$. The differential scattering cross section is given by

$$\begin{aligned}
\frac{d\sigma}{d\Omega} = L_x L_y \frac{k_0^4}{16\pi^2} \sum_{j=1}^{N} |n_j^2 - n_{j+1}^2|^2 [|(T_1^j T_2^j + R_1^j R_2^j)|^2 Q_{00}^j \\
+|(R_1^j T_2^j + T_1^j R_2^j)|^2 Q_{11}^j + 2Re\{(T_1^j T_2^j (R_1^j T_2^j)^* + T_1^j R_2^j (R_1^j R_2^j)^*) Q_{02}^j \\
+(T_1^j T_2^j (T_1^j R_2^j)^* + R_1^j T_2^j (R_1^j R_2^j)^*) Q_{01}^j + T_1^j T_2^j (R_1^j R_2^j)^* Q_{03}^j + T_1^j R_2^j (T_1^j R_2^j)^* Q_{21}^j \}]
\end{aligned} \tag{2.120}$$

where

$$Q^j_{mn} = \frac{1}{q^j_{mz}(q^j_{nz})^*} e^{(-\sigma_j^2((q^j_{mz})^2 + (q^j_{nz})^{*2})/2)} \int\int_{S_0} dX e^{(-i(q_x X))} e^{(q^j_{mz}(q^j_{nz})^* c_j(X))} - 1 \tag{2.121}$$

where the indices m and n refer to the indices given to the $\mathbf{q}^j_{nz}$ vectors.

It can been seen that each layer contains six terms corresponding to the possible combinations of q^j_{nz} in expression 2.121 for each layer in a multilayer. Each of the six terms has a combination of T and R coefficients. The reflectivity is the summation of the individual reflectivities for each interface, where interface j is the interface between $j-1$ and j. It assumes that there is no interference effects between the layers. Pynn [70] performs a calculation on a 2 layer system, and assuming a semi infinite 2nd layer replaces the wave function for the bottom layer with that below the $z = 0$, which simplifies the above expression back to expression 2.113 for the bottom layer.

The effect of adding more layers on the reflectivity is to give lines of higher intensity scattering which correspond with the spacing of the specular fringes at $\theta_i = \theta_f$, $q_x = 0$. On a θ, λ plot of reflectivity these lines can be seen to point toward the origin as shown in figure 2.37. The Yoneda peak [105] at the critical angle is still the dominant line of higher intensity, although other lines of higher intensity scattering originating at $q_x = 0$ and pointing to the axis origin are visible.

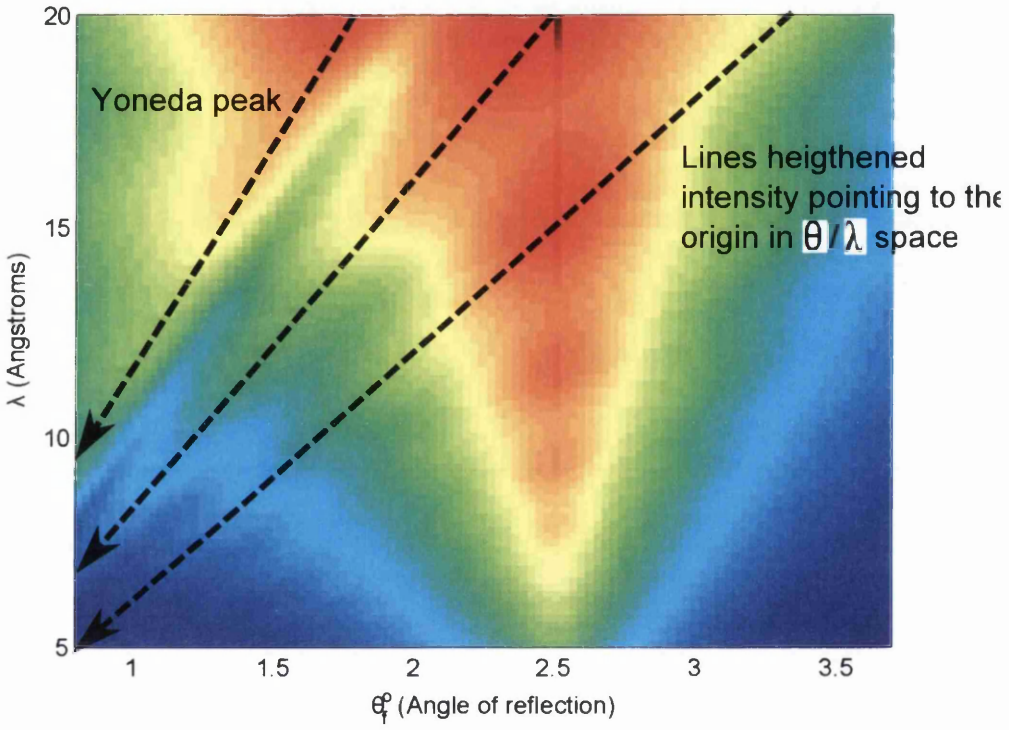

Figure 2.37: Uncorrelated 2 layer DWBA plot in θ, λ space, showing Yoneda and lines of heightened intensity pointing to the origin. Layer 1 $\sigma = 15$, $h = 0.7$, $z = 482$Å$, \xi = 10000$Å, $NB = 6.8e-6$. Layer 2 $\sigma = 1$, $h = 0.7$, $z = 0$Å, $\xi = 10000$Å, $NB = 2.073e-6$.

2.10.1 Correlation between interfaces

If there is a correlation between the morphology of the interfaces then interference effects can be seen. Holy et al [42] discuss this effect. These effects need to be taken into account, even if it is only a partial correlation. The correlation between interfaces is modelled in a similar way to the height to height correlation of a single interface and again is discussed in section 2.8. The Fourier transform which gives inference effects between layers is similar to that of the single layer in equation 2.121 and is given by

$$Q_{mn}^{jk} = \frac{1}{q_{mz}^{j}(q_{nz}^{k})^{*}} e^{(-\sigma_j^2((q_{mz}^{j})^2+(q_{nz}^{k})^{*2})/2)} \int\int_{S_0} dXdY e^{(-i(q_x X+q_y Y))} e^{(q_{mz}^{j}(q_{nz}^{k})^{*} c_{jk}(X,Y))} - 1, \ (j \neq k) \tag{2.122}$$

where j and k are the indexes over the layers and c_{jk} is the cross correlation function between the layers. The complete expression for scattering including correlation between layers is written compactly as [79] [42]

$$\left(\frac{d\sigma}{d\Omega}\right)_{\text{offspec}} = L_x L_y \frac{k_0^4}{16\pi^2} \left[\sum_{j=1}^{N} |n_j^2 - n_{j+1}^2|^2 Q_{mn}^{j} |(G_j^0 + G_j^3) + (G_j^1 + G_j^2)|^2 \right] \tag{2.123}$$

$$+ L_x L_y \frac{k_0^4}{16\pi^2} \left[\sum_{j=1, j\neq k}^{N} (n_j^2 - n_{j+1}^2)(n_k^2 - n_{k+1}^2)^{*} Q_{mn}^{jk} \sum_{m,n=0}^{3} G_j^m G_k^{n*} \right]$$

$$G_j^0 = T_{1,j} T_{2,j} e^{-iq_{z,j}^{m} z_j} \tag{2.124a}$$

$$G_j^1 = T_{1,j} R_{2,j} e^{-iq_{z,j}^{m} z_j} \tag{2.124b}$$

$$G_j^2 = R_{1,j} T_{2,j} e^{-iq_{z,j}^{m} z_j} \tag{2.124c}$$

$$G_j^3 = R_{1,j} R_{2,j} e^{-iq_{z,j}^{m} z_j} \tag{2.124d}$$

where $e^{-iq_{z,j}^{m} z_j}$ is a phase factor between the layers and z_j is the height of the layer. This needs to be taken into account to show interference effects from scattering from different layers. There are sixteen possible combinations of the G coefficients adding an extra sixteen terms to the scattering. The above equations assume that the wavefunction across the interface takes the form of the wavefunction above the interface. This is due to the analytic continuations of

the wavefunction across the interface as mentioned in section 2.9.3. Using the wavefunction below the interface to approximate the wavefunction across the interface is also valid.

Figure 2.38 shows an off specular reflectivity plot with a layer correlation added. The layer correlation used is the one suggested by Schlomka [79] (see section 2.8). It can be seen that at $q_x = 0$ ($\theta_i = \theta_f$) there are lines of heightened intensity that correspond with the specular fringes and those given by the uncorrelated multilayer in section 2.10, however away from $q_x = 0$ these lines point to $-\theta_f$ rather than to the origin as for the uncorrelated multilayer. The fringes given by the uncorrelated multi layer are still in the reflectivity, and while the Yoneda peak is still strong other fringes are dominated by the cross correlation fringes. The reason for difference the in direction of the fringes comes from their origins within the DWBA expression. The lines in the uncorrelated part of the model come from the $e^{2ik_{zf}t} = e^{iq_zt}$ (where $\theta_i = \theta_f$) factor in the Fresnel coefficients, where t is the thickness of the medium. The fringes in the correlated terms are from the phase factor between interfaces e^{iq_zd} (where d is the distance between the interfaces). At the specular $2k_{zi} = k_{zi} + k_{zf} = q_z$, hence the fringes correspond at $q_x = 0$. The lines of heightened intensity caused by the cross correlation terms follow constant q_z contours.

2.10.2 The effect of different roughness contributions

For the liquid/liquid polymer interfaces used in this work there are two contributions to the interfacial roughness an 'intrinsic' roughness σ_{int} due mixing of polymer on a molecular level and lateral roughness σ_{lat} due to thermal capillary wave fluctuations (this is discussed in the next chapter). The square of the total roughness σ_{tot} is given by the sum in quadrature of the two contributions [77]

$$\sigma_{tot}^2 = \sigma_{int}^2 + \sigma_{lat}^2 \tag{2.125}$$

As discussed in chapter 3 intrinsic mixing results in a graded scattering length density profile normal to the interface in a bilayer system and there will be no off specular scattering from a system with intrinsic roughness alone. The specular and off specular reflectivity are sensitive to σ_{tot} in the q_z direction, so σ_{int} will affect the rate of fall off of off specular reflectivity, provided there is off specular scattering due to σ_{lat} contribution to the sample.

Off specular neutron scattering will be sensitive to the amplitude and wavelength of capillary wave modes at the interface. Gelfand et al [32] show that the Born approximation and DWBA

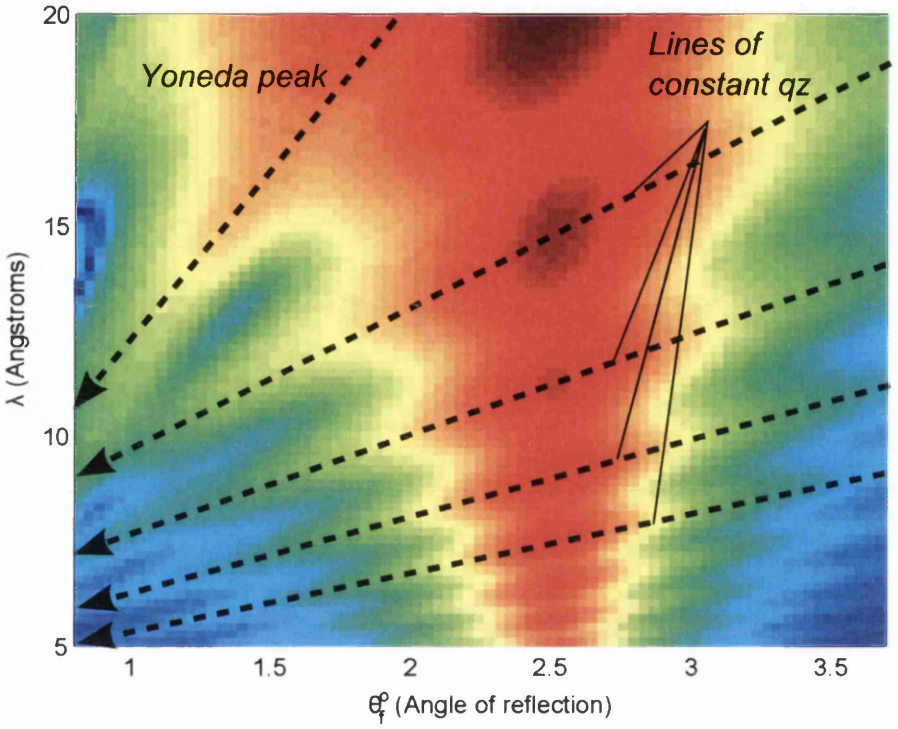

Figure 2.38: Correlated 2 layer DWBA plot in θ, λ space, showing Yoneda and lines of heightened intensity pointing $-\theta_i$, along constant q_z contours. Layer 1 $\sigma = 15$, $h = 0.7$, $z = 482$Å, $\xi = 10000$, $NB = 6.8e-6$. Layer 2 $\sigma = 1$, $h = 0.7$, $z = 0$Å, $\xi = 10000$Å, $NB = 2.073e-6$, $\xi_\perp = 10000$Å

can be used to describe two component surface roughness. Equation 2.114, which describes the intensity of scattering from an interface in the DWBA, is sensitive to the total interfacial roughness and the lateral structure. The σ term in the coefficient represents the total roughness ($\sigma = \sigma_{tot}$). The integral expression is dependent on the lateral structure of the interface because it contains the height to height correlation function $C(X, Y)$. If the height to height correlation function is the self affine height to height correlation function (described in section 2.8) it contains the lateral roughness σ_{lat}. By fitting the off specular experimental data using the DWBA expression, σ_{tot} and σ_{lat} can be found by using them as fitting parameters and σ_{int} can be calculated. The effect that σ_{tot} has on the calculated reflectivity is to change its decay as a function of decreasing q_z. The lateral roughness term σ_{lat} changes the rate of decay of the reflectivity in the q_x away from $q_x = 0$.

McClain et al [58] perform off specular x-ray experiments on a liquid/liquid interface of hexane and perfluorohexane at various temperatures. They show that the interfacial roughness is due to 'firstly, an intrinsic width over which the fluid density varies smoothly from one coexistence composition to the other, and, secondly, that the interface acquires an additional and larger statistical interfacial width as a result of capillary fluctuations'. The off specular scattering data is fitted using a single layer DWBA approximation with the capillary wave height to height correlation function described in section 3.2. The capillary wave height to height correlation is a function of the surface tension and the longest and shortest wavelength capillary modes. The σ_{tot} and σ_{lat} were extracted by simultaneous fitting of specular and off specular data, while the intrinsic width was extracted using a variation of equation 2.125.

Stone et al [91] perform off specular x-ray experiments on hydrocarbon and halogenated polymer bilayers of chlorinated polybutadiene and polystyrene respectively. The bilayers are annealed at different temperatures and fitted with a 3 layer DWBA approximation, with no cross correlation terms between the three interfaces. Two different models of the interfacial roughness between annealed bilayers are used. The first model is described as a 'correlated' model. The buried polymer/polymer interface is described by 20 ideal films with continuously varying density, which are used to describe a composition profile for σ_{int}. A roughness is then added to each of these ideal films, which is constant for all films, which is used to describe σ_{lat}. In this model σ_{tot} is dominated by σ_{lat}. The second so called 'uncorrelated' model again uses 20 layers to describe the buried polymer/polymer interface, but the roughnesses of the layers are not correlated. In both cases the self affine height to height correlation function [88] is used to describe the lateral structure of the capillary wave contributions, with the author claiming that it is intrinsically able

to describe a system of capillary waves. The papers author found that both descriptions of the interface could be used to adequately fit the experimental data. The results for the roughness contributions and the interfacial tension are compared with self consistent field theory with the correlated model matching the theory more closely. The uncorrelated model suggests that the composition profile of the interface is uncorrelated at different points in the x, y plane. This seems unphysical so in this work a correlated model approach is used, where a single intrinsic profile is superimposed onto a lateral roughness due to capillary waves.

Chapter 3

Polymers and Capillary Waves

3.1 Polymers

A polymer is a large molecule composed of repeating structural units known as monomers, which can be thought of as links in a chain. They encompass a large range of natural and synthetic materials, including DNA, rubber and plastics. Some polymers are made up of one type of monomer, some are made up of more than one type.

An example of a polymer commonly used in applications such as packaging or laboratory petri dishes is polystyrene. It has a chemical formula $(C_8H_8)_N$ where the N subscript is the number of repeating units. The monomer is a vinyl benzene (styrene) monomer, which contains a double bond between it's outer carbon atoms. The polymer is formed when this bond is opened allowing bonding between adjacent monomers as shown in figure 3.1.

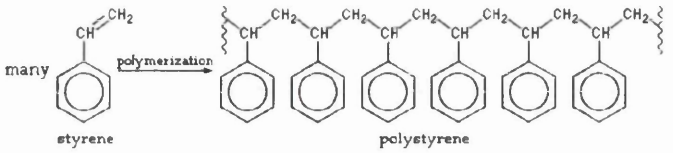

Figure 3.1: Styrene monomer and polystyrene polymer

3.1.1 Basic properties

The molar weight of a single polymer is simply $M_N = M_{mon}N$ where M_{mon} is the weight of a monomer and N is the number of monomers in a chain. The degree of polymerisation refers to the number of monomers in a polymer chain. In most synthetic polymers the number of monomers in a chain is not constant . There will be a distribution of different chain lengths in a polymer sample so an average molar weight is required. There are two methods of defining the average weight of a polymer sample.

Number average molar mass

The number average molar mass is given by

$$M_n = \sum_i n_i M_i \tag{3.1}$$

where n_i is the fraction of polymer molecules in the mix with degree of polymerisation i and $M_i = M_{mon}i$.

Weight average molar mass

The weight average molar mass is given by

$$M_w = \sum_i w_i M_i \tag{3.2}$$

where w_i is the fraction of the total mass of the mixture made up by polymers with degree of polymerisation i. For a system containing polymer chains of lengths a and b where $a < b$ and containing equal numbers of each length chain, then $n_a = n_b$ while $w_a < w_b$ because a greater fraction of the total mass is made up of the longer b chains. This means that $M_w \geq M_n$.

Polydiversity index

The polydiversity index used in order to measure the width of the distribution of chain lengths and is the ratio of M_w/M_n. If $M_w/M_n = 1$ then the polymers are monodisperse. Higher polydispersity index mean a broader polymer chain length distribution [74].

Stereochemistry

Carbon based polymers can have more than one chemical side groups attached to the main carbon chain. For linear carbon based polymer chains with two different groups there are three possible molecular architectures; i) isotatic where side groups of the same type would all be on the same side. The polymer molecule in figure 3.1 is isotatic if laid out in a planar zig zag ii) syndiotactic where the side groups alternate between sides of the chain systematically iii) atactic where the side chains are arranged randomly. These configurations are shown in figure 3.2.

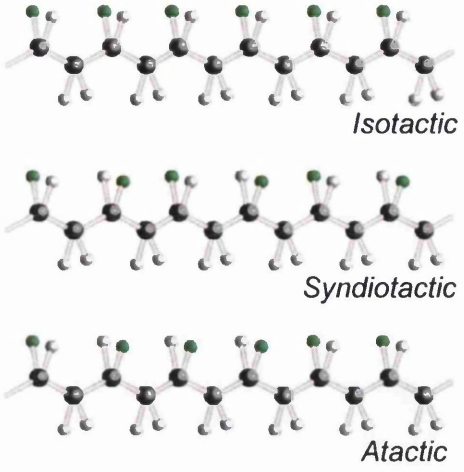

Figure 3.2: Stereochemistry of polymer chains (taken from reference [1])

Crystallinity

Atatic polymers will form glassy solids with no order. Isotatic and syndiotactic polymers can crystalise. However in most polymers the degree of crystallisation is below $\sim 50\%$ and cascades of crystalline lamellae separated by amorphous regions form as shown in figure 3.3.

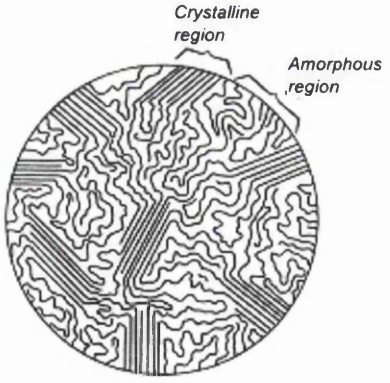

Figure 3.3: Morphology of a semi crystalline polymers (taken from reference [13])

Polymers can be heated to form a bulk liquid, or melt. For amorphous polymers the temperature above which this occurs is called the glass transition temperature T_g. The bulk polymer changes from being a brittle glass like material to a rubbery material. Crystalline polymers exhibit a change from a solid to a disordered melt at a melting temperature T_m, exhibiting a discontinuous

increase in volume at T_m. Semi crystalline polymers exhibit both behaviours. The bulk will form a disordered melt above both T_g and T_m. On rapidly cooling a semi crystalline polymer melt, the crystalline domains do not have time to form and a glassy solid is formed, keeping the liquid structure of the melt [33]. In recent years a substantial body of evidence has been accumulated which demonstrates that T_g and T_m can differ significantly from the bulk values in thin films (typically $< 100nm$) [3]. Some polymers can be described as liquid crystal polymers. Above T_g and T_m the polymer enters a nematic phase. In the nematic phase individual polymer molecules are free to flow and their locations in the melt are random but on a larger lengthscale they align to maintain long range directional order.

Polymer chain length

The simplest description of a linear polymer chain is the mean square end to end distance. The bonds between monomers are assumed to be freely jointed, so there is no correlation between the orientation of adjacent monomer molecules. The mean squared end to end distance $\langle R_{ee}^2 \rangle$ is given by

$$\langle R_{ee}^2 \rangle = Na^2 \tag{3.3}$$

where N is the number of monomers and a is the monomer length. This is simply a random walk. In reality bonds between monomers will have stiffness, so the orientation between monomers adjacent to eachother or close together in the chain have correlation. The statistical segment length b is introduced to take into account chain stiffness. The statistical segment length is the length which must be traveled along the chain before there is no correlation between the orientation of monomers. In this case the mean squared end to end distance becomes

$$\langle R_{ee}^2 \rangle = Nb^2 \tag{3.4}$$

Another commonly used measure of chain stiffness is the persistence length l_{ps}. This can be shown to be equivalent to

$$l_{ps} = \frac{b^2}{a} \tag{3.5}$$

Not all polymers are linear chains and their size cannot be accurately described by the mean

square end to end distance. The square radius of gyration is a means to describe the size of polymers regardless of their structure. It is defined as the average square distance between the monomers and the centre of mass of a polymer molecule. The radius of gyration is given by

$$R_g^2 \equiv \frac{1}{N}\sum_{i=1}^{N}(\mathbf{R}_i - \mathbf{R}_{cm})^2 \tag{3.6}$$

where $\mathbf{R}_i$ is the position vector of monomer i in the polymer molecule and $\mathbf{R}_{cm}$ is the position vector of the centre of mass of the molecule. $\mathbf{R}_{cm}$ is given by the number average of the monomer position vectors [29].

$$\mathbf{R}_{cm} \equiv \frac{1}{N}\sum_{j=1}^{N}\mathbf{R}_j \tag{3.7}$$

where $\mathbf{R}_j$ is the monomer position vector. The radius of gyration for various polymer conformations are tabulated [74]. A linear freely jointed polymer for example has a radius of gyration of $\langle R_g^2 \rangle = Na^2/6$. The mean squared end to end distance in this case is $\langle R_{ee}^2 \rangle = \langle R_g^2 \rangle /6$.

3.1.2 Conjugated polymers

Conjugated polymers are polymers which can possess conducting or semi-conducting properties. There is considerable interest in the use of conjugated polymers in electronic devices as they possess many desirable properties over traditional silicon electronics. These include good mechanical properties allowing, for example, flexible displays. The main drive to improve polymer electronics is due to their low cost relative to inorganic materials such as silicon and their potential for large area fabrication.

Most polymers act as insulators as their chemical bonding localises the electrons to each monomer. The carbon backbone of a conjugated polymer has alternate single/double or single/triple carbon to carbon bonds. Two typical conjugated polymer geometries are shown in figure 3.4.

The double or triple bond will contain a localised σ bond and a delocalised π bond. The electrons in the π bonds delocalise throughout the molecule giving the polymer conductive properties. The electrons exist in molecular orbitals at different quantised energy levels. The highest energy level molecular orbital which is occupied by electrons is called the highest occupied molecular

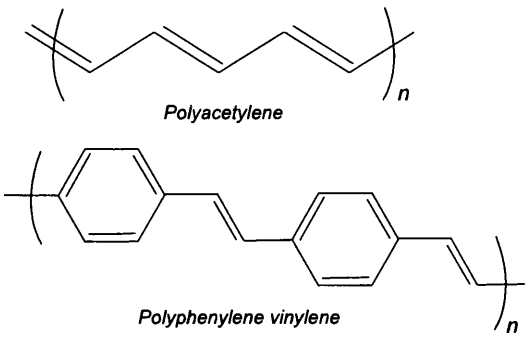

Figure 3.4: Typical conjugated polymer carbon bond geometries

orbital (HOMO) and the lowest energy unoccupied orbital is called the lowest unoccupied molecular orbital (LUMO). An excitation (for example by the absorption of a photon) can lift an electron from the HOMO to the LUMO creating a hole/electron pair called an exciton. The energy difference between the HOMO and the LUMO is roughly analogous to the band gap difference in inorganic semi conductors. This is shown in figure 3.5. For further discussion on molecular orbitals, and conjugated polymer properties see reference [51].

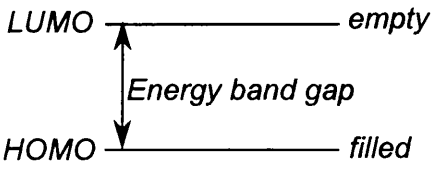

Figure 3.5: Band gap difference in a conjugated polymer

Many electronic devices require interfaces between materials of different conductive properties, for example for the purpose of electron and hole recombination in light emitting diodes (LEDs) and charge separation in photovoltaics (PVs). Both these types of device require conjugated/conjugated polymer interfaces (known as hetrojunctions). Electronic devices have been fabricated using conjugated polymer blends for devices such as organic LEDs (oLEDs), PV cells and organic field effect transistors (oFETs). Currently one of the main drives of research is to improve the performance of these devices [47].

The interfacial structure between polymer films is likely to be important to device performance. Several groups have looked into the effect of interfacial roughness on charge mobility and exciton separation. Chang et al [14] show that increasing the interfacial roughness of F8T2/PMMA and F8T2/SiO_2 by changing the solvents used in fabrication decreases charge mobility in oFET

systems. They measure the interfacial roughness using specular neutron reflectivity. Yan et al [103] found for an PF8/ F8BT bilayer used in a photovoltaic device that interfacial roughness affected device performance. Using x-rays to measure interfacial roughness and photoluminescence to measure exciton separation also shows that device efficiency decreases as the interfacial roughness increases. This is attributed to the decreased charge mobility in the annealed polymers, which counteracts the increased ratio of exciton separation due to increased interfacial area.

The form of the interfacial roughness between two amorphous polymers is considered by Sferrazza et al [84] who demonstrate there are two contributions to the interfacial roughness an intrinsic roughness caused by interfacial molecular level mixing (discussed the next section) and a capillary wave contribution (discussed in section 3.2). Attempts to separate out the two roughness contributions by direct measurements for halogenated polymers and simple liquids have been made by Stone [91]and McClain [58] respectively using off specular x-ray scattering. The results and implications of their work are discussed in section 2.10.2.

Higgins et al [37] suggest that different roughness contributions may affect device performance in different ways and they attempt to separate out these roughness contributions for a poly(9,9'-dioctylfluorene-cobenzothiadiazole)(F8BT)/F8 conjugated polymer system. Using specular neutron reflectivity to measure the total interfacial roughness inferring the interfacial mixing contribution to the roughness by measuring its photo physical properties the two contributions to the total roughness can be found. There are no examples in the literature of measuring the contributions to the roughness in conjugated polymer systems in the way that Stone [91] has for halogenated polymers and McClain [58] has for simple liquids.

The physics of the behaviour of conjugated polymer molecules is not as well understood as the behaviour of amorphous polymer molecules. Since conjugated polymer chains contain double and triple carbon bonds they are stiffer than amorphous polymer chains [40]. The persistence length for amorphous polymers PMMA and PS is 9 Å[74] compared with $9nm$ for conjugated polymer $F8$ [34]. This will affect the intrinsic molecular level mixing.

3.1.3 Polymers at interfaces

Most of the work in this thesis is concerned with layered polymer films which are then annealed. In the melt the individual polymer molecules have freedom to move and arrange themselves

to minimise the free energy of the system. This section looks at the entropic and enthalpic properties of polymers, to describe the mixing of the polymer bulk phases. It can be shown that most polymers are immiscible, but there is some mixing at the interface caused by the entropic effects, which will be referred to as interfacial mixing. This is illustrated in figure 3.6 showing two polymer films in a melt in which the two phases are pure, except for a small amount of mixing at the interface.

Figure 3.6: Small amounts of mixing at the interface, while the majority of the system is in one of two homogeneous phases (A or B)

3.1.4 Thermodynamics of polymer mixtures

Considering a homogeneous mixture of two types of polymer labeled A and B at constant pressure the volume fraction of A and B are Φ_A and Φ_B respectively where $\Phi_A + \Phi_B = 1$. The system aims to minimise the Gibbs free energy of mixing. Ignoring surface effects the free energy of mixing F_{mix} for a system containing only polymers A and B is given by

$$F_{mix} = F_{A+B} - (F_A + F_B) \tag{3.8}$$

where F_A and F_B are the free energies of pure A and B respectively and F_{A+B} is the free energy of the mix. This mixing is shown in figure 3.7. F_{mix} has enthalpic and entropic contributions. The Gibbs free energy is given by $G(T,p) = H - TS$ where T is temperature, p is pressure, H is enthalpy and S is entropy. In a physical system mixing occurs at a constant pressure but the Flory Huggins model assumes there is no volume change due to mixing. Therefore the simpler Helmholtz free energy is used $F(T) = U - TS$ where U is the internal energy of the system. The internal energy contributions are mainly dependent on interactions between polymers, such as van der Waals forces. If these interactions act to reduce the free energy of the system then mixing is favourable.

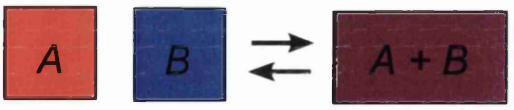

Figure 3.7: A system of two pure polymers A and B are mixed to create the mixed system $A + B$. The free energy of mixing F_{mix} is the change in energy in going from one state to the other

3.1.5 Flory Huggins theory

The Flory Huggins model is a simplified model of the thermodynamic interactions of a polymer in a solvent or with another polymer. However it does give a representation of the minimisation of the free energy of a system by considering the competition between the configurational entropy of mixing and the internal energy contributions. The reader is referred to Rubenstein and Colby [74] for a fuller description.

The model consists of a simple cubic or square lattice as shown in figure 3.8 with coordination number of z. Each of the points on the lattice can either be occupied by a monomer of type A or B. The size and shape of monomers are not considered. The polymer chain is represented by a random walk of monomers across the lattice. The polymers are subject to the conditions that no chains intersect (they cannot cross each other), each lattice point can only be occupied once and the degree of polymerisation for all chains of the same species is the same.

The enthalpy of mixing shall be considered first. The internal energy of a particular configuration ρ of the polymers A and B on a lattice is given by

$$E(\rho) = \in_{AA} n_{AA} + \in_{BB} n_{BB} + \in_{AB} n_{AB} \tag{3.9}$$

where $\in$ is the enthalpy of the interaction between neighbouring segments. Due to the amount and complexity of the possible configurations of the polymers in a melt an analytical solution does not exist and numerical solutions are very difficult to calculate. A mean field approach is

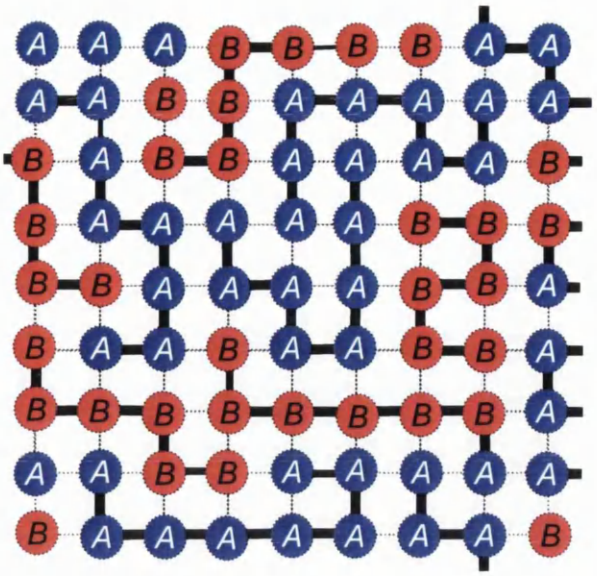

Figure 3.8: Illustration of 2D Flory Huggins model with polymers on a lattice. Blue circles represent polymer species A with degree of polymerisation 8 and red circles polymer species B with degree of polymerisation 6. The black lines represent covalent bonds between neighbouring monomers within each polymer chain

applied to find the average energy of a lattice point in a mix of A and B. The energy of mixing is found by subtracting the energy of the lattice sites in pure A and B phases from the energy for the mixed site. The expression for the enthalpy of mixing U_{mix} is given by [83]

$$U_{mix} = \Phi_A \Phi_B \chi k_B T \tag{3.10}$$

Which gives rise to the dimensionless Flory Huggins interaction parameter χ

$$\chi = z \frac{(2 \in_{AB} - \in_{AA} - \in_{BB})}{k_B T} \tag{3.11}$$

The parameter χ is the change in energy when a monomer of A is taken from an environment of pure A and swapped with a monomer of B from an environment of pure B in units of $k_B T$. If the χ parameter is positive then the energy of the system increases and mixing is unfavourable energetically. If it is negative then mixing is energetically favourable.

The entropy of mixing of polymers A and B with degrees of polymerisation N_A and N_B is given

by

$$\frac{S_{mix}}{k_B} = \frac{\Phi_A}{N_A} ln\Phi_A + \frac{\Phi_B}{N_B} ln\Phi_B \tag{3.12}$$

and is based on a lattice gas model, with the degrees of polymerisation of the chains reducing the translational entropy, which gives rise to the N denominators in both terms on the right hand side. For further discussion see Jones and Richards [49].

Combining expressions 3.10 and 3.11 give the following expression for the Flory Huggins free energy of mixing

$$\frac{F_{mix}}{k_B T} = \frac{\Phi_A}{N_A} ln(\Phi_A) + \frac{\Phi_B}{N_B} ln(\Phi_B) + \chi \Phi_A \Phi_B \tag{3.13}$$

The free energy for a constant temperature is then a function of χN. The simplest case to analyse is when polymers A and B have the same degree of polymerisation $N_A = N_B = N$. Figure 3.9 shows the phase diagram for such a system for different χN parameters, plotting the free energy against volume fraction of polymer. The curves are symmetric around $\Phi = 0.5$. If $N_A \neq N_B$ as in figure 3.10 then the curves show asymmetry.

Considering the situation in figure 3.9 where $N_A = N_B = N$ it can be seen for values of χN lower than a critical value of 2 the free energy curves are convex everywhere and the entropy term dominates, which favours the polymers mixing into a single phase. When χN is greater than a critical value then there is a concave part to the curve and minimisation of free energy favours phase separation of the polymers into two pure phases. The critical value of χ above which mixing is favourable, occurs at $\chi_c = \frac{2}{N}$. Hence the critical value of χ is lower for higher molecular weight polymers and so they are more likely to phase separate. A coexistence curve showing regions on a $\chi N/\Phi$ plot where mixing is favourable or phase separation is favourable can be calculated from the condition $\frac{\delta F}{\delta \Phi} = 0$, which gives a $\chi_{coexistence}$ value [49].

$$\chi_{coexistence} = \frac{1}{N} \frac{1}{2\Phi - 1} ln \frac{\Phi}{1 - \Phi} \tag{3.14}$$

If $\chi N < 2$ then separation of phases will result in the free energy of the system increasing, so the system is stable in the mixed state. This situation is seen in figure 3.11 a). If $\chi N > 2$ then separation of phases will result in the free energy decreasing. The mixed phase is unstable and

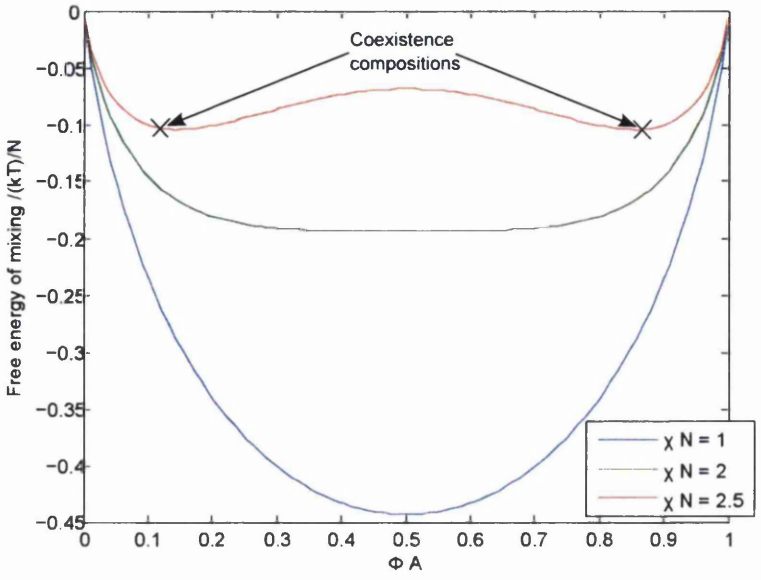

Figure 3.9: Free energy curves for various χN values for $N_a = N_b$ calculated form the Flory Huggins model

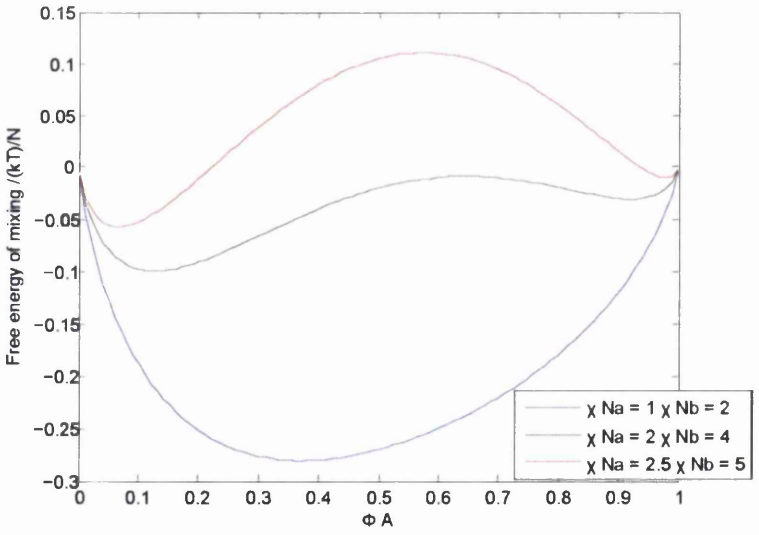

Figure 3.10: Free energy curves for various χN values for $N_a \neq N_b$ calculated from the Flory Huggins model

the system will phase separate into coexisting phases. This can be seen in figure 3.11 b).

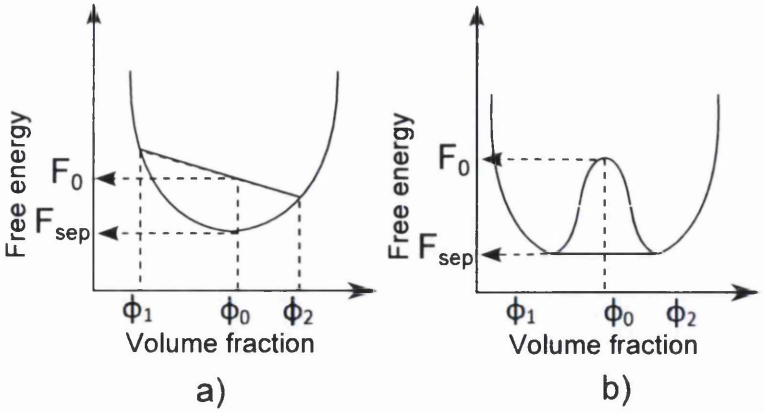

Figure 3.11: a) Free energy of curve for $\chi < 2$. Phase separation will result in free energy increasing b) Free energy of curve for $\chi > 2$. Phase separation into specific compositions will result in free energy decreasing

Solutions to equation 3.14 only exist for values of χ greater than $2/N$. When χN is only slightly greater than 2 phase separation requires nucleation from a droplet of a pure phase in the mixed phase. As χN becomes much greater than $\chi_c N$ then a free energy region is entered where the phases separate into pure domains spontaneously. This is known as the spinodal region. The spinodal region is between the curve defined by the condition $\frac{\delta^2 F}{\delta \Phi^2} = 0$ and the coexistence curve. The curve defined by the expression $\frac{\delta^2 F}{\delta \Phi^2} = 0$ is known as the spinodal curve and is solved in terms of χ and Φ as

$$\chi_{spinodal} = \frac{1}{2N_A\Phi} + \frac{1}{2N_B(1-\Phi)} \tag{3.15}$$

The coexistence curve and the spinodal curve showing the limits of the spinodal and coexistence regions as a function of χ are shown in figure 3.12

To understand why the spinodal region occurs the free energy curve needs to be looked at in more detail. The curvature of a free energy curve $\frac{d^2 F}{d\phi^2}$ for $\chi > 2$ can be positive or negative. Figure 3.13 shows that for small fluctuation in the volume fraction of material b the free energy decreases from F_b to F_b' and the system will begin to phase separate. However for a similar fluctuation in the volume fraction of material a the free energy increases from F_a to F_a' and

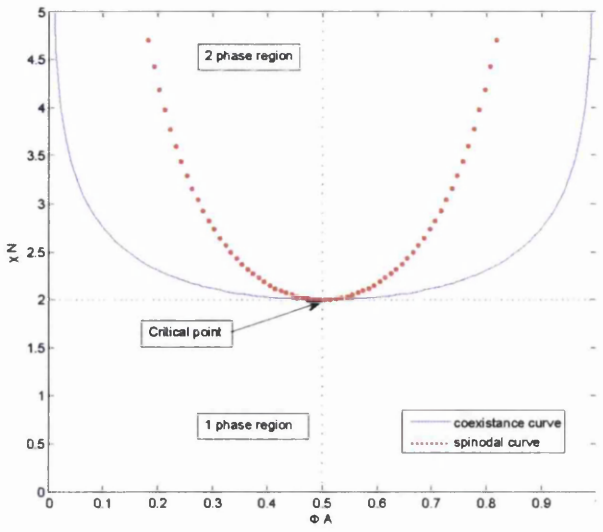

Figure 3.12: Phase diagram showing the coexistence and spinodal curves as a function of χ_N

phase separation does not take place. However for much larger fluctuations in a the free energy will decrease and phase separation will take place. Therefore for compositions on this section of the curve there is an energetic barrier which must be overcome for phase separation to take place. The system is locally stable to small fluctuations but globally unstable, which results in the spinodal state.

Negative values of χ correspond to polymer pairs which are miscible. Generally this is related to to specific interactions such as chemical bonding between complimentary groups on the polymer chains. Otherwise the polymers interact via the van der Waals force, which always results in a positive χ parameter. Because of the smallness of the χ_c and its dependency on the number of monomers in the polymer chain, it can be said that for high enough molecular weight polymer pairs with no specific interactions, they will always tend to be immiscible.

In the Flory-Huggins model the χ parameter is entirely enthalpic, $\chi \propto \frac{1}{T}$, suggesting that phase separation will take place below a critical temperature. Experiments have shown that for many polymer mixes phase separation takes place above a critical temperature. This shows the physical χ parameter has an entropic component within it and the Flory Huggins scheme is inadequate to describe the mixing thermodynamics of polymers. However the usual approach to this is to adapt the Flory Huggins theory by allowing χ to become a function of Φ and temperature.

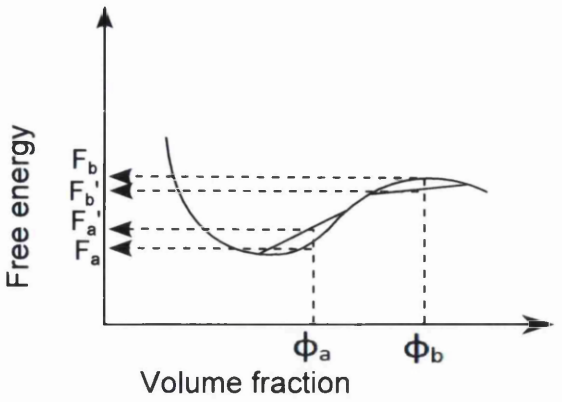

Figure 3.13: Diagram showing how small fluctuations of volume fraction Φ_a will result in free energy increasing whereas a small fluctuation of volume fraction Φ_b will result in the free energy decreasing.

3.1.6 Interfacial width and tension

Two immiscible polymers will seperate into two bulk phases with an interface between them. However this interface will not be atomically sharp due to the entropic effects. The interfacial composition profile will be characterised by the interfacial width which is a measure of the distance from the mean interface where mixing occurs and the surface tension. Flory Huggins theory is a mean field theory and therefore cannot describe the interfacial profile. Jones [48] describes the width of the interface as the balance between enthalpy and entropy, which favour narrower and broader interfacial widths respectively and uses the following argument to find expressions for the width and surface tension, a summary of which is shown below.

Under equilibrium conditions assume that a loop of polymer A protrudes from a region of pure A into a region of pure polymer B as shown in figure 3.14.

The number of monomers of polymer A protruding into the B region is given by N_{loop}. If the loop is a random walk the interfacial width is given by

$$w \sim a\sqrt{N_{loop}} \tag{3.16}$$

where a is the monomer size. The unfavourable energy of mixing U_{int} will depend on the number of contacts between A and B segments

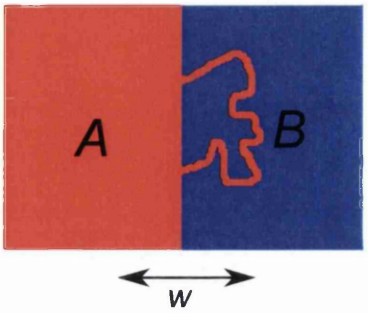

Figure 3.14: Polymer A from region A protruding into region B

$$U_{int} = \chi N k_B T \tag{3.17}$$

Because the system is at equilibrium U_{int} will be of order $k_B T$ so

$$\chi N_{loop} \sim 1 \tag{3.18}$$

from equations 3.16 and 3.17 comes the expression

$$w \sim \frac{a}{\sqrt{\chi}} \tag{3.19}$$

and the interfacial tension can be shown to be given by [49]

$$\gamma = \frac{k_B T}{a^2}\sqrt{\chi} \tag{3.20}$$

This argument gives the basic form of the equations for w and γ. Theories have been developed in order to describe the mixing of polymers more accurately, including self consistent field theory (SCFT). Self consistent field theory was developed by Edwards [27] after noticing the similarity between the problem of interacting polymers and interacting electrons. This section will outline the main results. For further information please refer to appendix C and references [49] and [74].

SCFT is dependent on the χ parameter calculated in the Flory Huggins model. The volume fraction profile across the interface for polymer A is given by

$$\phi_A(z) = \frac{1}{2}\left[1 + tanh\left(\frac{z}{w}\right)\right] \tag{3.21}$$

where w the interfacial width is given by

$$w = \frac{b}{(6\chi)^{1/2}} \tag{3.22}$$

The volume fraction profile is shown in figure 3.15

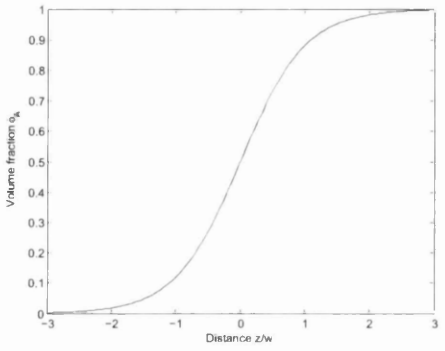

Figure 3.15: Volume fraction profile for infinite chain length polyers given by SCFT

where a is an average statistical segment length of the polymer chain. The interfacial tension is then given by [49]

$$\frac{\gamma}{k_B T} = \rho a \left(\frac{\chi}{6}\right)^{1/2} \tag{3.23}$$

where ρ is the unit volume of a monomer. These equations have the same forms as those given by expressions 3.19 and 3.20.

Modifications to equation 3.22 have been made by several authors to account for finite chain lengths [10] [80] [93]. A modified version of equation 3.22 for two polymers with different degrees of polymerisation is [93]

$$w = \frac{b}{(6\chi)^{1/2}}) \left[\frac{3}{4}\left(1 - \frac{2}{\chi N}\right) + \frac{1}{4}\left(1 - \frac{2}{\chi N}\right)^2\right]^{-1/2} \tag{3.24}$$

where N is the degree of polymerisation. The main difference between this and other forms offered is the term multiplying the $(1/\chi N)$ term in the denominator. From this expression it can be seen that the interface will broaden as the length of the polymers decreases. This is due to increased entropy of mixing of the shorter chains.

The interfacial width is related to the roughness σ measured by neutron scattering. The roughness σ is assumed to be Gaussian. The distribution of mixing across the mean interface for a Gaussian roughness is given by an error function with Gaussian width σ $(erf(x/\sigma))$, which is the convolution of a Gaussian and a step function. The error function $(erf(x/\sigma))$ and $tanh$ $(tanh(x/w))$ curves are almost identical if $\sigma = \sqrt{2\pi}w$.

3.1.7 Semi flexible polymers

The theory described above used to calculate the interfacial width assumes the chains are flexible. The theory breaks down when the chain stiffness of the polymers becomes too large and the polymers begin to become rod like. In order to deal with stiff chains Morse and Fredrickson [62] introduce a dimensionless bending modulus κ which is proportional to the persistence length. The bending modulus κ is given by

$$\kappa = \frac{b^2}{2a^2} \tag{3.25}$$

where b is the statistical segment length and a is the monomer length.

It is shown that $\kappa\chi << 1$ is the limit at which SCFT to describe flexible chains can be used. In the flexible regime $\kappa\chi << 1$ equations 3.21 and 3.22 are still valid to calculate the composition profile and the interfacial width. Equation 3.22 can be rewritten as

$$w = a\sqrt{\frac{\kappa}{3\chi}} \tag{3.26}$$

In the $\kappa\chi >> 1$ regime where the polymers are stiff the interfacial width is given by

$$w = \frac{b^2}{a}\left(\frac{1}{\kappa\chi}\right)^{3/2} \tag{3.27}$$

This gives an interfacial width which is a factor of $1/\kappa\chi$ narrower than predicted by completely flexible chains.

3.2 Capillary waves

3.2.1 Introduction

The results of specular neutron scattering studies on amorphous polymer bilayers have shown the RMS roughness of the interfaces to be larger than that predicted by intrinsic interfacial mixing of polymers by self consistent field theory [4], [28]. Shull [87] and others have suggested the extra roughness measured is caused by capillary wave fluctuations at the interface. Sferrazza et al [84] provides evidence using specular neutron scattering that this hypothesis is correct for amorphous polymer/polymer interfaces between PS and PMMA.

In this section the basics of capillary wave theory will be developed based on the initial work by Buff and Stillinger [11]. The interface is described as an ideal (abrupt) dividing surface $\zeta(x, y)$ between two pure phases with densities ρ_1 and ρ_2, where $\zeta(x, y)$ is the displacement of the surface from an ideal plane surface x, y at $z = 0$. Thermal energy gives rise to fluctuations of a liquid surface or interface. This results in a spectrum of capillary waves of different wavelengths and amplitudes imposed on the ideal intrinsic profile [73]. The density change across an interface due to the capillary wave fluctuations is shown in figure 3.16.

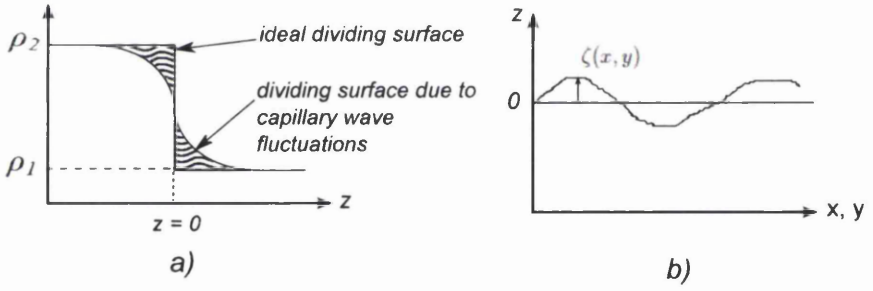

Figure 3.16: a) Density gradient at an interface. The ideal dividing surface represents a step function between 2 fluids of densities ρ_1 and ρ_2. The intrinsic profile is imposed on top. b) The lateral displacement of the ideal dividing surface from its average position at $z = 0$

3.2.2 Capillary wave theory

Buff et al [11] describe the work done to displace the surface a distance $\zeta(x, y)$ from the ideal surface by equation 3.28

$$W = \frac{1}{2}(\rho_1 - \rho_2)mg \int_A \int_0^{\zeta(x,y)} \zeta(x,y)dxdy + \gamma_0 \int \int_A (1 + \zeta_x^2 + \zeta_y^2)^{1/2} dxdy \tag{3.28}$$

where γ_0 is the interfacial tension between the phases, m is the mass of both phases and ζ_x and ζ_y are derivatives of $\zeta(x,y)$ with respect to x and y. If the surface is made up of capillary waves (surface waves of different wavelengths) then it can be represented by a Fourier series of decoupled harmonic surface waves.

$$\zeta(x,y) = \sum_k A(\mathbf{k}) e^{i\mathbf{ks}} \tag{3.29}$$

where $\mathbf{s} = x\hat{i} + y\hat{j}$ and A is the amplitude of the waves. Because $\zeta(x,y)$ is a small deviation from $z = 0$ then $(1+\zeta_x^2+\zeta_y^2)^{1/2}$ can be approximated as $1+\frac{1}{2}\zeta_x^2+\frac{1}{2}\zeta_y^2$. Substituting expression 3.29 into 3.28 gives

$$W = \gamma_0 A + \frac{1}{2}\sum_{k,k'} A(\mathbf{k})A(\mathbf{k}') \int_0^L \int_0^L e^{i(\mathbf{k}+\mathbf{k}')\mathbf{s}}[(\rho_1 - \rho_2)g - \gamma_0(k_x k_x' + k_y k_y')]dxdy \tag{3.30}$$

Using periodic boundary conditions $\zeta(0,x) = \zeta(L,x)$ and $\zeta(0,y) = \zeta(L,y)$ the allowed values for $\mathbf{k}$ are

$$\mathbf{k} = \frac{2\pi}{L}(n_x\hat{i} + (n_y\hat{j})) \qquad n_x, n_y = 0, \pm 1, \pm 2, ... \tag{3.31}$$

Integrating over x and y terms the $\mathbf{k} \neq \mathbf{k}'$ vanish. The expression for W is now

$$W = \gamma_0 L^2 + \sum_k |A(\mathbf{k})|^2 \frac{1}{2}([\rho_1 - \rho_2)g - \gamma_0(k^2)]L^2 \tag{3.32}$$

The mean values of the fluctuations ζ and the square of the fluctuations ζ^2 for a set of amplitudes $A(\mathbf{k})$ are

$$\overline{\zeta} = \frac{1}{A}\int_0^L \int_0^L \zeta dxdy = A(0) \tag{3.33}$$

$$\overline{\zeta^2} = \frac{1}{A}\int_0^L \int_0^L \zeta^2 dxdy = \sum_k |A(\mathbf{k})|^2 \tag{3.34}$$

The mean value $\overline{\zeta} = 0$ implies $A(0) = 0$ so $\mathbf{k}$ cannot be equal to 0 in the summation in equation 3.32. The mean square value of the amplitudes of the capillary waves are found by averaging the expression for ζ^2. The probability of a particular amplitude $A(\mathbf{k})$ of a capillary wave occurring due to a thermal fluctuation is proportional to the Boltzmann factor $\exp^{-\frac{W}{k_B T}}$ where k_B is the Boltzmann constant and T is the absolute temperature. Averaging over all possible $A(\mathbf{k})$ at $z = 0$ gives

$$\langle\overline{\zeta^2}\rangle = \sum_{k>0}\left[\frac{2k_BT}{L^2(g(\rho_1 - \rho_2) + \gamma_0 k^2)}\right] \tag{3.35}$$

Expression 3.35 gives the mean squared roughness of the surface caused by the capillary wave contribution so $\langle\overline{\zeta^2}\rangle = \sigma_{cw}^2$. The minimum and maximum possible capillary wave wavelengths will be limited by the system. The maximum k allowed is $\frac{2\pi}{l_m}$ where l_m is the minimum wavelength allowed for the system. Buff et al [11] define this to be fixed by the mean thickness of the mediums, although other authors [73] [84] define this to be of the order of the diameter of molecules in the system. The minimum k allowed is limited by the size of the system and is given by $\frac{2\pi}{L}$.

The sum over $\mathbf{k}$ (equation 3.35) can be written in the form of an integral with the above limits and with the relation $\Delta n_x \Delta n_y = \left(\frac{L}{2\pi}\right)^2 \Delta k_x \Delta k_y$ where n_x and n_y are in plane distances on the surface. The integral equation gives

$$\sigma_{cw}^2 = \langle\overline{\zeta^2}\rangle = \frac{k_BT}{2\pi^2\gamma_0}\int\int_{\frac{2\pi}{L}\leq k\leq\frac{2\pi}{l_m}} (a^2 + k^2)^{-1} d^2k = \frac{k_BT}{4\pi^2\gamma_0} ln\left(\frac{a^2 + (2\pi/l_m)}{a^2 + (2\pi/L)}\right) \tag{3.36}$$

where $a^2 = \frac{\Delta\rho}{2\gamma_0}$ and is known as the capillary length (see Rowlinson and Widom [73] page 10) and helps determine the length scale on which capillary wave effects occur for liquid surfaces. From equation 3.36 it can be seen that the major contribution to the mean square roughness comes for small values of k corresponding to large wavelengths. In the case where the minimum and maximum wavelengths are determined by factors other the capillary length and the size of the system and the system is subject to external fields that affect the capillary wave vector distribution then equation 3.36 is written as [84]

$$\sigma_{cw}^2 = \frac{k_B T}{4\pi\gamma_0} ln \frac{k_M^2 + k_v^2}{k_m^2 + k_v^2} \tag{3.37}$$

k_M^2 and k_m^2 are the largest and smallest wave vectors the system can contain, with no external potentials. The term k_v represents the effect on the surface of an external potential such as gravity or any other external potentials experienced by the interface. These external potentials may modify the largest and smallest wave lengths of the system. The numerator in this expression represents the maximum wave vectors and the denominator the minimum wave vectors of the system. k_M^2 is normally limited by the minimum wavelength (maximum k) which can be detected by the experimental setup due to resolution. In the case of a polymer interface measured using neutron reflectivity Sferrazza et al [84] suggest that $k_M = \frac{2\pi}{\sigma_0}$ and $k_m = \frac{2\pi}{\lambda_{coh}}$ where σ_0 is the intrinsic interfacial width given by self consistent field theory, λ_{coh} is the in plane coherence length of neutrons and represents the maximum capillary wave wavelength which can be detected by the neutron reflectivity experiment [75]. Assuming that these two terms for k_M and k_m are large compared with k_v equation 3.37 becomes

$$\sigma_{cw}^2 = \frac{k_B T}{4\pi\gamma_0} ln \frac{(\frac{2\pi}{\sigma_0})^2}{(\frac{2\pi}{\lambda_{coh}})^2} \tag{3.38}$$

3.2.3 Dispersive forces

Van der Waals (vdW) forces are attractive forces present between all pairs of neutral atoms. They are caused by either permanent or temporary (fluctuating) dipoles. Their effects are only significant on a lengthscale up to several hundred Angstroms. The van der Waals forces between a pair of isolated molecules has the form

$$w \approx -\frac{C}{R^6} \tag{3.39}$$

where C is a parameter describing the strength of the interaction between the atoms and R is the distance between them. Hamaker [35] derived an expression for the interaction of all atoms in two adjacent mediums by summing over the interactions of each pair of atoms, resulting in the Hamaker constant A where

$$A = \pi^2 C \rho_1 \rho_2 \tag{3.40}$$

where ρ_1 and ρ_2 are the number density of atoms in each medium. Generally values for A are around $10^{-19}J$ for interactions across a vacuum. Integrating over all atoms in the mediums the total VdW interactions are given by

$$w = -\frac{A}{12\pi l^2} \tag{3.41}$$

where l is the distance separating the two media. Since the interactions are dipole interactions then a third atom type in a system containing two interacting atoms will affect the interaction between the pair. Simply summing the interactions between pairs of atoms in a medium does not take into account the effect of the third medium. Liftshitz theory [46] ignores atomic structure and assumes continuous media in terms of the bulk properties of dielectric constant and (electromagnetic) refractive index. The final result for the effective Hamaker constant for two media interacting across a third media from Liftshitz theory is

$$A_{eff} = \frac{3}{4}kT\frac{\epsilon_1 - \epsilon_2}{\epsilon_1 + \epsilon_2}\frac{\epsilon_2 - \epsilon_3}{\epsilon_2 + \epsilon_3} + \frac{3h\nu_e}{8\sqrt{2}}\left[\frac{(n_1^2 - n_3^2)(n_2^2 - n_3^2)}{\sqrt{n_1^2 + n_3^2}\sqrt{n_2^2 + n_3^2}(\sqrt{n_1^2 + n_3^2} + \sqrt{n_2^2 + n_3^2})}\right] \tag{3.42}$$

where the ϵ_i is the dielectric constant of medium i, n_i is the refractive index of medium i, h is Planck's constant and ν_e is the main electronic UV absorption frequency. The order of the layers is shown in figure 3.17

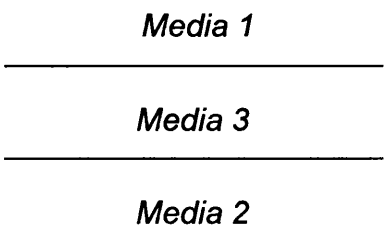

Figure 3.17: Order of layers for calculation of Hamaker constant by Liftshitz theory

Depending on the values of n_1, n_2, n_3 and ϵ_1, ϵ_2 and ϵ_3, A can either be positive or negative. For the case of liquid films on a substrate if A is negative then the film is stable. If A is positive then the film is not stable and may dewet from the substrate. In this work only stable films have been used. In a stable film architecture vdWs forces can act to suppress large wavelength capillary waves, defining a vdW cut. The smallest wave vector fluctuation the system can sustain may now depend also on the vdW contribution. For a scattering experiment where the gravitational

cut off is much larger than the coherence length the mean square roughness will depend on the coherence length of the radiation or the vdW cut off. If the high wavelength capillary modes suppressed by vdW forces are smaller than the coherence length of the neutrons then the scattering experiment will 'see' all possible capillary modes and the roughness measured will be due to the high wavelength cut off caused by vdW forces. If the high wavelength capillary wave modes are larger than the coherence length, then the scattering experiment will not 'see' these larger modes and the roughness measured will not take into account these higher wavelength capillary waves. Equation 3.37 can be written [84]

$$\sigma_{cw}^2 = \frac{k_B T}{4\pi\gamma_0} ln \frac{\left(\frac{2\pi}{\sigma_0}\right)^2}{\left(\frac{2\pi}{\lambda_{coeh}}\right)^2 + \left(\frac{2\pi}{a_{dis}}\right)^2} \tag{3.43}$$

For thin films the low wavevector cut off due to vdW forces is given by [26], [95]

$$q_{vdW} = \frac{(A_{eff}/2\pi)^2}{d^2} \tag{3.44}$$

3.3 Height to height correlation functions for capillary waves

Equation 3.35 for an individual capillary wave mode at a simple liquid interface may be written [59]

$$\langle \zeta(\mathbf{k})\zeta(-\mathbf{k}) \rangle = \left[\frac{2k_B T}{L^2(g(\rho_1 - \rho_2) + \gamma_0 k^2)} \right] \tag{3.45}$$

which is the average displacement from $z = 0$ as a function of $\mathbf{k}$. The height to height correlation function $c(R)$ for capillary waves may be obtained from the Fourier transform of equation 3.45 [21] [20] [50] which gives

$$c(R) = \langle \zeta(0)\zeta(R) \rangle = \frac{k_B T}{2\pi\gamma} K_0 \left(R\sqrt{\frac{\Delta\rho g}{\gamma}} \right) \tag{3.46}$$

where K_0 is the modified Bessel function of the second kind of order 0. At the limit $x \to \infty$,

$K_0(x) \to 0$. As $x \to 0$, $K_0(x)$ can be approximated by [58], [77]

$$K_0(x)_{x\to 0} \cong ln(2) - \gamma_E - ln(x) \tag{3.47}$$

where γ_E is Euler's constant.

This height to height correlation function is used by several groups [77], [26] to find the off specular scattering from a surface exhibiting capillary waves see section 2.9. Expressions 3.46 and 3.47 are divergent as $R \to 0$. Clearly the wavelength of capillary waves in a physical system must have a limit so a cut off is introduced, which corresponds to the maximum wavevector (k_M) of the capillary wave spectrum (as introduced in section 3.2.3). There is also the minimum wavevector k_m to consider. The general expression for off specular scattering from a single interface within the DWBA is given by equations 2.112 and 2.113 which are re-written below for clarity.

$$\frac{d\sigma}{d\Omega}_{\text{offspec}} = (L_x L_y)\frac{|k_0^2(1-n)^2|^2}{16\pi^2}|T(\mathbf{k}_1)|^2|T(\mathbf{k}_2)|^2 S(\mathbf{q}_t) \tag{2.112}$$

where

$$S(\mathbf{q}_t) = \frac{1}{|q_z^t|^2}e^{-((q_z^t)^2+(q_z^{t*})^2\sigma^2/2)}\int\int_{S_0} dXdY(e^{|q_z^t|^2 c(X,Y)} - 1)e^{i(q_x X + q_y Y)} \tag{2.113}$$

Meunier et al [59] define limits of integration between a and L the molecular length, which is the smallest wavelength of a capillary wave on the surface and the largest capillary wavelength measurable on the surface respectively. Meunier et al [59] define a as the capillary length and it corresponds with the largest wavevector of the capillary wave spectrum $a = 2\pi/k_M$ and L with the smallest wavevector $L = 2\pi/k_m$

Tostmann et al [98] and Dailiant and Gibaud [20] show that in the limit $k_m >> \sqrt{\Delta\rho g/\gamma}$ and integrating between a and L then equations 2.112 and 2.113 can be written

$$\frac{d\sigma}{d\Omega}_{\text{offspec}} = (L_x L_y)\frac{|k_0^2(1-n)^2|^2}{16\pi^2}|T(\mathbf{k}_1)|^2|T(\mathbf{k}_2)|^2\frac{k_B T}{\gamma q_R^2}\left(\frac{q_R}{k_M}\right)^{\eta} \tag{3.48}$$

where $\eta = (k_B T/2\pi\gamma|q_z|^2)$.

To define a minimum wavelength for capillary wave fluctuations some authors introduce a term which is dependent on the bending rigidity of the surface [59] [58]. This gives a minimum wavelength cut off to prevent divergence as $c(R) \rightarrow 0$. In this case the largest wave vector of the capillary wave spectrum is limited by κ the bending modulus of the surface. In this case 3.45 becomes [59]

$$\langle \zeta(\mathbf{k})\zeta(-\mathbf{k})\rangle = \left[\frac{2k_BT}{L^2(g(\rho_1-\rho_2)+\gamma_0 k^2)+\kappa k^4}\right] \tag{3.49}$$

Taking the Fourier transform of expression 3.49 yields for the height to height correlation $c(R)$ [91]

$$c(R) = \langle \zeta(0)\zeta(R)\rangle = \frac{k_BT}{\pi\gamma} K_0\left(R\sqrt{\frac{\Delta\rho g}{\gamma}}\right) - K_0\left(R\sqrt{\frac{\gamma}{K}}\right) \tag{3.50}$$

where K is the bending rigidity of the interface [59]. Including additional terms such as dispersive forces modify 3.50.

In the literature there have been examples of workers using the self affine fractal height to height correlation function (equation 2.76) to represent a spectrum of capillary waves. Stone [91] states that the self affine height to height correlation function $c(R) = \sigma^2 e^{-\left(\frac{x}{\xi}\right)^{2h}}$ (described in section 2.8) is able to represent a spectrum of capillary waves at a polymer/polymer interface. Akgun et al [2] also use the self affine height to height correlation function to fit off specular scattering from a polymer brush. Fits of the self affine height to height correlation to the capillary wave height to height correlation function is shown below for typical values of the constants. All units are in metres. The parameters for the capillary wave correlation function are $\gamma = 3e-3J/m^2$, $A = 2.5e-20$, $T = 453K$ and minimum cut off is $8e-9m$ (assuming on the length scale fitted bending rigidity and gravity terms are small). For $R < 8e-9, c(R) = c(8e-9)$. These parameters are typical of an amorphous polymer pair. The fitted values of the self affine correlation function are $h = 0.26$, $\sigma = 1.37e-9$ and $\zeta = 3.35e-7$.

3.3.1 Limits of the capillary wave model

Several authors have performed off specular scattering experiments on thin film systems using x-rays and fitted the data using the Born approximation. Sanyal et al [77] show that for the

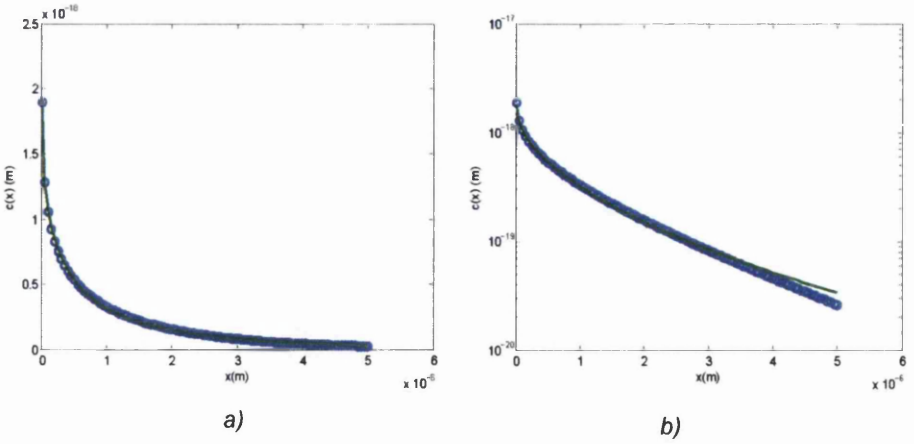

Figure 3.18: a) Fit of capillary wave height to height correlation function against self affine height to height correlation function b) Log fit of same function

capillary wave height to height correlation model described in equation 3.46 that the intensity of the scattering follows the relationship

$$I(q_x, q_z) = q_x^{\eta(q_z - 1)} \tag{3.51}$$

where $\eta = k_B T / \pi \gamma_{cw} q_z^2 / 2$. The data fitted is in the region between the specular peak (broadened due to resolution) and the Yoneda peak as a function of q_x at several fixed values of q_z. Doerr et al [26] show that for simple liquid films the capillary wave model can fit surface capillary waves with the predicted q_x, q_z dependence and a d^{-2} dependent cut off predicted by equation 3.44. However specular measurements show that the roughnesses of the films deviate from roughnesses predicted by the capillary wave model for films that are thicker than $\sim$ 10 Å. The suggested reason for this is retardation effects in the vdW forces which lowers the effective Hamaker constant, when the distance between the film surface and substrate becomes larger than $\sim$ 50Å. Doerrs work also gives evidence supporting the theory proposed by Napiórkowski and Dietrich which suggests the surface tension is reduced by capillary wave fluctuations. However Seo et al [82] show that for polymer systems (polystyrene film on Si substrate with thicknesses $\sim$ 45Å- $\sim$ 800 Å) the q cut off varies as a function $d^{-1.1}$ not d^{-2}. The suggested reason for this is chemical grafting of polymer chains to the substrate surface during annealing. The polymers would therefore have a constrained conformation similar to a polymer brush. Their results are consistent with theoretical polymer brush models derived by Fredrickson et al [31]. Akgun [2] use the Born approximation to fit off specular x-ray data

from polymer brushes. They find that the capillary wave behaviour (equation 3.51) was not observed but the data could be fitted using the self affine fractal height to height correlation function (see expression 2.76). The cut off lengths again agreed with theory from Fredrickson [31]. Wang et al [101] and Tolan et al [96] also find similar discrepancy between the capillary wave cut off predictions and experiment for polystyrene thin films and state the interaction of the polymer with the substrate as a cause for this.

Given the various discrepancies of expected fit parameters between the capillary wave theory and the experiment for a variety of liquid/liquid interfaces and the ability of the self affine height to height correlation function to represent data from a number of polymer systems the self affine model will be used in this work to attempt to fit the conjugated polymer system.

Chapter 4

Data Collection, Reduction and Experimental Optimisation

4.1 Neutron Scattering Experiments

Neutron scattering experiments were carried out on the reflectometers D17 at the ILL in Grenoble, France and CRISP and offspec at ISIS in Didcot, UK. All off specular data which has been fitted using the DWBA model developed was collected on D17. CRISP has provided some supplementary results, with the specular data fitted. Offspec is a newly commissioned instrument and we were fortunate enough to be some of its first users. However the off specular data obtained had fairly low count statistics due to count times being too low. The specular data from offspec was fitted, which gave results supplementary to the D17 data.

4.1.1 Aims and objectives of experimental optimisation

The aim of these experiments was to obtain good off specular reflectivity data with a good count statistics over a large q_x range. This will allow a large range in plane length scales of a samples buried interface to be probed. The obtained data can be fitted and the different roughness contributions extracted directly.

4.2 Sample preparation

4.2.1 Sample geometry

Samples in this work consisted of either single layer or bilayer geometries of thin films on a substrate. The materials used to make the films are described in the next subsection. Circular silicon blocks of two inches in diameter and four millimetres thickness with their native oxide layer intact were used as substrates. Sample geometry is shown in figure 4.1

4.2.2 Polymers and fullerenes used to make thin film samples

Poly(9,9-dioctylfluorene (F8)

F8 is a semi crystalline conjugated polymer. Above its glass and melting temperatures it enters a nematic phase, exhibiting long range directional order. The melting temperature

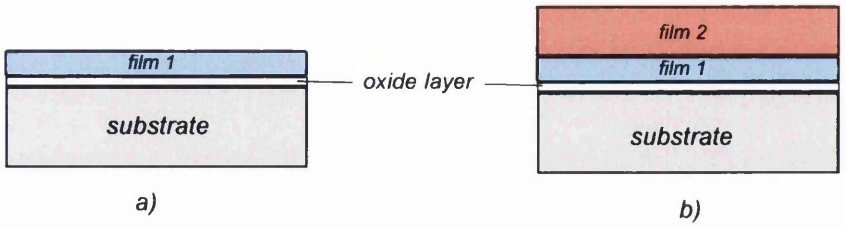

Figure 4.1: Sample geometry of a) a single layer film b) a bi layer film

T_m is $\sim 160^oC$ [40]. The batch used in this work has a number average molar mass M_n of 100 kg/mol and a weight average molar mass M_w of 204kg/mol found using gel permeation chromatography [25] resulting in a polydiversity index of $M_w/M_n = 204$. If the molecular number M_n is calculated using membrane osmometry this gives a value of $M_n = 34.9$kg/mol. It was provided by Cambridge Display Technologies.

Deuterated poly(methyl methacrylate) (dPMMA)

PMMA is an amorphous polymer, commonly used as a shatter-proof alternative to glass. It has a glass transition temperature of 105^oC. The batch used in this work is deuterated in order to provide contrast with other polymers for neutron scattering experiments. It has a number average molar mass M_n of 124kg/mol and a polydiversity index M_w/M_n of 1.02. It was supplied by Polymer Laboratories, UK.

Polystyrene (PS)

PS can be amorphous or semi crystalline. The batch used in this work is atactic and therefore amorphous. It has a weight average molar mass of $M_w = 343$kg/mol, a molecular number of $M_n = 327$kg/mol and a polydiversity of $M_w/M_n = 1.05$. It is supplied by Polymer Source Inc.

Poly(3-hexylthiophene) (P3HT)

P3HT is a conjugated polymer. The P3HT used in this work has a weight average molar mass of $M_w \sim 50,000$kg/mol and is manufactured by Rieke Metals Ltd. For more information about P3HT refer to section 7.1.1.

[6,6]-phenyl C61-butyric acid methylester (PCBM)

PCBM is a fullerene derivative. The PCBM used in this work has a weight average molar mass is M_w = 910.9kg/mol and it has a purity of greater than or equal to 99.5% when measured by High Performance Liquid Chromatography (HLPC) with respect to fullerene content. It is manufactured by Solenne BV in the Netherlands. For more information about P3HT refer to section 7.1.2.

4.2.3 Polymer solutions

Polymer and fullerene solutions were prepared by dissolving in toluene, chloroform, chlorobenzene solvents, or a mixture of chloroform and chlorobenzene. Their concentration was measured by mass by measuring the weight of the polymer and then measuring the weight of the polymer in solution using a micro-balance. The polymer solutions were heated in sealed vials at 70°C to aid dissolution.

4.2.4 Spin coating

Spin coating is a technique which produces thin uniform films of polymer of the order of tens of nanometers on a substrate. A spin coater machine is used to spin the substrate with polymer or fullerene solution on it. The substrate is held in place via a vacuum. One or two drops of polymer solution are then pipetted onto the substrate and the spin coater is immediately turned on. The spin coater quickly accelerates up to a steady rotational velocity which ranges between 1000-6000rpm and can be controlled by the user. Lowering rotational speed and increasing concentration of the polymer or fullerene solutions will give thicker films. The thickness of the film can be controlled to good accuracy.

4.2.5 Film floating

To create a single layer film/substrate system the polymer or fullerene is spin coated straight onto the silicon substrate. To create a bilayer the bottom layer is spin coated onto the silicon substrate and the top layer is spin coated onto mica, which has been cleaved in order to reveal a clean surface. The film and silicon substrate are then submerged in a beaker of deionised

water. The film on the mica is slowly submerged at an angle into the beaker which peels the film off the mica, leaving it floating on the surface. Not all of the mica is submerged, leaving a small part of the film still attached. The silicon substrate is then drawn up under the floating film to create the bi layer. Care must be taken to not trap water between the films.

4.2.6 Annealing

Samples were bought to thermodynamic equilibrium by annealing in a preheated oven under vacuum conditions ($\sim$ 10 mbar). The times and temperatures used to reach equilibrium were based on those found by Higgins et al [39].

4.2.7 Samples

The main range of samples consist of bilayer films of $\sim$ 1000Å F8 on top dPMMA of various thicknesses on silicon, and films of $\sim$ 1000nm F8 on top $\sim$ 480Å dPMMA annealed for various times. These are supplemented by single films of $\sim$ 1000Å F8 and $\sim$ 480Å dPMMA on silicon as well as a silicon block and a bilayer of $\sim$ 1800Å PS on $\sim$ 1700Å dPMMA. The P3HT and PCBM were used to make samples in bilayer and single layer geometries on Si substrates of various thicknesses. They were heated at different temperatures for different times. The P3HT/PCBM samples are described in section 7.2. The same batches of polymer were used for all samples.

The different thickness samples of F8/dPMMA were used to test the hypothesis that interfacial roughness is a function of film thickness as discussed in section 3.2 [84]. These samples were all annealed for three hours under vacuum conditions. The different thickness dPMMA series of samples are labeled with the prefix *th* (see table 4.1). The single layer samples and the bare silicon substrate sample were used to give insight into the scattering from the air/ F8 interfaces and the dPMMA/silicon interfaces of the bilayers. These samples are labeled with the prefix *sl*. The different annealing time samples were used to show that the different thickness samples were annealed for enough time in order to achieve thermodynamic equilibrium. These samples are labeled with the prefix *an*. The PS/ dPMMA sample was used as a comparison to see if the interface between a conjugated polymer and an amorphous polymer is similar to the interface between two amorphous polymers.

Initial investigations were also made into P3HT/PCBM bilayers on Si substrate. The samples were prepared in the same way, though annealing times and temperatures were different.

4.3 D17 ILL

Three experiments were carried out on the reflectometer D17 at the ILL in November 2007, December 2008 and October 2009. The aim of these experiments was to collect specular and off specular data on conjugated/amorphous polymer bilayer samples. Table 4.1 gives details of the samples tested at the ILL. Reflectivity was performed at two angles on all samples. The flux of the instrument in 2009 was $\sim$ 3 times greater than in 2008, so count times could be reduced. A fourth supplementary experiment on D17 was carried out in June 2010 to obtain specular data for two more F8/dPMMA samples of different thicknesses.

4.4 D17 instrument settings

D17 was used in time of flight mode. The instrument collects specular and off specular data simultaneously using an area detector. It has a useful wavelength range of between $\sim$ 3Å to $\sim$ 25 Å and a θ coverage of the detector of $\sim 4^o$. In order to get a q_z range from $\sim 0\text{Å}^{-1}$ to 0.2 Å^{-1} the reflectivity needs to be measured at two angles, which are then added together to give specular reflectivity over the required range. The angles of incidence used were $\theta_1 = 0.6^o$ and $\theta_2 = 2.5^o$ which covered the required q_z range.

The detector was set so that the sample horizon at $2\theta = 0$ could be measured, so that the Yoneda scattering detected was only limited by the lowest wavelength neutron. Two different slit settings were used for the first and second angles, with the slits being opened wider for the second angle due to the fall off in reflectivity as the angle of incidence is increased. The slit openings are a compromise between neutron flux and resolution. For $\theta_i = 0.6$ the slits were opened 0.6mm and 0.3mm respectively. For $\theta_i = 2.5$ the slit were opened 5mm and 1.1mm respectively. This gives resolution $d\theta/\theta$ of 0.75% and 5% for angles one and two respectively.

The choppers were left in a closed position giving a q independent wavelength resolution of $d\lambda/\lambda = 1\%$ (see section 2.4.8)

Throughout all the experiments on D17 the slit settings, sample detector distance and the footprint of the beam on the sample were kept constant. The chopper settings were kept constant for the 2007, 2008 and 2010 experiments keeping the resolution constant. They were changed slightly for the 2009 experiment to allow larger neutron flux, though the change in resolution in λ was small and the q resolution was still dominated by the the slit settings. The

Experiment year 2007							
Sample label	**Polymer layer 1**	**Polymer layer 2**	**Thickness layer 1 (nm)**	**Thickness layer 1 (nm)**	**Annealing time (hrs)**	**Count time θ_1 (s)**	**Count time θ_2 (s)**
an1	F8	dPMMA	100	48	0	1200	18000
an2 / th4	F8	dPMMA	100	48	3	1200	18000
Experiment year 2008							
sl1	-	dPMMA	-	48	3	1800	18000
sl2	-	F8	-	100	3	1800	18000
an3 / th4	F8	dPMMA	100	48	3	1800	72000
th1	F8	dPMMA	100	16	3	1800	18000
an2	F8	dPMMA	100	48	0	1800	72000
an6	F8	dPMMA	100	48	67	1800	72000
Si block	-	-	-	-	-	1800	18000
Experiment year 2009							
th3	F8	dPMMA	100	42	3	1800	25200
th5	F8	dPMMA	100	62	3	1800	25200
th2	F8	dPMMA	100	22	3	1800	25200
th1	F8	dPMMA	100	16	3	1800	25200
	PS	dPMMA	180	170	24	1800	25200
Experiment year 2010							
th6	F8	dPMMA	100	12	3	1800	7200
th7	F8	dPMMA	100	85	3	1800	7200

Table 4.1: Neutron reflectivity experiments conducted on D17 at ILL 2007, 2008 and 2009

same detector was used for all experiments.

4.5 Data reduction

An area detector is used on D17. The instrument uses a ribbon beam, so that pixels are summed vertically along the y-axis. This leads to two hundred and eighty six pixels arranged at different horizontal distances from the direct beam. By knowing the angle of incidence on the sample, the flight path and the angle of the detector the angle of reflection subtended by each detector pixel the angle of reflection θ_f can be calculated. The resolution of the detector is given by the angular acceptance of each pixel. In TOF mode the wavelength of each neutron that hits the detector is found by knowing the time that it left the chopper, the neutron flight path and the time it hit the detector. D17 has one thousand time channels, so the time of flight of a neutron can be put into one of a thousand bins. The raw data is presented in a 2D colour map plot with the detector pixel number on the x axis and the time channel on the y axis.

4.5.1 Reflectivity normalisation

The raw count data from D17 is normalised with respect to the efficiency of the detector and the distribution of neutron wavelengths in the beam. In order to normalise for the detector efficiency the beam is scattered for half an hour at the beginning of each experiment using a water cell. The scattering from the water cell is completely incoherent, so the scattering intensity will be constant over all angles. The data is then averaged over the time channel for each detector pixel, as shown in figure 4.3.

For the direct beam run the beam is incident directly on the detector with no refraction or reflection after leaving the choppers. The slit settings are set to those used in the reflectivity experiments, so each angle requries its own direct beam run. The direct beam run is a measure of the distribution of neutron wavelengths in the beam. The direct beam measurement is averaged over all detector pixels as shown in figure 4.5.

All experimental data is divided through by the averaged water run and direct beam. In addition to normalising the data it also allows different data sets from different experiments can be compared, as although the flux may change between experiments it is normalised by the direct beam count.

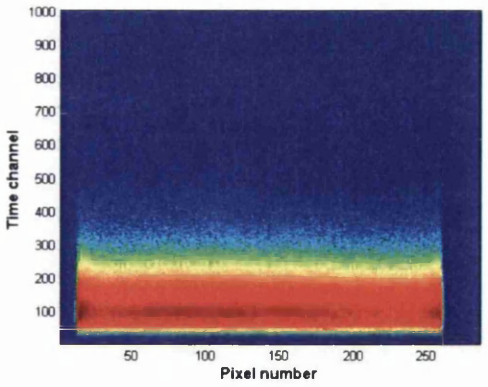

Figure 4.2: Raw count data from water cell run (from 2008 experiment) (counts are on a log scale)

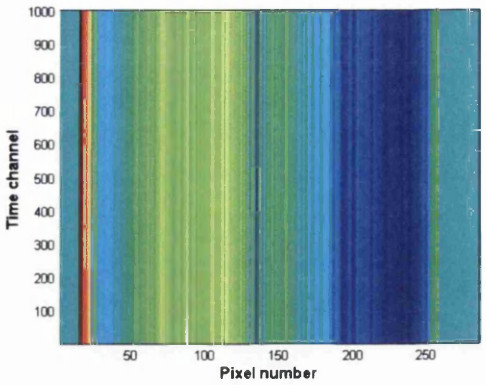

Figure 4.3: Data from water cell run averaged over all time channels (counts are on a log scale)

4.5.2 Background

There are several sources of background in this neutron scattering experiment. These include neutrons straying from other instruments, scattering from the air and incoherent scattering from the sample. To take into account background that is not from the sample, background runs are taken with the instrument set up as it would be to measure a sample without sample in the beam. The background runs should count for the same length of time as the experimental runs and then can be subtracted directly.

Flight path in air

Around the sample mounting a small amount of the D17 neutron flight path is in air, which can cause background scattering. In order to reduce the background in 2008 and 2009 a vacuum chamber was used in this region with quartz windows. This reduced the air flight path of the neutrons to less than 10mm. Five hour counts of the background reflectivity and reflectivity from sample 5.3 were taken in 2007 and 2008 with and without the vacuum chamber respectively. Far lower backgrounds were achieved using the vacuum chamber as can be seen from data cuts in figure 4.6 for the second angle.

A far wider q range can be probed. In the region between the specular peak and the Yoneda fringe for $\lambda = 5$ wavelength with no vacuum chamber the scattering from the sample is a factor of ~ 1.3 greater than the background. However with the vacuum chamber the sample

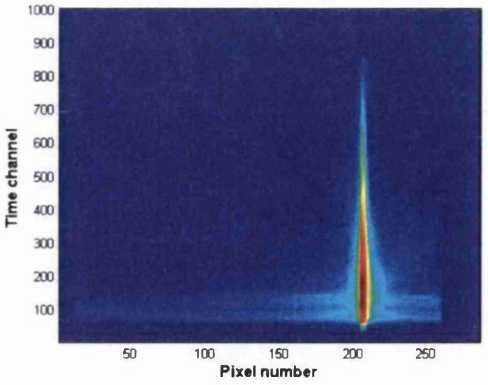

Figure 4.4: Raw count data from direct beam run (from 2008 experiment) (counts are on a log scale)

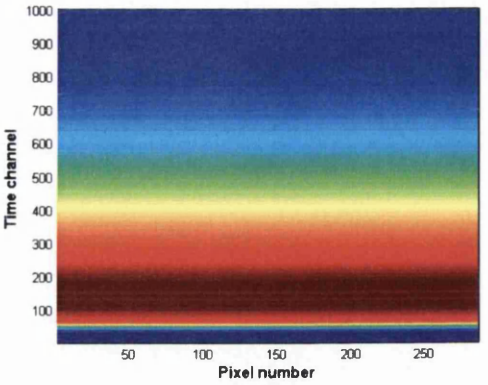

Figure 4.5: Data from direct beam run averaged over all detector pixels (counts are on a log scale)

reflectivity is approximately a factor of ~ 8 greater than the background (see fig 4.6 c). From figure 4.6 a) and b) it can be seen that without the vacuum chamber the reflectivity of the sample becomes swamped by the background at ~ 5 Å. With the vacuum chamber in place the range of wavelengths probed can be extended down to ~ 3 Å with the sample reflectivity still greater than the background reflectivity by a factor of 2.

This result shows that air scattering is a significant source of background scattering for neutron scattering experiments, and minimising the air flight path of the neutron beam is important to achieving good statistics in regions of low reflectivity. The slightly lower counts of the 2007 experiment for the same counting time can be attributed to the neutrons scattered out of the beam due to air scattering.

4.5.3 Scattering from Si and F8 interfaces

The bilayer architecture for samples used in this work is chosen so that scattering will be dominated by the buried interface. However there will be scattering from other interfaces. Using scattering from bare silicon substrate and the single F8 layer on a substrate these can be compared with the background to see if they give any significant off specular scattering. Comparison between scattering from a silicon substrate and from an F8/Si sample will show if the strength of scattering from the air/F8 interface and incoherent scattering from the F8 film gives significant off specular scattering. The scattering length density of the silicon substrate is approximately a factor of four greater than that of the F8. It is expected that the scattering from

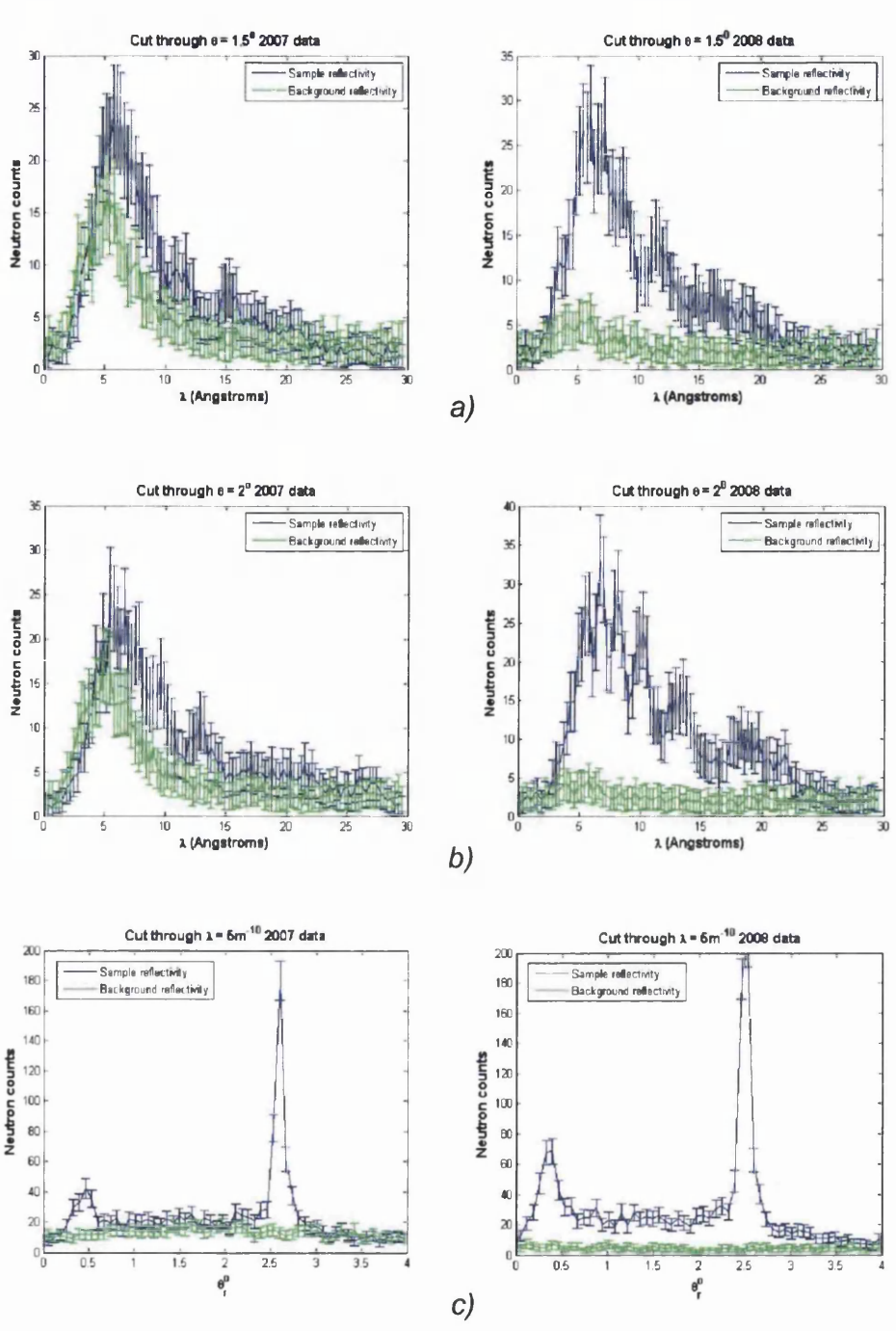

Figure 4.6: a) Cuts of data without (2007) and with (2008) vacuum chamber around $\theta = 1.5^o$ Cut over 9 λ pixels b) Cuts of data without (measured in 2007) and with (measured in 2008) vacuum chamber around $\theta = 2^o$ Cut over 9 λ pixels c) Cuts of data around $\lambda = 5$ without (measured in 2007) and with (measured in 2008) vacuum chamber. Cut is over 11 θ pixels

the air/F8 interface will be small when compared with the scattering from the F8/ Si interface as in the Born approximation the off specular scattering is a function of the absolute difference of the squares of the scattering length density of the material either side of an interface. Figures 4.7, 4.8 and 4.9 show θ/λ unnormalised reflectivity plots for the substrate, the single F8 layer and background with the beam not on the detector respectively. The off specular regions show very little intensity.

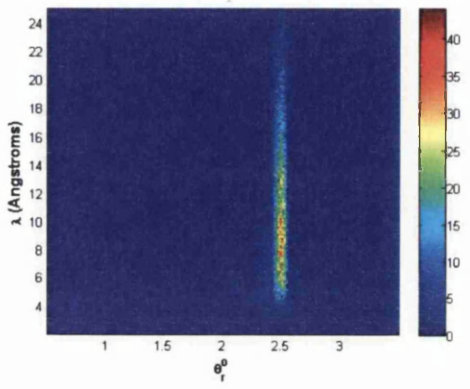

Figure 4.7: θ/λ reflectivity plot of Si substrate at $\theta_i = 2.5^o$ for 5 hour count time (Scale bar shows neutron counts)

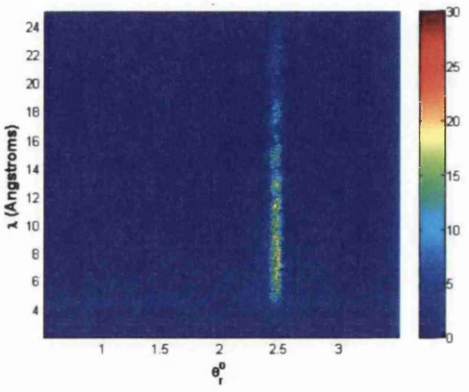

Figure 4.8: θ/λ reflectivity plot of single layer of F8 on Si at $\theta_i = 2.5^o$ for 5 hour count time (Scale bar shows neutron counts)

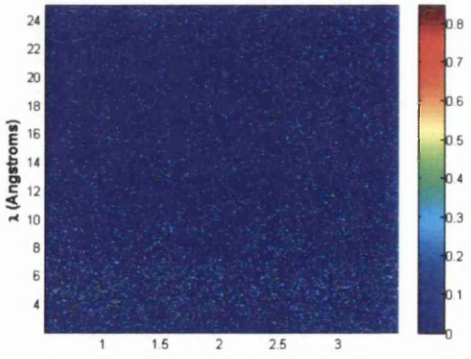

Figure 4.9: θ/λ background counts plot for 5 hour count time with $\theta_i = 2.5^o$ slit settings with the beam not on the detector (Scale bar shows neutron counts)

Figures 4.10 and 4.11 show cuts through θ of the raw count data of the silicon substrate compared with background runs counted for the same time. They show that slightly higher off specular scattering from the Si substrate when compared with the background. The intensities of the background and silicon in the off specular are peaked around $\lambda = 5$Å which corresponds

with the direct beam spectrum which can be seen by comparing with figure 4.5.

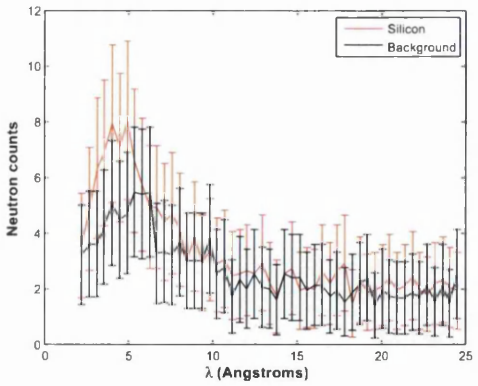

Figure 4.10: Cut through $\theta = 1.5^o$ for silicon substrate and background reflectivities

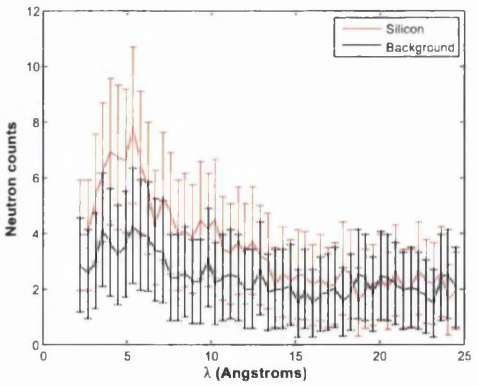

Figure 4.11: Cut through $\theta = 2^o$ for silicon substrate and background reflectivities

Figures 4.12 and 4.13 show cuts through the same θ values for the F8/Si sample and the silicon. The cuts are eleven pixels wide. The difference in off specular scattering is small, suggesting that the off specular scattering from the air/F8 interface is insignificant when compared with the F8/silicon interface.

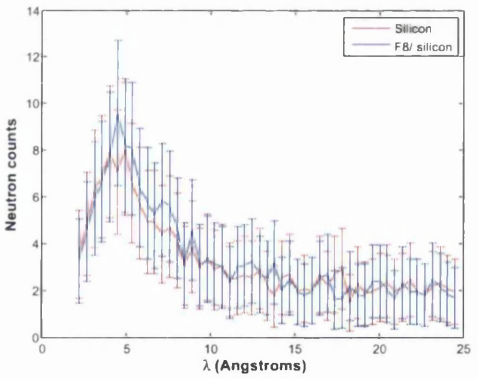

Figure 4.12: Cut through $\theta = 1.5^o$ for silicon substrate and F8/Si reflectivities

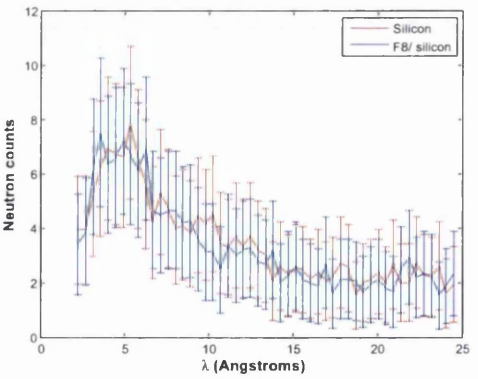

Figure 4.13: Cut through $\theta = 2^o$ for silicon substrate and F8/Si reflectivities

In conclusion the main source of background comes from scattering by the air, which is minimised using the vacuum chamber. The second most significant source of background comes from the sample. Background from the silicon is large compared with incoherent scattering from the F8 film, which is negligible.

4.5.4 Data reduction

Data reduction was performed using LAMP software provided by the ILL, and specular data was extracted using the COSMOS routine within LAMP. A road map of the route to extract usable off specular and specular data from the D17 instrument is outlined in figure 4.14 and explained in the following list.

a) Neutron reflectivity is recorded by the detector, measuring the number of neutrons hitting each pixel and the time taken between the neutron leaving the chopper and hitting the detector

b) The reflectivity is plotted as a function of pixel number and the time of flight of neutrons. Background run data is subtracted from the raw reflectivity data. The data is then divided through by the water run and the direct beam run to normalise.

c) The x axis converted to 2θ (where $2\theta = \theta_i + \theta_r$). The y axis converted to λ. This gives a plot of the off specular data in θ/λ space. Data analysis, cuts and rebinning can be carried out on the off specular data

d) Sum all pixels over the λ direction to find the width of the specular peak, which will be smeared by the resolution

e) Make a cut in the specular data that corresponds to the width of the specular peak, then sum all these pixels in over the θ direction for both angles

f) Plot against q_z of the angle of incidence ($q_z = 4\pi/\lambda \sin\theta_i$ for specular data), and rebin the reflectivity data to smooth the curves

g) Scale the reflectivity below the critical edge of the first angle to 1. Match the fringes of the 2nd angle to the fringes of the 1st in the overlap region to create complete curve over q_z range. The specular reflectivity data is now ready for analysis

Error

The error bars for each pixel are calculated as the square root of the counts, using Poisson's statistics [86]. The error bars were normalised in the same way as the reflectivity data. When background was subtracted from the reflectivity the error was given by the square root of the reflectivity counts plus the square root of the background counts.

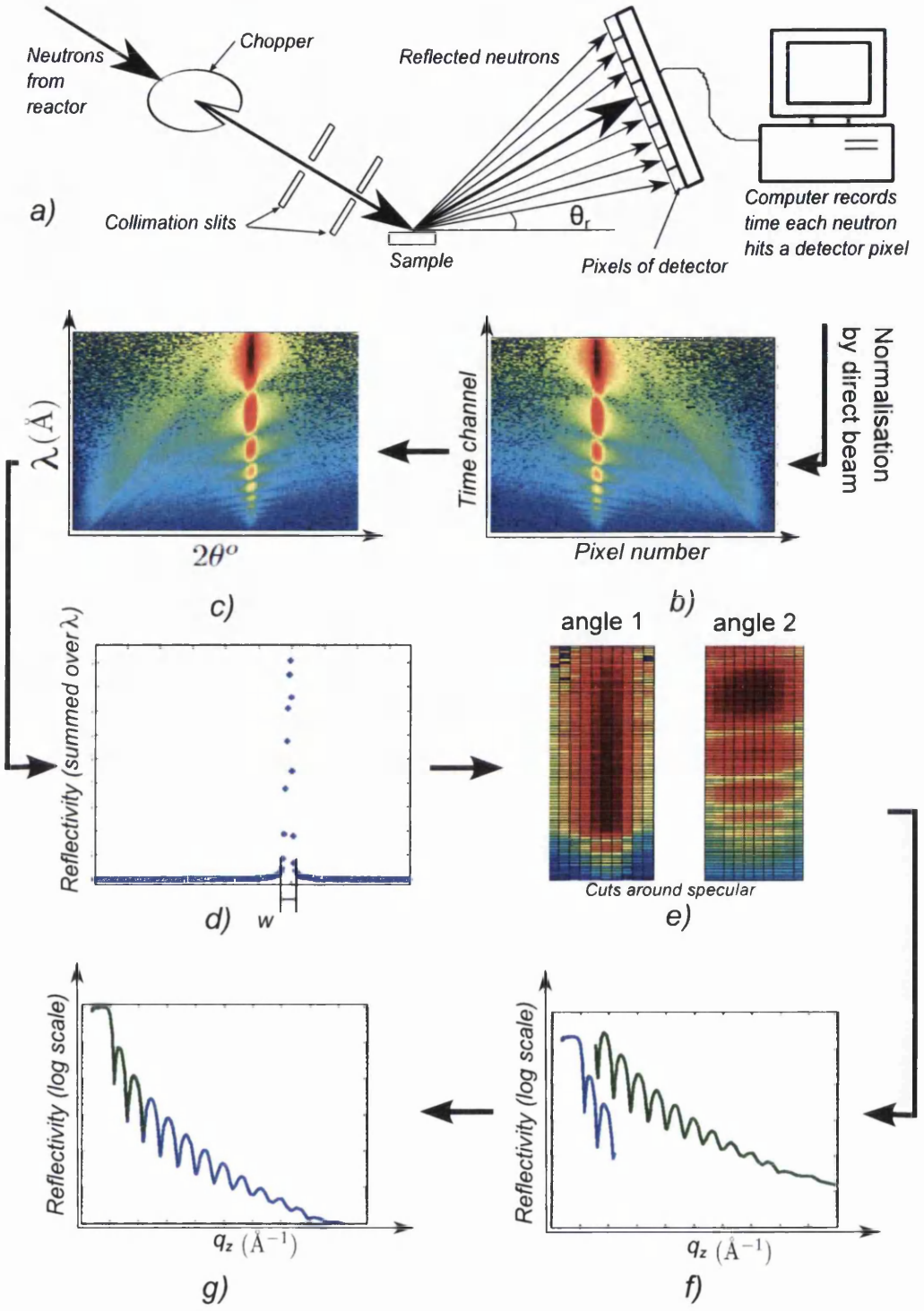

Figure 4.14: Steps to extraction of off specular and specular data from D17. Steps are outlined in the text

4.5.5 Comparison between different experiments

In order to check the instrument and samples between different experiments data collected from sample $th4$ in 2007 and 2008 is compared and data collected from sample $th1$ in 2008 and 2009 is compared. Figure 4.15 shows that the specular data for sample $th1$ is nearly identical between 2008 and 2009, showing that results from each experiment can be directly compared.

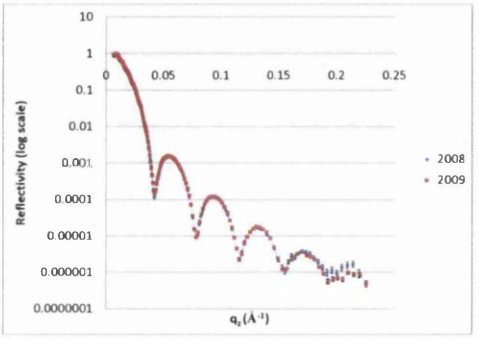

Figure 4.15: Comparison of specular reflectivity data for sample $th1$ on D17 for 2008 and 2009 experiments

4.5.6 Experimental Data

The experimental results for the single layers, the different thickness F8/dPMMA bi layers and the PS/PMMA bilayer are shown below. Examples of the specular and the normalised off specular results for the second angle are shown below. The second angle gives more features in the off specular reflectivity. Figure 4.16 shows the normalised off specular data for the first angle ($\theta = 0.6^o$) from sample th4, with $\sim$ 1000Å on $\sim$ 480Å dPMMA film annealed for three hours. The off specular scattering at this angle for this sample and all other samples tested is relatively featureless and so off specular scattering will not be modelled for this angle.

Blank silicon and single layers

There is very little off specular scattering from the bare silicon substrate and the F8 single layer. There are fringes in the specular of the F8 sample due to interference in scattering between the two air/F8 and F8/Si interfaces. It can be seen that there is significant off specular scattering from the dPMMA single layer. The Yoneda scattering is weak, suggesting low interfacial

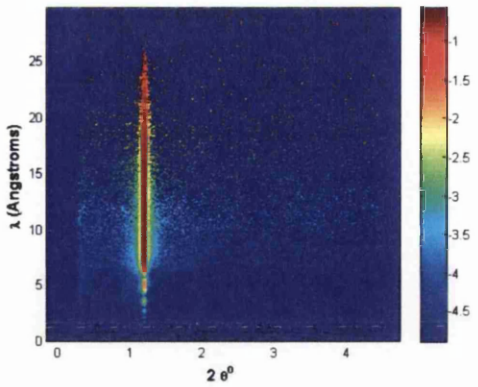

Figure 4.16: Normalised off specular scattering from sample th4 (thickness 48nm) for $\theta_i = 0.6$ annealed three hours

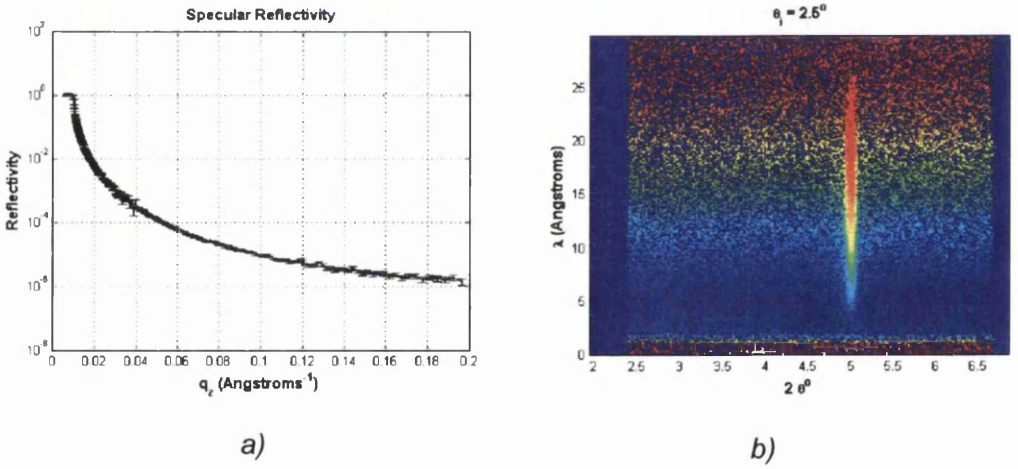

Figure 4.17: Experimental results for bare silicon substrate at $\theta_i = 2.5^o$ a) Specular reflectivity b) Off specular reflectivity

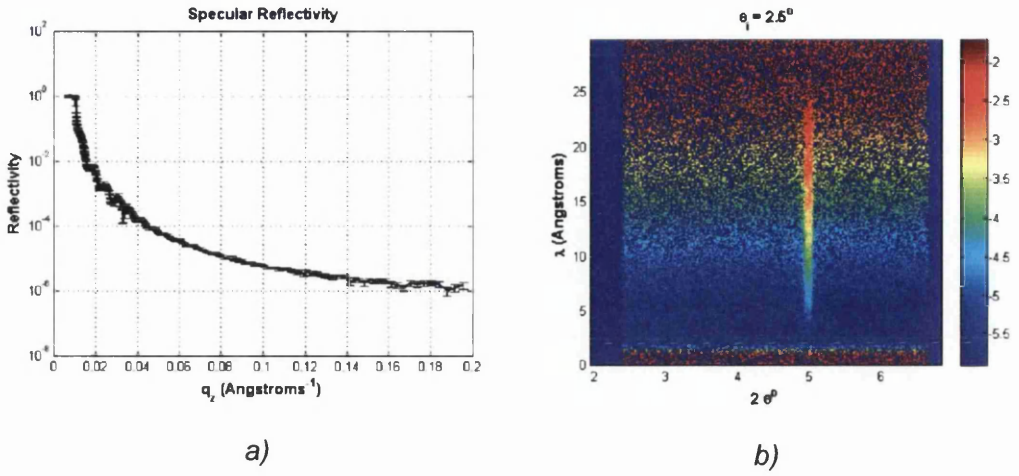

Figure 4.18: Experimental results for single layer F8 on Si substrate of thickness $\sim$ 1000Å, annealed 3 hrs at $\theta_i = 2.5^o$ a) Specular reflectivity b) Off specular reflectivity

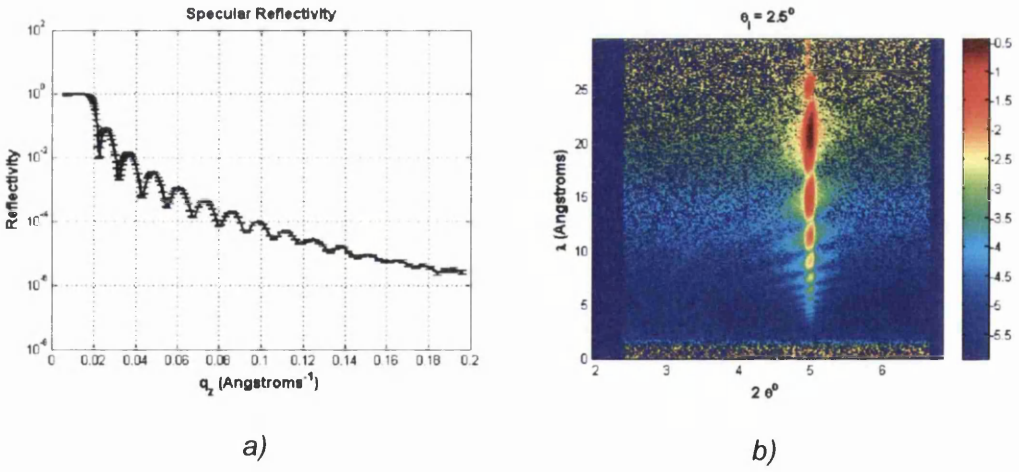

Figure 4.19: Experimental results for single layer dPMMA of thickness $\sim$ 480Å on Si substrate annealed 3 hrs at $\theta_i = 2.5^o$ thickness, a) Specular reflectivity b) Off specular reflectivity

roughness, but the lines of heightened intensity running along constant q_z are very well defined suggesting strong correlation between the morphology of the air/dPMMA interface and the dPMMA/Si interface (see section 2.10.1).

F8/dPMMA bi layer unannealed

Results for the unannealed F8/ dPMMA system

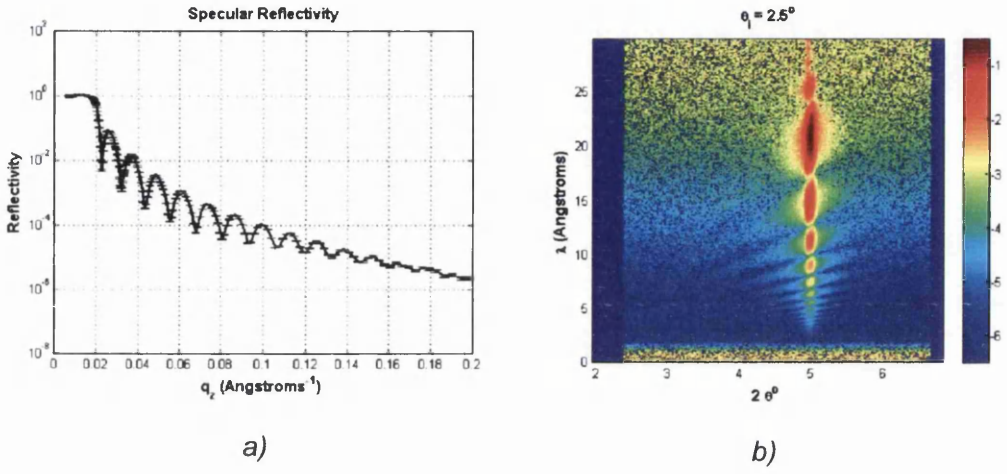

Figure 4.20: Experimental results for unannealed F8/ dPMMA bilayer of thickness $\sim$ 480Åat $\theta_i = 2.5^o$ a) Specular reflectivity b) Off specular reflectivity

F8/dPMMA bi layers of different thicknesses annealed for three hours

An example of an experimental result for an annealed F8/dPMMA bilayer is shown below

The fringe spacing of the specular reflectivity decreases with increasing thickness as expected. All samples show strong Yoneda scattering suggesting roughness at the F8/ dPMMA interface. The Yoneda scattering becomes systematically stronger as the thickness of the dPMMA layer is increased, suggesting that the interfacial roughness is increasing with thickness. Lines of constant q_z are present for all the samples, but are not as strong or well defined as for the unannealed sample suggesting that the correlation between the F8/ dPMMA interface and the dPMMA/ Si interface is diminished by annealing.

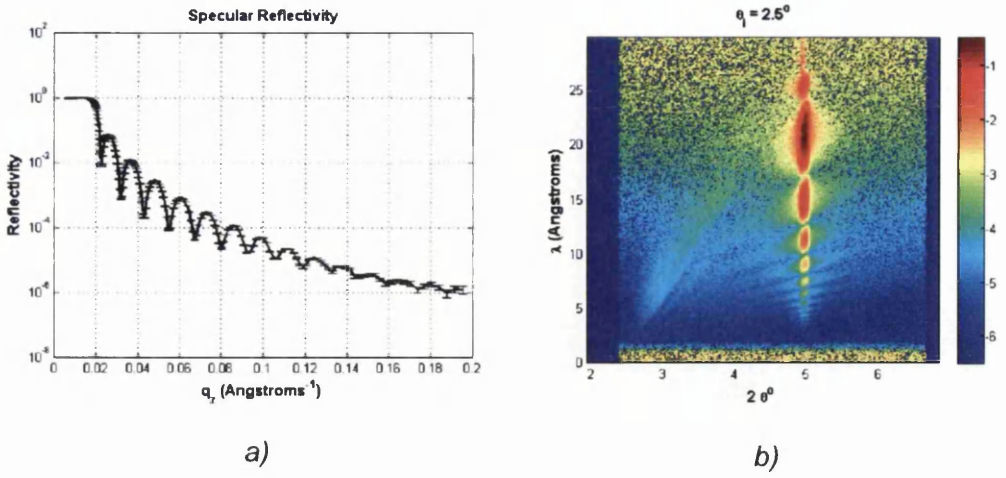

Figure 4.21: Experimental results for F8/dPMMA bilayer of thickness ~ 480Å annealed for 3 hours at $\theta_i = 2.5^o$ a) Specular reflectivity b) Off specular reflectivity

PS/PMMA results

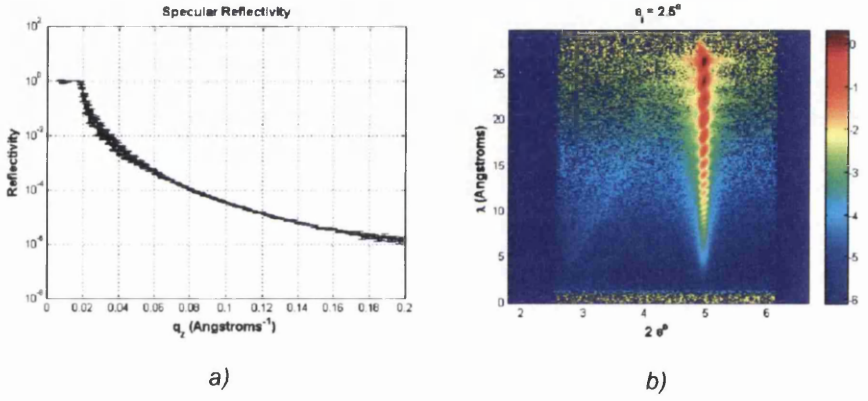

Figure 4.22: Experimental results for PS/dPMMA bilayer a) Specular results b) Off specular results

The off specular scattering from this system seems weak when compared with the F8/ dPMMA system.

4.6 CRISP

CRISP was used to perform an experiment on sample an4 a $\sim$ 1000Å F8 on $\sim$ 480Å dPMMA bilayer annealed for twenty four hours. The specular reflectivity was extracted from the off specular reflectivity and fitted. To achieve the required q_z range reflectivity has to be measured at three angles. The angles used were 0.35^o, 0.65^o and 1.5^o with respective current of $80\mu A$, $300\mu A$ and $450\mu A$. The slit settings and angular resolution are

Angle	**Slit 1** (mm)	**Slit 2** (mm)	**Angular resolution** (%)
0.35	0.672	0.308	1.4
0.65	1.243	0.567	2.8
1.5	2.87	1.31	6.4

Table 4.2: Neutron reflectivity experiments conducted on CRISP at ISIS 2007

where the sample detector distance is 1.87m. The data is normalised by dividing through by the wavelength distribution of the main beam and the detector efficiency. The wavelength distribution is measured by a monitor throughout the experiment which is between the lsit and the sample. The specular reflectivity was extracted from the off specular reflectivity using a MatLab code written at ISIS by Dr. Tim Charlton and Dr. Rob Dalgliesh.

4.7 Offspec

Offspec at ISIS was used to measure reflectivity on further examples of the 3 hour annealed F8/ dPMMA range and also different annealing times of 1000/Å F8 on 480Å dPMMA bilayers to check that 3 hour annealed samples have reached thermodynamic equilibrium. The P3HT/PCBM samples were tested on offspec. They were all annealed for ten minutes under vacuum conditions, although the annealing temperature was varied. A PS/dPMMA bilayer sample was also measured. Table 4.3 shows the samples measured on offspec. Reflectivity was measured at angles of incidence of $\theta_i = 0.5^o$ and $\theta_i = 1.6^o$.

The slit settings for offspec were giving $d\theta/\theta$ to be . No background was subtracted. The data was normalised using a direct beam run and by the detector efficiency as for D17. The instrument has a constant q_z resolution of $\sim$ 2.5%.

Experiment year 2009							
Sample No.	**Polymer layer 1**	**Polymer layer 2**	**Thickness layer 1 (nm)**	**Thickness layer 1 (nm)**	**Annealing time (hrs)**	**Count current θ_1 (μA)**	**Count current θ_2 (μA)**
an5	F8	dPMMA	100	48	24	1	40
an7	F8	dPMMA	100	48	67	1	40
th6	F8	dPMMA	100	12	3	1	40
th7	F8	dPMMA	100	85	3	1	40
-	PS	dPMMA	180	170	3	1	40
Sample No.	**Polymer layer 1**	**Polymer layer 2**	**Thickness layer 1 (nm)**	**Thickness layer 1 (nm)**	**Annealing temp (^oC)**	**Count current θ_1 (μA)**	**Count current θ_2 (μA)**
p1	P3HT	-	11	-	140	1	40
p2	PCBM		130	-	140	1	40
p3	P3HT	PCBM	11	130	140	1	40
p4	P3Ht	PCBM	11	130	150	1	40
p5	P3HT	PCBM	20	130	140	1	40

Table 4.3: Neutron reflectivity experiments conducted on offspec at ISIS 2009

4.8 Atomic Force Microscopy

Atomic force microscopy (AFM) was used to measure the roughness and the Hurst parameter of the single layer dPMMA sample and the roughness of the bare silicon, in order to fix these parameters as constants in the off specular fitting.

4.8.1 AFM background

AFM is a type of scanning probe microscopy first introduced by Binnig, Quate and Gerber [6] in 1986. It can be used to give high resolution three-dimensional images of sample surfaces down to the nanoscale. AFM was used to probe the surface morphology and find the roughness and other properties of Silicon substrate surfaces and top surfaces of polymer single layer and bilayer samples.

AFM uses a micro scale cantilever with a sharp tip on it with the tip radius in the order of nanometers. The tip is brought close enough to the surface to interact with its van der Waals forces. The interaction between tip and surface causes the cantilever to deflect. The deflection of the cantilever is measured by shining a laser on the back of the cantilever and measuring its reflection on an array of photo diodes. The tip is then rastered over the surface using a piezoelectric tube which can move in the x, y and z directions. The distance between tip and surface is kept constant using a feedback loop between the photodiode and the piezoelectric tube. From the deflection of the cantilever the height of the surface can be found at each point. The whole surface is scanned by performing a series of adjacent one dimensional line scans and adding them together to construct the three dimensional image of the surface where the direction of the lines is called the fast scan direction and the perpendicular direction is the slow scan direction. This is known as contact mode AFM. The AFM can also be used in tapping mode, where the cantilever oscillates at its natural frequency. When the cantilever is close to the surface the interaction will cause the frequency of the vibration to change and the feedback loop is used to keep this frequency constant by adjusting the height of the tip above the surface, which is used to measure the height of the surface features. A diagram of AFM operation is shown in figure 4.23. Gain parameters of the feedback loop can be adjusted. Adjusting the gains appropriately is important to get good images.

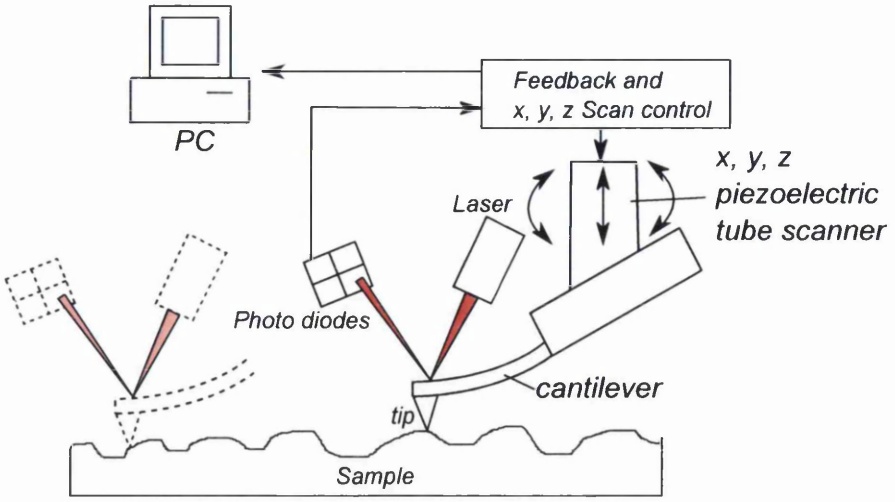

Figure 4.23: Operation of AFM

4.8.2 Data collection

Measurements were collected using a Park systems XE100 AFM in contact mode. The XE100 uses a separate piezo in the scanning stage for x, y movements, separating x, y and z movements, which helps minimise bowing artifacts in the scans. Scan lines were normalised to each other using inbuilt functions in the data acquisition software. AFM work was carried out on the silicon substrate and a duplicate of the single layer dPMMA sample used in the scattering experiments. AFM scan datasets were analysed using Gwyddion software [64] distributed by the Czech Metrology Institute.

Extracting RMS roughnesses for dPMMA and Silicon substrate

To extract the roughness of the dPMMA and silicon substrate $45\mu m \times 45\mu m$ scans were used which is of the same order as the coherence length of the neutrons in the reflectivity experiments. Scans were repeated on different areas of the sample and the RMS roughness was analysed for each. These averages were then averaged to give an average RMS roughness for the single layer dPMMA and the Si substrate, to be used in fitting of off specular data. The average RMS roughness for the dPMMA was 0.886nm and the average RMS for the silicon substrate was found to be 0.432nm. Figures 4.24 and 4.25 show trace and retrace of $45\mu m \times 45\mu m$ scans for the dPMMA layer and the silicon substrate respectively, used for finding RMS roughness.

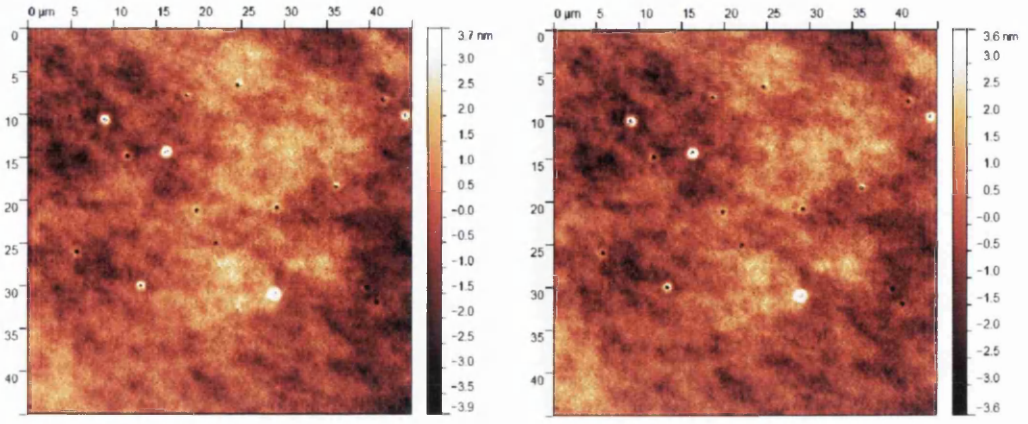

Figure 4.24: $45\mu m \times 45\mu m$ AFM scans of dPMMA polymer film on Si substrate showing trace and retrace

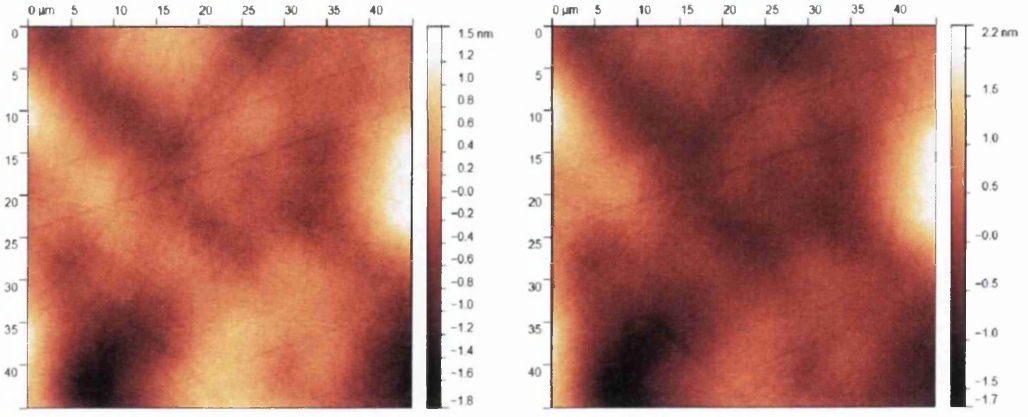

Figure 4.25: $45\mu m \times 45\mu m$ AFM scans of Si substrate showing trace and retrace

Extracting Hurst parameter for dPMMA film

Work by Teichert et al [94] and Stone et al [92] show that the height to height correlation $c(x, y)$ and the auto correlation $g(x, y)$ (see section 2.9.1 for definitions of $c(x, y)$ and $g(x, y)$) can be extracted directly from AFM data, where x, y are in plane distances on the sample. The Hurst parameter can be extracted from $g(x, y)$. Gwyddion was used to extract the $g(x)$ curves from AFM scans, where x is the fast scan direction. The $g(x)$ can be fitted with the self affine fractal model $g(x) = 2\sigma^2(1 - e^{-(\frac{|x|}{\xi})^{2h}}) = 2\sigma^2 - c(x)$. Yang et al [104] show that in the asymptotic limit where $\xi << x$ that

$$g(x) \sim x^{2h}, \ (x << \xi) \tag{4.1}$$

On length scales smaller than the cut off ξ the surface is described as fractal and characterised by the Hurst parameter h. On larger length scales the surface is flat. Plotting the logs x against $g(x)$ gives a straight line for small x as shown in figure 4.26. The gradient is equal to $2h$. AFM scans of area $1 \times 1\mu m$ have been taken in order to extract $g(x, y)$ and the gradient has been fitted linearly giving values for h between ~ 0.5 and ~ 0.65 for dPMMA. The average h value given by fitting is 0.601. Figure 4.26 shows $g(x)$ for eight AFM scans and the fits at low $x << \xi$, including the equations of the lines. From figure 4.26 *a*) it can be seen that the range in which $g(x)$ is reasonable is limited by the size of the scan. In order to get a complete $g(x)$ curve then scans at different sizes should be added together in the regions that they are valid. It was found for scans of these sizes on silicon that due to its low roughness, good $g(x)$ statistics could not be extracted at low $x << \xi$.

Figures 4.27 show trace and retrace of $1\mu m \times 1\mu m$ scans for the dPMMA layer and the silicon substrate respectively, used for extracting the Hurst parameter.

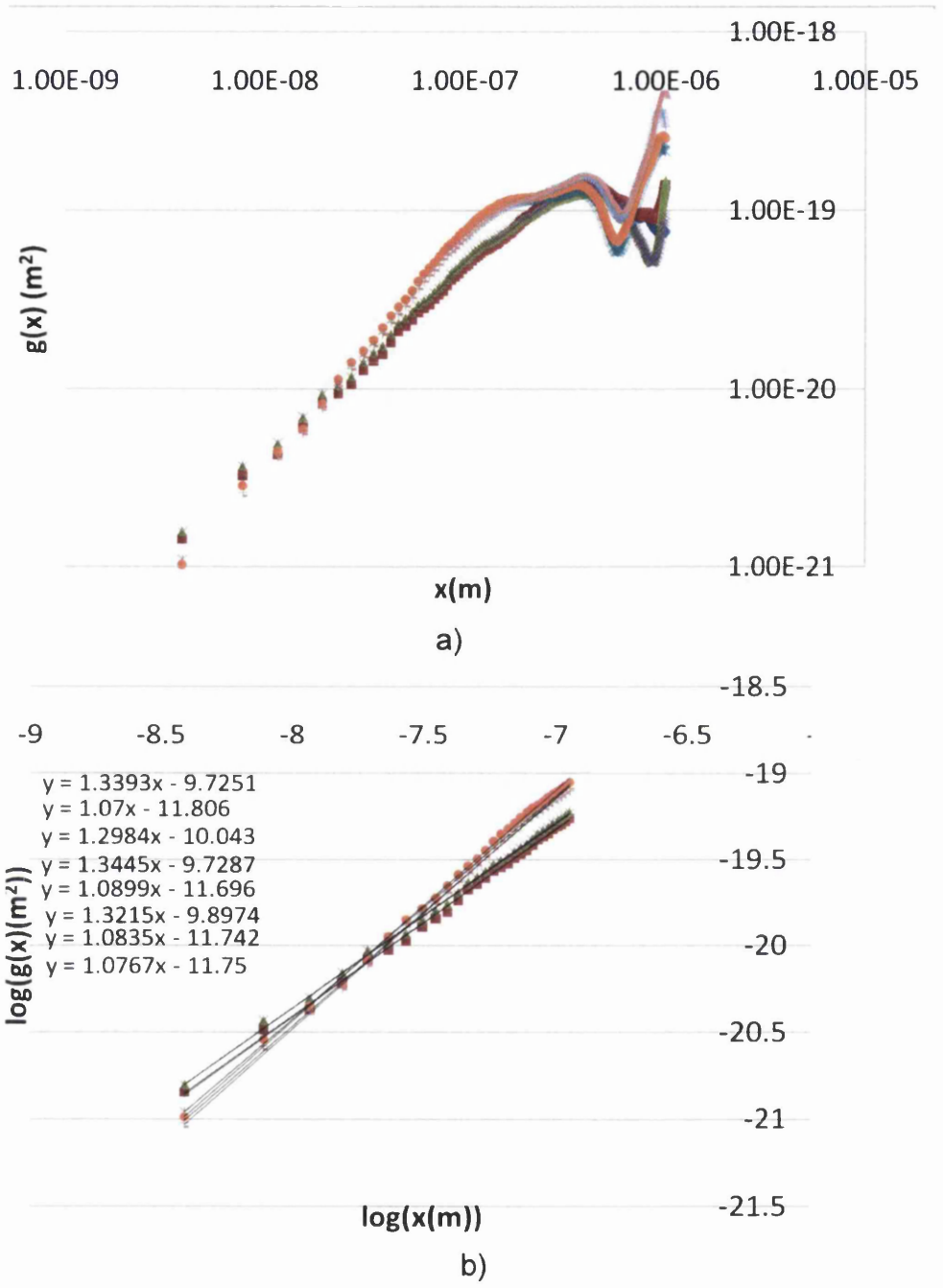

Figure 4.26: a) $g(x, y)$ for dPMMA for eight different $1\mu m$ scans b) Linear fits of $log(g(x, y))$ against $log(x)$ in the region $g(x) \sim x^{2h}$

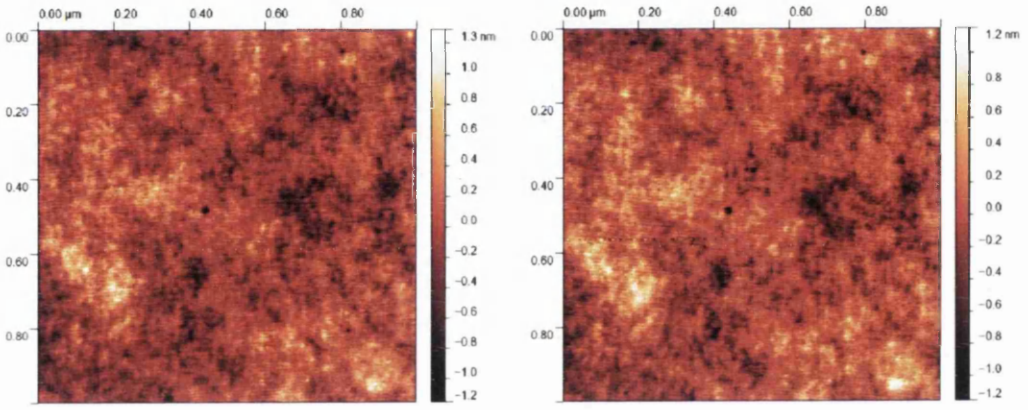

Figure 4.27: $1\mu m \times 1\mu m$ AFM scans of dPMMA polymer film on Si substrate showing trace and retrace

Chapter 5

Numerical Modeling of Off Specular Reflectivity Data

Fitting of the off specular data was the most challenging part of this work. As far as the author is aware no attempts have previously been made to fit off specular neutron reflectivity from a multilayer stack in θ/λ space. This chapter describes the model developed using the distorted wave Born approximation theory described in section 2.9 and how it was implemented to fit the experimental data. The code was written in the Matlab language.

5.1 Modeling in θ/λ space

The DWBA theory is derived in terms of q_x and q_y. Monochromatic reflectivity experiments have an advantage over TOF experiments in that they experimental data can be measured directly in q space with experimental set up allowing reflectivity to be measured at constant q_z for a range of q_x values. TOF experiments record data in terms of θ and λ. Every pixel on a θ/λ map will have a different value of q_z and q_x which are not linearly related to the q_x/q_z values of the surrounding pixels (see section 2.3.1). This causes difficulties when converting data from θ/λ space to q space, including artifacts due to regridding and non linear pixel size. For this reason it was decided to model the experimental data in θ/λ. There are very few examples of this in the literature. Pynn [70] has shown examples of model reflectivity maps in θ/λ space but has not fitted any data, or shown how he has transformed from θ/λ to q_x/q_z and then transformed back θ/λ into space. In this work it was decided to use the q_x and q_z values at the centre of each pixel of the experimental off specular reflectivity in order to calculate the off specular reflectivity for each pixel in the model. This assumes that the reflectivity will not vary greatly with the q range across a pixel.

5.2 Modelling off specular reflectivity from a single interface

5.2.1 Breakdown of terms of the DWBA for a single interface

The simplest system to model is that of a single interface. The off specular scattering for an isotropic surface with resolution relaxed in the y direction is given by equations 2.112 and 2.114 [88]. The expression for the differential scattering cross section can be broken up into four main terms, which are shown in table 5.1

DWBA term break down		
	Name	**Formula**
1	Integral prefactor	$\frac{1}{\lvert q_z^t \rvert^2} e^{-((q_z^t)^2+(q_z^{t*})^2\sigma_{tot}^2/2)}$
2	Scattering strength coefficient	$(L_x L_y)\frac{\lvert k_0^2(1-n)^2 \rvert^2}{16\pi^2}$
3	Fresnel coefficients	$\lvert T(\mathbf{k}_1) \rvert^2 \lvert T(\mathbf{k}_2) \rvert^2$
4	Fourier transform	$\int_x dX(e^{\lvert q_z^t \rvert^2 c(X)} - 1)e^{i(q_x X)}$

Table 5.1: Terms used to calculate off specular scattering from a single interface in the DWBA

The integral prefactor is the result of integrating over the z direction (see Sinha [88] equation 4.20). The scattering strength coefficient is related to the strength of scattering a neutron travelling through a vacuum with wavevector k_o will experience when incident on a surface with refractive index n. It is a function of SLD and λ only. The area of the beam on the sample is $L_{x,y}$ and is constant for TOF experiments, so it can be assumed to be a constant scaling factor for the reflectivity. The Fresnel coefficients will determine features of the off specular reflectivity caused by interference effects. In the single layer system they determine the location of the Yoneda peak. The Fourier transform, in combination with the integral prefactor term, determines the slope of the off specular reflectivity in both q_x and q_z directions. The Fourier transform contains the height to height correlation function to describe the interface of the sample. The self affine fractal height to height correlation function is used in this work, discussed in section 2.8. The Fourier transform term containing the self affine height to height correlation has the following form

$$\mathcal{F} = \int_{-\infty}^{\infty} dX(e^{\lvert q_z^t \rvert^2 \sigma_{lat}^2 e^{-(\lvert X \rvert/\xi)^{2h}}} - 1)e^{i(q_x X)} \tag{5.1}$$

where

$$e^{\lvert q_z^t \rvert^2 \sigma_{lat}^2 e^{-(\lvert X \rvert/\xi)^{2h}}} - 1 \tag{5.2}$$

is the function to be transformed. Because it is an even function the Fourier transform is just over the cosine terms and can be written

$$\mathcal{F} = 2\int_{0}^{\infty} dX(e^{\lvert q_z^t \rvert^2 \sigma_{lat}^2 e^{-(\lvert X \rvert/\xi)^{2h}}} - 1)\cos(q_x X) \tag{5.3}$$

5.2.2 Input parameters

The initial input parameters required by the model are set to mimic a TOF experiment. The terms required from the instrumental geometry are; i) the angle of incidence θ_i, ii) the array of angles of reflection θ_r and iii) the array of wavelengths λ. From the sample the square of the scattering length density N^2B^2 of the scattering medium is required. From these four terms all the wavevectors, angles and transmittance and reflectance coeffcients can be calculated above and below the interface as shown in figure 5.1. The other input parameters that are required by the four terms in table 5.1 are:

- The integral prefector requires the total roughness of the interface σ_{tot}
- The height to height correlation term within the Fourier transform requires i) Hurst parameter h, ii) lateral cut off ξ and iii) lateral roughness σ_{lat}

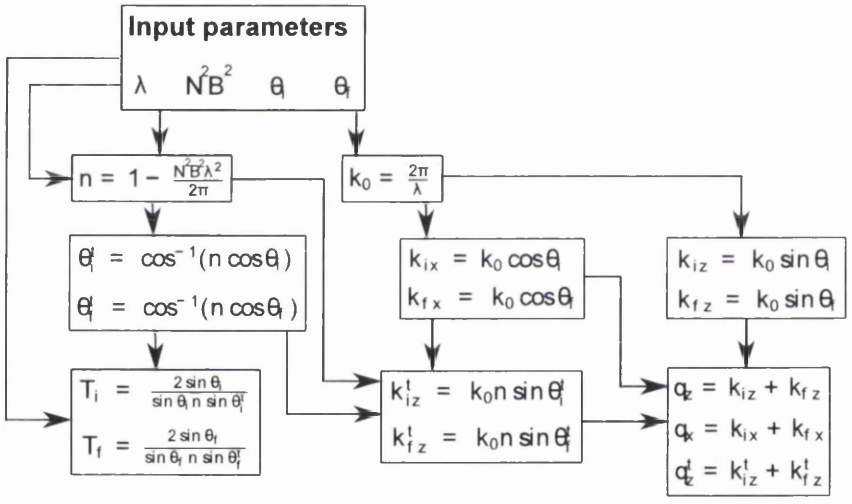

Figure 5.1: Road map of how all terms required for the single layer DWBA are calculated from the input terms

Initially a model was created to find the off specular reflectivity for a single λ value, with the reflectivity a function of θ_i and θ_f. Solving the first three terms in table 5.1 is quite straightforward. Solving the Fourier transform integral analytically for the self affine height to height correlation function is only possible for certain values of h. Solving it numerically is not trivial.

5.2.3 Solving the Fourier transform integral

A Fourier transform over a surface transforms the surface structure into frequency space in terms of a range of Fourier coefficients. Expression 5.1 transforms the surface from a function of x to a function of q_x. In monochromatic mode where q_z can be kept constant for a range of pixels while q_x varies a single Fourier transform can be used to solve for all the pixels at the same q_z value. In a TOF experiment the integral in expression 5.1 has to be solved independently for each pixel, as q_z cannot be kept constant over a range of pixels but changes whenever q_x changes. This makes the TOF model far more computationally intensive than a monochromatic mode model.

Expression 5.2 tends to zero as x tends to ∞. The integral in expression 5.3 is over $x = 0$ to $x \to \infty$. The range of x that the integral is numerically solved for needs to be over a range from $x = 0$ to a value of x where the function tends to 0. The function is extremely sharply peaked as $x \to 0$ as it contains exponential of an exponential of a negative number. The sharpness of the peak makes the function computationally intensive to solve numerically. The sharpness of the peak increases as a function of σ_{lat} and q_z and h. Multiplying by $\cos(q_x X)$ (as in the cos transform) makes the function oscillating. The period of the oscillations increases as q_x decreases. Figures 5.2 and 5.3 show typical forms of equations 5.2 and 5.3

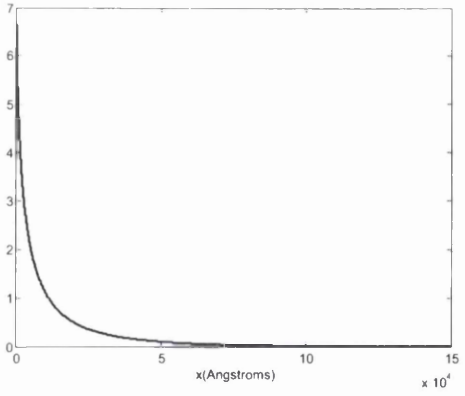

Figure 5.2: Function given by equation 5.2, $q_x = 5.4e-7$, $q_z = 0.0571$, $\sigma = 25$, $\xi = 10000$, h = 0.35

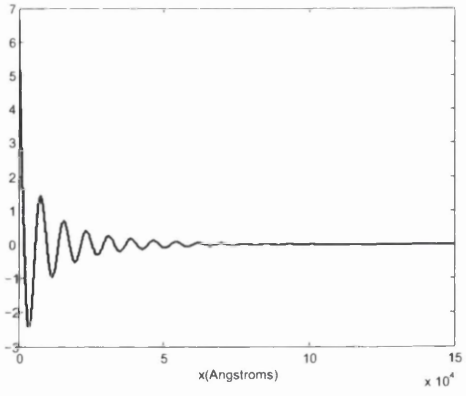

Figure 5.3: Integrand of equation 5.3, $q_x = 5.4e-7$, $q_z = 0.0571$, $\sigma = 25$, $\xi = 10000$, h = 0.35

Several authors have suggested computationally efficient ways to solve the integral expression. Bowen et al [8] solve the integral for a range of parameter values and then store these in look up tables which can be accessed by their fitting routine. Sinha [89] shows that the expression can

be broken down into an infinite series, with the individual terms less computationally intensive to solve. Only the first ten terms of the series need to be solved and fast Fourier transforms (FFTs) could be used to solve them. Pynn [70] suggests that the Fourier transform term could be represented by a Voight function, which is the convolution of a Lorentzian and a Gaussian.

In this work two methods of solving the integral were formulated and the results checked using Sinhas [89] infinite series method. The first method used FFTs to solve the integral and the second method breaks down expression 5.3 into sections then solves each using numerical integration or an approximation to the area under the curve.

Fast Fourier transform method

FFTs are computationally efficient discrete Fourier transforms which must contain 2^n discrete x values where n is an integer. For more information see reference [54]. An FFT can be seen as an approximation to a continuous Fourier transform. The number of points in q_x after performing an FFT on the function is the same as the number of points in x. The resulting function is mirrored around a central point, so effectively there are $N/2 + 1$ points on the q_x axis where N is the number of points on the x axis and the mirrored half is discarded. The FFT algorithm takes the $f(x)$ at every point and transforms it, without regard to their spacing in x. Transforming x axis into a q_x axis is determined by the sampling frequency of $f(x)$, which is given by

$$f_s = \frac{2\pi}{\tau} \tag{5.4}$$

where τ is the distance between points on the x axis. This gives a q_x axis of

$$q_x = f_s \frac{[0 : n : N/2]}{N} \tag{5.5}$$

where square brackets indicate an array of numbers and n is an integer between 1 and $N/2$. The minimum and maximum values of the array are 0 and $N/2$ respectively. From expressions 5.4 and 5.5 it can be seen that for two data sets with the same number of data points the one with the smaller range in x will actually give the larger range in q_x. However for two data sets with the same x range increasing the number of data points increases the q_x range because the sampling frequency is smaller. Figures 5.4 and 5.5 show how changing the number of points

and the range of x affect the FFT output.

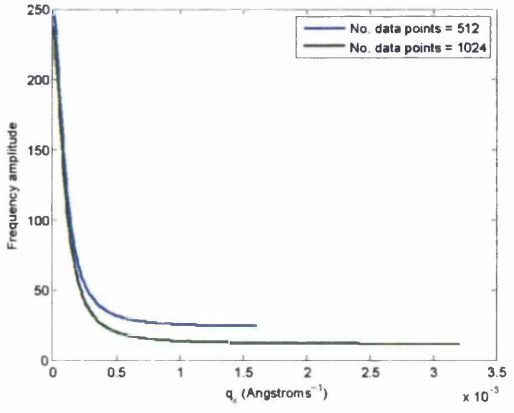

Figure 5.4: Comparison of changing number of data points in the FFT

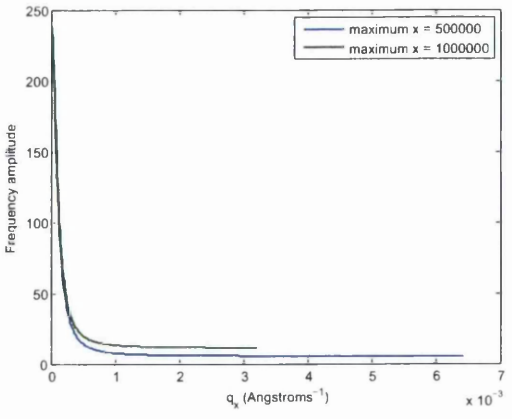

Figure 5.5: Comparison of changing the x range in the FFT

The accuracy of the FFT over a range in q_x is dependent on the sampling frequency. A higher sampling frequency will more closely approximate the continuous function. To increase the sampling frequency either the number of x points can be increased or the x range can be decreased. However increasing the number of points is costly computationally. Decreasing the x range of the function means that the spacing in q_x is larger.

The solve for term 4 (the Fourier transform term) for the TOF model a separate FFT needs to be performed for each pixel. The data point on the transformed function corresponding to a q_x value which is closest to the q_x value of the pixel needs to be selected to approximately find the value of the term 4. The steps taken in this process are listed below

1. Perform FFT over suitable x range with the parameter values of the pixel
2. Find the point on the transformed function that has the value of q_x that is closest to the value of q_x at the centre of the pixel
3. Use the value of the y coordinate of this point as the solution to the Fourier transform term

Figure 5.6 shows how the values of the fourth term are selected for a range of pixels. The continuous lines show the transformed function for a range pixel over a range of q_x, corresponding with step one. The point that is selected from the transformed function is shown by the circles

in figure 5.6, corresponding to steps two and three. Figure 5.7 shows the value of term 4 for a range of pixels plotted against the difference in the angle of reflection to the angle of incidence of the pixel. It can be seen that it peaks around $\theta_f - \theta_i = 0$ as expected.

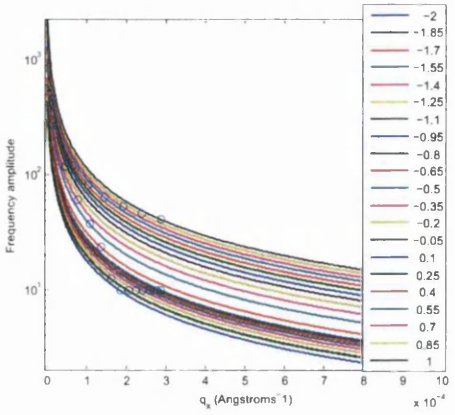

Figure 5.6: Picking points on FFT of function that correspond with pixel q_x. Legend shows the value of $\theta_f - \theta_i$

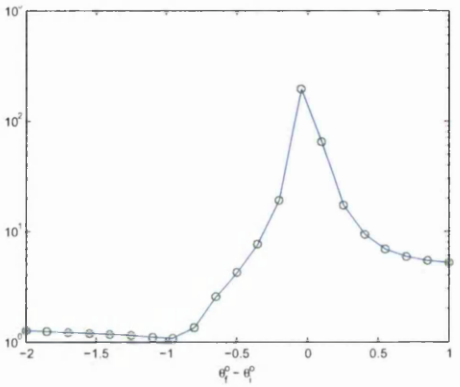

Figure 5.7: Representation of equation term 4 (see table 5.1) for 21 pixels

Choosing the x range and number of points is critical to finding a good approximation to the continuous integral equation. In figures 5.4 and 5.5 the transformed functions plotted in green have higher sampling frequency and are more accurate. At low q_x the transformed functions with lower sampling frequency match the higher sampling frequency functions well, however as q_x increases they diverge. This shows that accuracy of the FFT decreases as it moves away from $q_x = 0$. To pick an accurate value of q_x the maximum of the q_x range should be much higher than the q_x value of the pixel being analysed. The x range should be small to give a larger q_x range. However, because of the picking mechanism, if the spacing of the points is too large then there may be no points in the transformed function that are suitably close to the q_x value of the pixel. Increasing the number of points means a proportionally smaller x range can be picked which will give the same q_x range with closer q_x point spacing. However this is more computationally intensive.

The maximum value of q_x from the experiments conducted in this work is $\sim 0.003\text{Å}^{-1}$ when $\lambda = 2$ Å, $\theta_i = 2.5^o$ and $\theta_f = 0^o$. For this work the x range was chosen to be 800000 and the number of x points 8192, which gives a distance of $1.47e-5$ Å^{-1} between q_x points and a maximum q_x range of ~ 0.03, a factor of ten greater than the minimum possible q_x value of a pixel. These values were used for all pixels. A possible way of optimising the model is to

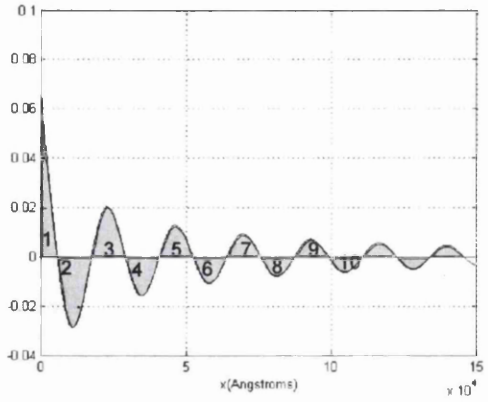

Figure 5.8: Breaking the function into sections in order to integrate each separately

optimise the x range and number of points for each pixel separately.

Numerical integration method

Numerical integration of the function requires integration of the whole integral in expression 5.3, which is a sharply decaying cosine curve (see figure 5.3). The integration would be performed for each pixel separately. Due to the sharpness of the decay rate and the oscillating nature of the function mean it is difficult to integrate the whole expression numerically. A scheme was developed to integrate each segment above and below the x axis independently and then sum all the contributions of each segment. Breaking the function into segments is shown in figure 5.8. Because of the cosine curve the integral will cross the x axis at $n\pi/(2q_x)$ where n is an integer. The largest contributions to the integral will come from the segments closest to $f(x) = 0$ and will decrease as x increases. Each segment is integrated using the intrinsic MatLab function *quadl*, which performs an adaptive Lobatto quadrature routine on the curve between the limits. The adaptive Lobatto quadrature routine optimises the number of sections it divides the curve into dependent on its gradient. It is best suited to smooth integrands [45]. It is well suited to the steep and smooth function of expression 5.3. Each successive segment will contribute less to the integral than the previous one, and due to the decaying nature of the curve the difference between the area of two adjacent segments will decrease with x. The function is converging on 0. This allows a limit to be set on the x range used.

As $x \to \infty$ the gradient of 5.2 (the function inside the Fourier transform integral) tends towards 0. In this case it can be shown that to a close approximation the area under a segment

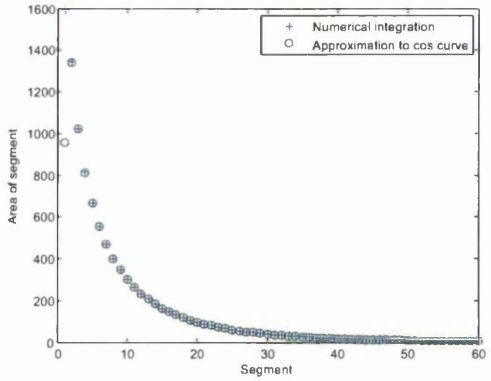

Figure 5.9: Comparison of segment area for numerical integration and approximating the area under the curve to a cos function

of expression 5.1 $\sim w \int \cos(q_x X)$ where w is the value of expression 5.2 at the x value at the centre of the segment. The cosine integral can be easily solved analytically. Figure 5.9 shows the area of each segment using the *quadl* function and approximating the area to the integral of a cosine curve for typical model parameters. It can be seen that as the index of the segment increases the cosine integral becomes a better approximation to the numerically solved integral. In fact after the first few segments they are almost indistinguishable. The model developed therefore calculates the area of each segment in order using numerical integration, and calculating the cosine integral for that segment also. When the area of a segment calculated by the numerical integration is found to be within 0.5% of that calculated by the cosine integral, the model approximates the area of all other sections to their cosine integral, which is far less computationally intensive.

Comparison of different techniques to calculate term 4

The Fourier transform integral was evaluated using the two methods described in the preceding paragraphs and evaluating the first ten elements of the infinite series as described by Sinha [89]. The curves produced should be smooth and continuous. Comparisons show the h parameter and the ξ have the largest effect on the integrals. Figures 5.10 to 5.12 show the integral calculated for different values of h and ξ using the the three different calculation schemes. It can be seen that when h is large (greater than 0.3) the functions behave fairly well and match one another well, although the FFT method shows some small oscillations. However when h is small the integral method and Taylor series method curves become discontinuous, whereas the

FFT method curve remains smooth. When ξ is made larger for a small h the discontinuities of the integral method and Taylor series method become larger, while the FFT method still produces a relatively smooth curve. A possible reason for the breakdown of the integral method at low h is the steepness of the curve being too great for the numerical integration scheme to approximate accurately. For this reason the FFT method was chosen to solve the integral when fitting the experimental data, as it works well over the all h ranges.

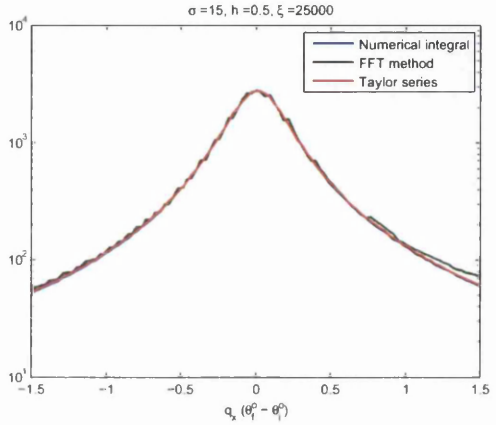

Figure 5.10: Different methods of calculating term 4 in table 5.1 with $h = 0.5$ and $\xi = 25000$

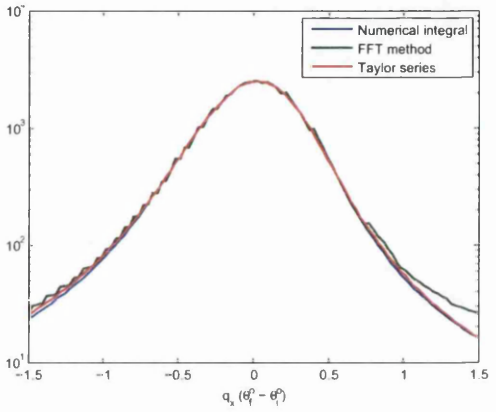

Figure 5.11: Different methods of calculating term 4 in table 5.1 with $h = 0.8$ and $\xi = 25000$

Complete θ/λ map

Extending the calculation for a single λ cut to a complete θ/λ map requires simply calculating the reflectivity over the θ range at each value of λ and arranging the cuts in an array.

5.3 Modelling off specular reflectivity multiple interfaces

The DWBA model has been extended to multilayer systems. In this section when referring to multilayer stacks of films on a substrate it is assumed that air or vacuum is the first medium and will be referred to as medium or layer 1. The interface between air and the top surface will be referred to as interface 1. The interface between the bottom of the last film and the substrate is interface N and the substrate is layer $N + 1$ where N is the number of interfaces in the multilayer. With a single layer model interference effects between the layers are not seen

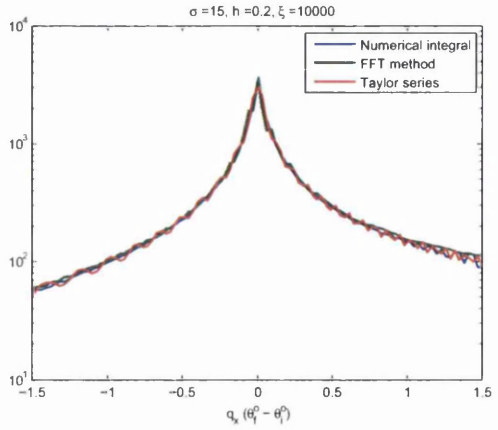

Figure 5.12: Different methods of calculating term 4 in table 5.1 with $h = 0.2$ and $\xi = 10000$

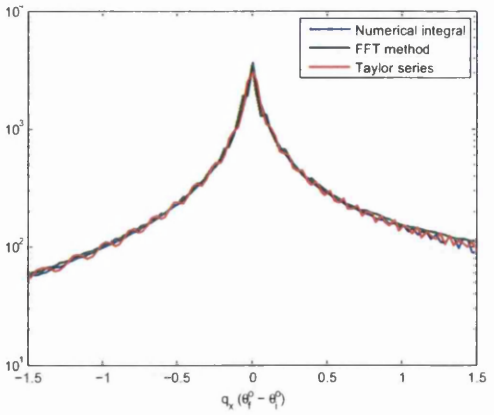

Figure 5.13: Different methods of calculating term 4 in table 5.1 with $h = 0.2$ and $\xi = 10000$

and there are no fringes in the off specular reflectivity at $q_x = 0$, because the T coefficients from a single interface alone do not contain this information. From equation 2.121 in section 2.9 it can be seen that there are now six terms for each interface in the multilayer. The six terms are caused by the different q_z^j vectors (see equation 2.119). Each of these terms can be broken into four parts as in the single interface expression shown in table 5.1. Like the single interface calculation the DWBA expression for reflectivity from each interface in the multilayer can be broken down into four terms. The four terms for the scattering from each interface are given in table 5.2

The model developed allows the off specular reflectivity of a multilayer stack of any number of layers to be calculated. The reflectivity data is stored in a three dimensional array with dimensions $M \times O \times N$, where M is the number of angles of reflection, O is the number of wavelengths and N is the number of interfaces in the multilayer. The reflectivity is calculated pixel by pixel for each interface. To find the total reflectivity of the multilayer the array is summed over N. The parameters required to calculate the reflectivity are either defined by the user or calculated before the reflectivity calculation. They are stored in arrays whose indexes correspond with the indexes of the reflectivity array. These parameters have to be calculated for each layer. Some parameters will be constant for all pixels in a direction, for instance the angle of incidence θ_i is constant for every pixel or array element in a layer, but changes between layers. The R and T coefficients require knowledge of θ_i in the substrate which is after the final interface so θ_i requires a $1 \times 1 \times (N+1)$ size array. Table 5.3 shows all the parameters required,

DWBA term break down		
	Name	**Formula**
1	Integral prefactor	$\frac{1}{q^j_{mz}(q^j_{nz})^*} e^{(-\sigma_j^2((q^j_{mz})^2+(q^j_{nz})^{*2})/2)}$
2	Scattering strength coefficient	$L_x L_y \frac{k_0^4}{16\pi^2} \lvert n_j^2 - n_{j+1}^2 \rvert^2$
3	Fresnel coefficient terms	$\lvert (T_1^j T_2^j + R_1^j R_2^j) \rvert^2$ $\lvert (R_1^j T_2^j + T_1^j R_2^j) \rvert^2$ $2Re\ (T_1^j T_2^j (R_1^j T_2^j)^* + T_1^j R_2^j (R_1^j R_2^j)^*)$ $2Re(T_1^j T_2^j (T_1^j R_2^j)^* + R_1^j T_2^j (R_1^j R_2^j)^*)$ $2Re(T_1^j T_2^j (R_1^j R_2^j)^*)$ $2Re(T_1^j R_2^j (T_1^j R_2^j)^*)$
4	Fourier transform	$\int\int_{S_0} dX e^{(-i(q_x X))} e^{(q^j_{mz}(q^j_{nz})^* c_j(X))} - 1$

Table 5.2: Terms used to calculate off specular scattering from multiple interfaces in the DWBA where $m = 0, 1, 2, 3$ and $n = 0, 1, 2, 3$ and are the indices of the q_z^j terms and 0 refers to q_z^{j+}, 1 to $-q_z^{j+}$, 2 to q_z^{j-} and 3 to $-q_z^{j-}$ (see equation 2.119).

whether they are defined by the user or how they are calculated and the size of the array they are stored in. A pseudo code for calculating the reflectivity from a multilayer is shown in figure 5.14

5.3.1 T and R coefficients

The Fresnel coefficient terms become considerably more complicated and now both T and R coefficients for each interface are required. The two techniques to calculate T and R terms in a multilayer are the transfer matrix and the Parratt formalism which are both discussed in section 2.7. The transfer matrix calculates the T and R terms starting from the top interface, whereas the Parratt formalism calculates from the bottom interface. This is discussed in detail in section 2.7.6. This means that in a multilayer the R coefficient should be calculated using the Parratt formalism or the transfer matrix with the order of the layers in the multilayer reversed. The T coefficient should be calculated using the transfer matrix or the Parratt formalism with the order of the layers in the multilayer reversed. The beam transmitted through the multilayer will see the interfaces in ascending order from 1 to N. However a beam reflected from an interface will see the interfaces in the descending order from $n : 1$ where n is the index of the interface

Parameters for multilayer DWBA			
Parameter	**Equation**	**Description**	**Array size**
λ	User defined	Incident wavelength	$1 \times O \times 1$
N^2B^2	User defined	Scattering length density	$1 \times 1 \times N$
σ_{tot}	User defined	total roughness	$1 \times 1 \times N$
σ_{lat}	User defined	lateral roughness	$1 \times 1 \times N$
h	User defined	Hurst parameter	$1 \times 1 \times N$
ξ	User defined	Cut off length	$1 \times 1 \times N$
n	$n^j = 1 - ((N^2B^2)^j \lambda^2/2\pi)$	Refractive index	$1 \times O \times N$
θ_i	$\theta_i^j = \cos^{-1}(\cos\theta_i^{j-1}/n^{j-1})$	Angle on incidence	$1 \times 1 \times (N+1)$
θ_f	$\theta_f^j = \cos^{-1}(\cos\theta_f^{j-1}/n^{j-1})$	Angle on incidence	$1 \times 1 \times (N+1)$
k_{iz}	$k_{iz}^j = \frac{2\pi}{\lambda}\sin\theta_i^j$	Incident wave vector z direction	$1 \times O \times (N+1)$
k_{fz}	$k_{fz}^j = \frac{2\pi}{\lambda}\sin\theta_f^j$	Reflected wave vector z direction	$M \times O \times (N+1)$
k_{ix}	$k_{ix}^j = \frac{2\pi}{\lambda}\cos\theta_i^j$	Incident wave vector x direction	$1 \times O \times (N+1)$
k_{fx}	$k_{fx}^j = \frac{2\pi}{\lambda}\sin\theta_f^j$	Reflected wave vector x direction	$M \times O \times (N+1)$
q_z^+	$q_z^{+j} = k_{iz} + k_{fz}$	q_z type vector	$1 \times O \times (N+1)$
q_z^-	$q_z^{-j} = k_{iz} - k_{fz}$	q_z type vector	$M \times O \times (N+1)$
q_x	$q_x^j = k_{ix} - k_{fx}$	q_x vector	$1 \times O \times (N+1)$
R_i	see equation 2.68	Reflectivity coefficient of incident beam	$1 \times O \times N$
R_f	see equation 2.68	Reflectivity coefficient of reflected beam	$M \times O \times N$
T_i	see equation 2.64	Transmission coefficient of incident beam	$1 \times O \times N$
T_f	see equation 2.64	Transmission coefficient of reflected beam	$M \times O \times N$

Table 5.3: Parameters used in a multilayer DWBA reflectivity calculation where M is the number of angles of reflection, O is the number of wavelengths and N is the number of interfaces

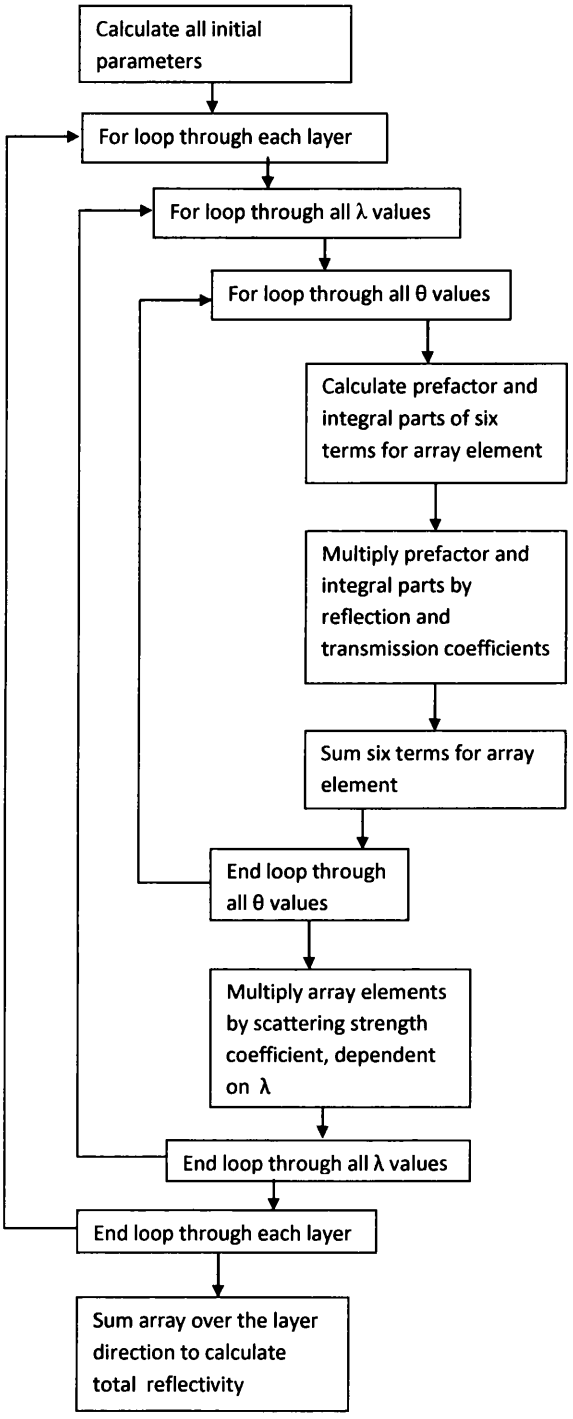

Figure 5.14: Pseudo code to calculate reflectivity from a thin film multi layer

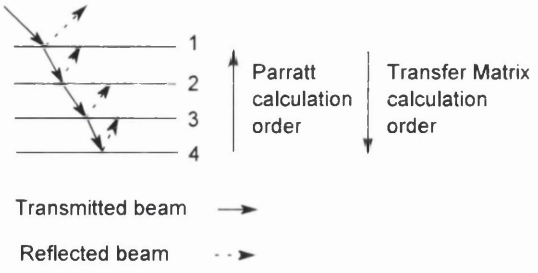

Figure 5.15: Calculation order of transfer matrix and Parratt formalism

it is reflected from. This is shown in figure 5.15.

The transmitted beam will have no 'knowledge' of the interfaces below the ones it has been transmitted through, whereas the reflected beam will only have 'knowledge' of the interfaces it has been transmitted through after reflection. Calculating the T coefficients with the Parratt formalism for interface n will give them knowledge of interface structure below interface n, which a physical neutron would not have. This will result in interference fringes in the scattering which would not be present in the physical situation. A similar argument is true for calculating the R coefficient with the transfer matrix. When measuring T and R in air above the multilayer both calculation schemes will give the same results, however measuring them inside the multilayer they will give different results at each interface as shown in section 2.7.6.

The T and R coefficients are required for each interface to calculate the total reflectivity from the multilayer. The effective T and R coefficients in each layer for the two calculation schemes are only different due to the order the individual T and R coefficients in each layer are evaluated when calculating the total reflectivity of the multilayer. Figure 5.17 shows the effect of using the transfer matrix to calculate both T and R for an F8 /dPMMA bilayer with film thicknesses 1000Å and 500Å respectively. The interfaces between the F8/ dPMMA and dPMMA/ Si have dominant scattering.

It can be seen from figures 5.16 and 5.17 that using the transfer matrix to calculate R gives the wrong result. This is because when calculating R for the F8/dPMMA interface the scattering from the air/F8 interface has already been calculated and is added to the dPMMA result, whereas in the physical system the reflected neutrons will not have experienced the air/F8 interface. However in the physical system reflected neutrons will have experienced the dPMMA/Si interface, which in the transfer matrix scheme it will not have.

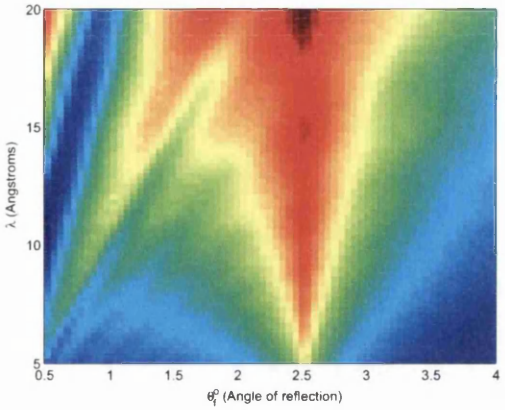

Figure 5.16: Model of F8/ dPMMA bilayer on Si with film thicknesses 1000Å and 500Å respectively with T calculated using transfer matrix and R calculated using Parratt formalism

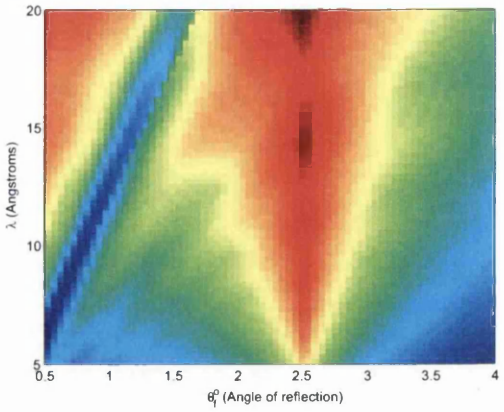

Figure 5.17: Model of F8/dPMMA bilayer on Si with film thicknesses 1000Å and 500Å respectively with both R and T calculated using the transfer matrix. The Yoneda scattering is in the wrong location for a multilayer with dominant scattering F8/dPMMA interface

5.4 Modelling off specular reflectivity with correlations between interfaces

The experimental data shows lines of heightened intensity along constant q_z contours on the θ/λ maps. This shows there are correlations between the morphology of the polymer film and the underlying substrate. The model has to be extended to include these terms. There is potentially correlation between every interface with every other interface in the multilayer. The interface correlation between any two interfaces a and b are found by multiplying the matrix element of a by the complex conjugate of the matrix element of b. This results in sixteen terms for each interface pair (see equation 2.124). Each of these terms can again be broken down into four parts. In the uncorrelated model interfering neutron waves are reflected from the same interface and so are in phase. In the correlated model a phase factor needs to be included to take into account the interference effects of waves reflecting from different interfaces. It is the phase factor that causes the lines of intensity along constant q_z (see section 2.10.1) as they are a function of the film thickness. The cross correlation terms can be calculated alongside the six single layer terms for each interface and them added to the single layer terms to give the total reflectivity. The pseudo code for the model developed including the cross correlation terms is

shown in figure 5.18

Due to the phase factor the cross correlation terms oscillate between positive and negative maxima and minima. If the magnitude of minima is greater than the reflectivity given by the single layers then the reflectivity becomes negative at these points, which is not physical. The effect of these oscillations is to increase the height difference in the fringes at $q_x = 0$ and create the fringes in the off specular data corresponding to the lines of heightened intensity along constant q_z. Figures 5.19 and 5.20 show the typical form of the correlation function terms for F8/dPMMA bilayer with film thicknesses 1000Å and 500Å respectively which is the same system described in the previous section without cross correlation terms.

The effect of the cross correlation terms on the model reflectivity can be seen in figure 2.38.

5.4.1 Interface to interface correlation function

The Fourier transform integral function between the different layers requires a interface to interface correlation function rather than a height to height correlation function as described in section 2.8.2. The interface to interface correlation used in this work is [79]

$$c_{jk}(\mathbf{R}) = \frac{1}{2}\left[\frac{\sigma_j}{\sigma_k}c_j(\mathbf{R}) + \frac{\sigma_k}{\sigma_j}c_k(\mathbf{R})\right] e^{-|z_j - z_k|/\xi_{\perp j,k}} \tag{2.81}$$

It contains the σ_{lat}, h and ξ terms of both layers and only one additional term $\xi_{\perp j,k}$ which is a correlation length scale term perpendicular to the interfaces. The Fourier transform integral for each pixel for this interface to interface correlation function is calculated in the same way as the height to height correlation function outlined in section 5.2.3 for the single layer. If $\xi_{\perp j,k} = 0$ there is no correlation between layers j and k and there will be no contribution to the reflectivity.

5.5 Resolution

An advantage of modeling in θ/λ space is that the resolution in θ and λ directions can be treated separately. Resolution of the experiment was taken into account by convolving the model reflectivity with a 2D Gaussian in the θ and λ directions independently. The FWHM of the Gaussian functions was set equal to the instrumental resolutions $d\theta/\theta$ and $d\lambda/\lambda$ (see section

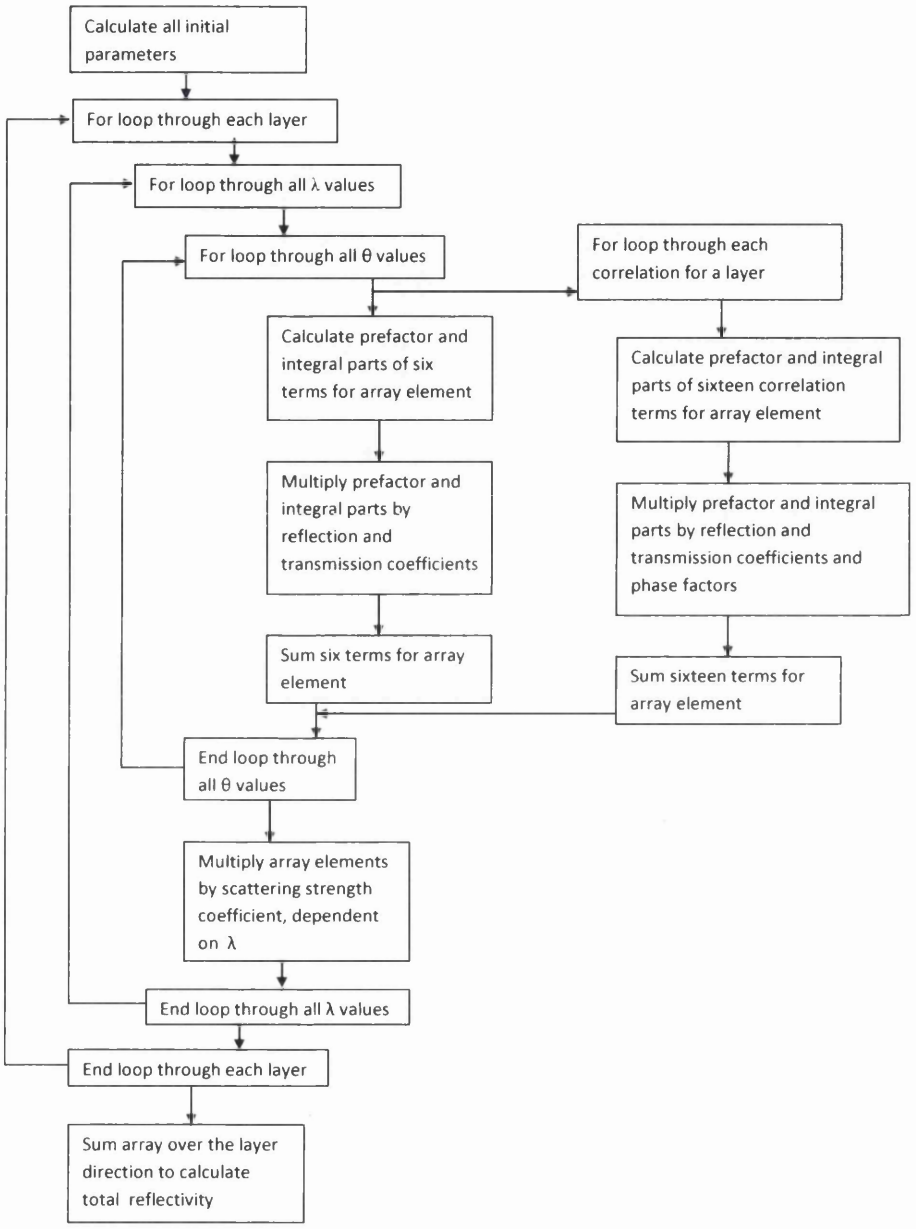

Figure 5.18: Psuedo code to calculate reflectivity from a thin film multi layer

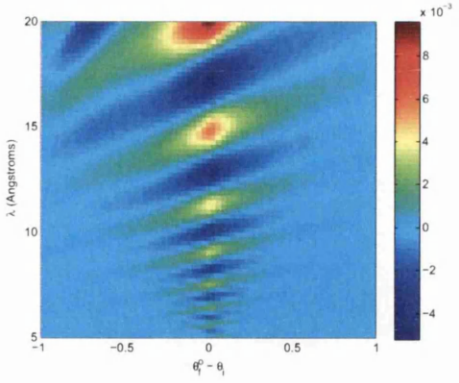

Figure 5.19: Cross correlation terms of F8/dPMMA bilayer on Si with film thicknesses 1000Å and 500Å showing maxima and minima (note: these are not on a log scale due to the negative terms)

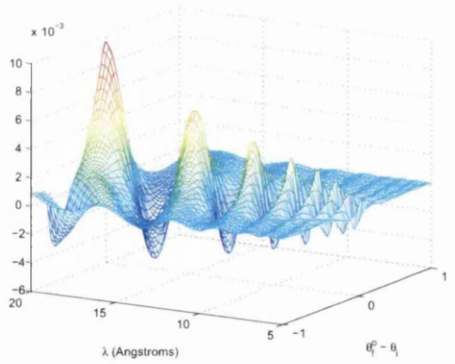

Figure 5.20: Cross correlation terms of F8/dPMMA bilayer on Si with film thicknesses 1000Å and 500Å showing maxima and minima (note: these are not on a log scale due to the negative terms)

2.4.6). In the model each time the reflectivity is calculated, the resolution function is applied to it in both directions.

Reflectivity beyond the limit of the range that is detected by the experimental geometry will have some effect on the experimental data due to the resolution. Therefore reflectivity for a buffer of pixels is calculated around the edges of the θ/λ range of the experimental data. This takes into account reflectivity in the θ/λ range adjacent to the range measured by the experiment. In this work the buffer is set to be three pixels wide.

5.6 Fitting algorithm

5.6.1 Differential evolution

Differential evolution (DE) was chosen as the type of fitting algorithm. DE is a population based stochastic minimising scheme aiming to minimise a cost function [67]. The population are vectors and the elements of the vectors are the fitting parameters and each population member is labelled with an index. For each generation after the first generation the algorithm iterates through every population vector and changes their fitting parameters to create a mutant

vector based on the original population vector. If the mutant vector is a better solution (has a lower value for the cost function) then the algorithm replaces the original population vector with the mutant and the original population vector is removed. If the original population vector is a better solution than the mutant the original population vector is retained. Once all the population vectors have had mutants generated a new generation iteration begins and the algorithm repeats the process. Generation of a mutant vector relies on 'breeding' with other population members. The 'breeding' steps are shown below

1. Choose population vector to create mutant from (by iteration)
2. Randomly select two other population vectors
3. Sum the difference between the elements of the randomly chosen population vectors and multiply by a weighting factor between 0 and 1
4. Add the weighted sum of the difference to the original vector to create a temporary mutant vector
5. Randomly replace some elements of the temporary mutant vector with elements from the original population vector to create the mutant vector
6. If the mutant vector is a better solution than the original vector replace the original vector with the mutant vector

As the number of generation iterations increase the difference between population vector elements decreases and the entire population move towards the optimum solution. The DE scheme is therefore self organising with no probability distributions required [30]. A schematic of the basic principles of the DE algorithm is shown in figure 5.21.

The differential evolution scheme in this work was developed to fit the 2D colour map of the experimental data. Any of the input parameters listed in the first six rows of table 5.3 and the cross correlation parameters $\xi_{\perp j,k}$ for each layer can be chosen as fitting parameters. Limits are placed on the possible values of the fitting parameters. If a fit parameter in a mutant vector goes outside these limits then it is returned to the value of the original vector. Initially only the off specular reflectivity was fitted so a region around $q_x = 0$ containing the specular reflectivity was excluded from the fitting area. Also a region above the critical angle θ_c of the polymer with the highest SLD θ_c was excluded from the fit. In this region the incoherent scattering dominates the coherent scattering. The cost function used is a χ^2 function which is given by

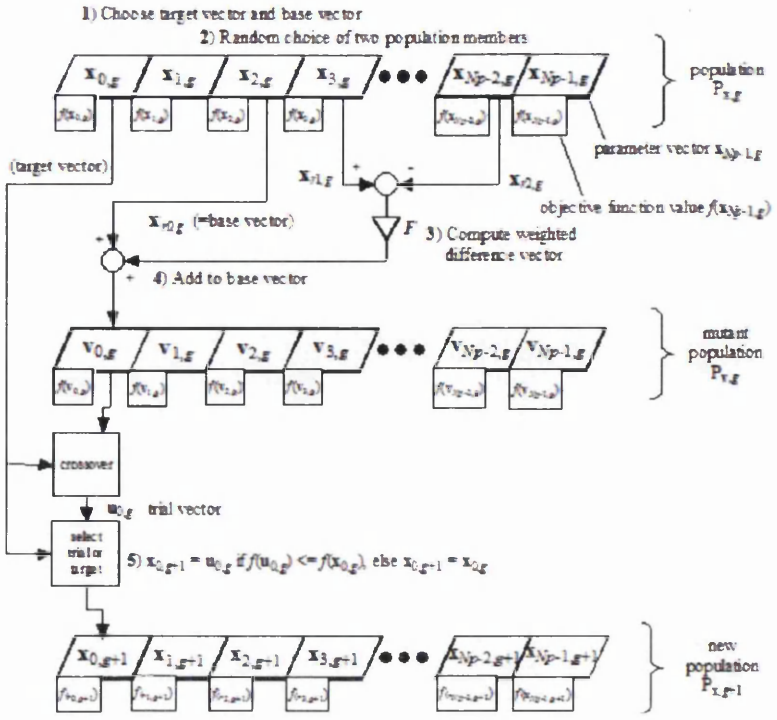

Figure 5.21: Basic differential evolution fitting algorithm (taken from reference [30])

$$\chi^2 = \frac{1}{N_i N_j} \sum_{i=1}^{N_i} \sum_{j=1}^{N_j} \frac{(R_{exp(i,j)} - R_{mod(i,j)})^2}{e_{i,j}^2} \tag{5.6}$$

where $R_{exp(i,j)}$ is the experimental reflectivity of a pixel, $R_{mod(i,j)}$ is the model reflectivity of a pixel, $e_{i,j}$ is the error, N_i is the number of θ_f values and N_j is the number of λ values. Also included in the DE scheme was a function which eliminates the population member with the highest χ^2 value after every generation iteration until a specified minimum population size has been reached. Details of fitting and results are discussed in chapter 6.

5.7 Combining specular and off specular reflectivity calculations

Since the instruments used measure specular and off specular reflectivity simultaneously, to fit the experimental data including the region around $q_x = 0$ the specular reflectivity needs to be added into the model. It is shown in section 2.9 that the reflectivity at $q_x = 0$ is not only

specular reflectivity but there will be an off specular component to it. The specular reflectivity extracted by taking a cut of the data around $q_x = 0$ is not the true specular reflectivity due to this off specular component. The off specular component will make the specular reflectivity seem to fall off at a slower rate with increasing q_z than the true specular reflectivity, as the specular reflectivity falls off as a function of q_z^{-4} whereas the off specular reflectivity falls off as a function of q_z^{-2}. Schlomka et al [79] show that fits of specular reflectivity predict interfacial RMS roughnesses which are lower than the actual RMS roughnesses. This is because the rate of fall off of the specular is a function of the total RMS roughness σ_{tot} (see section 2.7.7). The true specular reflectivity should have the off specular reflectivity subtracted from it.

Schlomka et al [79] develop a model for x-ray reflectivity in q space which fits the specular and off specular reflectivity simultaneously using the DWBA to fit the off specular part and the Parratt formalism (see section 2.7.5) to fit the specular part. At $q_x = 0$ the model reflectivity is the sum of the DWBA and the Parratt fits. The reflectivity is fitted using the same total roughness (σ_{tot}), thickness and SLD parameters for both parts of the model. In this way the two components at $qx = 0$ can be separated. This is the basis of the model developed to fit the specular and off specular data simultaneously in this work.

The specular reflectivity plots extracted from the experimental data in section 6.2 are summed over a range of pixels in the θ direction, due to broadening of the specular reflectivity because of instrumental angular resolution. In the model developed specular reflectivity is added to pixels where $q_x = 0$. This specular reflectivity is broadened using a Gaussian convolution with the FWHM of the Gaussian found by fitting a Gaussian to cuts in λ of the direct beam measurement (see section 4.5.1 for details of the direct beam measurement). There is no scattering in the direct beam measurement, so the broadening of the beam is due purely to instrumental resolution. The averaged FWHM over several cuts of the direct beam for D17 data was found to be 0.064^o.

Specular reflectivity occurs when $\theta_f = \theta_i$. There may be error in the instrument positioning motors, so the location of the specular reflectivity data on the detector will give a truer value of θ_i than the motors. Since each pixel subtends a small range of θ_f the exact angle of incidence may lie anywhere within the range of the pixel onto which the beam is reflected specularly. To more precisely define the angle of incidence for each data set a small range of angles centered on the pixel containing the specular reflectivity are fitted with a Gaussian, with the centre and the width of the Gaussian as fitting parameters. Care is taken to keep the θ_f range over which the Gaussian is fitted small to minimise the off specular contribution. This is important when

broadening the specular as if the value of θ_f at the centre of the pixel corresponding to $q_x = 0$ is taken as the angle of incidence then the model reflectivity will be broadened symmetrically around that pixel. If the beam is not reflected exactly at the θ_f value of the centre of the pixel the broadening in the experiment will be asymmetric. This will impact on the quality of the fits. The Gaussian broadening of the model specular reflectivity is therefore centred on the value of θ_i found from fitting the Gaussian.

The specular reflectivity is calculated and broadened on a grid the same size as the experimental data. Any rebinning that is carried out on the experimental data is then carried out in the same manner on the model θ/λ map containing the broadened peak. Since the off specular data is rebinned then the broadened map containing the specular data must be rebinned also.

The steps to calculating the the specular and off specular reflectivity simultaneously in order to fit the model are outlined below:

1. Fit experimental specular peak to find the true θ_i
2. Calculate the model specular reflectivity over the λ range of the experiment using Parratt formalisation and put on empty θ/λ map. The θ pixels in which it is located should be the same as the maximum of the specular peak of the experiment
3. Broaden the specular peak around $\theta_f = \theta_i$ using Gaussian convolution with FWHM $d\theta/\theta$ and centred at the true θ_i
4. Rebin the θ/λ map
5. Calculate off specular reflectivity using DWBA formalisation on θ/λ map of the same size
6. Sum the θ/λ map containing the model specular and θ/λ map containing the model off specular

Figures 5.22, 5.23, 5.24 and 5.25 show plots of steps 2, 3, 5 and 6 respectively.

The DE fitting scheme was still used in the same way with the χ^2 minimisation function in order to fit all the data.

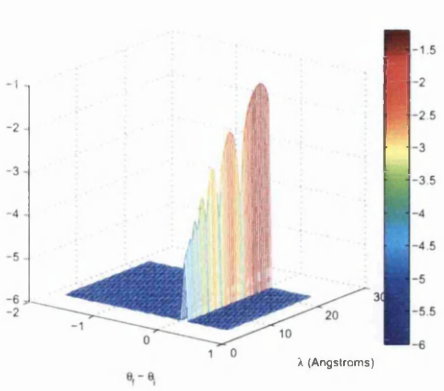

Figure 5.22: Model specular reflectivity plotted at $q_x = 0$ on θ/λ map

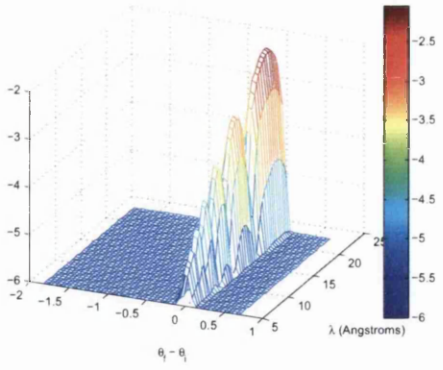

Figure 5.23: Model specular reflectivity plotted at $q_x = 0$ on θ/λ map and broadened by Gaussian function

5.7.1 Scaling between specular and off specular reflectivities

The intensity of the specularly scattered neutrons I_{spec} at the detector is dependent on the specular reflectivity and the intensity of the incident beam I_0. The intensity of the off specularly scattered neutrons $I_{offspec}$ is dependent on the off specular differential scattering cross section $\left(\frac{d\sigma}{d\Omega}\right)_{offspec}$, I_0 and the geometry of the instrument [88]. There is a constant scaling factor which is dependent on the experimental geometry which is not a fitting parameter which scales the specular and off specular reflectivities [79]. However in practice this scaling parameter was not known and it was found by fitting the single layer sample, which has the most parameters predefined and is the simplest to model. Once the scaling parameter is found it should be fixed for all experiments carried out under the same conditions on the same instrument.

5.8 Conclusions

In this chapter a modeling scheme has been proposed and implemented in order to model off specular reflectivity from a multilayer stack using the first order DWBA in θ/λ space. The scheme outlined can potentially be used to model a multilayer with any number of layers. One of the biggest challenges of the model is solving the integral expression in equation 2.114. This is computationally intensive as the integral needs to be solved numerically for every pixel on the map and the function in the integral is sharply peaked. The resolution is taken into account by separating out the θ and λ components and smoothing using a Gaussian convolution.

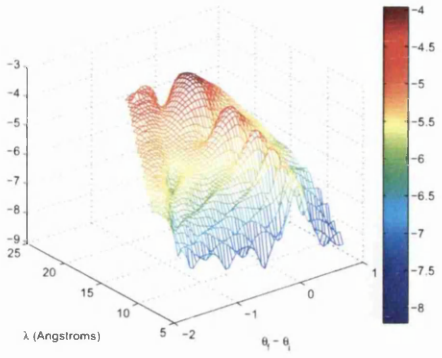

Figure 5.24: Model off specular reflectivity plotted θ/λ map

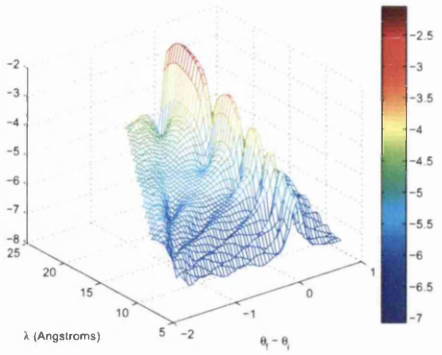

Figure 5.25: Model specular and off specular reflectivity summed and plotted θ/λ map]

Specular reflectivity is added to the off specular by adding a specular fringe along $\theta_i - \theta_r = 0$, which is broadened by the resolution function. Fitting of the model to experimental data uses an evolutionary computer approach, which has been shown to converge quickly and exhibit robustness. This model is a first attempt to fit off specular neutron reflectivity in θ / λ space.

Chapter 6

Study of F8/dPMMA Interfaces using Specular and off Specular Neutron Scattering

6.1 Introduction

In this chapter the specular and off specular reflectivity datasets from F8/dPMMA bilayer samples with different thickness dPMMA films annealed for three hours at 180^oC are fitted. This allows information about the structure of the buried F8/dPMMA interface of each of the samples to be obtained. To check the samples are at thermodynamic equilibrium specular reflectivities from duplicate samples annealed for different lengths of time at 180^oC are also fitted. At 180^oC the F8 polymer is in a nematic liquid crystalline state [33], which shows both crystal and liquid properties [17]. Reflectivity datasets from two PS/PMMA bilayer samples annealed at 180^oC for three hours and twenty four hours are also fitted. This is to compare the nematic liquid crystalline/amorphous polymer interfaces with an amorphous/amorphous polymer interface.

The main aim is to measure the total interfacial roughness σ_{tot} of the F8/dPMMA interface for bilayer samples with different thickness dPMMA films and separate out the the two roughness contributions. These contributions are an intrinsic roughness σ_{int} which is caused by the polymer chains mixing at the interface at a molecular level (see section 3.1.3) and a lateral contribution σ_{lat} caused by thermally excited capillary wave fluctuations (see chapter 3.2). The theory of capillary waves at polymer/polymer interfaces outlined by Sferrazza et al [84] predicts the capillary wave contribution σ_{lat} to the total roughness (σ_{tot}) will increase with film thickness (see section 3.2.3), while the intrinsic contribution σ_{int} will not depend on the thickness of the polymer films. The capillary wave spectrum will be dependent on the thinner of the films in the bilayer. The roughness contributions can be calculated by fitting the specular and off specular reflectivity data from the samples, allowing the theory that the interface is broadened by a capillary wave spectrum to be tested.

Fitting of specular scattering data is well established. However it can only give information about the structure of the bilayer normal to the interface and only the total roughness σ_{tot} can be obtained from fits. Fitting of off specular data is not well established and fitting techniques have been developed in this work (see chapter 5). Off specular scattering is sensitive to the lateral structure of interfaces as well as the in plane structure, so both σ_{tot} and σ_{lat} can be obtained from fitting off specular data. The intrinsic roughness σ_{int} can be calculated as $\sigma_{tot}^2 = \sigma_{lat}^2 + \sigma_{int}^2$ allowing the two contributions to be separated.

Specular reflectivity only occurs at $q_x = 0$. There is also off specular contribution to the reflectivity at $q_x = 0$ as shown in section 2.9.3. Usually it is assumed that the off specular

reflectivity at $q_x = 0$ is small when compared with the specular reflectivity and no allowances are made for it. However the fall of the specular reflectivity is a function of q_z^{-4} while the fall off of off specular reflectivity is a function of q_z^{-2}. The off specular reflectivity becomes an increasingly significant fraction of the specular reflectivity with increasing q_z. If the off specular reflectivity from a sample is significant, to fit the true specular reflectivity the off specular component should be subtracted. Otherwise it is actually the sum of the specular and off specular reflectivities that is fitted, which may result in false value for σ_{tot}. Separating the specular and off specular at $q_x = 0$ is not simple. In this chapter efforts have been made to subtract the off specular component at $q_x = 0$ from the specular data and refitting the specular data. This off specular component subtracted is calculated using the numerical model. Ideally both specular and off specular components should be fitted together. A method for doing this is outlined in section 5.7 and is implemented for the F8/dPMMA system.

Fitting specular reflectivity data

Section 6.2 describes fitting of the specular reflectivity data and is set out as follows:

1. Specular model: The model and routine used to fit the data is described
2. Modeling with an oxide layer: description of the native oxide layer on the silicon substrate and how it is modeled
3. Fitting single layer: Fits of single films of F8 and dPMMA on Si substrate used to fix the parameters at the air/F8 and dPMMA/Si interfaces in the bilayer fit
4. F8/dPMMA bilayers annealed for different times: Fitting of reflectivity from F8/dPMMA bilayers annealed for different time durations to check the system has reached thermodynamic equilibrium
5. F8/dPMMA 3 hour annealed series of different thickness: Fitting of reflectivity for the bilayers with different thickness dPMMA and the effect the film thickness has on the roughness
6. Modeling with no oxide layer: A repeat of the fits made in the previous subsection with the substrate assumed to be pure silicon, to allow easy comparison with off specular fits
7. PS/dPMMA samples: Fits of the PS/PMMA system for comparison with F8/dPMMA systems

Fitting off specular reflectivity data

For each interface in an experimental sample there are up to five fitting parameters that are required to characterise the interface and fit the off specular reflectivity using the DWBA. There is an additional fitting parameter required for each pair of interfaces that are correlated. There is also a scaling factor to scale the experimental reflectivity to the model reflectivity which is fixed by the instrumental geometry. The aim is to fit the model to the experimental data with as many of these fitting parameters as possible fixed. The parameters of the buried F8/dPMMA interfaces can only be extracted by fitting the reflectivity data with a bilayer model. This will allow the buried interface to be characterised and the roughness contributions separated. The methodology for fitting off specular data is not well established, so several methodologies are explored.

The parameters of the air/polymer and the polymer/Si interface are fixed by using AFM (described in section 4.8) and by fitting the off specular reflectivity of the single layers. These parameters are assumed not to change for the bilayer samples. It can be shown that both the specular and off specular reflectivity from the air/F8 interface is insignificant when compared with the F8/dPMMA interface. The off specular reflectivity from the dPMMA/Si interface is insignificant compared with the F8/dPMMA interface. However it is important that the parameters of the dPMMA/Si interface are reasonable, as they are included in the layer correlation term between the F8/dPMMA interface and the dPMMA/Si interface. It is assumed that there are no correlations between the F8/dPMMA interface and the air/F8 interface or the air/F8 interface and the dPMMA/Si interface. From visual inspection of the off specular data it is clear that the heightened intensity along constant q_z corresponds with correlations between the F8/dPMMA interface and the dPMMA/Si interface, as they correspond to the Kiessig fringes in the specular reflectivity, which are dominant acting across the dPMMA medium (see section 2.10.1). Therefore only the interface to interface correlation between the F8/dPMMA interface and the dPMMA/Si interface are included in the fits in this work.

In section 6.3 fitting of the off specular reflectivity data from the F8/dPMMA bilayer samples of different thicknesses is described. The different methods to try and fit the data and extract information about the buried polymer/polymer interfaces are described in the list below:

1. The initial attempts to fit the data fitted only the off specular part of the data assume that the off specular contribution to the specular data is negligible, so the total roughness σ_{tot} could be taken as the value obtained from specular fits. The scaling factor was used

as a fitting parameter. This resulted in poor fits, which suggests that the off specular data is significant at $q_x = 0$ and σ_{tot} obtained from fitting the specular data is lower than the true value.

2. The off specular reflectivity is then fitted with σ_{tot} as a fitting parameter and the scaling factor as a fitting parameter. This gave much better fits and there was a significant increase in σ_{tot} for all the samples when compared to the value of σ_{tot} obtained from the specular fits.

3. The scaling factor should be the same for fits of all the reflectivity data sets as the instrumental geometry is the same for all the samples measured. However using it as a scaling parameter showed some sample to sample variation. The scaling factor is then fixed to the value obtained from fitting the dPMMA/Si single layer and the data refitted. The scaling factor from this sample is chosen as it has the fewest adjustable parameters and has strong features in its off specular reflectivity. The off specular data is refitted with the scaling factor fixed and it is found that the fits were still good. The repeatability of the fits is tested.

4. It is found that the lateral cut off ξ_{lat} obtained from the fits was smaller for samples with a thinner dPMMA film than the samples with thicker dPMMA film. A sensitivity analysis is conducted in order to characterise the effect of varying ξ_{lat} on two samples with a thin and thick layer of dPMMA.

5. The off specular reflectivity from the model at $q_x = 0$ is subtracted from the experimental specular reflectivity and then refitted using the specular model, to see if σ_{tot} predicted from fitting the off specular alone is the same as that from fitting the specular data with the off specular subtracted. Compared with σ_{tot} values obtained from fitting the specular reflectivity with no off specular subtraction the values for σ_{tot} increase significantly. However they are still lower than the values obtained from fitting the off specular reflectivity alone.

6. To confine the fit further Schlomka et al [79] suggest that the specular and off specular components should be fitted simultaneously. The model for the combined specular and off specular fit outlined in section 5.7 is used to fit the data. It is found that the total roughnesses predicted are between that obtained from fitting the specular fit the off specular subtracted and fitting the off specular. Trends in both the lateral roughness and the total roughness for different thickness dPMMA films are maintained.

7. A thin layer with variable fit parameters was included between the dPMMA and Si substrate in the combined fits to attempt to model the native oxide layer found on the Si substrate.

8. The lateral cut off values predicted for the combined fits for the thicker samples are significantly lower than those obtained from fitting the off specular data. It is suggested that this is due to the fitting algorithm and the lack of sensitivity to the lateral cut off for the thicker samples. The reflectivity data from two of the thicker samples is fitted again with ξ_{lat} fixed to the value obtained from the off specular fits. The reflectivity data could still be fitted, but the roughnesses were slightly affected.

The off specular reflectivity of the PS/dPMMA bilayer is not fitted, as the off specular scattering from this sample had poor count statistics.

6.2 Specular Fitting

6.2.1 Specular fitting model

Specular reflectivity curves were fitted using a program written in house, based upon Parratt formulisation for specular reflectivity of a multilayer stack (see section 2.7.5) and the a Nevot la Croce factor to find the Gaussian RMS roughness (see section 2.7.7). A differential evolution fitting scheme based on minimising the χ^2 of the difference between the data and the model was used to optimise the fit, as used by Wormington et al [102] to fit specular x-ray data. For information on differential evolution see section 5.6.1 and the the references contained within. Resolution is accounted for by calculating the reflectivity at a series of equally spaced q_z values centred on the q_z value of the experimental data point and averaging them with a Gaussian weighting. The resolution is fixed by the experimental geometry and is not a fit parameter.

6.2.2 Modelling with an oxide layer

The surface of the silicon substrate is covered in a so called 'native oxide layer'. This layer is amorphous and its composition is potentially non-uniform. It's roughness and thickness may vary with wafer fabrication conditions [94]. For this reason all measurements were performed on samples using silicon substrates from the same batch. This layer will have some affect on

the scattering of neutrons from the sample, generally making the reflectivity reduce at a greater rate with q_z. A satisfactory way to treat this oxide layer is not found in the literature. The thickness of the oxide layer could not be found using neutron reflectivity on a Si substrate because the q range of the experiment is too small to see any fringes from such a small layer. In this work specular reflectivity for samples with dPMMA on Si were fitted by including an oxide layer in the calculation, between the Si substrate and the dPMMA. The oxide layer was assumed to be a very thin discrete layer with a scattering length density equal to that of SiO_2. The parameters of this layer were fixed to be the same for every sample with the dPMMA / Si interface. It was found that an oxide layer of $\sim$ 9Å and a roughness between 5Å and 7Å gave good fits to the specular data and worked for all samples modeled. Fits of the data were made and repeated for values of oxide layer roughness 5Å and 7Å. These parameters for the oxide layer may be different for bare Si because the dPMMA may fill nanoscale pores in the oxide layer, causing the effective scattering length density of the layer to change.

Including the oxide layer in the off specular calculations is computationally intensive and also because the roughness is large compared to the thickness potentially causing the DWBA perturbation model will break down. For this reason the oxide layer was not considered in most of the off specular fits. So that comparison could be made with the off specular fits specular fits were performed on all samples without an oxide layer included and the roughness for Si found from AFM data was used.

The scattering for bilayer samples will be dominated by scattering from the F8/dPMMA interface and the dPMMA/Si interface. The scattering from the air/F8 interface will be almost insignificant in the bilayer samples and therefore the F8 scattering length density, thickness and roughness will be fixed at values found from fitting the specular data of the single annealed F8 layer on Si substrate. The roughness of the silicon substrate was set to 0 for fits including an oxide layer and 4.3 Å for fits with no oxide layer, which is the roughness found by AFM.

As q_z tends toward 0.2Å $^{-1}$ the decay in reflectivity means that the background scattering becomes dominant. Therefore a constant value to represent the background scattering (which is assumed to have no q_z dependence) is added to the calculated reflectivity in the fits for all q_z. The background scattering was set for each sample by examining the experimental reflectivity curves in the region where the reflectivity stops falling off at high q_z values, which shows that the reflectivity is being dominated by background scattering. The same background was used for all samples measured on the same experiment.

6.2.3 Fitting specular reflectivity single layer samples

Fits were made of the single F8 sample and the single layer dPMMA sample reflectivities with the oxide layers discussed in the previous section. In each case the scattering length density of the Si substrate was fixed at $2.073e - 6\text{Å}^{-2}$. Figures 6.1 and 6.2 show the fits for the F8 and dPMMA single layers respectively. The parameters found for the thicknesses, scattering length density,surface roughnesses and χ^2 parameter for the two oxide layer roughnesses are given in table 6.1. Experiments on both samples were performed on D17 at the ILL.

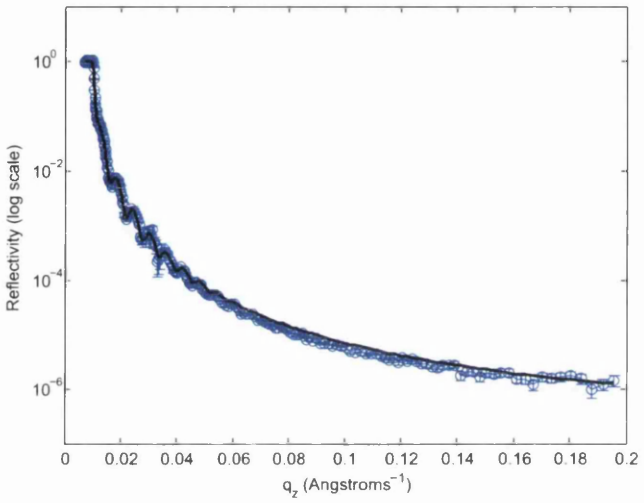

Figure 6.1: Fits of specular data from D17 for a thin film of F8 on silicon substrate annealed for 3 hours, assuming an oxide layer of thickness 9Å and roughness 5Å (errorbars are smaller than the data points)

The roughness for the top surface of the dPMMA is in close agreement with that found by AFM studies (see section 4.8).

6.2.4 Fitting specular reflectivity from F8/dPMMA bilayer samples annealed for different times

To check that the systems examined were at thermodynamic equilibrium bilayer samples of $\sim$ 1000 Å F8 on $\sim$ 480Å dPMMA were made and annealed for different times to see if the

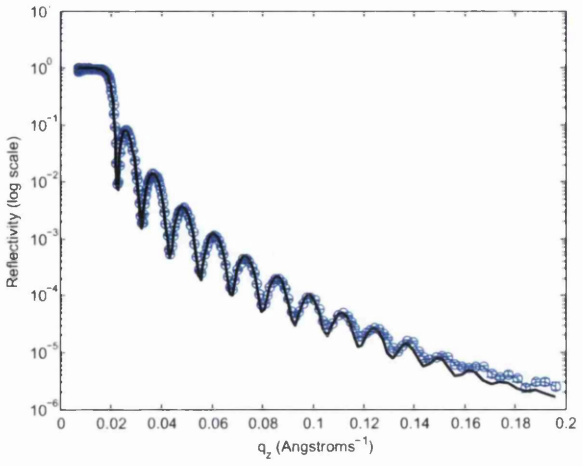

Figure 6.2: Fits of specular data from D17 for a thin film of dPMMA on silicon substrate annealed for 3 hours, assuming an oxide layer of thickness 9 Å and roughness 5Å (errorbars are smaller than the data points)

Fits of single layers					
Sample	σ $Si0_2$	χ^2	d Å	SLD Å^{-2}	σ
F8	5	7.35	1050.51	5.34e-7	33.39
	7	3.31	1050.88	5.34e-7	31.27
	Mean	-	1050.70	5.34e-7	32.33
dPMMA	5	22.31	482.9	6.79e-6	9.31
	7	20.48	482.78	6.79e-6	8.60
	Mean	-	482.84	6.79e-6	13.61

Table 6.1: Table showing the fitted parameters of single layer annealed F8 and dPMMA films on Si substrate with oxide layers included on the fit

roughness changed as a function of time.

Fits of ~ 1000 Å F8 on ~ 500 Å dPMMA for different annealing times					
Annealing time (hrs)	σ $Si0_2$	χ^2	dPMMA d Å	dPMMA SLD $Å^{-2}$	F8/ dPMMA σ
0	5	17.45	479.30	6.85e-6	9.67
	7	21.16	479.17	6.84e-6	8.98
	Mean	-	**479.24**	**6.85e-6**	**9.33**
3	5	20.25	483.35	6.83e-6	16.83
	7	16.38	483.34	6.84e-6	16.21
	Mean	-	**483.34**	**6.83e-6**	**16.52**
24 †	5	14.57	482.86	6.87e-006	13.92
	7	18.64	482.82	6.87e-006	13.40
	Mean	-	**482.84**	**6.87e-6**	**13.66**
67	5	48.67	506.14	6.95e-6	23.16
	7	53.77	506.16	6.95e-6	22.29
	Mean	-	**506.15**	**6.95e-6**	**22.73**
67 *	5	8.40	476.40	6.79e-6	21.01
	7	8.89	476.34	6.79e-6	20.16
	Mean	-	**476.37**	**6.79e-6**	**20.59**

Table 6.2: Parameters obtained from fitting specular neutron reflectivity data for ~ 1000Å F8 on ~ 480Å dPMMA bilayer samples annealed for various times (* refer to experimental data from offspec, † refers to experimental data from CRISP)

From table 6.2 it can be seen that annealing increases the interfacial roughness significantly. The three hour annealed sample is rougher than the twenty four hour annealed sample, though since the experiments were on different instruments this may account for the difference.

From these results it is not possible to conclude whether a three hour annealing time is long enough for F8/dPMMA bilayer samples to reach thermodynamic equilibrium and more experimental data is required. However Higgins et al [38] show that for an F8/dPMMA annealed at 163° that three hours annealing time was enough to reach thermodynamic equilibrium.

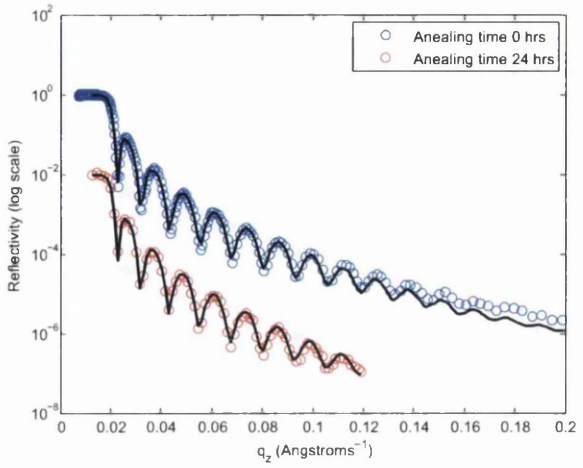

Figure 6.3: Best fits of specular reflectivity data from bilayers of $\sim$ 1000Å F8 on $\sim$ 480Å dPMMA on Si substrate for 0hr and 24hr annealing times (fits are separated by 10^{-2} for clarity) (note: reflectivity data becomes dominated by the background for $q_z > 0.12$ for 24hr annealed sample (errorbars are smaller than the data points)

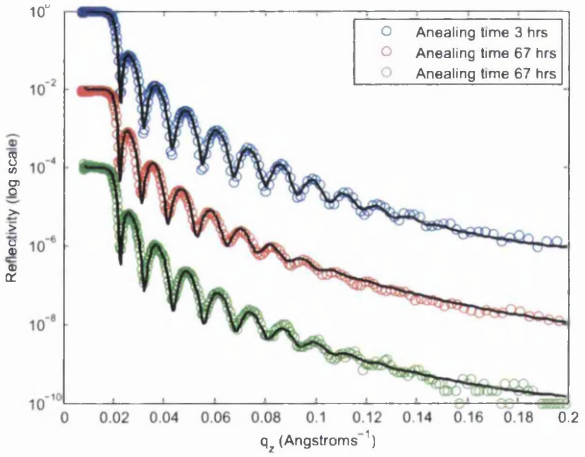

Figure 6.4: Best fits of specular reflectivity data from bilayers of $\sim$ 1000Å F8 on $\sim$ 480Å dPMMA on Si substrate for 3hr and 67hr annealing times (fits are separated by 10^{-2} for clarity) (errorbars are smaller than the data points)

6.2.5 Fitting specular reflectivity from F8/dPMMA 3 hour annealed bilayer samples of different thickness dPMMA films

The specular data is analysed for the $100nm$ F8/dPMMA bilayers with different thickness dPMMA to find the RMS roughness σ of the F8/dPMMA interfaces. It is expected that the RMS roughness of the interface $\sigma = \sigma_{tot}$ will increase as a function of the thickness of the dPMMA layer if the interface is broadened by thermally excited capillary waves as discussed in section 3.2. The fits were made assuming the oxide layers described at the beginning of this section. Figure 6.5 shows fits to experimental data. Table 6.3 shows the parameters obtained from the fits for each sample for the two different oxide layer models.

Small sample to sample variation in the fitted dPMMA scattering length density can be caused by small errors in the angle of incidence measured by the instrument. Figure 6.6 shows a plot of the thickness of the dPMMA layer against the F8/dPMMA interfacial roughness found from fits of the specular data.

The general trend is that the interfacial roughness increases as the thickness of the dPMMA film increases and then saturates due to the coherence length of the neutrons. This trend is the same as found by Sferrazza et al [84] for PS/PMMA interfaces which suggest that capillary wave fluctuations contribute significantly to interfacial roughness at liquid/liquid interfaces (see section 3.2). In a reflectivity experiment neutrons will not be sensitive to capillary waves with wavelengths greater than the neutron coherence length. Therefore for thick films where the film contains capillary waves with wavelengths larger than the coherence length the roughness measured will be around the same value. Even though the capillary wave spectrum still increases with film thickness, the neutrons will not be sensitive to these larger wavelengths. This is the case for the for the three thicker samples measured.

The χ^2 parameters for the specular reflectivity are high compared to the usual values found from specular reflectivity. This is because of the large count times of the data in this work due to the simultaneous collection of specular and off specular data, resulting in small error bars and therefore large χ^2. In this work typical counts times at $\theta_i = 2.5^o$ were $\sim$ 15 hours, compared with $\sim$ 1 hour required to collect specular data alone.

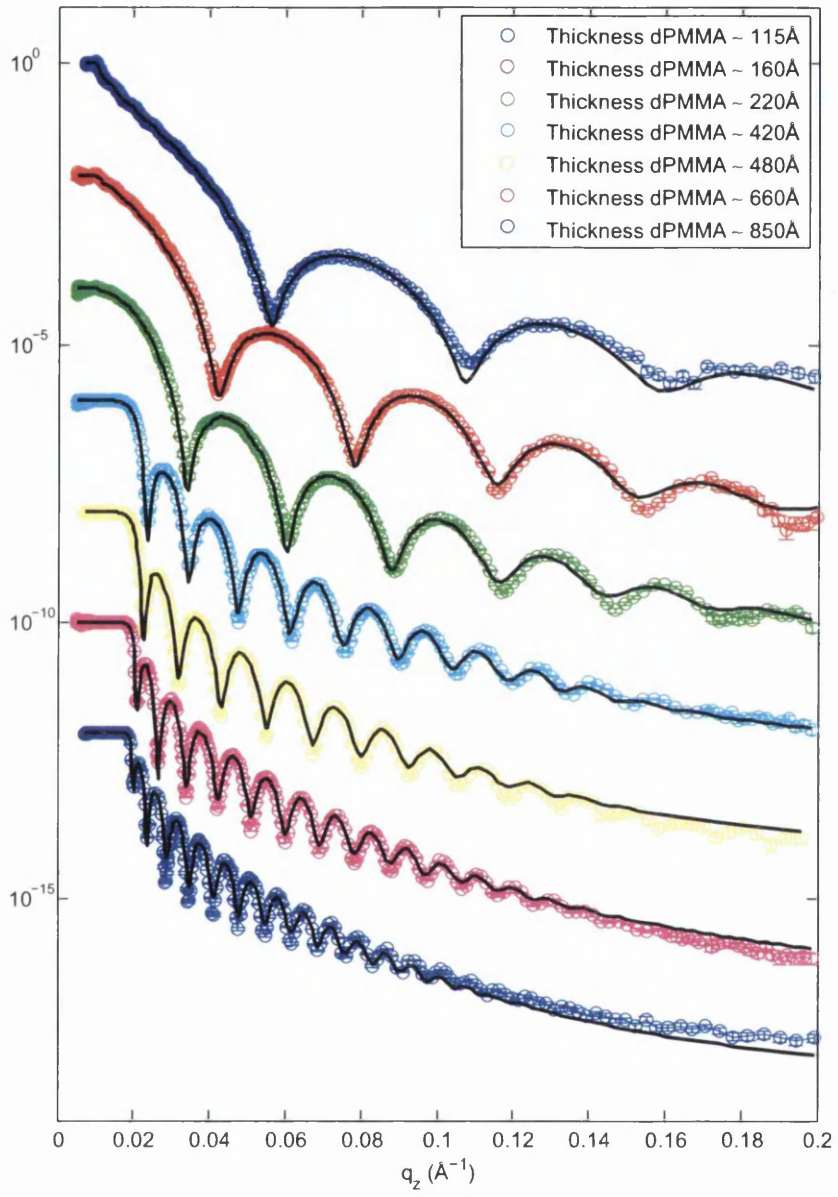

Figure 6.5: Best fits of specular reflectivity data from bilayers of $\sim$ 1000Å F8 on $\sim$ 110Å, $\sim$ 160Å, $\sim$ 220Å, $\sim$ 420Å, $\sim$ 480Å, $\sim$ 660Å and $\sim$ 850Å dPMMA on Si substrate annealed for 3hrs (fits are separated by 10^{-2} for clarity) (errorbars are smaller than the data points)

dPMMA thickness series fits					
Approx thickness dPMMA (Å)	σ $Si0_2$	χ^2	dPMMA d Å	dPMMA SLD $Å^{-2}$	F8/ dPMMA σ
120	5	4.37	116.04	6.71e-6	9.67
	7	4.64	115.94	6.71e-6	8.98
	Mean	-	**115.95**	**6.71e-6**	**9.33**
160	5	8.82	162.95	6.80e-7	11.28
	7	10.04	162.83	6.79e-6	10.48
	Mean	-	**162.89**	**6.80e-6**	**10.88**
220	5	20.58	217.02	6.91e-6	13.15
	7	23.85	216.90	6.91e-6	12.33
	Mean	-	**216.96**	**6.91e-6**	**12.74**
420	5	40.11	428.27	6.86e-6	14.92
	7	44.41	428.18	6.86e-6	14.16
	Mean	-	**428.23**	**6.86e-6**	**14.54**
480	5	20.25	483.35	6.83e-6	16.83
	7	16.38	483.34	6.84e-6	16.21
	Mean	-	**483.34**	**6.83e-6**	**16.52**
660	5	65.36	660.54	6.97e-6	15.63
	7	62.05	660.84	6.97e-6	14.84
	Mean	-	**660.69**	**6.97e-6**	**15.24**
850	5	41.94	854.99	6.90e-6	15.82
	7	44.30	854.92	6.89e-6	14.94
	Mean	-	**854.96**	**6.89e-6**	**15.38**

Table 6.3: Parameters obtained from fitting specular neutron reflectivity data for $\sim$ 1000Å F8 on various thickness dPMMA bilayer samples annealed 3 hours

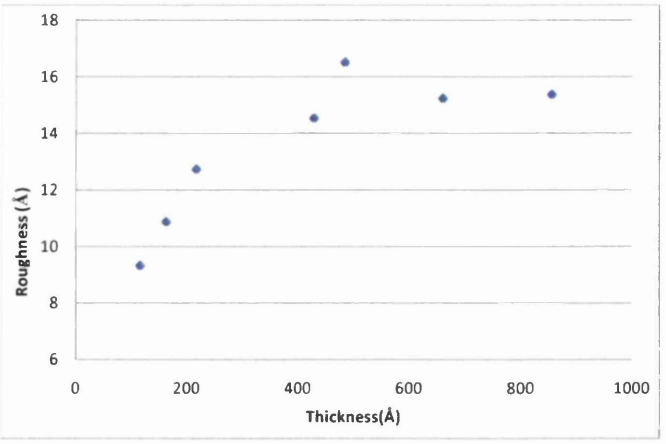

Figure 6.6: A plot of F8/dPMMA interfacial roughness against the thickness of the dPMMA layer from fits of specular reflectivity

6.2.6 Fitting specular reflectivity from F8/dPMMA samples without an oxide layer

Specular fits were made of the layer thickness series samples in order to compare directly with off specular fits where no oxide layer is included. Fits of the specular data without an oxide layer are shown figure 6.7 and the fitted parameter values for all of the samples in the series are tabulated in table 6.4.

The χ^2 values of the fits are generally higher than those where the oxide layer is considered. The interfacial roughness obtained for each sample is higher for fits that don't include an oxide layer. The effect of the oxide layer is to increase the fall off of the reflectivity. Examination of the fits show without the oxide layer the rate of reflectivity fall off is too low and the reflectivity given by the fits is above that of the experimental reflectivity at high q_z values. It is expected that the reflectivity should increase when the oxide layer is included as it has a higher scattering length density than Si. However the roughness of it will cause the reflectivity to fall off at a greater rate, showing that the roughness of the oxide layer is dominant over its scattering length density in its effect on the reflectivity.

Figure 6.8 shows the F8/dPMMA interfacial roughness plotted against the dPMMA thickness for the two different oxide layers and no oxide layer. While the roughness for each sample is

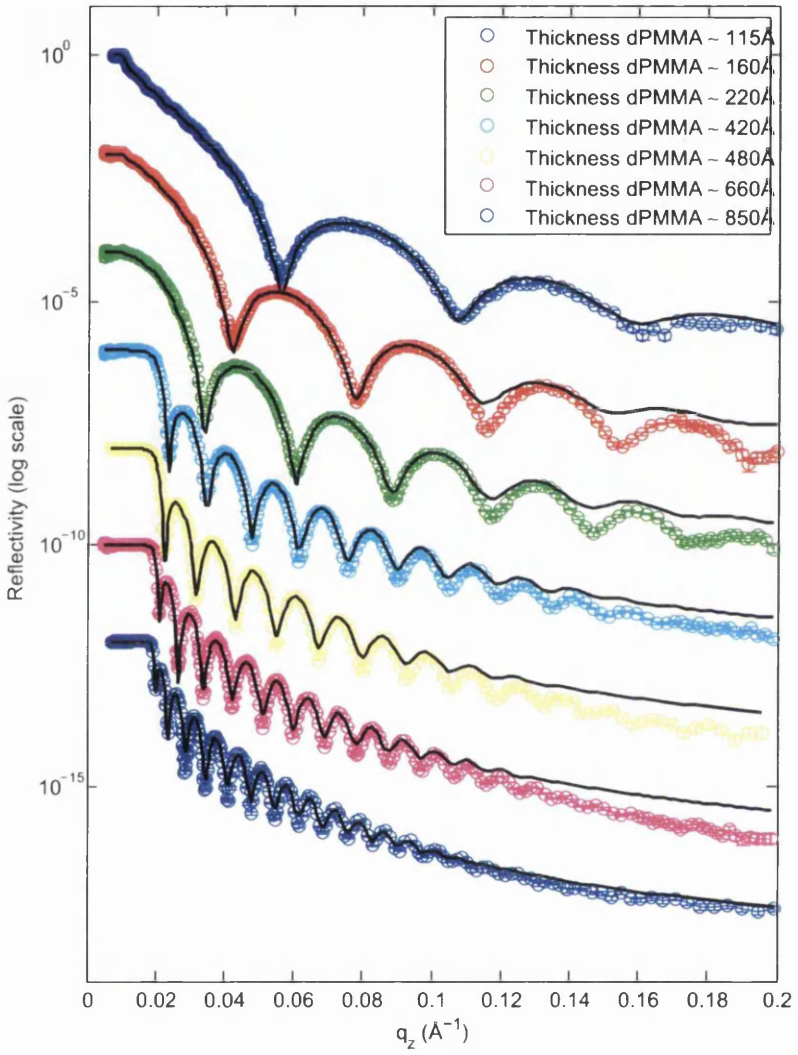

Figure 6.7: Best fits of specular reflectivity data assuming no oxide layer from $\sim$ 1000Å F8 on $\sim$ 160Å $\sim$ 480Å and $\sim$ 660Å dPMMA annealed for 3hrs (fits are separated by 10^{-2} for clarity) (errorbars are smaller than the data points)

dPMMA thickness series fits with no oxide layer				
Approx thickness dPMMA (Å)	χ^2	dPMMA d Å	dPMMA SLD $Å^{-2}$	F8/ dPMMA σ
120	4.38	118.81	6.71e-6	10.30
160	28.04	166.37	6.80e-6	12.79
220	36.22	219.64	6.89e-6	13.619
420	34.89	428.71	6.92e-6	15.045
480	39.89	485.87	6.81e-6	17.39
660	63.6	662.88	6.96e-6	16.34
850	43.58	857.62	6.89e-6	16.65

Table 6.4: Parameters obtained from fitting specular neutron reflectivity data for $\sim$ 1000ÅF8 on various thickness dPMMA bilayer samples annealed 3 hours assuming no oxide layer and using the roughness of the silicon substrate taken from AFM

larger with no oxide layer the dependency on dPMMA thickness shows the same trend.

Comparison of fitting regime against Parratt 32 software

In order to check the validity of the model and the fitting scheme fits of the specular data were made using Parratt 32 software for comparison [12]. It is well regarded and frequently used to fit neutron data in published work. The Parratt 32 scheme uses the Parratt formalism [66] and a Newton- Rhapson fitting scheme to minimise χ^2. Fits using Parratt 32 were made for three of the samples with and without an oxide layer (with the roughness of the oxide set at 5 Å). The background is set to be constant and both background and resolution were set at the same values used in the model used in this work. The values for the parameters describing the air/F8 interface and the dPMMA/Si interface are fixed to the same values described in the previous sections. Table 6.5 shows values obtained from fitting three samples using the in house differential evolution fitting program and using Parratt 32 software. Figure 6.9 shows the calculated reflectivities for one sample using the in house differential evolution fitting regime and using Parratt 32 software.

From table 6.5 it can be seen that the parameters obtained from the fits are almost identical for

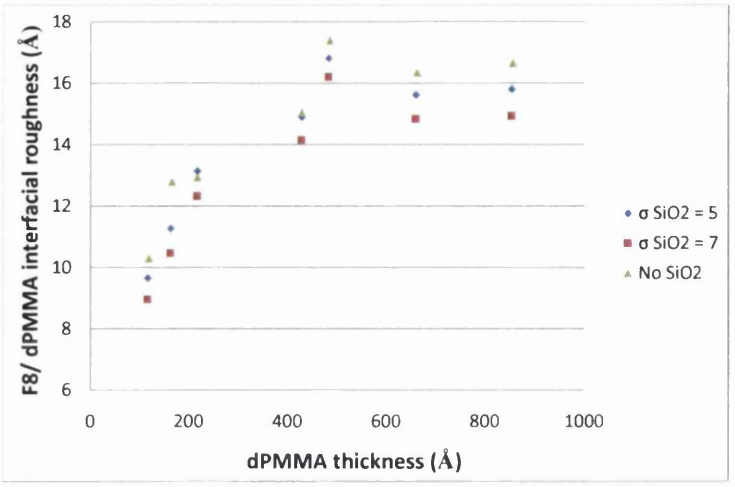

Figure 6.8: A plot of F8/dPMMA interfacial roughness against the thickness of the dPMMA layer from fits of specular reflectivity with different oxide layer models

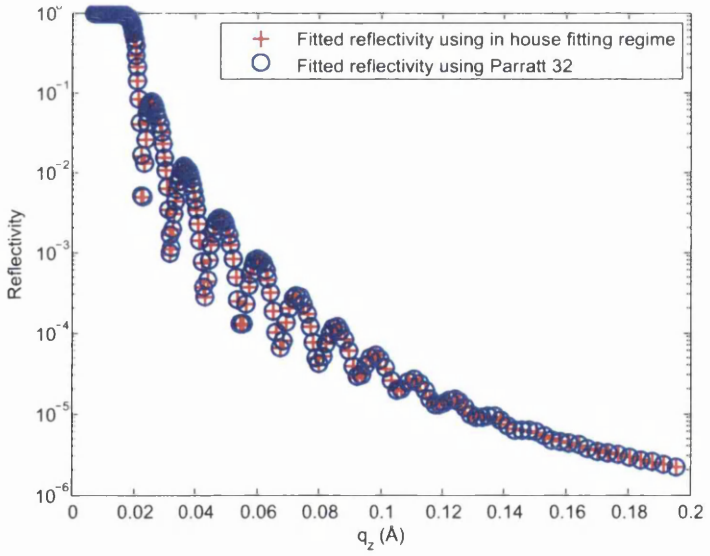

Figure 6.9: Comparison of calculated reflectivity from fits of $\sim$ 1000Å F8 on $\sim$ 480Å dPMMA bilayer sample using in house differential evolution fitting regime and using Parratt 32 software)

dPMMA thickness series fits with no oxide layer				
Approx thickness dPMMA (Å)	Fit method	dPMMA d Å	dPMMA SLD $Å^{-2}$	F8/ dPMMA σ
220	Diff ev with oxide	217.02	6.91e-6	13.15
	Parratt 32 with oxide	217.2	6.87e-6	13.09
	Diff ev without oxide	219.64	6.89e-6	13.62
	Parratt 32 without oxide	219.88	6.90e-6	13.57
480	Diff ev with oxide	483.35	6.83e-6	16.83
	Parratt 32 with oxide	483.44	6.82e-6	16.86
	Diff ev without oxide	485.87	6.81e-6	17.39
	Parratt 32 without oxide	485.92	6.82e-6	17.32
660	Diff ev with oxide	660.54	6.97e-6	15.63
	Parratt 32 with oxide	660.03	6.98e-6	15.36
	Diff ev without oxide	662.88	6.96e-6	16.34
	Parratt 32 without oxide	662.98	6.96e-6	16.02

Table 6.5: Comparsion of parameters obtained from fitting specular neutron reflectivity data for $\sim$ 1000Å F8 on various thickness dPMMA bilayer samples annealed 3 hours using the in house differential evolution fitting program and Parratt 32 software with and without including an oxide layer in the fit

the two fitting programs, verifying the values obtained by the in house program. The calculated reflectivity curves in figure 6.9 are indistinguishable showing that the implementation of the Parratt formalism in the in house program is correct.

6.2.7 Fitting specular reflectivity data from PS/dPMMA samples

Two bilayers of PS/ dPMMA annealed for twenty four and three hours were studied using neutron reflectivity to compare with the F8/dPMMA system. The two different annealing times were used to see if the system reached thermodynamic equilibrium. From comparison of the specular reflectivity curves it was apparent that the reflectivity curves exhibited the same rate of fall off and thermodynamic equilibrium for the samples had been reached. The analysis presented here is for the three hour annealed sample. The interface in the F8/dPMMA system is between a polymer in a nematic crystalline phase (at 180^oC [33])and an amorphous polymer. The PS/PMMA system contains an interface between two amorphous polymers. The mixing of amorphous polymer pairs has been the subject of a large body of research and is well understood (see chapter 3), whereas the interfacial mixing of the nematic crystalline/ amorphous polymers is not well understood. Comparison of the two systems will allow us to see if the theory developed for amorphous polymer pairs can be applied to the F8/ dPMMA system. Fits of the specular data for the PS/dPMMA sample annealed for three hours are shown in figure 6.10 and the fitting parameters are tabulated in table 6.6.

PS/ dPMMA fits			
Parameter	$Si0_2 = 5$	$Si0_2 = 7$	**Average**
PS d Å	1824.9	1830.0	1827.45
dPMMA d Å	1747	1745.1	1746.05
PS SLD $Å^{-2}$	1.09e-6	1.24e-6	1.17e-6
dPMMA SLD $Å^{-2}$	6.92	6.91	6.91
PS σ Å	7.27	23.7	15.49
dPMMA σ Å	17.25	15.00	16.13
χ^2 Å	59.8	76.5	-

Table 6.6: Fit parameters obtained from fitting specular reflectivity data from a PS/dPMMA bilayer on Si substrate

It can be seen that PS/ dPMMA interfacial roughness is similar to that of the thicker F8/dPMMA

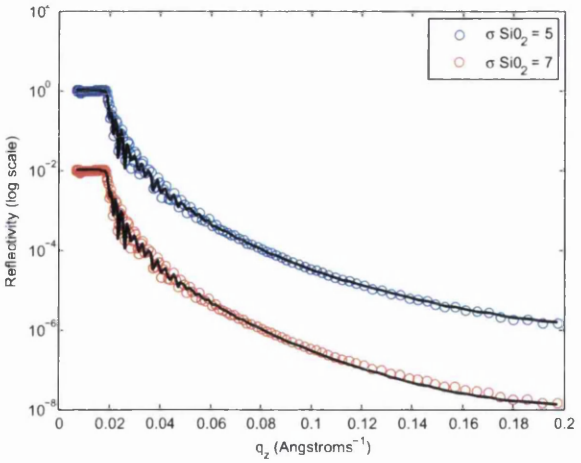

Figure 6.10: Fits of specular reflectivity data for $\sim$ 1800Å PS on $\sim$ 1700Å dPMMA sample assuming an oxide layer of thickness 9 Å and roughness 5Å and 7Å (fits are separated by 10^{-2} for clarity) (errorbars are smaller than the data points)

samples suggesting that the dynamics of mixing at the interface are similar. However the off specular data contained few features and so could not be fitted. It is possible that the thickness of the films meant that there was little off specular scattering. To test this further experiments will be carried out supplementary to the work presented in this thesis on PS/dPMMA samples with thinner films. It is also possible that the lack of off specular is due to different interfacial dynamics than the F8/dPMMA system. In either case further experimental data is required for verification.

Conclusions

Specular reflectivity has been fitted for F8/dPMMA bilayers as well as a PS/dPMMA bilayer. The main focus is the roughness of interfaces with different thickness dPMMA layers. The fits show that the roughness is a function of the thickness as predicted by the capillary wave model outlined by Sferrazza et al [84]. Larger wavelength capillary waves are suppressed by dispersion forces across the film. As the films thickness increases the effect of the dispersion forces is reduced and longer wavelength capillary waves exist. From fits of the specular neutron reflectivity data the roughness obtained saturate at a value of $\sim$ 16Å for the four thickest films measured which suggests the larger capillary wavelengths the interface can support are greater than the coherence length of the neutrons.

6.3 Off specular data fitting

6.3.1 Introduction

In this section the off specular data for five bilayer F8/dPMMA samples (samples th1 - th5) with varying thickness of dPMMA are fitted using the off specular model described in chapter 5. All samples in this section are made on Si substrate and annealed at 180^oC for three hours. The reflectivity was measured on D17 and the reflectivity has background subtracted and is normalised by the direct beam and water runs as described in section 4.1. The self affine height to height correlation is used to model each interface in the system and the correlation between interfaces is described by the interface to interface correlation function defined by Schlomka et al [79].

6.3.2 Rebinning the data

From examination of the raw reflectivity data a θ_f range of $0.6^o - 3.2^o$ and a λ range of $5 - 22$ Å was chosen as the limits of the reflectivity to be fitted. The raw reflectivity data θ/λ space contains 286 θ pixels $\times 1000\lambda$ pixels. However in the off specular region many of these pixels from the experimental reflectivity do not contain any neutron counts. Rebinning creates a smoothed map with fewer pixels. The data in the pixels of the rebinned map are calculated by averaging over the data in a range of pixels in the original map. This facilitates faster computation. In this work each bin in the θ direction contains 3 pixels and each bin in the λ direction contains 13 pixels, resulting in a θ/λ map of 50×44 pixels. The spacing of pixels on the detector is smaller than the instrumental resolution, so rebinning makes the pixel spacing of the same order as the resolution.

Resolution

Since the resolution of D17 in both θ and λ directions is constant and has no q dependence (assuming the choppers are closed) $\frac{d\theta}{\theta}$ was calculated to be 0.05 and $\frac{d\lambda}{\lambda}$ was calculated to be 0.01 (see section 2.4.6). These values were used in the resolution convolution.

Removing areas not to be fitted

For fits of the off specular reflectivity alone the region of the colourmap containing the specular reflectivity was removed. A region of 0.18^o was removed either side of the angle of incidence. Outside of the Yoneda peak the model reflectivity is small and the experimental data is dominated by background scattering, therefore this region is excluded from the fit. Figure 6.11 shows experimental reflectivity for sample $th5$ and figure 6.12 shows the data rebinned and the areas where the data will not be fitted removed.

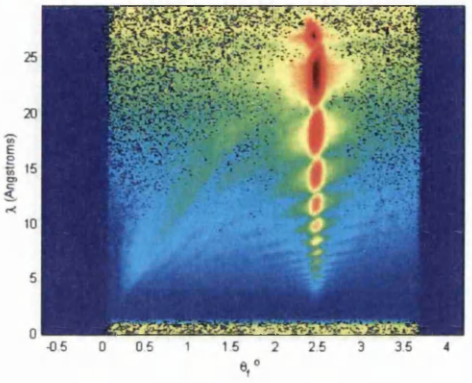

Figure 6.11: Experimental reflectivity (counts are on a log scale)

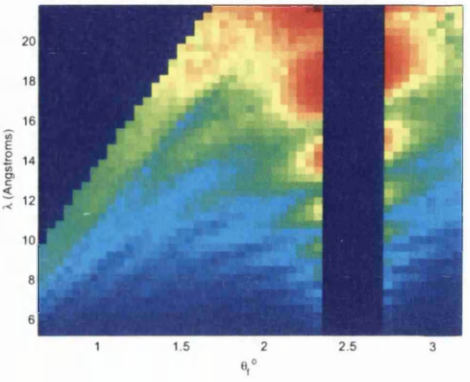

Figure 6.12: Normalised experimental reflectivity rebinned and areas not to be fitted removed (counts are on a log scale)

6.3.3 Lateral length scales probed

The lateral length scales on the sample probed d are dependent on the q_x range with $d = \frac{2\pi}{q_x}$. Figure 6.13 shows the length scales probed as a function of θ and λ.

6.3.4 Fixed and variable parameters

In the model the reflectivity from each interface is a function of σ_{tot} the total roughness, σ_{lat} the lateral roughness, h the Hurst parameter, ξ_{lat} the lateral cut off length and the SLD of the materials either side of the interface (see section 2.8 for description of these parameters). The reflectivity from interface to interface correlation between each pair of interfaces is a function of these five parameters from both interfaces and also the length between interfaces $\xi_{\perp}$. There

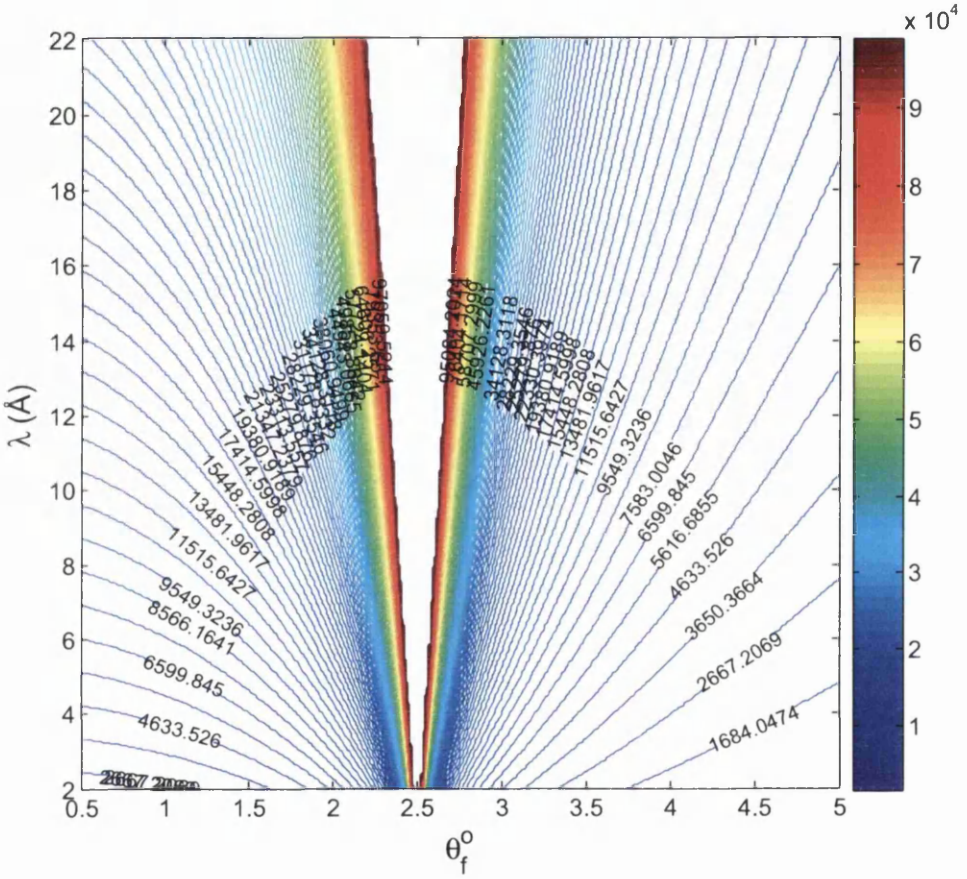

Figure 6.13: Contours of length scale probed ($2\pi/q_x$) in Å by off specular scattering as a function of θ_f and λ

is also a scaling parameter to be considered which scales the off specular reflectivity with the specular reflectivity. It also scales the model off specular reflectivity to the experimental reflectivity. It will be a constant scaling factor for the entire off specular reflectivity. It is fixed by the instrumental geometry and is dependent on the solid angle of each pixel on the detector[88] and is constant for all θ/λ in TOF experiments. Initially it is used as a fitting parameter. The F8/dPMMA interface is the interface of interest. The parameters of the F8 top layer and the Si substrate should be the same for every sample and will be fixed.

Fixing parameters at Air/F8 interface

The off specular reflectivity from the F8 layer is orders of magnitude smaller than the reflectivity from the buried interface. Because there is no intrinsic mixing (at a molecular level) between the air and F8 it is assumed that $\sigma_{tot} = \sigma_{lat} = 32.33$Å for all bilayer samples. The scattering length density of the F8 is fixed to $5.34e-7$Å $^{-2}$ as found from specular fits. It was found that the effect of the F8/ air interface on the the model was negligible and the fits were insensitive to changes in the parameters. For this reason the other parameters for the F8 interface h and ξ are fixed at 0.7 and 50000Å respectively.

Fixing parameters at dPMMA/Si interface

The parameters of the Si interface were fixed by using the AFM data and fitting the off specular reflectivity from sample $sl1$ a single layer of $\sim$ 480Å dPMMA on Si. It was assumed that there was no oxide layer and that $\sigma_{tot} = \sigma_{lat}$ for both the dPMMA top surface and the Si surface. The values of σ_{tot} for the dPMMA and Si were fixed to those found by AFM which gave roughnesses of 8.9Å and 4.3Å respectively (see section 4.8).

The off specular reflectivity from sample $sl1$ was fitted. The SLD of Si was fixed to $2.073e-6$Å $^{-2}$. The h parameter of dPMMA is fixed to 0.6 as found by AFM. The thickness is allowed to vary slightly around the thickness calculated by fitting of the specular data, and the angle of incidence was allowed to vary slightly around $\theta_i = 2.5^o$ to allow for any error in the angle of incidence (caused by inaccuracy of the positioning motor on the instrument). Table 6.7 shows the parameters that were fixed and the limits on each parameter during fitting. Figure 6.14 and figure 6.15 show the experimental reflectivity and model reflectivity for sample $sl1$ respectively. It can be seen from the fit that for the Si interface the h value tends to the higher limit.

Off specular fit parameters of dPMMA on Si			
Parameter	**minimum**	**maximum**	**value**
ξ (Å) dP-MMA	0	100000	43518.07
h Si	0.1	0.99	0.99
ξ (Å) Si	0	100000	25594.59
scaling factor	0.01	1	0.051
$\xi_{\perp}$ (Å)	0	100000	7185.05
θ_i^o	2.4	2.6	2.488
Thickness dPMMA (Å)	470	500	482.37
χ^2	-	-	6.93

Table 6.7: Parameters obtained from fitting off specular reflectivity data for a $\sim$ 480Å single layer of dPMMA on Si substrate

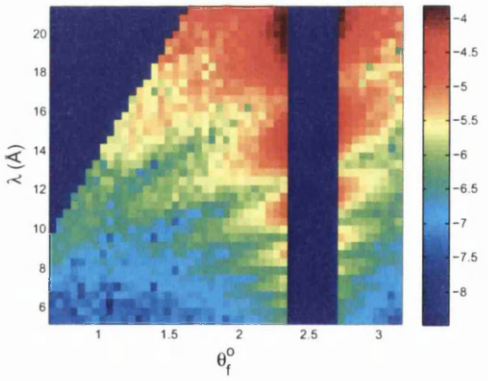

Figure 6.14: Experimental reflectivity data for sample *sl*1 480Å dPMMA on Si (counts are on a log scale)

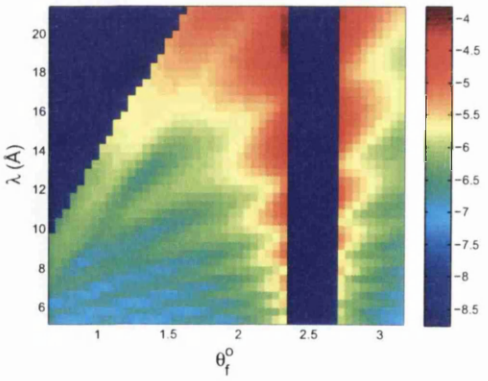

Figure 6.15: Fitted model reflectivity data for sample *sl*1 480Å dPMMA on Si (counts are on a log scale)

For all bilayer fits the Si σ, ξ and h parameters are fixed to 4.3Å, 25594.59Å and 0.99 respectively. From this point on it is assumed that fitting parameters refer to the F8/ dPMMA interfaces unless otherwise stated.

6.3.5 Total roughness fixed by value obtained from specular

Following the methodology of Holy et al [43] the first attempt to fit the off specular reflectivity fixes the total roughness at the value found from fitting the specular data without an oxide layer. The results are tabulated below. The intrinsic roughness σ_{int} is calculated from the total roughness σ_{tot} and the lateral roughness σ_{lat} ($\sigma_{tot}^2 = \sigma_{lat}^2 + \sigma_{int}^2$). Fits of the samples with the thinnest and thickest dPMMA layer are shown in figures 6.17 and 6.19.

Fits with total roughness fixed to value extracted from specular fits					
	Sample number				
Parameter	**th1**	**th2**	**th3**	**th4**	**th5**
Thickness (Å)	162.42	215.62	418.78	478.10	652.33
$\sigma_{tot}(fixed)$ (Å) (fixed)	10.30	12.94	15.05	17.39	16.34
σ_{lat} (Å)	5.58	6.31	15.06	10.38	15.05
σ_{int} (Å)	8.14	11.29484425	-	13.9548314	6.368023233
h	0.63	0.56	0.18	0.13	0.10
$\xi_{\perp}$ (Å)	5860.82	8818.77	48289.66	1339.26	5170.69
scaling factor	0.17	0.15	0.04	0.10	0.08
ξ_{lat} (Å)	29440.59	22827.30	838.49	16251.42	1555.89
χ^2	16.89	10.51	21.21	15.14	48.62

Table 6.8: Parameters obtained from fitting off specular reflectivity data for $\sim$ 1000Å F8 on different thickness dPMMA bilayers on Si substrate, fixing σ_{tot} to value obtained from fitting specular reflectivity

From figure 6.19 it is clear that the fits for thicker samples are very poor. In the fit for sample th3 $\sim$ 1000Å F8 on $\sim$ 420Å dPMMA the lateral roughness is actually larger than the total roughness which is unphysical. It is evident from the theory of off specular scattering that

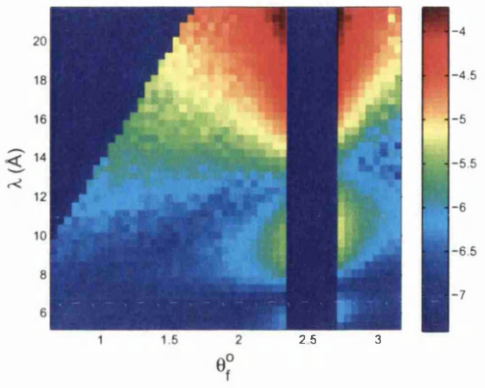

Figure 6.16: Experimental reflectivity for $\sim$ 1000Å F8 on $\sim$ 160Å dPMMA (counts are on a log scale)

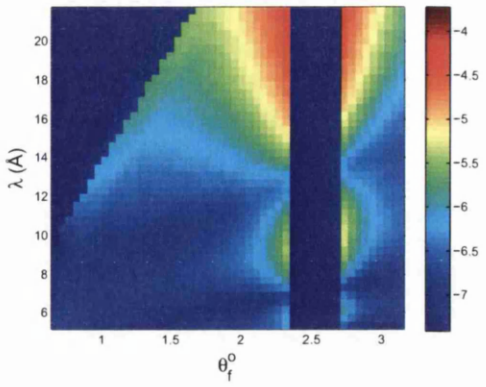

Figure 6.17: Model reflectivity for $\sim$ 1000Å F8 on $\sim$ 160Å dPMMA with σ_{tot} fixed to value extracted from specular fit (counts are on a log scale)

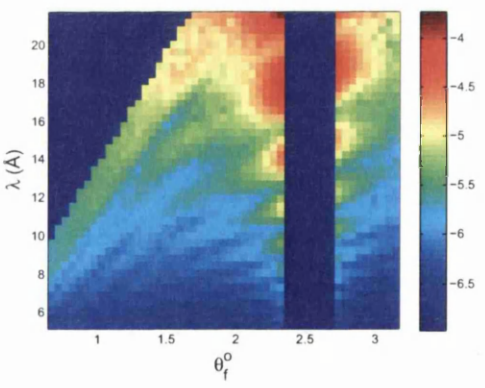

Figure 6.18: Experimental reflectivity for $\sim$ 1000Å F8 on $\sim$ 660Å dPMMA (counts are on a log scale)

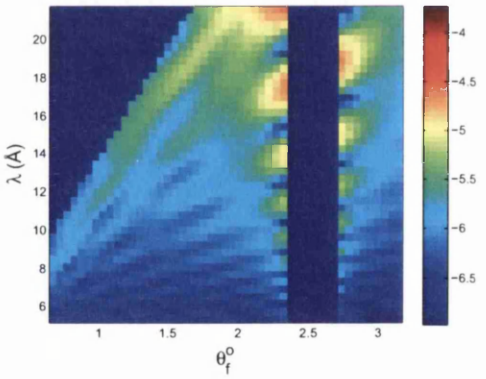

Figure 6.19: Model reflectivity for $\sim$ 1000Å F8 on $\sim$ 660Å dPMMA with σ_{tot} fixed to value extracted from specular fit (counts are on a log scale)

the roughness extracted from fits of specular reflectivity is artificially small because there is off specular reflectivity at $q_x = 0$ which should be subtracted [75]. Schlomka et al [79] suggest that the correct methodology is to simultaneously fit the specular and off specular reflectivity.

6.3.6 Total roughness as a fitting parameter

Using the value of σ_{tot} extracted from specular data resulted in poor fits to the off specular data. The expression for the off specular reflectivity used in the model contains both σ_{tot} and σ_{lat}. This allows both roughnesses to be used as fit parameters.

Table 6.9 shows the results of the fitting parameters for all the samples. Fits of the samples with the thinnest and thickest dPMMA layer are shown in figures 6.21 and 6.23.

Fits with total roughness as a fitting parameter					
	Sample number				
Parameter	**th1**	**th2**	**th3**	**th4**	**th5**
Thickness (Å)	161.4	215.04	418.6	479.7	650.1
σ_{tot} (Å)	26.0015	22.67	31.24	29.3	30.43
σ_{lat} (Å)	10.111	9.66	27.91	22.37	26.023
σ_{int} (Å)	23.95	20.51	14.03	18.92	15.77
h	0.69	0.65	0.15	0.321	0.25
$\xi_{\perp}$ (Å)	99419	37410.1	173510.7	18465.7	172013.2
scaling factor	0.143	0.122	0.045	0.052	0.059
ξ_{lat} (Å)	20324.78	18943.4	154797.13	127776.6	149748.7
χ^2	6.08	5.49	6.22	6.81	17.17

Table 6.9: Parameters obtained from fitting off specular reflectivity data for $\sim$ 1000Å F8 on different thickness dPMMA bilayers on Si substrate, with σ_{tot} as a free fit parameter

Fitting the off specular reflectivity data with σ_{tot} as a fitting parameter results in values of σ_{tot} that are larger than obtained by the fitting the specular data. This is due to off specular data at $q_x = 0$ and discussed further on in this chapter. The fits visually look much better than the fits with σ_{tot} fixed to the specular value. The scaling factors obtained vary between

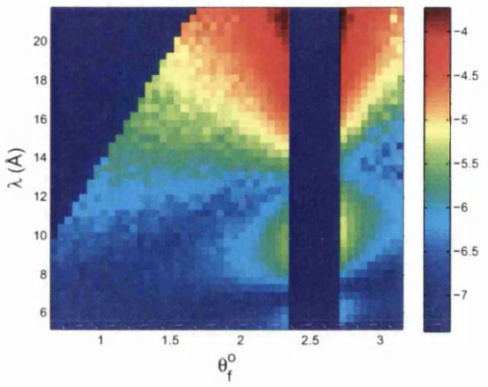

Figure 6.20: Experimental reflectivity for $\sim$ 1000$\mathring{A}$ F8 on $\sim$ 160$\mathring{A}$ dPMMA (counts are on a log scale)

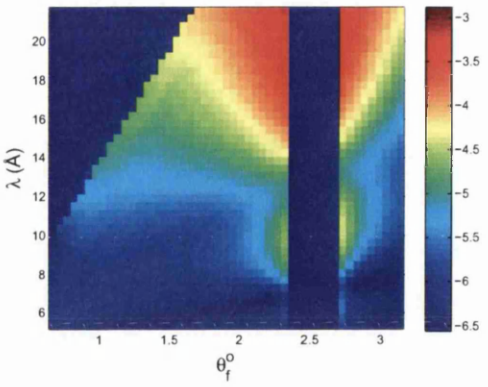

Figure 6.21: Model reflectivity for $\sim$ 1000Å F8 on $\sim$ 160Å dPMMA with σ_{tot} as a free fit parameter (counts are on a log scale)

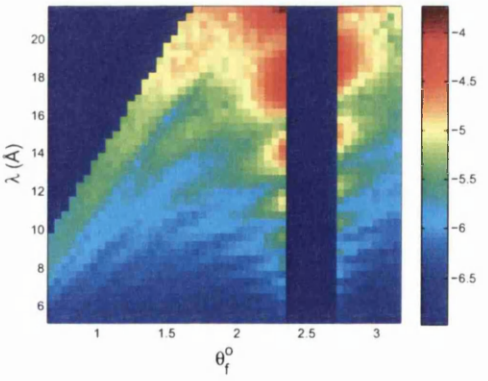

Figure 6.22: Experimental reflectivity for $\sim$ 1000Å F8 on $\sim$ 660Å dPMMA (counts are on a log scale)

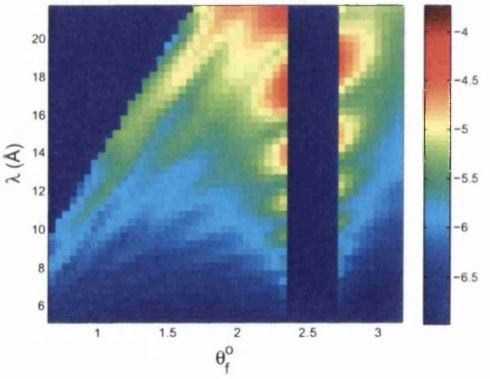

Figure 6.23: Model reflectivity for $\sim$ 1000Å F8 on $\sim$ 660Å dPMMA with σ_{tot} as a free fit parameter

samples whereas it should be the same for all samples, as it is dependent on the instrumental geometry (beam footprint and solid angle per pixel see equation 2.84) which is consistent for all measurements. The scaling factor for the three thicker samples is similar to that found from fitting the dPMMA single layer. However the scaling factor for the two thinner samples is larger. The thinner samples contain less fringes to fit due to the thickness of the dPMMA layer in the θ/λ. Therefore it is expected that the fit will be less sensitive to the other fitting parameters and more dependent on the overall scaling as there are less distinct features to fit.

6.3.7 Fixing scaling parameter

In order to treat the reflectivity data correctly a single scaling factor should be used for fits to all the samples measured on the same instrument under the same conditions. The scaling factor was fixed at 0.051 for a series of fits, the value fitted from the dPMMA on Si sample. Fits of the data for samples and line cuts through the data are shown in figures 6.24 to 6.43. Table 6.10 shows the results of the fitting parameters for all the samples with the scaling factor fixed.

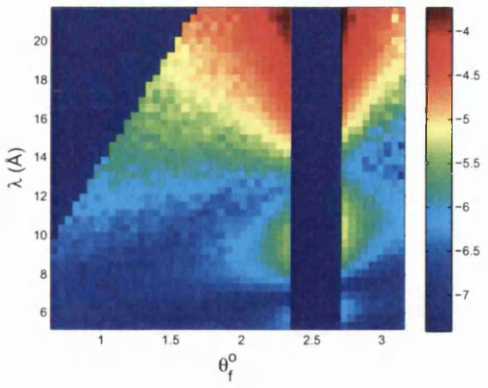

Figure 6.24: Experimental reflectivity for ~ 1000Å F8 on ~ 160Å dPMMA (counts are on a log scale)

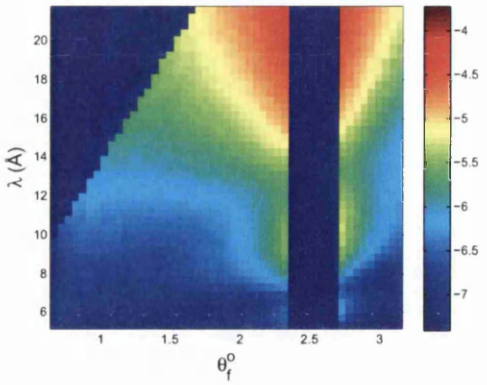

Figure 6.25: Model reflectivity for ~ 1000Å F8 on ~ 160Å dPMMA (counts are on a log scale)

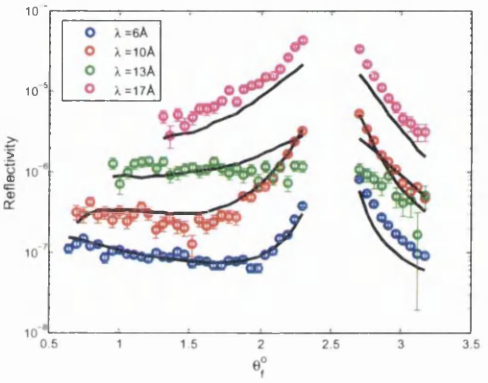

Figure 6.26: Cuts through λ showing for experimental reflectivity and model reflectivity for ~ 1000Å F8 on ~ 160Å dPMMA (counts are on a log scale)

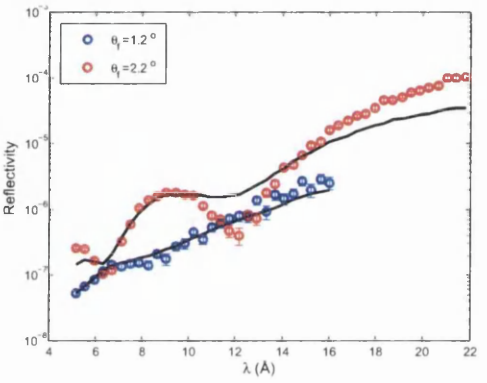

Figure 6.27: Cuts through θ_f showing for experimental reflectivity and model reflectivity for ~ 1000Å F8 on ~ 160Å dPMMA (counts are on a log scale)

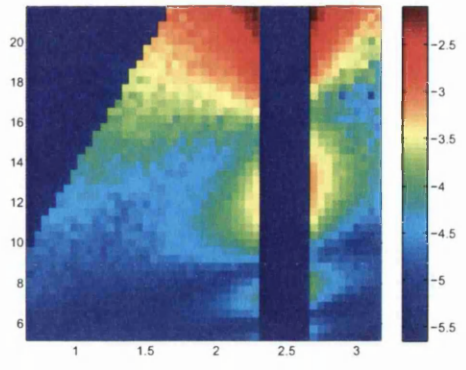

Figure 6.28: Experimental reflectivity for $\sim$ 1000Å F8 on $\sim$ 220Å dPMMA (counts are on a log scale) (note reflectivity not scaled by specular)

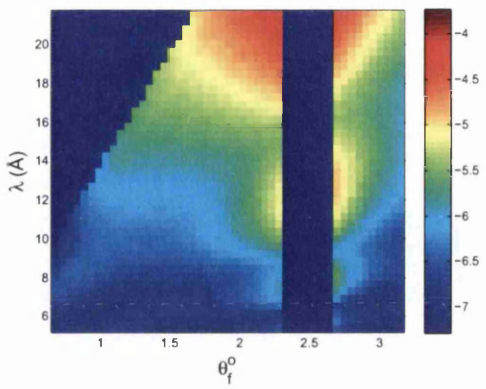

Figure 6.29: Model reflectivity for $\sim$ 1000Å F8 on $\sim$ 220Å dPMMA (counts are on a log scale) (note reflectivity not scaled by specular)

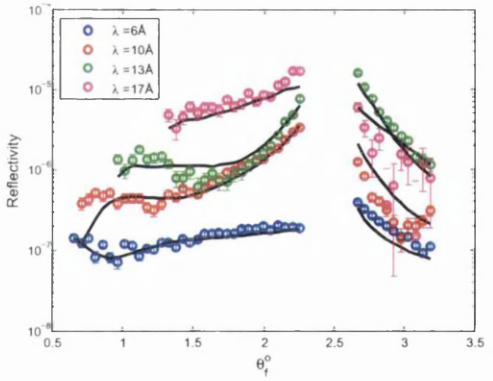

Figure 6.30: Cuts through λ showing for experimental reflectivity and model reflectivity for $\sim$ 1000Å F8 on $\sim$ 220Å dPMMA (counts are on a log scale)

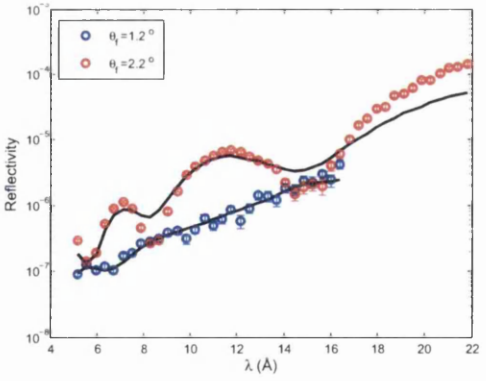

Figure 6.31: Cuts through θ_f showing for experimental reflectivity and model reflectivity for $\sim$ 1000Å F8 on $\sim$ 220Å dPMMA (counts are on a log scale)

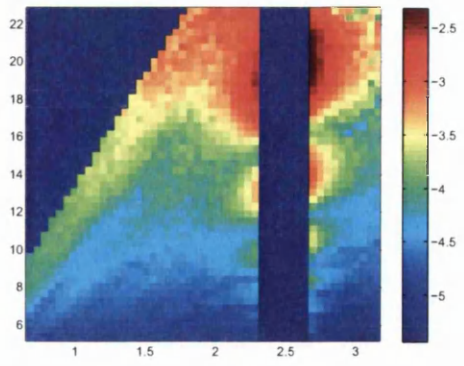

Figure 6.32: Experimental reflectivity for $\sim$ 1000Å F8 on $\sim$ 420Å dPMMA (counts are on a log scale)

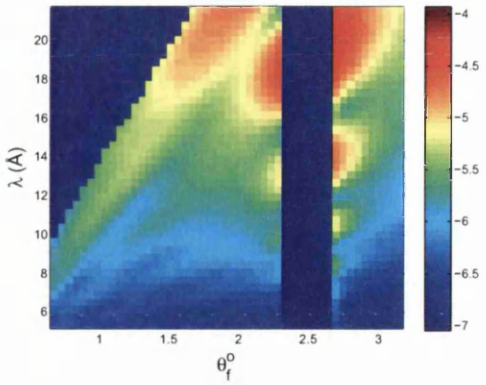

Figure 6.33: Model reflectivity for $\sim$ 1000Å F8 on $\sim$ 420Å dPMMA (counts are on a log scale)

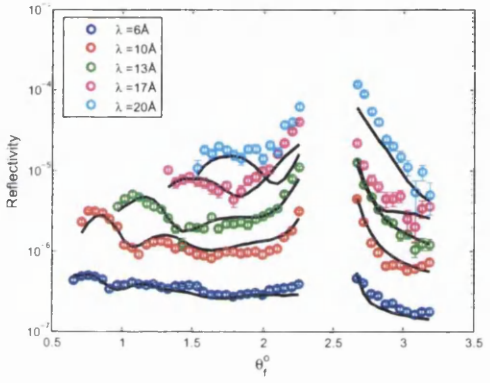

Figure 6.34: Cuts through λ showing for experimental reflectivity and model reflectivity for $\sim$ 1000Å F8 on $\sim$ 420Å dPMMA (counts are on a log scale)

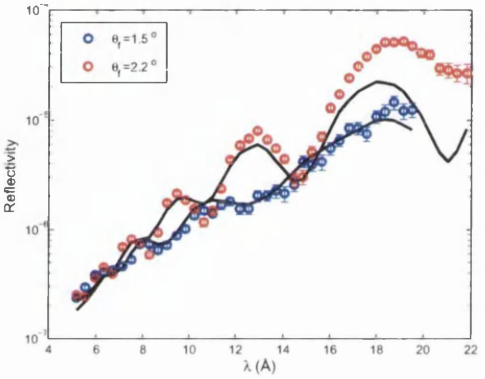

Figure 6.35: Cuts through θ_f showing for experimental reflectivity and model reflectivity for $\sim$ 1000Å F8 on $\sim$ 420Å dPMMA (counts are on a log scale)

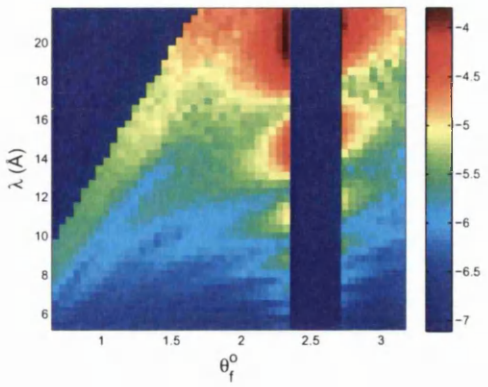

Figure 6.36: Experimental reflectivity for ~ 1000Å F8 on ~ 480Å dPMMA (counts are on a log scale)

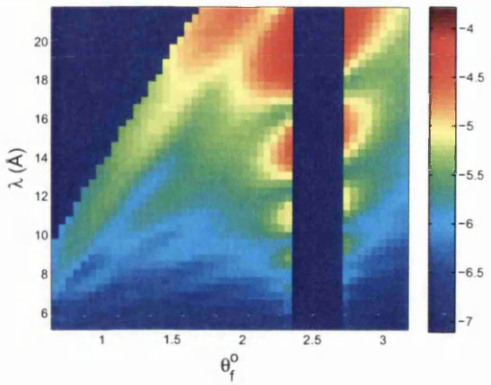

Figure 6.37: Model reflectivity for ~ 1000Å F8 on ~ 480Å dPMMA (counts are on a log scale)

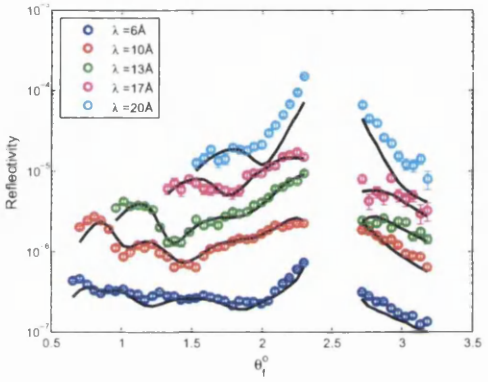

Figure 6.38: Cuts through λ showing for experimental reflectivity and model reflectivity for ~ 1000Å F8 on ~ 480Å dPMMA (counts are on a log scale)

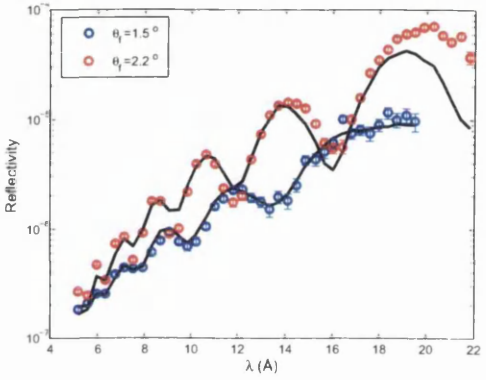

Figure 6.39: Cuts through θ_f showing for experimental reflectivity and model reflectivity for ~ 1000Å F8 on ~ 480Å dPMMA (counts are on a log scale)

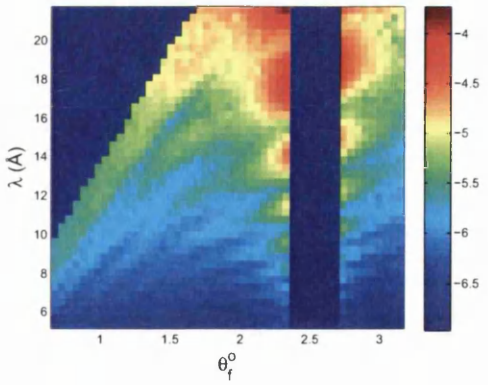

Figure 6.40: Experimental reflectivity for ~ 1000Å F8 on ~ 660Å dPMMA (counts are on a log scale)

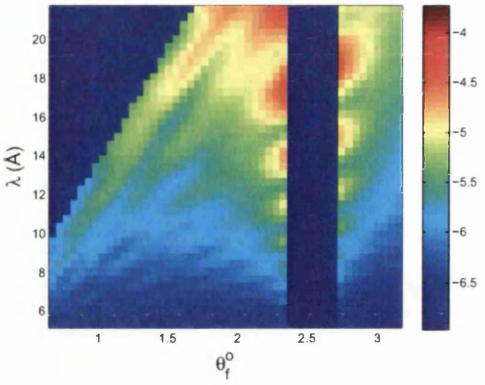

Figure 6.41: Model reflectivity for ~ 1000Å F8 on ~ 660Å dPMMA (counts are on a log scale)

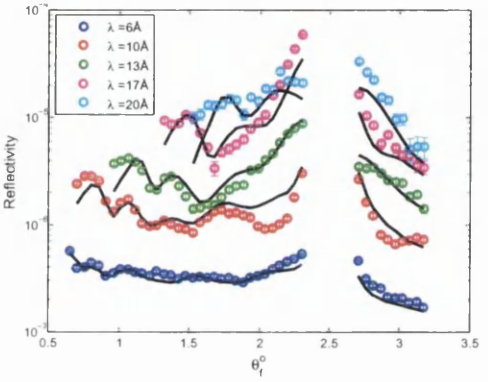

Figure 6.42: Cuts through λ showing for experimental reflectivity and model reflectivity for ~ 1000Å F8 on ~ 660Å dPMMA (counts are on a log scale)

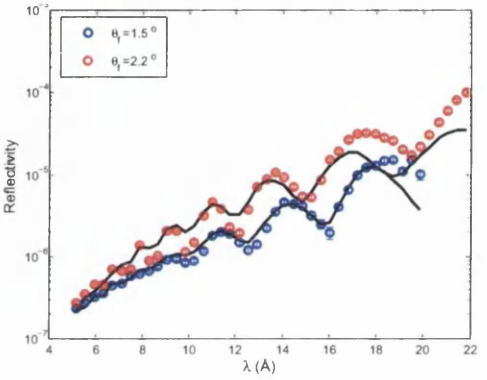

Figure 6.43: Cuts through θ_f showing for experimental reflectivity and model reflectivity for ~ 1000Å F8 on ~ 660Å dPMMA (counts are on a log scale)

Parameters fitted with fixed scaling factor					
	Sample number				
Parameter	**th1**	**th2**	**th3**	**th4**	**th5**
Thickness (Å)	161.79	215.06	418.88	480.69	650.21
σ_{tot} (Å)	20.64	20.68	30.23	26.66	28.59
σ_{lat} (Å)	13.07	13.28	29.06	20.74	25.51
σ_{int} (Å)	15.97	15.85	8.33	16.75	12.91
h	0.61	0.60	0.10	0.21	0.20
$\xi_{\perp}$ (Å)	197814.16	99956.63	153873.36	186313.76	164693.94
ξ_{lat} (Å)	16677.88	15247.72	71016.73	113202.07	60432.67
χ^2	11.20	8.64	5.83	7.86	19.67

Table 6.10: Parameters obtained from fitting off specular reflectivity data for $\sim$ 1000Å F8 on different thickness dPMMA bilayers on Si substrate, with the scaling factor fixed to 0.051

With the scaling factor fixed at 0.051 all of the experimental data can be fitted. There is a small increase in χ^2, which is to be expected as the number of fit parameters has been reduced. The roughness of the two thinner samples has decreased substantially from fixing the scaling factor. From these fits it is evident that σ_{int} and σ_{lat} both make significant contributions to the total roughness σ_{tot}. As a general trend σ_{tot} and σ_{lat} increase with film thickness, corresponding with the capillary wave theory for polymers at interfaces described in section 3.2. The intrinsic roughness σ_{int} does not seem to have any film thickness dependence.

The fits are good for all the samples at low wavelength. However at higher wavelength the intensity of the reflectivity is under estimated around $q_x = 0$. This can be seen in the θ_f cuts where the model reflectivity does not match the features of the experiment at high λ when θ_f approaches 2.5^o, the angle of incidence. This is clearly seen in the λ cuts for every sample. The highest λ value cut for each sample shows the fitted reflectivity not matching the experimental reflectivity well around $\theta_f = 2.5^o$, with the discrepancy more noticeable as the dPMMA film thickness increases. The fits become poorer as λ is increased and as θ_f becomes closer to θ_i.

In general the main features of the off specular reflectivity are represented well by the model. Examining the cuts in λ for the three thicker samples show that oscillations in the experimental data are matched, especially at the lower values of λ. Examining the θ/λ maps for all samples

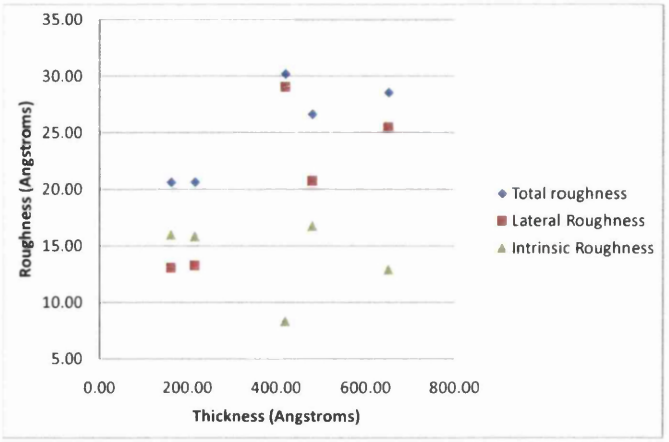

Figure 6.44: Plot of σ_{tot}, σ_{lat} and σ_{int} against thickness dPMMA for F8/ dPMMA bilayers fitted with the scaling factor fixed at 0.051

show that the lines of intensity at constant q_z and the Yoneda are replicated, again this is seen more clearly on the three thicker samples. The reflectivity around the Yoneda peak in the model decays away more rapidally when $\theta_f < \theta_c$ than in the experimental reflectivity. This is most likely due to background incoherent scattering in the experimental data which is not included in the model. Smaller oscillations which can more easily be seen on the thinner films (with smaller amplitude and wavelength) in the data are not matched well by the model. This is particularly evident in the cuts in λ for the two thinner samples. These smaller oscillations are probably caused by correlations between the F8/dPMMA interface and the air/F8 interface. Interface to interface correlation terms for these two interfaces were set to zero in the model, so the model cannot replicate the smaller oscillations. This was to reduce computation time. Including this correlation in the model reflectivity is simply a case of assigning the $\xi_\perp$ in the interface to interface correlation function for the interface pair to a value greater than 0.

The lateral correlation length ξ_{lat} is considerably smaller for the two thinner samples than the thicker samples. This agrees with the theory that long wavelength capillary waves in the capillary wave spectrum are suppressed by dispersive forces acting across the thin film. The thinner the dPMMA film the stronger the dispersion forces and the shorter the wavelength at which the capillary wave spectrum is cut off (see chapter 3). The length scale of correlations of the three thicker films may be cut off by the in plane coherence length of the instrument in this case. The values of ξ_{lat} for the thicker films corresponds to q_x contours under the resolution

broadened specular peak (see figure 6.13), where the off specular reflectivity is not fitted. This is discussed further in the next section. Therefore the fits will be less sensitive to ξ_{lat} for the thicker films than the thinner films, where the values of ξ_{lat} are well within the range of the off specular reflectivity data that has been fitted. The cut off length obtained from fitting the data ξ_{lat} should correspond with the dispersive cut off from suppression of the capillary wave spectrum a_{disp}. Rough calculations based on a PS/PMMA polymer interface show that the capillary wave cut offs ξ_{lat} are of the same order as those obtained from the fits of F8/dPMMA layers. The maximum cut off length of a capillary wave spectrum a_{disp} suppressed by dispersive forces as a function of film thickness is given by [84].

$$a_{disp}^2 = \frac{4\pi\gamma l^4}{A} \tag{6.1}$$

where l is the film thickness, γ is the interfacial tension and A is the Hamaker constant (described in section 3.2.3). The surface tension and Hamaker constant for an F8/ PMMA interface are unknown. The surface tension and Hamaker constant for a PS/PMMA interface are $3e-3J/m^2$ and $2e-20J$. It is likely that these will be similar to the F8/PMMA values, as the overall roughness σ_{tot} for both systems from specular neutron reflectivity is similar (see section 6.2.7) implying that the combination of intrinsic and capillary wave roughnesses are similar. Using the PS/PMMA values for γ and A

$$a_{disp}^2 \sim 2e18l^4 \tag{6.2}$$

For a film thickness of 220Å $a_{disp} = 6.8448e3$Å and for a film thickness of 650Å $a_{disp} = 5.9751e4$Å . This compares with ξ_{lat} values of $1.524e4$Å and $6.043e4$Å obtained from the fits providing further evidence of the validity of the surface being roughened by capillary wave fluctuations.

The cross correlation lengths are large compared with the thickness of the films, showing that the dPMMA interface and the underlying Si substrate are well correlated for all samples measured. The Hurst parameters h are notably higher for the thicker films than the thinner films. The reason for this is unclear at present.

Sensitivity analysis of ξ_{lat}

The effect of varying the lateral correlation length ξ for a thin and a thick sample was studied ($th2$ and $th4$). Figure 6.45 shows the effect of varying ξ_{lat} for a thin and a thick sample on the χ^2 parameter. The ξ_{lat} values are varied around the the value found from fits of the off specular reflectivity with the scaling factor fixed. All other parameters are fixed to the values from these fits.

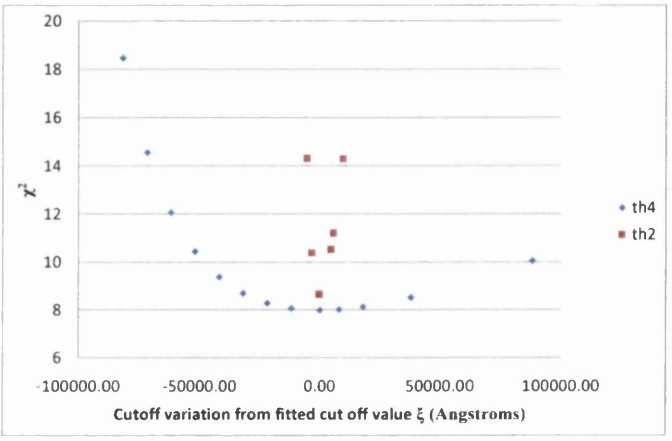

Figure 6.45: Effect of varying the cut off value ξ of χ^2 for samples $th2$ ($\sim$ 1000Å F8 on $\sim$ 220Å dPMMA) and $th4$ ($\sim$ 1000Å F8 on $\sim$ 480 Å dPMMA). The parameter ξ_{lat} is varied around the value obtained from fits of off specular reflectivity

It can be seen from the χ^2 values the quality of the fits of the thin sample is very sensitive to changes in ξ_{lat} whereas the thicker sample is less sensitive, which agrees with the discussion in the previous section. The thicker sample is far more sensitive to decreasing ξ_{lat} than increasing it. Figures 6.46 to 6.49 show cuts through the calculated reflectivity of the thinner of the two samples with ξ_{lat} varying and figures 6.50 to 6.53 show cuts through the calculated reflectivity of the thicker of the two samples with ξ_{lat} varying. From the cuts it is clear that the thicker sample is far less sensitive to changes in ξ_{lat} than the thinner sample. It can be seen that increasing ξ_{lat} increases the reflectivity close to $q_x = 0$ and decreases it away from $q_x = 0$. It has been found that the sensitivity of the fits to ξ_{lat} is dependent on the value of the Hurst parameter h. The thinner film has a relatively high value of $h =\sim 0.6$ whereas for the thinner film $h =\sim 0.2$. So it is the h value rather than the film thickness that is the cause of this sensitivity. The effect of the h value on describing the capillary wave spectrum is unclear at

present.

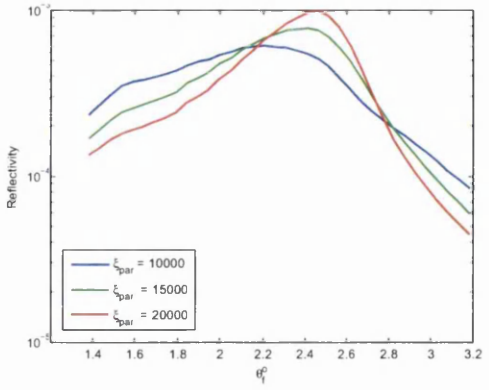

Figure 6.46: Cuts through λ = 13 Å for model reflectivity from sample th2 (dPMMA film thickness $\sim$ 220Å) with parameters given in table 6.10 except for ξ_{lat} which is varied

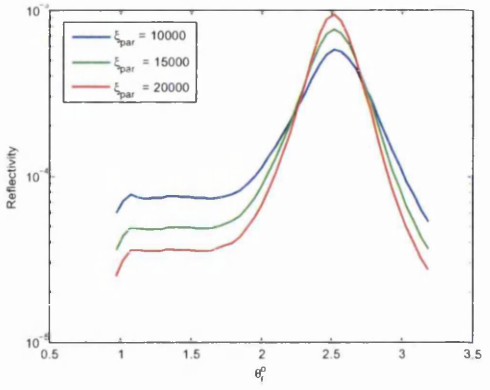

Figure 6.47: Cuts through λ = 18 Å for model reflectivity from sample th2 (dPMMA film thickness $\sim$ 220 Å) with parameters given in table 6.10 except for ξ_{lat} which is varied

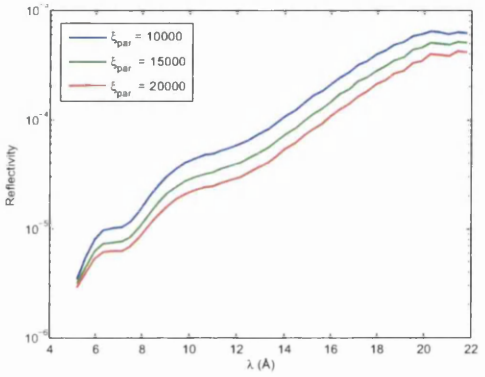

Figure 6.48: Cuts through θ_f = 2.2^o for model reflectivity from sample th2 (dPMMA film thickness $\sim$ 220Å) with parameters given in table 6.10 except for ξ_{lat} which is varied

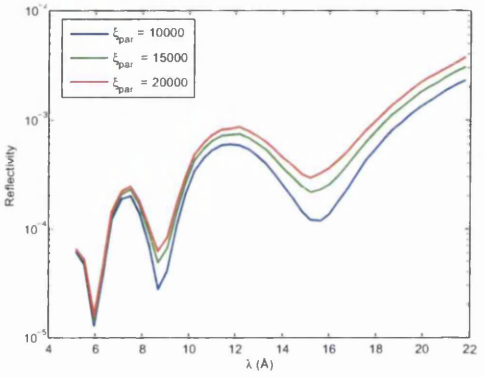

Figure 6.49: Cuts through θ_f = 2.2^o for model reflectivity from sample th2 (dPMMA film thickness $\sim$ 220Å) with parameters given in table 6.10 except for ξ_{lat} which is varied

Repeatability

Fits of sample th4 $\sim$ 1000Å F8 on $\sim$ 480Å dPMMA were repeated several times to check the robustness of the fitting algorithm. The fitting algorithm relies on generating a population of randomly generated vectors, containing possible solutions and 'breeding' and 'mutating' them over many iterations to minimise χ^2. Since the fitting process is stochastic, fits should be

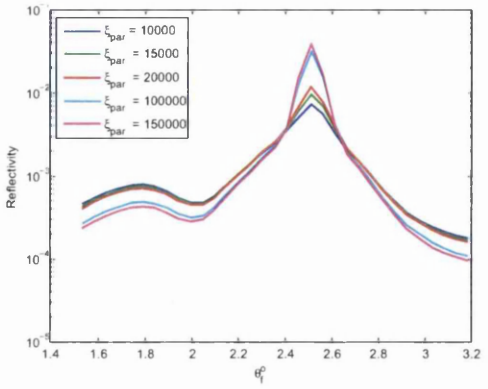

Figure 6.50: Cuts through $\lambda = 14$ Å for model reflectivity from sample th4 (dPMMA film thickness $\sim$ 480Å) with parameters given in table 6.10 except for ξ_{lat} which is varied

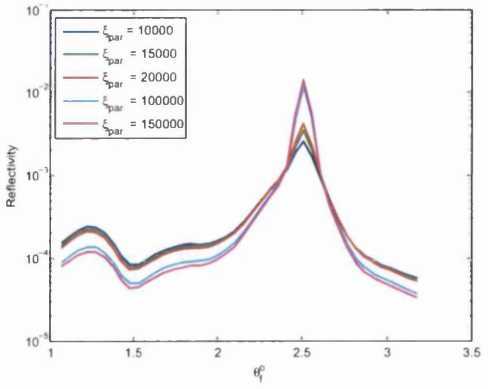

Figure 6.51: Cuts through $\lambda = 20$ Å for model reflectivity from sample th4 (dPMMA film thickness $\sim$ 480Å) with parameters given in table 6.10 except for ξ_{lat} which is varied

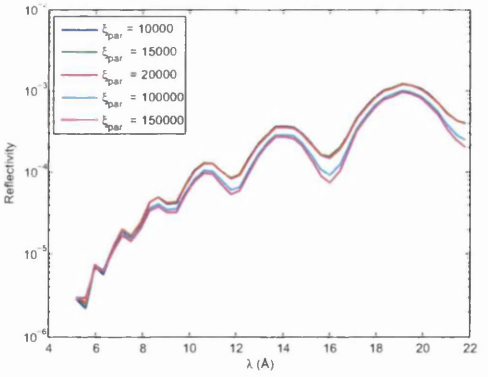

Figure 6.52: Cuts through $\theta_f = 2.2^o$ for model reflectivity from sample th4 (dPMMA film thickness $\sim$ 480Å) with parameters given in table 6.10 except for ξ_{lat} which is varied

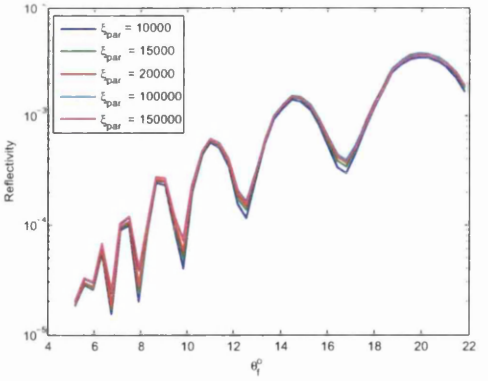

Figure 6.53: Cuts through $\theta_f = 2.2^o$ for model reflectivity from sample th4 (dPMMA film thickness $\sim$ 480Å) with parameters given in table 6.10 except for ξ_{lat} which is varied

repeated to check that the solutions found are repeatable. The results of repeated fits for one sample are shown in table 6.11.

Repeat fits sample th4												
Parameter	**1**	**2**	**3**	**4**	**5**	**6**	**7**	**8**	**9**	**10**	**Mean**	**Std dev**
Thickness	480.87	480.74	480.77	480.72	480.83	480.69	480.57	480.80	480.48	480.69	480.72	0.12
σ_{tot} (Å)	26.89	26.79	26.69	26.52	26.84	26.86	26.67	26.62	26.79	26.92	26.76	0.13
σ_{lat} (Å)	21.05	20.92	20.77	20.56	20.99	21.06	20.76	20.66	20.92	21.01	20.87	0.17
σ_{int} (Å)	16.73	16.74	16.75	16.75	16.72	16.67	16.74	16.79	16.74	16.83	16.75	0.04
h	0.21	0.21	0.21	0.21	0.21	0.21	0.21	0.21	0.21	0.21	0.21	0.00
$\xi_{\perp}$ (Å)	135661	186144	153596	188496	66723	189421	182439	185404	183097	149664	162064	38646
ξ_{lat} (Å)	124109	118971	113084	106389	123264	126339	114280	108391	118249	118591	117167	6617
χ^2	7.87	7.86	7.87	7.87	7.88	7.87	7.87	7.87	7.87	7.87	7.87	0.00

Table 6.11: Parameters obtained from repeated fits of the off specular reflectivity data for $\sim$ 1000Å F8 on $\sim$ 480Å thickness dPMMA bilayers on Si substrate

The standard deviation of the σ_{tot} and σ_{lat} are less than 0.2Å, showing that these numbers are robust. The standard deviation of $\xi_{\perp}$ is large, although the correlation length is greater than the thickness of the dPMMA by several orders of magnitude for each run. This shows that the lateral morphology of the F8/ dPMMA interface is well correlated with the underlying Si substrate. In the DWBA expression $\xi_{\perp}$ is contained in the expression $exp(|d|/\xi_{\perp})$ where d is the thickness of the layer. The Hurst parameter h has a standard deviation of 0, so achieving a good fit is strongly dependent on its value. The lateral cut off length ξ_{lat} has a fairly large spread of values. The fit is not very sensitive to ξ_{lat} as discussed in the previous section. The q_x region of the colourmap which corresponds to such a value of the cut off length is in the part of the plot around the specular peak, which is not fitted. It is therefore expected that the fits for this sample will be fairly insensitive to ξ_{lat} as shown in the previous section. The repeated fits show that the values obtained from fitting are repeatable, especially the roughnesses which are of most interest in this work.

6.3.8 Subtracting off specular scattering at $q_x = 0$ to find the 'true' specular reflectivity

The fall off of specular reflectivity for an ideal smooth sample with q_z is proportional to q_z^{-4}. However the fall off of off specular reflectivity is proportional to q_z^{-2} [88]. As q_z increases the ratio of off specular to specular reflectivity at $q_x = 0$ will increase. The rate of fall off of rough samples is related to the roughness by equation 2.69 with increased roughness resulting in a faster rate of fall off. If the off specular scattering at $q_x = 0$ becomes a significant percentage of the specular reflectivity then the off specular scattering at $q_x = 0$ must be subtracted from the data to obtain the true off specular reflectivity [79]. If this subtraction is not carried out then the apparent specular reflectivity will be higher than the true value. Fitting the specular data will result in roughness being obtained that is smaller than the true roughness. The correct way to treat the specular data therefore is to subtract the off specular data. However separating the specular and off specular reflectivities is difficult.

In the next section the specular and off specular reflectivities are fitted simultaneously. In this section initial calculations of the true total roughness σ_tot are made by subtracting the off specular contribution from the specular data. The off specular reflectivity to subtract was calculated using the parameters found from fitting the off specular data alone (see table 6.10).

As q_z gets higher the calculated off specular reflectivity represents an increasing fraction of the scattering at $q_x = 0$ the specular. The specular reflectivity with the off specular subtracted was therefore only fitted for a q_z range of $0-0.12$ Å^{-1}. Beyond $q_z = 0.12$Å^{-1} the data becomes noisy as the calculated off specular data is at some points greater than the experimental reflectivity data. No oxide layer was included in the fits and the roughness of the F8 and Si were fixed to the same parameters used in section 6.2.6. The roughnesses are tabulated in table 6.12 along with the roughnesses found for the specular reflectivity without the off specular reflectivity subtracted and no oxide layer in the fit. Figures 6.54 and 6.55 show fits for two of the samples.

From figures 6.54 and 6.55 it can be seen that there is an increase in the fall off of the reflectivity with increasing q_z caused by subtracting the calculated off specular reflectivity. It is clear that the contribution of the off specular to the specular is significant. Subtracting the off specular data generally results in an significant increase in the roughness (see table 6.12). However the total roughnesses are not as large as those obtained by fitting the off specular data alone. From looking at the specular fits without an oxide layer in section 6.2.6 it is clear that the fitted reflectivity is over estimated when compared with the experimental data at high q_z. The

Roughness from specular fits with off specular reflectivity subtracted			
Sample	**Thickness (Å)**	**σ_{tot} (Å) off spec not subtracted**	**σ_{tot} (Å off spec subtracted**
th1	166.37	12.79	15.135
th2	217.78	12.94	12.89
th3	428.71	15.045	19.73
th4	485.87	17.39	23.27
th5	662.88	16.34	27.04

Table 6.12: Roughnesses obtained from fits of specular data with off specular data at $q_x = 0$ subtracted

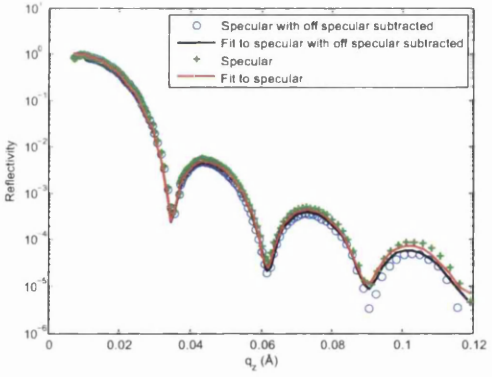

Figure 6.54: Fit of specular reflectivity with calculated off specular reflectivity subtracted and specular reflectivity without off specular reflectivity subtracted for $\sim$ 1000Å F8 on $\sim$ 220Å dPMMA (reflectivity is on a log scale)

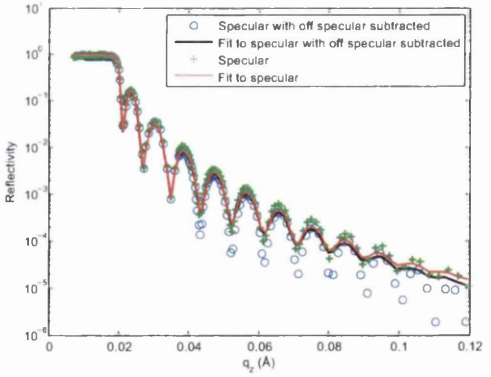

Figure 6.55: Fit of specular reflectivity with calculated off specular reflectivity subtracted and specular reflectivity without off specular reflectivity subtracted for $\sim$ 1000Å F8 on $\sim$ 660Å dPMMA (reflectivity is on a log scale)

model off specular reflectivity subtracted from the area around $q_x = 0$ from the experimental data becomes larger than experimental data at high q_z. This suggests that the off specular reflectivity calculated by the off specular model is too high for high q_z and low q_x values. In the case of the specular reflectivity it has been shown in section 6.2 that including an oxide layer in the model reduces the reflectivity at high q_z and better fits to the experimental data are obtained. This suggests that some allowance should be made for the oxide layer in the off specular model. However since the DWBA is a perturbation theory the oxide layer used in fitting the specular reflectivity with a roughness more than half the thickness will not be valid. The perturbation theory relies on the perturbation (in this case the roughness) being small. In further work the model could include a series of layers with sharp interfaces to model the oxide layer.

6.3.9 Combined specular and off specular

Fitting the specular and off specular data separately gives inconsistent results for the samples interfacial roughness. Given this inconsistency attempts to fit both specular and off specular reflectivity simultaneously are made. The specular and off specular reflectivity were fitted simultaneously using the model described in section 5.7. This will constrain the fits further and check the robustness of the roughnesses found from fitting the off specular reflectivity alone. Table 6.13 shows the fitted parameters and figures 6.56 to 6.75 show the fits and cuts through the fits.

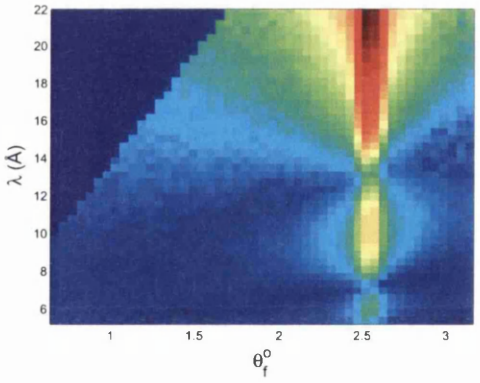

Figure 6.56: Experimental reflectivity for ~ 1000Å F8 on ~ 160Å dPMMA (counts are on a log scale)

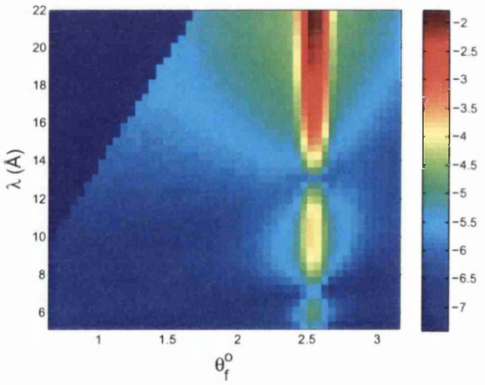

Figure 6.57: Model reflectivity for ~ 1000Å F8 on ~ 160Å dPMMA (counts are on a log scale)

Parameters fitted from combined specular and off specular fits					
	Sample number				
Parameter	**th1**	**th2**	**th3**	**th4**	**th5**
Thickness (Å)	162.50	215.10	423.52	482.23	647.18
σ_{tot} (Å)	16.60	17.13	17.8	22.20	26.47
σ_{lat} (Å)	9.59	10.47	15.405	15.46	25.69
σ_{int} (Å)	13.55	13.56	8.92	15.93	6.38
h	0.61	0.60	0.16	0.18	0.12
$\xi_{\perp}$ (Å)	200000.00	200000.00	1133.34	5126.09	200000
ξ_{lat} (Å)	12194.43	12100.70	3849.78	4789.24	19519.03
χ^2	38.50	49.30	82.04	148.29	806.49

Table 6.13: Parameters obtained from fitting combined specular and off specular reflectivity data for $\sim$ 1000Å F8 on different thickness dPMMA bilayers on Si substrate, with the scaling factor fixed to 0.051

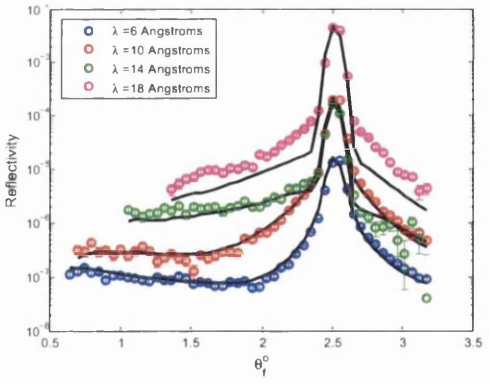

Figure 6.58: Cuts through λ showing for experimental reflectivity and model reflectivity for $\sim$ 1000Å F8 on $\sim$ 160Å dPMMA (counts are on a log scale)

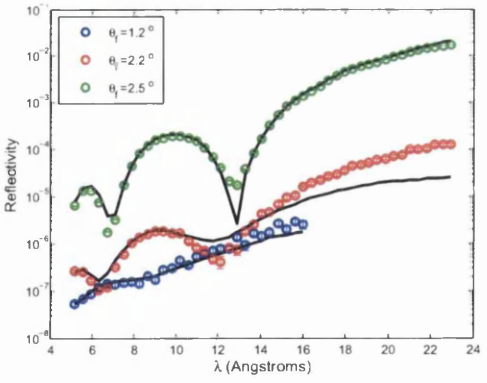

Figure 6.59: Cuts through θ_f showing for experimental reflectivity and model reflectivity for $\sim$ 1000Å F8 on $\sim$ 160Å dPMMA (counts are on a log scale)

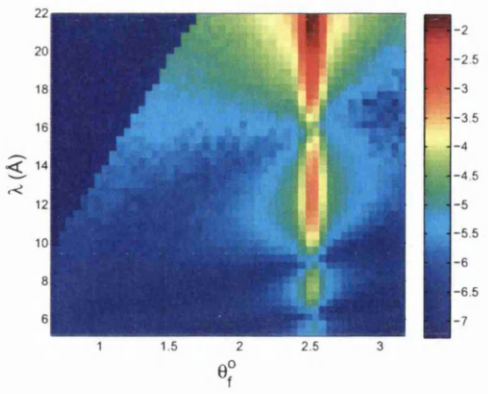

Figure 6.60: Experimental reflectivity for ~ 1000Å F8 on ~ 220Å dPMMA (counts are on a log scale)

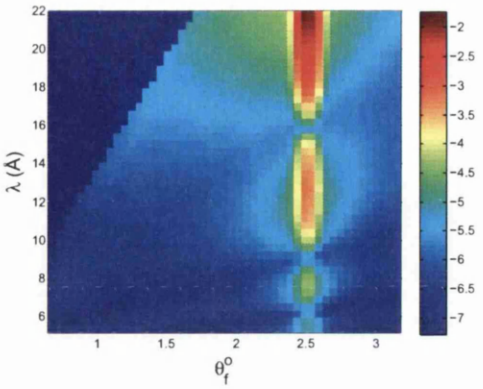

Figure 6.61: Model reflectivity for ~ 1000Å F8 on ~ 220Å dPMMA (counts are on a log scale)

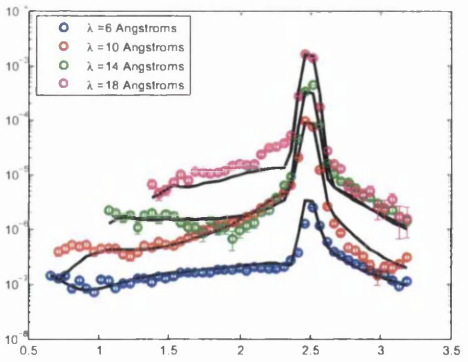

Figure 6.62: Cuts through λ showing for experimental reflectivity and model reflectivity for ~ 1000Å F8 on ~ 220Å dPMMA (counts are on a log scale)

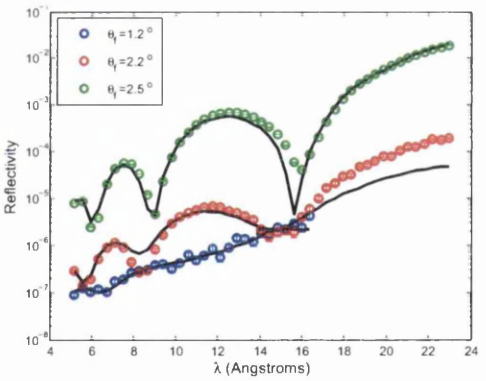

Figure 6.63: Cuts through θ_f showing for experimental reflectivity and model reflectivity for ~ 1000Å F8 on ~ 220Å dPMMA (counts are on a log scale)

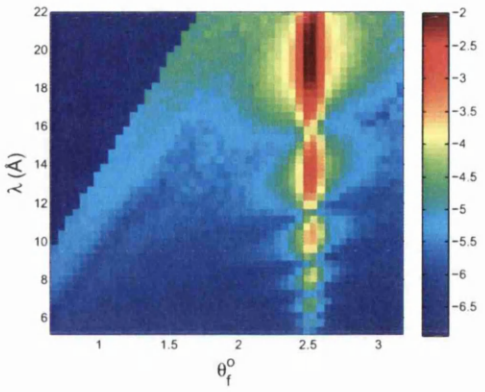

Figure 6.64: Experimental reflectivity for $\sim$ 1000Å F8 on $\sim$ 420Å dPMMA (counts are on a log scale)

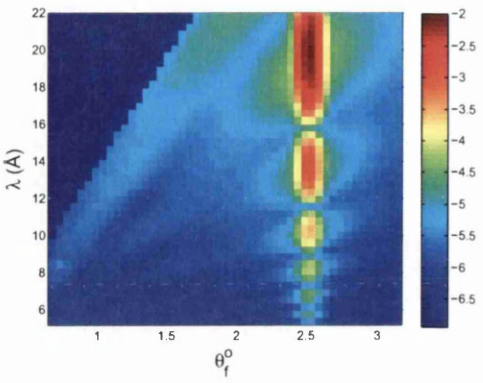

Figure 6.65: Model reflectivity for $\sim$ 1000Å F8 on $\sim$ 420Å dPMMA (counts are on a log scale)

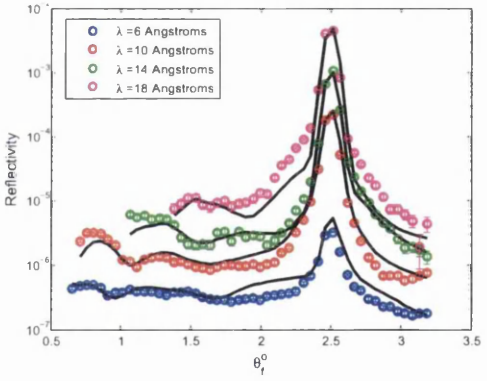

Figure 6.66: Cuts through λ showing for experimental reflectivity and model reflectivity for $\sim$ 1000Å F8 on $\sim$ 420Å dPMMA (counts are on a log scale)

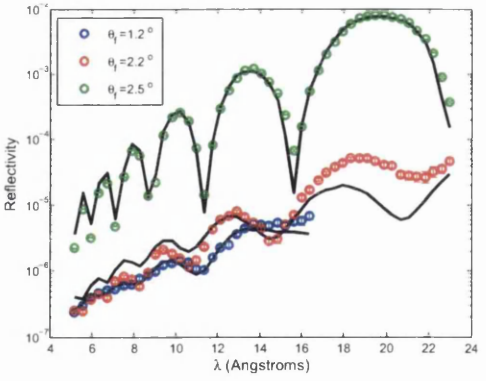

Figure 6.67: Cuts through θ_f showing for experimental reflectivity and model reflectivity for $\sim$ 1000Å F8 on $\sim$ 420Å dPMMA (counts are on a log scale)

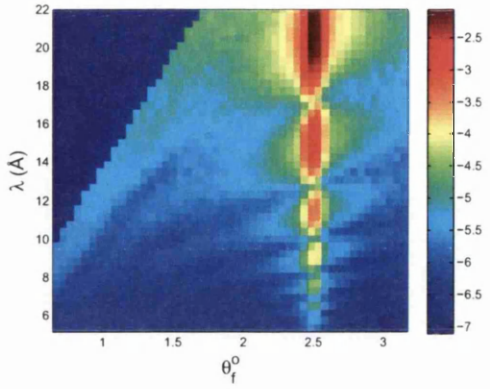

Figure 6.68: Experimental reflectivity for ~ 1000Å F8 on ~ 480Å dPMMA (counts are on a log scale)

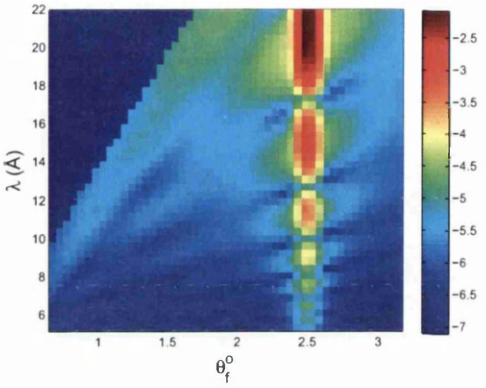

Figure 6.69: Model reflectivity for ~ 1000Å F8 on ~ 480Å dPMMA (counts are on a log scale)

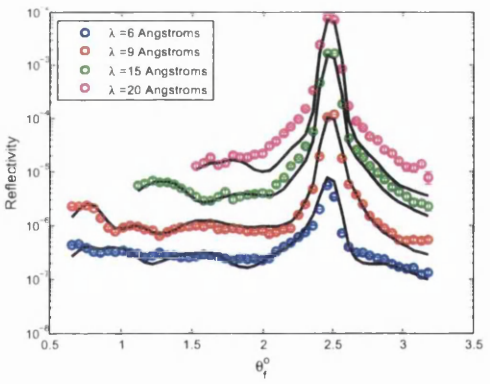

Figure 6.70: Cuts through λ showing for experimental reflectivity and model reflectivity for ~ 1000Å F8 on ~ 480Å dPMMA (counts are on a log scale)

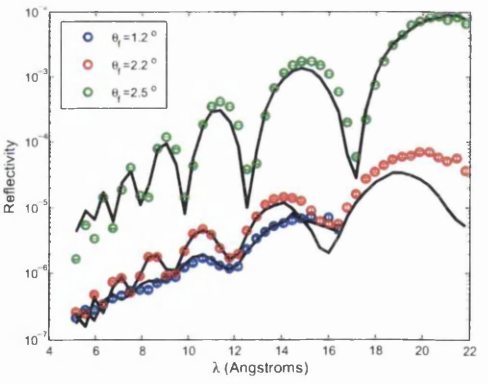

Figure 6.71: Cuts through θ_f showing for experimental reflectivity and model reflectivity for ~ 1000Å F8 on ~ 480Å dPMMA (counts are on a log scale)

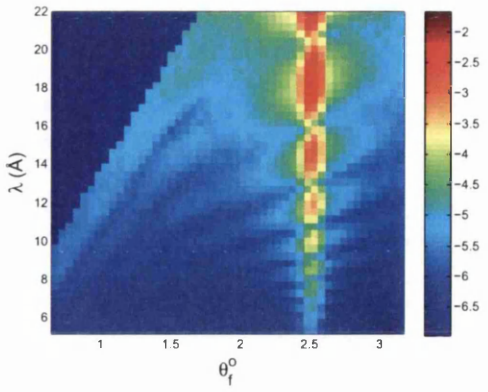

Figure 6.72: Experimental reflectivity for ~ 1000Å F8 on ~ 660Å dPMMA (counts are on a log scale)

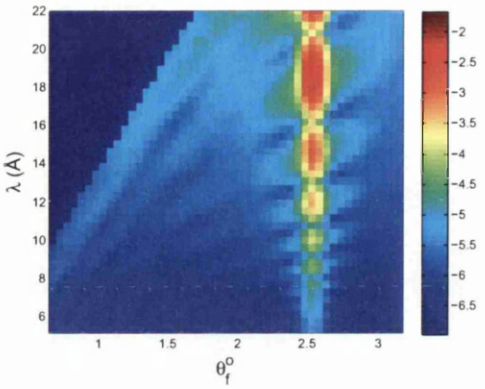

Figure 6.73: Model reflectivity for ~ 1000Å F8 on ~ 660Å dPMMA (counts are on a log scale)

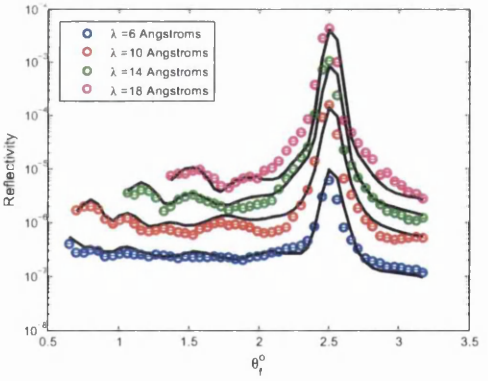

Figure 6.74: Cuts through λ showing for experimental reflectivity and model reflectivity for ~ 1000Å F8 on ~ 660Å dPMMA (counts are on a log scale)

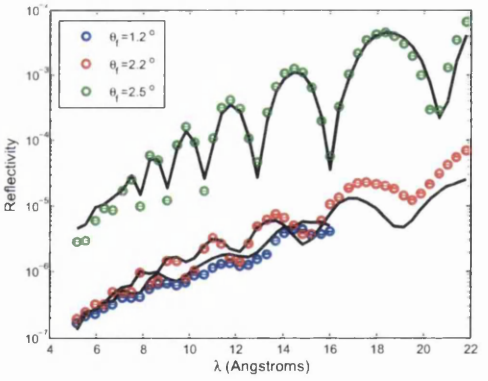

Figure 6.75: Cuts through θ_f showing for experimental reflectivity and model reflectivity for ~ 1000Å F8 on ~ 660Å dPMMA (counts are on a log scale)

The total roughnesses obtained from fitting the specular and off specular together lie between the fitted roughness values obtained when fitting the specular and off specular reflectivites separately. The trend of lateral and total roughnesses increasing with thickness is still present, while the intrinsic roughness has no dependence on dPMMA film thickness.. Comparisons between the roughnesses fitted by the different methods are shown in figures 6.76 to 6.78. From the cuts through constant θ_f t is clear that the specular ridge is fitted well. However the off specular data around $q_x = 0$ at the higher λ values is still clearly below the reflectivity of the experimental data.

The cut off ξ_{lat} is reduced by up to two orders of magnitude for the thicker samples when compared to the values obtained from fitting the off specular scattering alone. The Hurst parameter h is also reduced. Increasing ξ_{lat} increases the amount the region around $q_x = 0$ is peaked [70] [88]. The decrease in ξ_{lat} could be due to limitations of the fitting regime used in the model. Using the χ^2 (equation 5.6) value as the minimisation criteria will preferentially fit the areas with large numbers of counts over the areas with small numbers of counts. The χ^2 function divides the square of the difference between the model reflectivity and the experimental reflectivity by the square of the error bars. The error bars are the square root of the number of counts. For a pixel containing a large number of counts the error bar is a smaller fraction of the total counts than for a pixel containing a smaller number of counts. This can be seen by comparing the χ^2 values of the off specular fits with the combined specular and off specular fits. The region around $q_x = 0$ and the specular features have far higher counts than the regions where only the off specular data was fitted in section 6.3.7. Therefore the combined specular and off specular fits have far higher χ^2 values than the fits of the off specular region alone. By making ξ_{lat} small the model reduces the contribution to the scattering around $q_x = 0$ from the off specular component of the model. This area is then fitted mainly by the smeared specular component. This could explain why the values for σ_{tot} are smaller for the combined fits than for the off specular fit alone. The off specular component of the reflectivity around $q_x = 0$ is too low, so the smeared specular reflectivity around $q_x = 0$ increases to compensate. The rate of fall off of the specular component with increasing q_z is therefore lower than it should be, giving a higher value for σ_{tot} than expected. Since the fitting scheme acts to minimise the areas of high counts first it will preferentially use a σ_{tot} value that fits the specular component best, resulting in a value for σ_{tot} that is too low.

The interface to interface correlation length $\xi_\perp$ is also made smaller. Reducing this length acts to decrease the reflectivity contribution of the interface to interface correlation to the model

reflectivity. This will be most significant around $q_x = 0$. Around high wavelength the off specular reflectivity is still underestimated.

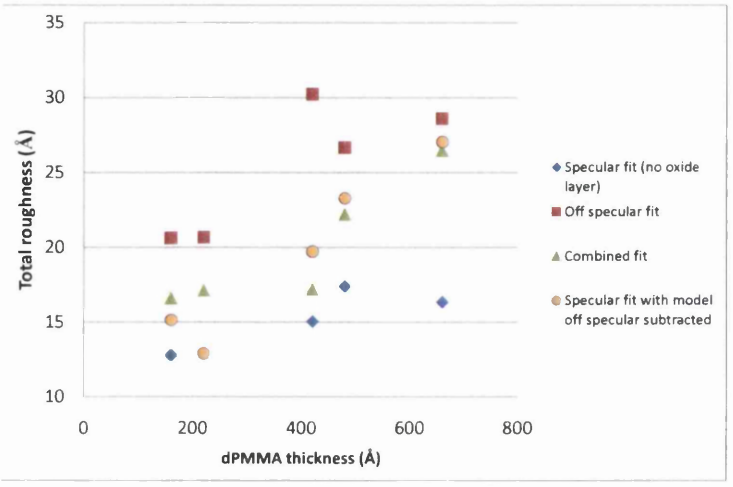

Figure 6.76: The total roughness values σ_{tot} calculated from specular data, off specular data and combined specular and off specular data and specular data with the calculated off specular data subtracted

Fixing ξ_{lat} and $\xi_{\perp}$ to the value calculated from fitting off specular reflectivity alone

Combined specular and off specular fits of the reflectivity for the two thickest samples with the lateral and interface to interface correlation lengths (ξ_{lat} and ξ_{bot}) fixed to the values found obtained from fitting the off specular data alone were made, with the other parameters used as fit parameters. The values of the fit parameters obtained from fits with ξ_{lat} and $\xi_{\perp}$ fixed are compared to the values of the fit parameters with ξ_{lat} and $\xi_{\perp}$ as fit parameters in table 6.14. Figures 6.79 to 6.82 show cuts through the data.

From examining the cuts it is clear that the fits are still reasonable with ξ_{lat} and $\xi_{\perp}$ fixed. The low values of h for both samples mean that the calculated off specular reflectivity is fairly insensitive to ξ_{lat}. The values for the roughnesses have not changed significantly, although the total roughness has decreased in both cases. This is as expected as off specular reflectivity around $q_x = 0$ is now larger due to the larger lateral correlation length ξ_{lat}. Reducing σ_{tot} reduces the contribution of the specular reflectivity in this region.

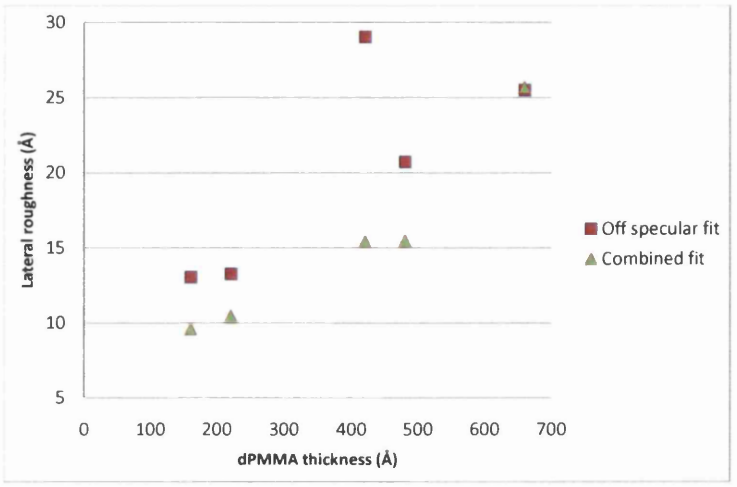

Figure 6.77: The lateral roughness values σ_{lat} calculated from off specular data and combined specular and off specular data

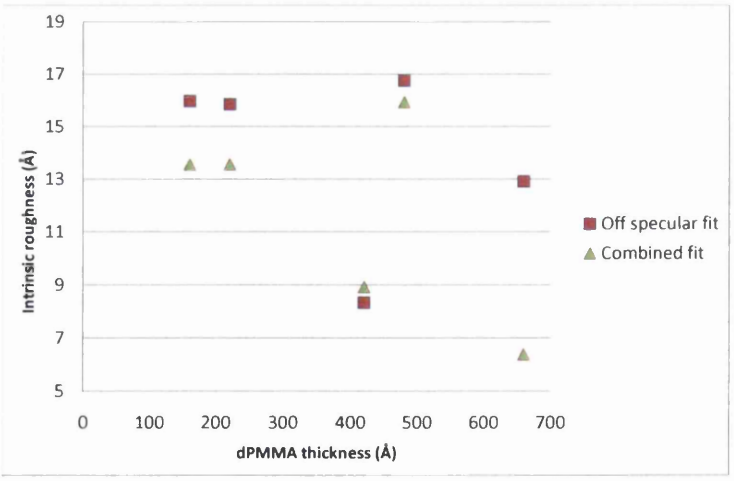

Figure 6.78: The roughness values from intrinsic mixing σ_{int} calculated from off specular data and combined specular and off specular data

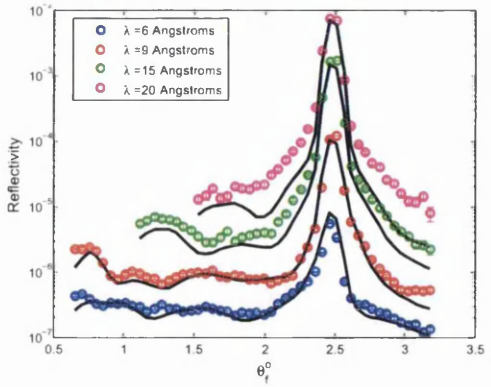

Figure 6.79: Cuts through λ showing for experimental reflectivity and model reflectivity for $\sim$ 1000Å F8 on $\sim$ 480Å dPMMA with ξ_{lat} and ξ_{bot} fixed to the values obtained from fitting off specular scattering alone (counts are on a log scale)

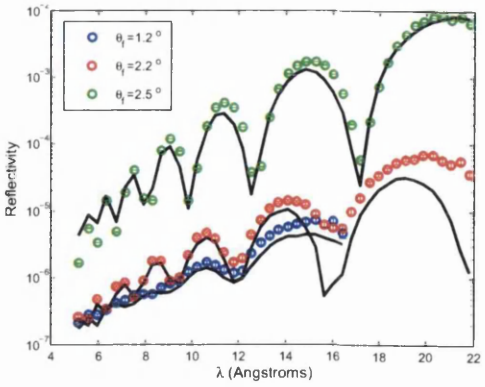

Figure 6.80: Cuts through θ_f showing for experimental reflectivity and model reflectivity for $\sim$ 1000Å F8 on $\sim$ 480Å dPMMA with ξ_{lat} and ξ_{bot} fixed to the values obtained from fitting off specular scattering alone (counts are on a log scale)

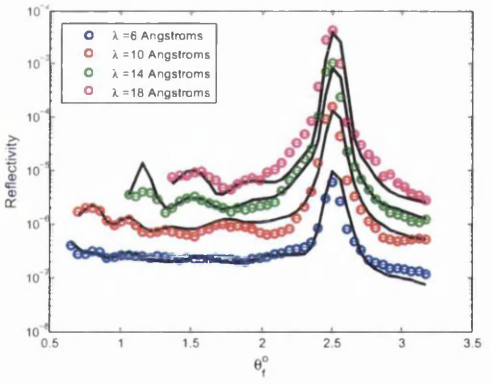

Figure 6.81: Cuts through λ showing for experimental reflectivity and model reflectivity for $\sim$ 1000Å F8 on $\sim$ 660Å dPMMA with ξ_{lat} and ξ_{bot} fixed to the values obtained from fitting off specular scattering alone (counts are on a log scale)

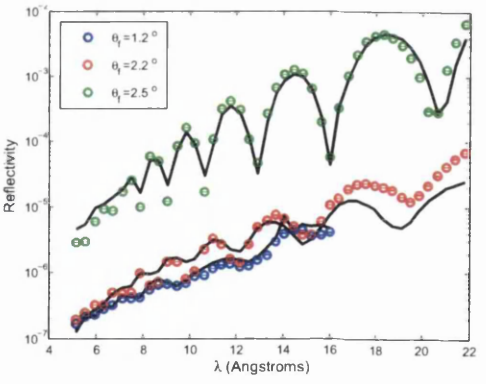

Figure 6.82: Cuts through θ_f showing for experimental reflectivity and model reflectivity for $\sim$ 1000Å F8 on $\sim$ 660Å dPMMA with ξ_{lat} and ξ_{bot} fixed to the values obtained from fitting off specular scattering alone (counts are on a log scale)

Parameters from combined specular/ off specular fits with ξ fixed				
Parameter	**Sample number**			
	th4 (ξ values fixed)	**th5** (ξ values fixed)	**th4** (ξ values fixed)	**th5** (ξ values fixed)
Thickness (Å)	482.11	482.23	646.63	647.18
σ_{tot} (Å)	23.38	22.20	27.07	26.47
σ_{lat} (Å)	18.46	15.46	25.30	25.69
σ_{int} (Å)	14.35	15.93	9.63	6.38
h	0.10	0.18	0.144	0.12
χ^2	164.10	148.29	819.25	806.49

Table 6.14: Parameters obtained from fitting combined specular and off specular reflectivity data for $\sim$ 1000Å F8 on different thickness dPMMA bilayers on Si substrate, with the ξ_{lat} fixed to value obtained from off specular fit

Adding a SiO_2 layer to the combined fits

A layer representing the SiO_2 layer discussed in section 6.2.2 is added to the combined specular and off specular model. It is not correct to use the model for the SiO_2 layer that is used for the specular fits as the off specular model is based on a perturbation theory and the roughnesses used in the specular reflectivity model were large compared with the thickness of the layer. Instead a thin layer is added inbetween the pure Si substrate and the dPMMA film to model the oxide layer. The model of the SiO_2 layer used for the specular is the best model that was found that could be used to consistently fit all the specular data. It may be different for the combined fits.

Ideally the parameters of this SiO_2 layer should be the same for each sample. However these values are not known and so they are used as fit parameters for fitting the reflectivity from each sample. The thickness of this layer was allowed to vary between 0 and 25Å. The scattering length density is allowed to vary between that of pure Si ($2.073e-6$Å^{-2}) and that of SiO_2 ($3.475e-6$ Å^{-2}). The roughness of the layer is allowed to vary between 0 and 5Å. The roughness, h parameter and lateral cut off of the Si substrate are set to be the same as that of the SiO_2 layer. The layer correlation is now between that of the SiO_2/ dPMMA interface and the F8/ dPMMA interface. It is expected that the fits will now be better as there are more fitting

parameters in the model. Table 6.15 shows the parameters obtained for the dPMMA layer and SiO_2 layer from fitting the combined specular and off specular reflectivity and figures 6.83 to 6.102 show the model to fits to the experimental reflectivity.

Parameters from combined specular/ off specular fits with SiO_2 layer					
	Sample number				
Parameter	**th1**	**th2**	**th3**	**th4**	**th5**
Thickness (Å)	161.44	214.56	423.11	480.65	647.95
σ_{tot} (Å)	16.43	17.41	18.09	21.89	26.36
σ_{lat} (Å)	10.00	10.35	15.33	14.89	24.68
σ_{int} (Å)	13.03	13.99	9.6	16.05	9.26
h	0.50	0.57	0.17	0.19	0.14
$\xi_{\perp}$ (Å)	80618.42	186580.54	130178.06	198947.32	129801.45
ξ_{lat} (Å)	16174.27	12950.95	7462.31	8695.83	25719.71
Thickness (Å) $Si0_2$	22.00	23.66	6.06	20.79	24.98
σ (Å) $Si0_2$	4.70	4.57	2.80	2.99	4.99
SLD $(Å)^{-2}$ $Si0_2$	2.47e-6	2.52e-6	2.54e-6	3.18e-6	2.66
χ^2	31.84	42.41	83.03	107.68	738.01

Table 6.15: Parameters obtained from fitting combined specular and off specular reflectivity data for $\sim$ 1000Å F8 on different thickness dPMMA bilayers on Si substrate, including a SiO_2 layer in the fitting model

From comparison of the combined specular and off specular fits with no oxide layer (table 6.16) it can be seen that the roughness values for both σ_{tot} and σ_{lat} have not changed significantly. The χ^2 values have decreased a small amount suggesting that the fits are slightly improved. The values for the thickness, scattering length density and roughness obtained for the SiO_2 layer are fairly consistent for all the fits. From visual inspection the fits are similar to the combined fits without the oxide layer included for all the samples. The roughness is between 2.8 and 5Å showing that the assumption of the roughness being 4.3Å is reasonable. The scattering length densities of the SiO_2 from the fits are closer to that of Si, than SiO_2 (apart from one sample). Scattering from the oxide layer that has been added to the model will be insignificant

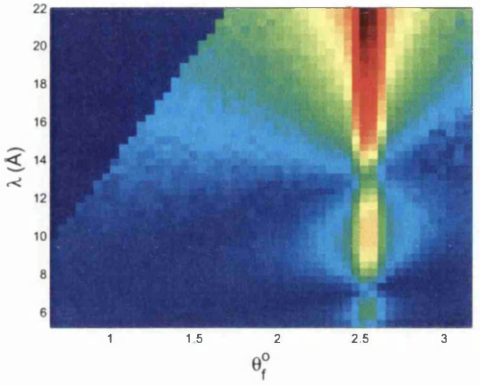

Figure 6.83: Experimental reflectivity for ~ 1000Å F8 on ~ 160Å dPMMA on Si substrate with SiO_2 layer (counts are on a log scale)

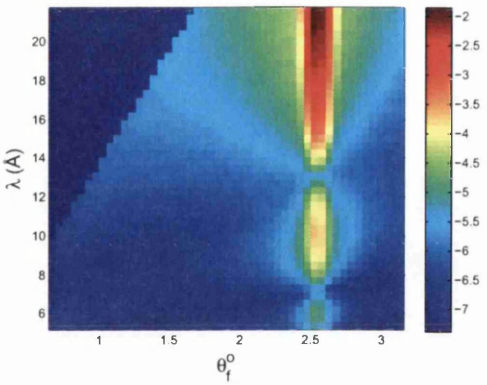

Figure 6.84: Model reflectivity for ~ 1000Å F8 on ~ 160Å dPMMA on Si substrate with SiO_2 layer (counts are on a log scale)

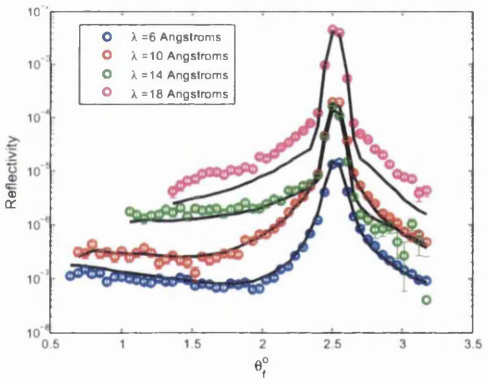

Figure 6.85: Cuts through λ showing for experimental reflectivity and model reflectivity for ~ 1000Å F8 on ~ 160Å dPMMA with SiO_2 layer (counts are on a log scale)

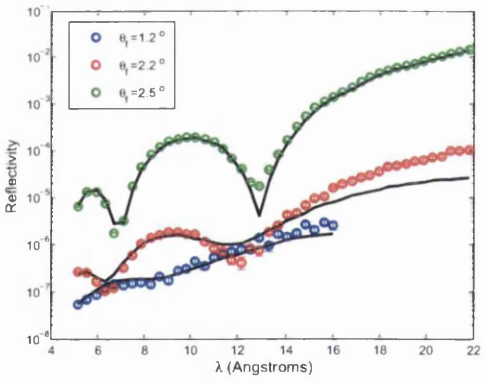

Figure 6.86: Cuts through θ_f showing for experimental reflectivity and model reflectivity for ~ 1000Å F8 on ~ 160Å dPMMA with SiO_2 layer (counts are on a log scale)

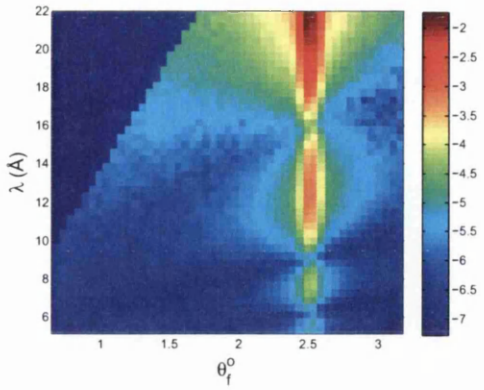

Figure 6.87: Experimental reflectivity for $\sim$ 1000Å F8 on $\sim$ 22Å dPMMA on Si substrate with SiO_2 layer (counts are on a log scale)

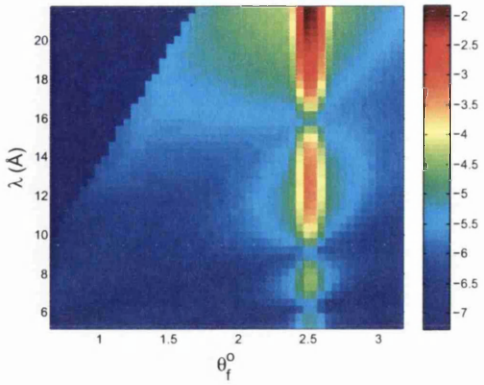

Figure 6.88: Model reflectivity for $\sim$ 1000Å F8 on $\sim$ 220Å dPMMA on Si substrate with SiO_2 layer (counts are on a log scale)

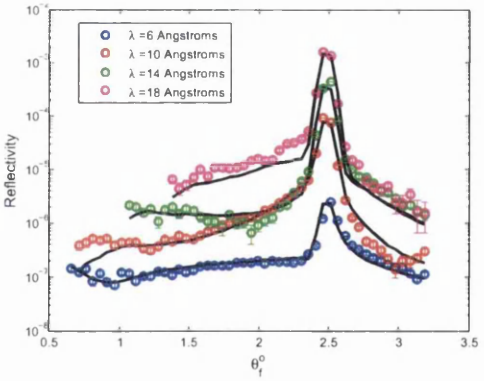

Figure 6.89: Cuts through λ showing for experimental reflectivity and model reflectivity for $\sim$ 1000Å F8 on $\sim$ 220Å dPMMA with SiO_2 layer (counts are on a log scale)

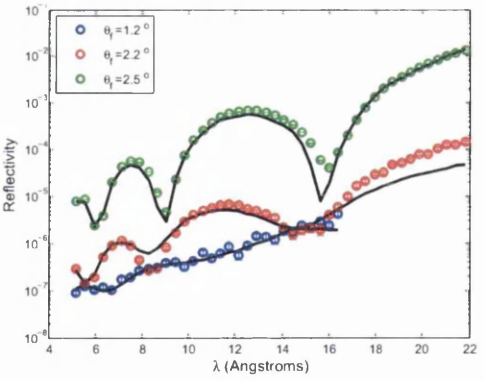

Figure 6.90: Cuts through θ_f showing for experimental reflectivity and model reflectivity for $\sim$ 1000Å F8 on $\sim$ 220Å dPMMA with SiO_2 layer (counts are on a log scale)

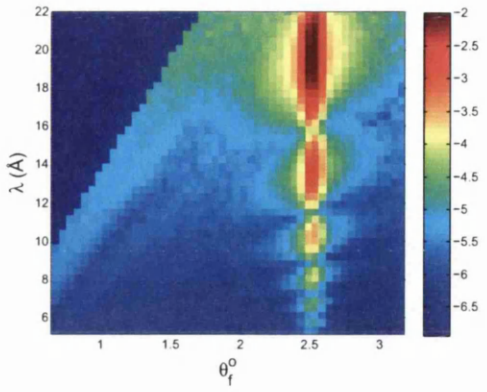

Figure 6.91: Experimental reflectivity for $\sim$ 1000Å F8 on $\sim$ 420Å dPMMA on Si substrate with SiO_2 layer (counts are on a log scale)

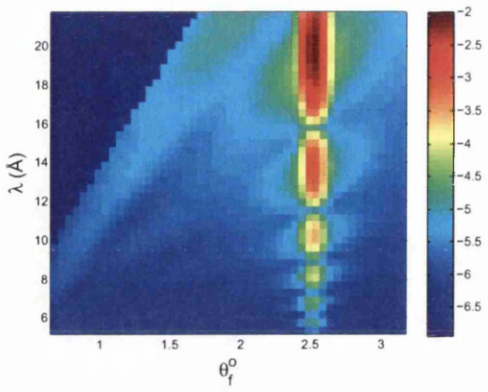

Figure 6.92: Model reflectivity for $\sim$ 1000Å F8 on $\sim$ 420Å dPMMA on Si substrate with SiO_2 layer (counts are on a log scale)

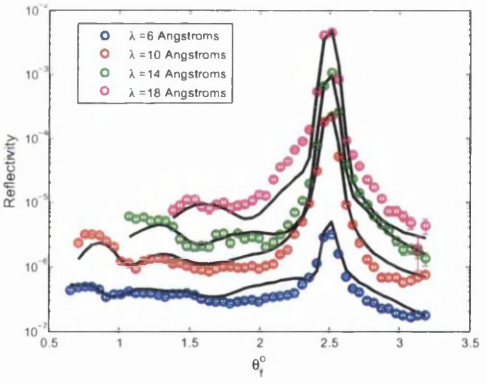

Figure 6.93: Cuts through λ showing for experimental reflectivity and model reflectivity for $\sim$ 1000Å F8 on $\sim$ 420Å dPMMA with SiO_2 layer (counts are on a log scale)

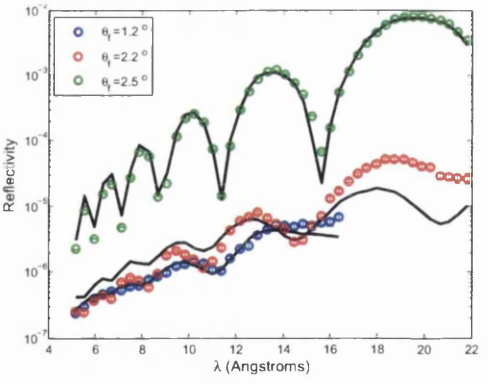

Figure 6.94: Cuts through θ_f showing for experimental reflectivity and model reflectivity for $\sim$ 1000Å F8 on $\sim$ 420Å dPMMA with SiO_2 layer (counts are on a log scale)

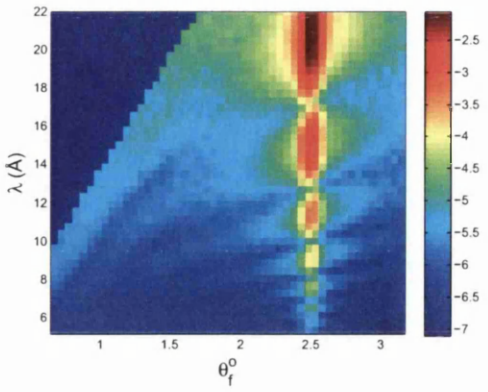

Figure 6.95: Experimental reflectivity for ~ 1000Å F8 on ~ 480Å dPMMA on Si substrate with SiO_2 layer (counts are on a log scale)

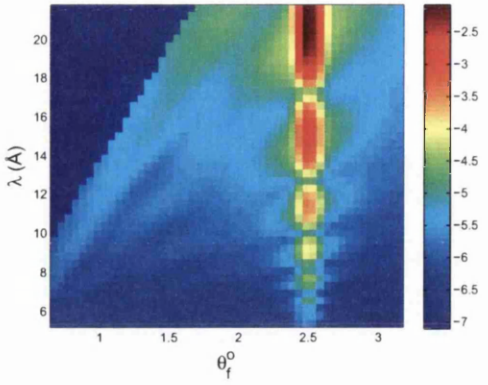

Figure 6.96: Model reflectivity for ~ 1000Å F8 on ~ 480Å dPMMA on Si substrate with SiO_2 layer (counts are on a log scale)

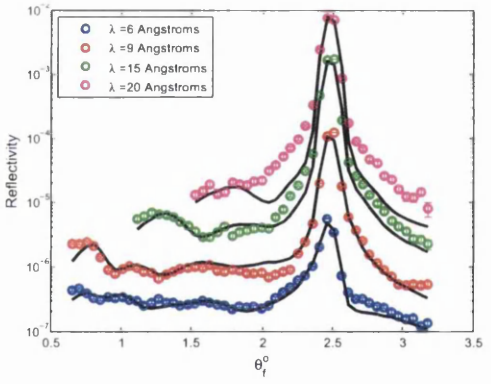

Figure 6.97: Cuts through λ showing for experimental reflectivity and model reflectivity for ~ 1000Å F8 on ~ 480Å dPMMA with SiO_2 layer (counts are on a log scale)

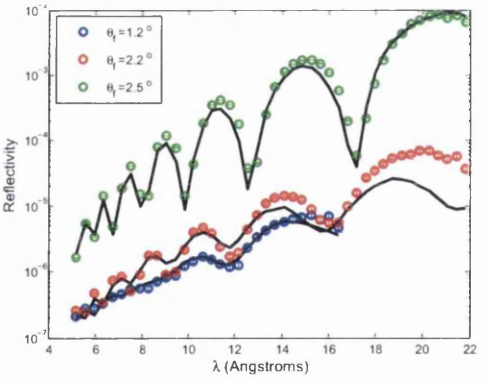

Figure 6.98: Cuts through θ_f showing for experimental reflectivity and model reflectivity for ~ 1000Å F8 on ~ 480Å dPMMA with SiO_2 layer (counts are on a log scale)

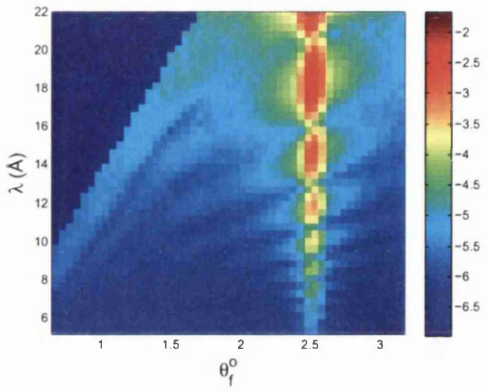

Figure 6.99: Experimental reflectivity for $\sim$ 1000Å F8 on $\sim$ 660Å dPMMA on Si substrate with SiO_2 layer (counts are on a log scale)

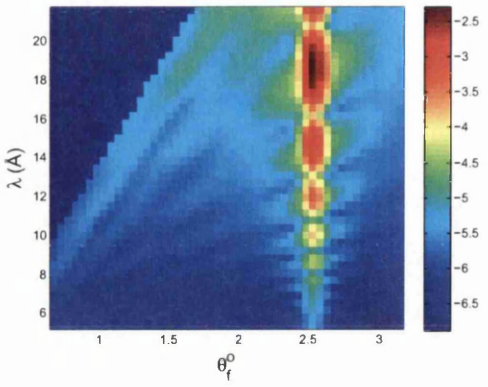

Figure 6.100: Model reflectivity for $\sim$ 1000Å F8 on $\sim$ 660Å dPMMA on Si substrate with SiO_2 layer (counts are on a log scale)

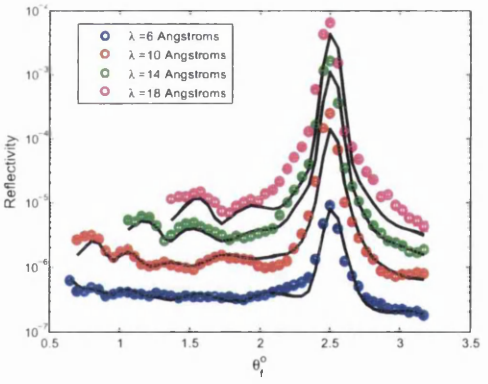

Figure 6.101: Cuts through λ showing for experimental reflectivity and model reflectivity for $\sim$ 1000Å F8 on $\sim$ 660Å dPMMA with SiO_2 layer (counts are on a log scale)

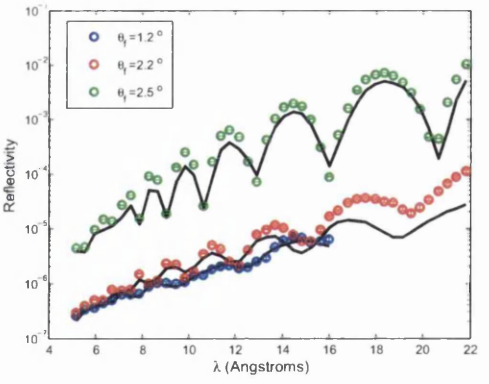

Figure 6.102: Cuts through θ_f showing for experimental reflectivity and model reflectivity for $\sim$ 1000Å F8 on $\sim$ 660Å dPMMA with SiO_2 layer (counts are on a log scale)

when compared with the scattering from the polymer/polymer interface, in the same way the scattering from the Si substrate will be. It is in the interface to interface correlation function between the polymer/polymer interface and the polymer/oxide interface where the oxide layer will have an affect. From equation 2.81 it can be seen that the roughness σ_{tot} (which is assumed to be equal to σ_{lat} for the oxide layer), the h parameter and the lateral correlation length ξ_{lat} of the oxide layer is included in determining the strength of the off specular reflectivity from the correlation between the polymer/polymer and the polymer/oxide interfaces. Allowing these parameters as variable fit parameters gives the model greater flexibility to scale the main contributions of the off specular reflectivity, the scattering from the polymer/polymer interface and the scattering from the correlation between the polymer/polymer interface and the polymer/oxide interfaces.

Changing the scaling factor

The scaling factor is assumed to be 0.051 from fitting the dPMMA single layer. To show that choosing the correct scaling factor is important the data is fitted with a different scaling factor. The scaling factor is set to 0.14 which is the average scaling factor of the two thinner samples from fits of the off specular scattering, to see if the data can still be fitted with a different scaling parameter. Table 6.16 shows the fitted parameters. Figures 6.103 to 6.106 show the experimental and model plots of the reflectivity for the two thickest samples with the scaling factor set to 0.14

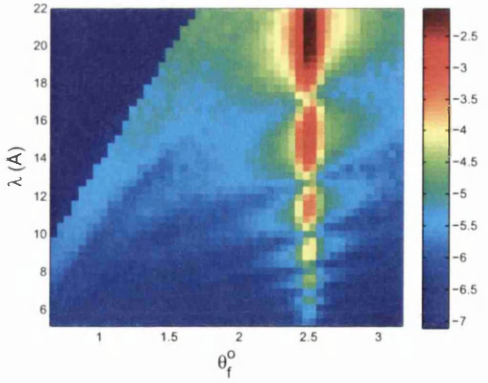

Figure 6.103: Experimental reflectivity for ~ 1000 Å F8 on ~ 480Å dPMMA (counts are on a log scale)

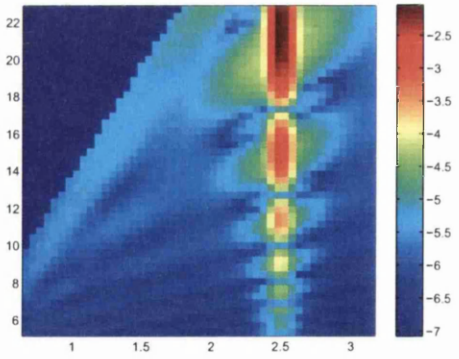

Figure 6.104: Model reflectivity for ~ 1000Å F8 on ~ 480Å dPMMA (counts are on a log scale)

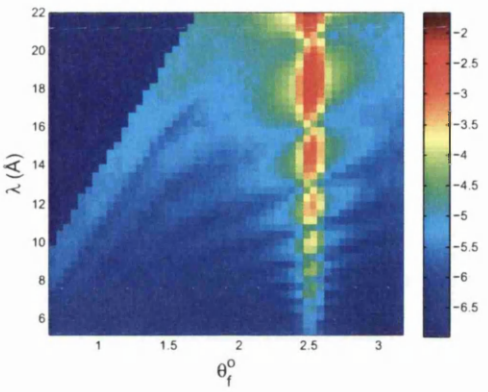

Figure 6.105: Experimental reflectivity for ~ 1000Å F8 on ~ 660Å dPMMA (counts are on a log scale)

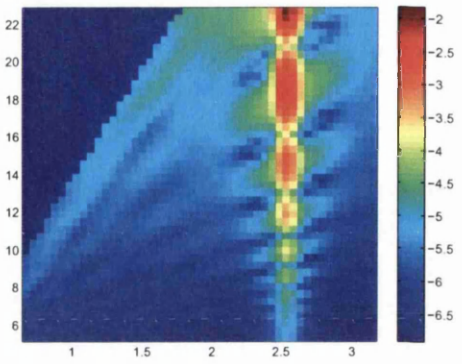

Figure 6.106: Model reflectivity for ~ 1000Å F8 on ~ 660Å dPMMA (counts are on a log scale)

Parameters from combined specular/ off specular fits with scaling factor of 0.14					
	Sample number				
Parameter	**th1**	**th2**	**th3**	**th4**	**th5**
Thickness (Å)	162.17	214.75	422.77	480.62	645.95
σ_{tot} (Å)	16.56	17.58	19.27	20.54	26.99
σ_{lat} (Å)	5.31	6.02	14.79	11.43	21.81
σ_{int} (Å)	15.68	16.52	12.36	17.06	15.89
h	0.59	0.61	0.05	0.20	0.077
$\xi_{\perp}$ (Å)	199999.98	200000.00	897.84	3955.20	74953.51
ξ_{lat} (Å)	9125.95	9356.17	1000.44	122.09	2005.92
χ^2	59.99	71.75	106.40	314.16	856.86

Table 6.16: Parameters obtained from fitting combined specular and off specular reflectivity data for ~ 1000Å F8 on different thickness dPMMA bilayers on Si substrate, with the scaling factor fixed to 0.14

It is clear that χ^2 increases compared with a scaling factor of 0.051 and the fits are not as good. This is evident from figures 6.104 and 6.106 showing the fitted data. These fits visually do not look as good as the fits with the other scaling factor. This shows that choosing the correct scaling factor is important. In the model around $q_x = 0$ there seem to be additional fringes not shown in the experimental data. This is due to the negative components of the layer correlation terms being larger in these areas than the scattering from the buried interface alone. This results in unphysical negative reflectivity. This effect is discussed in section 5.4. These negative reflectivites are shown to be positive on the plots as the absolute of the calculated reflectivity is plotted, because the plots are $log|R|$.

6.3.10 Reducing the λ range

Fits of the off specular reflectivity both including and excluding the specular reflectivity using the DWBA model result in good fits at low wavelength, but poorer fits at higher wavelength close to $q_x = 0$. To see if the values of the parameters obtained from the fits are reasonable, the λ range over which the reflectivity data is fitted is reduced to between 5 and 18Å. Table 6.17 shows the values of the fitted parameters for the reduced λ range against the fitted parameters for the original λ range.

From table 6.17 it can be seen that the reducing the λ range does change the values of the roughnesses slightly. However this is not a significant increase, and the intrinsic roughnesses are similar. The χ^2 values change and increase for the two thinner samples fitted, but significantly decreases for the thickest sample. Where the fit is good χ^2 is low. When reducing the maximum λ range both areas of low and high χ^2 contributions will be removed. The χ^2 value is dependent on the number of data points, which will decrease when the λ range is reduced. Therefore the overall χ^2 value of a fit may go up or down depending on the quality of the fits in all areas removed.

From all the fits conducted in this work it is clear that the model developed fails to match the off specular reflectivity around $q_x = 0$ for higher values of λ. The discrepancy between experiment and theory seems to increase as the film thickness increases. A possible cause is that the first order DWBA theory begins to break down in this region and second order terms should be introduced. Deriving such an expression would be an involved task and has not been carried out for the off specular component of scattering as far as the author is aware. Pynn et al [71] describe two regimes where the DWBA break down, when the cut off length is

Comparison of parameters from combined fits with different λ ranges						
Parameter	**Sample number**					
	th2 (λ range 5 – 22Å)	**th2 (λ range 5 – 18Å)**	**th4 (λ range 5 – 22Å)**	**th4 (λ range 5 – 18Å)**	**th5 (λ range 5 – 22Å)**	**th5 (λ range 5 – 18Å)**
Thickness (Å)	215.10	215.12	482.23	481.76	647.18	651.35
σ_{tot} (Å)	17.13	17.20	22.20	22.59	26.47	23.51
σ_{lat} (Å)	10.47	9.92	15.46	13.74	25.69	20.94
σ_{int} (Å)	13.56	14.05	15.93	17.93	6.38	10.69
h	0.60	0.63	0.18	0.30	0.12	0.17
$\xi_{\perp}$ (Å)	200000	200000	5126.09	4816.69	200000	199720.6
ξ_{lat} (Å)	12100.70	10265.64	4789.24	3614.63	19519.03	12716.59
χ^2	49.30	79.79	148.29	338.15	806.49	241.30

Table 6.17: Fits of off specular reflectivity over a reduced λ range

very large compared with the neutron wavelength and when the total roughness is too large. If the roughness is too large then the assumption that the wavefunction below an interface is a continuation of the wavefunction above the interface is not valid, as the wavefunction is extrapolated over too large a distance in z. From studies of the specular part of a second order DWBA formulation De Boer [23] states that for

$$\frac{\xi_{lat} k_{iz}^2}{|\mathbf{k}_i|} >> 1 \tag{6.3}$$

for the first order to DWBA formulation to be valid. Pynn et al [71] states that this criteria is also applicable to the off specular part of the DWBA formulation, however no derivation is shown. As far as the author is aware there are no examples in the literature which describe the q_x dependence of the validity of the DWBA. From initial examination of our results it would seem that the fits fail in the region where $2\pi/q_x$ is large. From figure 6.13 it can be seen that with increasing λ that the contours of $2\pi/q_x$ curve away from $q_x = 0$. If there is a region that the DWBA is invalid for along q_x contours that corresponds with a large value of $2\pi/q_x$ then it would affect a larger range of the scattering angle as λ increases. At lower wavelengths the region would be underneath or close to the smeared specular peak at low λ. This is shown in

figure 6.107.

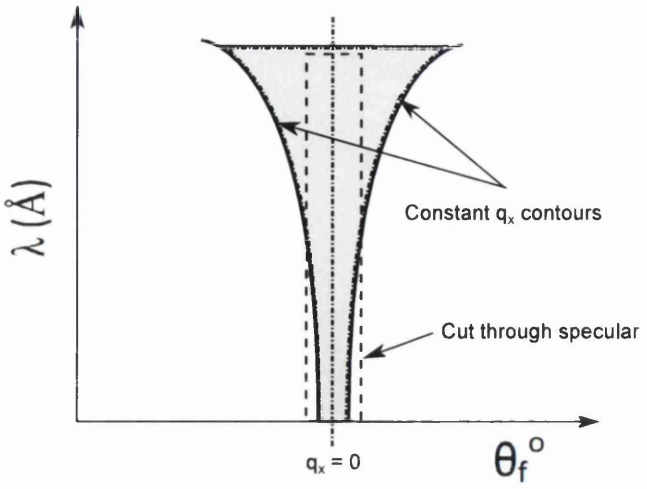

Figure 6.107: Diagram to show the regions where the DWBA for off specular reflectivity may break down if there is a dependence on $2\pi/q_x$

From looking at the results of the off specular fits this is a possible explanation for the reduced quality of the fits as λ increases and away from the specular region the model fits the data well. A detailed study of the theory would need to be implemented to verify or disprove this hypothesis. Workers fitting x-ray data using the DWBA have not reported this problem. This could be due to x-ray experiments using shorter wavelengths than neutrons and probing smaller length scales, therefore not reaching values of $2\pi/q_x$ where these discrepancies in the fits are noticeable.

Another possible reason for the poor fits at higher wavelengths could be due to the height to height correlation function used in this work being inadequate to explain the behaviour of the interface. Polyfluorines such as F8, in a nematic crystalline phase, form domains of orientated polymer chains measuring approximately 1 to 2 microns across [5]. It is therefore possible that the height to height correlation statistics of the sample are different on different length scales. To check this the sample should be re-measured using a different wavelength range allowing different length scales to be probed. Then the model can be fitted in both regimes, to see if different height to height correlation functions need to be used in order to fit the reflectivity on different lengthscales. Using a sample where there is no domain structure of either of the polymers could also be used to see if better fits of the reflectivity can be achieved using a single height to height correlation function.

6.3.11 Comparisons with self consistent field theory (SCFT)

The annealing temperature for the bilayer samples is above the glass transition temperature (T_g) for the PMMA layer and above the melt temperature (T_M) of F8 so the system is at thermodynamic equilibrium and SCFT calculations can be applied. The Flory Huggins χ parameter can be calculated from the width w of the interface between two polymers (see section 3.1.6). The interfacial width is given by $w = \frac{\sigma_{int}}{\sqrt{(\pi/2)}}$ where σ_{int} is obtained from the fitting. There is no systematic variation in σ_{int} with film thickness. The intrinsic width σ_{int} due to mixing at the molecular level is calculated from the fits of reflectivity data to be between ~ 7 and ~ 17 Å. This range will be used in the SCFT calculations. From the intrinsic width an estimate for the Flory Huggins χ parameter can be calculated. At an interface between two polymer pairs it is the stiffer polymer that dominates the dynamics of mixing [49]. In the case of the F8/dPMMA system the F8 conjugated polymer will be much stiffer. The statistical segment length b and the monomer length a of F8 are ~ 3.7nm and 0.795nm respectively [34]. As stated in chapter 3 the intrinsic interfacial width for finite molecular weight polymers is given by

$$w \sim \frac{b}{(6\chi)^{1/2}}) \left[\frac{3}{4}\left(1 - \frac{2}{\chi N}\right) + \frac{1}{4}\left(1 - \frac{2}{\chi N}\right)^2 \right]^{-1/2} \tag{3.24}$$

Given that the degree of polymerisation of an F8 molecule is typically between 90 (from M_n) and 258 (from M_w) (see section 4.1), for w between 7Å and 17Å results in a range of χ between ~ 0.8 and 5 (referenced to the size of an F8 monomer). To see if the polymers are in the flexible regime where equation 3.24 is valid an internal consistency check is performed using the $\kappa\chi$ value, where κ is the bending modulus defined as [62].

$$\kappa = \frac{b^2}{2a^2} \tag{3.25}$$

The value of κ for F8 is 10.8 and the range of $\kappa\chi$is between $6.38 - 151.7$. In the regime $\kappa\chi >> 1$ the polymer chains are too stiff to be modelled as flexible chains and the SCFT theory for flexible chains result for the interfacial width is invalid. The polymer molecules can become almost rod like in structure on the lengthscale of the intrinsic width and a random walk cannot be used to describe them. This has implications for the packing of molecules at the interface as the mixing will no longer be random. The persistence length of the polymer chains will be of the same order as the intrinsic width. The χ values calculated by expression 3.22 are not valid,

as they are only valid for polymers described by a random walk. Morse and Fredrickson [62] show that the interfacial width for two polymers with stiff chains would be a factor of $1/(\kappa\chi)^{1/2}$ narrower than that for flexible chains with the same χ parameter value. Multiplying expression 3.22 for the intrinsic width of the interface by this factor and rearranging for χ

$$\chi = \left(\frac{b}{\sqrt{6}\kappa w}\right)^{2/3} \tag{6.4}$$

Putting the values of σ_{int} between 7Å and 17Å results in a range of values for χ between ~ 0.2 and ~ 0.3. The value for $\kappa\chi$ is between ~ 2 and ~ 3 so is greater than 1. The system is in the regime where there is significant orientation of the polymer conformation in the plane of the interface.

6.3.12 Conclusions

In this section time of flight off specular neutron reflectivity data from a conjugated/amorphous polymer bilayer system has been fitted using a model based upon the DWBA. Values of the intrinsic σ_{int} and lateral σ_{lat} contributions to the total roughness σ_{tot} have been extracted. Both contributions are shown to be significant. The lateral roughness σ_{lat} is dependent on the thickness of the polymer films and saturates when the film reaches a certain thickness. This corresponds with the theory that the interface between immiscible polymer pairs is broadened by capillary waves and the roughness due to capillary waves will increase as a function film thickness. The saturation of σ_{lat} is thought to be due to the wavelengths of capillary waves in the system being larger than the coherence length of neutrons, so these larger wavelengths are not detected. The intrinsic roughness σ_{int} is caused by mixing of polymers at a molecular length scale. From the results it seems there is no dependence on film thickness. Fits of the off specular reflectivity alone show that thinner films have lower lateral cut off length ξ_{lat} than thicker films which is also predicted by the theory that the interface is broadened by capillary wave fluctuations.

Fitting the off specular data results in values of the total roughness that are greater than the values found by fitting the specular data alone. This is due to off specular scattering at $q_x = 0$. Neglect of this scattering leads to a value of σ_{tot} that is lower than the true value, due to the lower rate decay of the specular reflectivity due to the off specular being present. Separating out the specular and off specular scattering contributions is difficult. Techniques to

separate the contributions and fit both specular and off specular data simultaneously are used in this chapter. This allows the complete reflectvitiy data set from a TOF neutron reflectivity experiment to be fitted. A larger value of the total interfacial roughness is obtained from fitting combined specular and off specular data than by fitting specular data alone.

Using the values of σ_{int} extracted from the fits and SCFT predictions it has been shown that the F8 polymer chains are too stiff to be modeled as flexible polymer chains. It suggests that the persistence length of the F8 polymers is on the same length scale as the interfacial width and that the polymer chain configurations at the interface are not randomly orientated, but have some order. Further experimental work using techniques where the orientation of polymer chains at the interface are measured could be used to verify this.

Fits of the model to experimental data around $q_x = 0$ at the higher wavelengths were poor. This could be due to the theory breaking down in this region. Another possible explanation is that the height to height correlation function used is inadequate to explain the behaviour of the interface and different height to height correlation functions are required to model the interface on different length scales.

Chapter 7

Study P3HT/PCBM Interfaces using Specular and off Specular Neutron Scattering

7.1 Organic solar cells

Organic solar cells are the subject of a large amount of research due to potential properties such as low manufacturing costs, high production throughput and flexible devices. However, they are inefficient when compared to inorganic devices.

Organic solar cells typically involve a mixture of two semi conducting organic materials, one which will act as an electron donor and one that will act as an electron acceptor. A photon is absorbed by a molecule of either material and an electron is excited from the HOMO to the LUMO creating an exciton. Due to high binding energies in organic semi conductors excitons are usually separated at the interface between donor and acceptor materials, leaving a hole in the HOMO of the donor and an electron in the LUMO of the acceptor. The electron is transferred through the acceptor material to a cathode, the hole is transferred to an anode and current is generated [99]. For the charge to be separated in this way the exciton needs to reach the interface before the electron and hole can recombine. The lifetime of of an exciton is less than one picosecond [57]. An exciton diffusion coefficient of $\sim 1.8e^{-3}cm^2s^{-1}$ [85] results in a typical exciton diffusion distance of $\sim 10nm$ before recombination. If the electron is not transferred from the donor material within this time the exciton recombines, emitting a photon and no current is generated.

In an organic device the materials are normally mixed together to create a bulk heterojunction structure, to maximise the interface between the organic materials and give more efficient exciton separation. The overall efficiency of such a device depends on the efficiency of photon absorption, charge separation and transport to the electrodes. Since most charge separation takes place at the interface between the donor and acceptor materials it is likely that the efficiency of charge separation is affected by interfacial structure. It has been shown that the relative orientation of conjugated polymers across a heterojunction can strongly affect charge separation and emission spectra in optoelectronic devices (inferred from quantum-chemical calculations and time-resolved photoluminescence experiments) [63], so it is likely that this will have an affect on photovoltaic (PV) devices also. Higgins et al [37] show that for a F8 and poly(9,9 dioctylfluorene-alt-bezothiadiazole) (F8BT) bilayer system used in LEDs increasing the roughness of the interface and therefore changing the composition profile results in greatly enhanced exciton transfer between F8 and F8BT chains. The photophysics of charge separation at the interface in PV heterojunctions is more complicated than the photophysics of charge recombination at a F8/F8BT interface, and is also likely to be affected by the structure of the

interface.

Characterisation of the interfacial structure of bilayers and comparison with the photophysical effects of blends will allow the relationships between interfacial structure and composition and device performance to be established. The highest efficiency organic solar cells that have been produced to date use a blend of P3HT (Poly(3-hexylthiophene-2,5-diyl)) which acts as the electron donor and PCBM ([6,6]-phenyl-C_{61}-butyric acid methyl ester) which acts as the electron acceptor. The work described in this chapter aims to characterise the interface between P3HT/ PCBM films in a bilayer geometry using specular and off specular neutron reflectivity. There is a contrast in the scattering length density of the two materials which allows the interface to be investigated by neutrons.

7.1.1 P3HT

P3HT is a synthetic conjugated polymer. The monomer contains a five member ring, with two double carbon to carbon bonds and a sulphur atom. The π orbitals of the double bonds allow the molecule to act as an electron donor.

7.1.2 PCBM

PCBM is a fullerene derivative of a C60 bucky-ball with a functional group. The functional group consists of a benzene ring and a functionalised carbon tail. It is soluble in chlorobenzene, chloroform and toluene [9] allowing for a solution containing donor/acceptor mixes, which is necessary for printable solar cells.

7.1.3 Annealing of P3HT/PCBM solar cells

Annealing of P3HT/PCBM blends has been shown to increase their phase separation and the efficiency of solar cells, when the annealing temperature is kept below a maximum cut off. Above the cut off temperature large PCBM crystals start to form. However it has been shown that careful control of size and spacing of the PCBM crystals can further increase efficiency [53].

7.2 Sample preparation

Single layer and bilayer thin films were prepared on silicon substrates using spin coating and float coating techniques. Bilayers were prepared with P3HT on top of PCBM. The aim was to produce two smooth films and anneal them to study the interfacial roughness. The formation of PCBM crystals should be minimised.

7.2.1 Solvent and solution concentration

The P3HT was dissolved in toluene and smooth thin films could be formed at a range of concentrations. It was found that using chloroform, chlorobenzene or toluene as the solvent for the PCBM resulted in isolated dots appearing on the surface of the film, which could be seen under an optical microscope. AFM analysis of the dots showed that they had a maximum height of $\sim 100nm$ and an average distance between the dots of $\sim 3\mu m$. Filtering of the solutions did not reduce the dots. It was also found that spin casting the films resulted in Marangoni flows [81], where the film thickness is not even. Higher concentrations of PCBM in the solution helped to minimise Marangoni flows, resulting in thicker films. It was found that using a mixture of 50/50 chloroform and chlorobenzene as the solvent produced a uniform film with no dots or Marangoni flows. It is clear that particular care must be taken to produce uniform PCBM films. An AFM scan of a PCBM layer with isolated dots and a line profile of two dots close together is shown in figure 7.1. It can be seen that the dots have a maximum height of $\sim 150nm$.

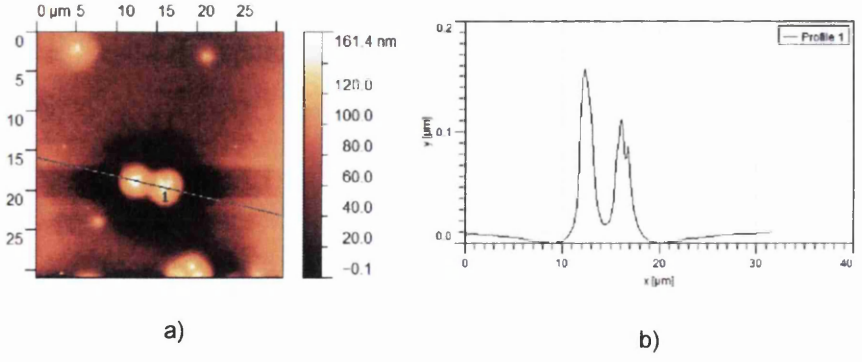

Figure 7.1: a) AFM scan of isolated dots on PCBM single layer b) Line cut of isolated dots. Location of line cut is shown on figure 7.1 a)

7.2.2 Crystalisation

It was found that the rate of crystalisation of the PCBM in the bilayer is related to the annealing temperature, the annealing time and the thickness of the thin films. For temperatures above 160^oC crystallites formed for all samples tested. For temperatures of 150^oC or less the extent of crystal formation was lower. It was found that for the bilayer system making the PCBM layer thin (< 150Å) and the P3HT layer thick (> 1000Å) minimised the formation of PCBM crystals.

7.2.3 Preparing single layers and bilayers

The effect of the P3HT film thickness was compared by studying samples with constant PCBM film thicknesses and two different P3HT film thicknesses. PCBM films were spin cast onto Si substrates using a solution of concentration 3.5% and a spin speed of $1.2K$rpm resulting in a film thickness of $\sim$ 122nm. The bilayers were prepared by float coating P3HT films onto the PCBM/Si samples. The P3HT films were prepared by spin casting onto mica using concentrations of P3HT 0.65% and 1% and spin speeds of 4K rpm and 4.5K rpm respectively to give different thickness films.

7.3 Results

7.3.1 Single layers

Specular off and specular reflectivity data were gathered from unannealed single layer PCBM and P3HT samples and three annealed bilayer samples (see table 4.3). Fits of the specular data from the P3HT and PCBM single layer samples are shown in figures 7.2 and 7.3 respectively. The scattering length densities, thicknesses, and roughnesses are tabulated in table 7.1. The Si substrate was assumed to have a native oxide layer of thickness 9Å and a roughness of either 5 or 7Å.

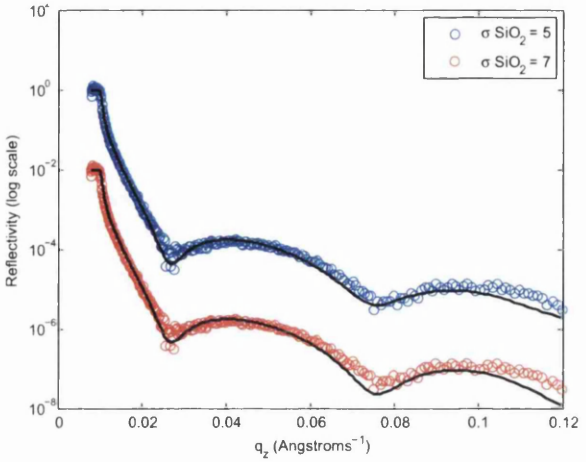

Figure 7.2: Fits of single layer P3HT film of Si substrate assuming $Si0_2$ layers with thickness 9Å and roughnesses 5 Å and 7Å (fits are separated by 10^{-2} for clarity)

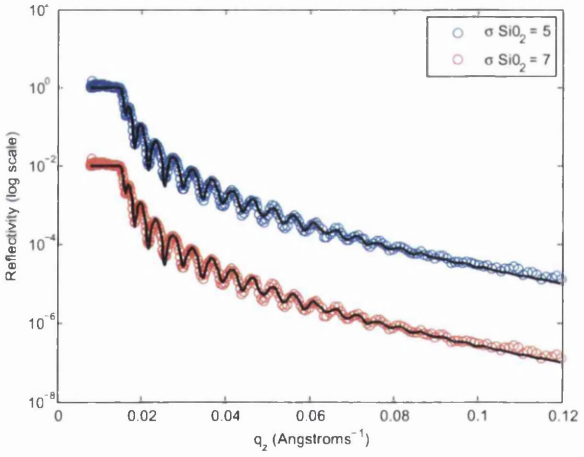

Figure 7.3: Fits of single layer PCBM film of Si substrate assuming $Si0_2$ layers with thickness 9Å and roughnesses 5 Å and 7Å (fits are separated by 10^{-2} for clarity)

Fits of single layers					
Sample	σ $Si0_2$	χ^2	d Å	SLD Å^{-2}	σ
P3HT	5	6.51	133.66	9.54e-7	11.32
	7	6.68	133.97	9.29e-7	7.80
	Mean	-	**133.82**	**9.42**	**9.56e-6**
PCBM	5	4.32	1213.3	4.54E-06	7.79
	7	4.33	1213.4	4.54E-06	7.56
	Mean	**4.33**	**1213.3**	**4.54e-6**	**7.68**

Table 7.1: Fitting parameters from fitting single layers of unannealed P3HT and PCBM on Si substrate

7.3.2 Bilayers

From figures 7.4 to 7.6 it can be seen that there is minimal off specular scattering from the P3HT/PCBM bilayers. This can be seen more clearly by comparing with figure 7.7 which shows off specular scattering from a 100nm F8 on 85nm dPMMA bilayer from experiments conducted at the same time on Offspec. This suggests there is little lateral structure of the interface in the x, y plane on the length scale that the neutrons are sensitive to (hundreds of nm to several microns). This is confirmed by fitting the specular data. Repeated fitting of the P3HT/PCBM specular reflectivity as a simple bilayer with a rough interface did not give a consistent set of fit parameters, suggesting that the simple bilayer model is inadequate to model the system. Figure 7.8 shows typical fits of the three bi layer samples with $\sigma = 5$Å for the oxide layer, modelling the P3HT/PCBM interface as a discrete interface with roughness. It can be seen that the fits are very poor, especially as q_z increases. Instead of forming a discrete interface, P3HT and PCBM mix to a significant extent during annealing. The lack of off specular scattering suggests that this broadening is due to significant molecular mixing rather than lateral roughening of the otherwise sharp interface.

The extent of this mixing is investigated by modelling the interface as a series of very thin films with no interfacial roughness between each layer. Fits are made using a system containing seventeen thin layers in order to simulate a smooth graded interface, with a maximum thickness of 50Å. The fringes in the experimental specular reflectivity show that there is a thick layer of a medium of constant scattering length density which is the unmixed PCBM on the substrate. Because of this beneath the seventeen layers used to model the mixed P3HT/PCBM is a layer of

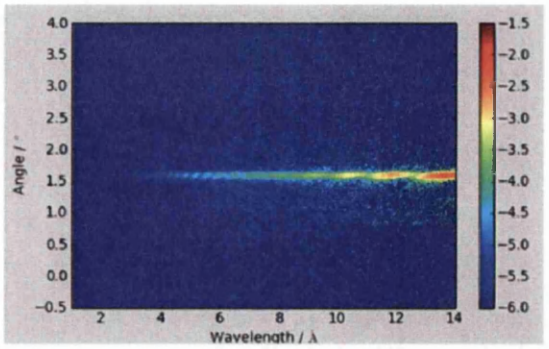

Figure 7.4: Raw count data from $\sim$ 130Å P3HT on $\sim$ 1300Å PCBM bilayer annealed at 140^oC for 10 minutes (counts are on a log scale)

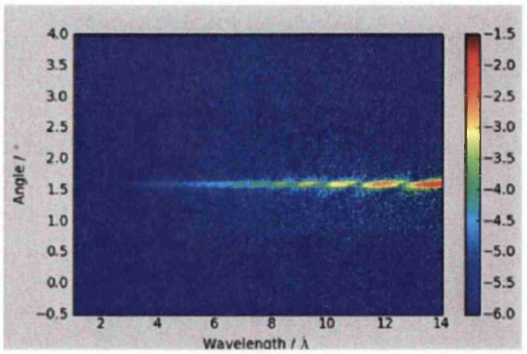

Figure 7.5: Raw count data from $\sim$ 130Å P3HT on $\sim$ 1300Å PCBM bilayer annealed at 140^oC for 20 minutes from (counts are on a log scale)

pure PCBM. Beneath the PCBM layer is a native oxide layer with thickness 9Å and roughness 5Å (see section 6.2.2) and the silicon substrate making twenty layers in total.

The Parratt formalism with a DE fitting algorithm was used to fit the specular data as described in section 6.2. The thickness and scattering length density of the pure PCBM layer was allowed to vary by 100Å and $0.2e-6$Å $^{-2}$ respectively from the values obtained from fitting the PCBM single layer reflectivity. The scattering length density of each mixed layers was restricted to lie between that of pure PCBM and pure P3HT. Initial boundary conditions are applied to the seventeen P3HT/PCBM mixed layers. This is to generate the first generation of random population vectors in the DE algorithm with roughly a linear gradient of scattering length density through the as z decreases from the air/P3HT interface through to the bulk PCBM. It was found that not including the initial conditions so the scattering length density for each of the mixed layers could be anywhere the two limits did not affect the result, though the fitting routine took longer to converge. The fits are shown in figure 7.9.

Figure 7.10 shows the scattering length density variation with depth for fits of the three samples using the series of smooth layers model. The general trend for all three samples is that the scattering length density increases from that of pure P3HT at the top surface to that of pure PCBM as would be expected if the materials mix.

The graded interface fits are far superior to the discrete rough interface fits, capturing most of the features and confirming that there is no discrete interface and the two materials have mixed. From figure 7.10 it is evident that the scattering length density varies from that of pure

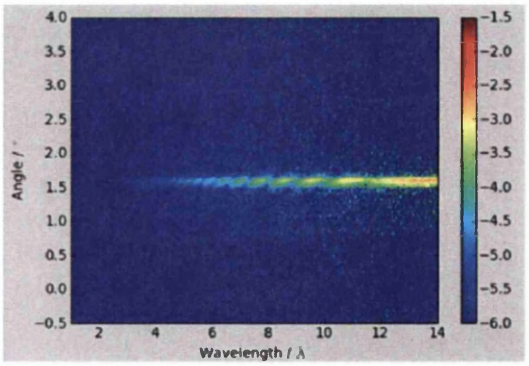

Figure 7.6: Raw count data from Raw count data from ~ 130Å P3HT on ~ 1300Å PCBM bilayer annealed at 150^oC for 10 minutes (counts are on a log scale)

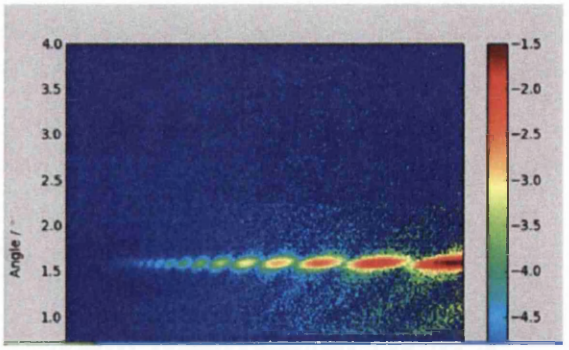

Figure 7.7: Raw count data from ~ 1000Å F8 on ~ 870Å dPMMA bilayer annealed at 180^oC for 3 hours for comparison (counts are on a log scale)

P3HT at the top surface to that of pure PCBM. There is a thick layer of pure PCBM on the Si substrate showing that the materials have mixed, although the P3HT has not had enough time to diffuse fully into the PCBM. The thick layer of PCBM gives the Kiesigg fringes. The miscibility of P3HT and PCBM has been recently found by other authors [15], [52], using lower resolution ion beam methods. This implies that the heterojunction formed in blends may not be formed as a result of liquid/ liquid phase separation but as a result of other processes such as crystalisation of the PCBM or P3HT phase.

Conclusions

P3HT and PCBM are miscible. There is no distinct interface between them after annealing, which means that there will be minimal off specular reflectivity. The DWBA model developed in this work cannot be used in this case. The composition profile of the interface can be approximated by fitting the specular neutron reflectivity with a graded interface of many discrete layers.

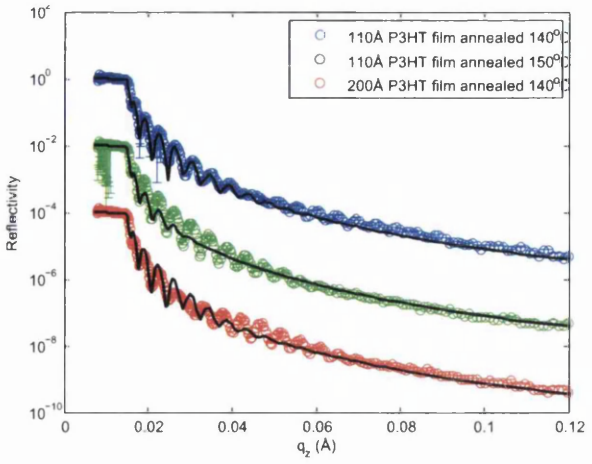

Figure 7.8: Fits of P3HT/ PCBM bilayer systems assuming a discrete rough P3HT/ PCBM interface. Samples are $\sim$ 110Å P3HT on 1210Å PCBM annealed at 140^oC for 10 minutes, $\sim$ 110Å P3HT on 1210Å PCBM annealed at 150^oC for 10 minutes and $\sim$ 200Å P3HT on 1210Å PCBM annealed at 140^oC for 10 minutes (fits are separated by 10^{-2} for clarity)

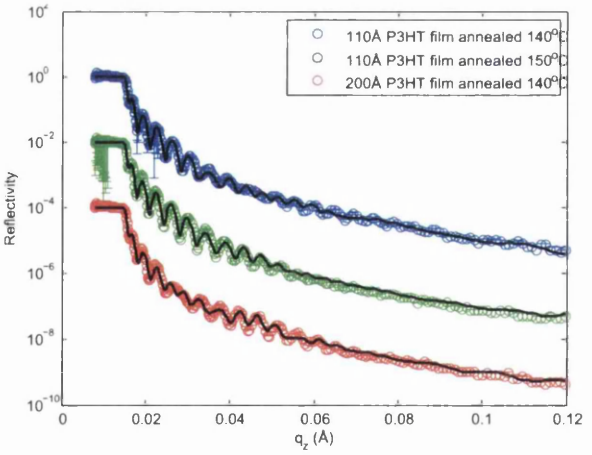

Figure 7.9: Fits of P3HT/ PCBM bilayer systems assuming a smooth graded interface with 20 layers. Samples are $\sim$ 110Å P3HT on 1210Å PCBM annealed at 140^oC for 10 minutes, $\sim$ 110Å P3HT on 1210Å PCBM annealed at 150^oC for 10 minutes and $\sim$ 200Å P3HT on 1210Å PCBM annealed at 140^oC for 10 minutes (fits are separated by 10^{-2} for clarity)

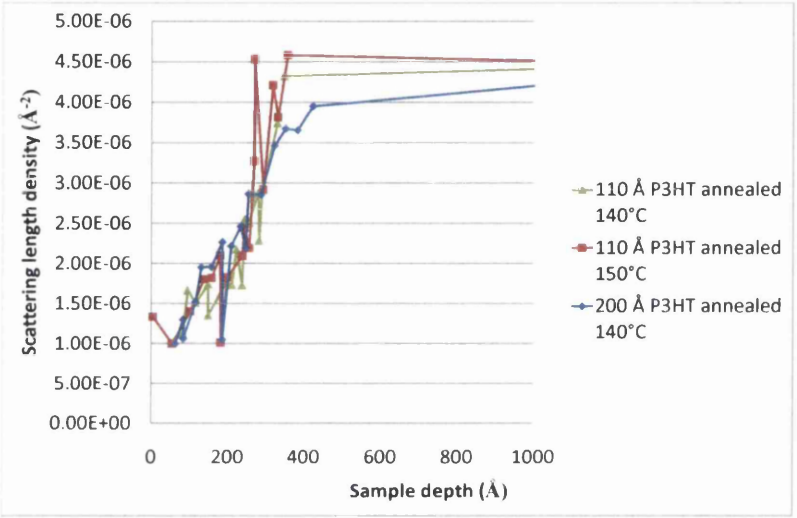

Figure 7.10: Scattering length density vs sample depth for the three P3HT/ PCBM bilayers. Samples are $\sim$ 110Å P3HT on 1210Å PCBM annealed at 140^oC for 10 minutes, $\sim$ 110Å P3HT on 1210Å PCBM annealed at 150^oC for 10 minutes and $\sim$ 200Å P3HT on 1210Å PCBM annealed at 140^oC for 10 minutes

Chapter 8

Conclusions

8.1 Conclusions

Although this work has produced some interesting results about the interfacial structure of polymer systems the main aim has been to understand and produce techniques in order to analyse off specular time of flight (TOF) neutron reflectivity data. This has been achieved by developing a computer model that is based upon the distorted wave Born approximation (DWBA) formulation derived for surfaces by Sinha [88] and extended to thin multilayers by Holy and Baumbach [42]. The model can be used to fit experimental off specular reflectivity data. As far as the author is aware this is the first time this has been achieved for TOF neutron reflectivity. The model has presented many challenges and the chapter describing the modeling techniques is justified so that people following this work may avoid many of the pitfalls that have slowed progress.

The DWBA model developed is able to robustly and repeatably fit the experimental data. The fitting algorithm developed uses differential evolution, which is an established evolutionary computing technique but its application to a 2D colour map is original.

The models of the reflectivity produced match all of the main features of the experimental data, showing that the first order DWBA is valid for neutron experiments conducted on samples with features on the lengthscales probed. In the q range that the TOF neutron scattering experiments in this work have been conducted the correlation between the lateral structure of the interface and the underlying substrate must be taken into account. This results in a far more complicated model than if there was no correlation between the two interfaces. However it is clear that this needs to be taken into account when analysing off specular neutron data, otherwise the model cannot replicate the lines of heightened intensity along constant q_z seen in the experimental data. The model seems to fail to match the off specular reflectivity at the higher neutron wavelengths measured. This is probably because the theory breaks down in this region and is discussed at the end of chapter 6, although further study is required to verify this.

It is clear from fitting the off specular data that the results of the roughness of the interface given by fitting specular data alone are too low. This is because of off specular scattering in the specular peak where $q_x = 0$. The off specular reflectivity should be subtracted from the specular reflectivity but separating out the two components is difficult. In order to fit the roughness accurately a model has been included that simultaneously fits the specular data (broadened by a resolution function) and the off specular data. A methodology to do this is developed in this work, summing the contributions of the Parratt formalism to model the specular reflectivity

and the DWBA to model the off specular reflectivity. Experimental data has successfully been fitted using this technique. The roughness values obtained seem reasonable, but further work is required because the fitting algorithm used appears to preferentially fit the specular ridge, meaning that off specular data is not fitted as well as when the specular data is excluded from the fit. At the specular ridge the specular and off specular reflectivities are summed, although the model seems to find the best solution is to reduce the off specular as much as possible in this region.

The two contributions to the total roughness σ_{lat} and σ_{int} can be separated out by direct measurement for a polymer bilayer system using neutron reflectivity which has not been achieved before. The results from this agree with the theory that interfacial roughness is caused by contributions from thermal capillary wave fluctuations and mixing of polymer chains at a molecular level at the interface. The size of the lateral roughness contributions are dependent on film thickness, which agrees with the theory that the interface is broadened by capillary waves. From the information gathered it was determined that F8 polymer chains are too stiff to be modeled using a flexible chain model. Without extracting the intrinsic roughness by direct measurement this result could not have been achieved. This shows that study of off specular data can reveal new insights into polymer properties.

The results from studies on the P3HT/PCBM interface show that these two materials are miscible. Therefore there is no lateral structure at the interface and little off specular reflectivity data. The composition profile of the P3HT/PCBM was studied using a thin layer model within the Parratt formulation. The miscibility of the the two materials will have implications device performance and why they are good materials to make photo voltaics.

In conclusion the models developed has sucessfully used to analyse off specular neutron scattering data and has produced robust results. It is designed to be adaptable and applicable to a multilayer system with any number of layers and it is hoped that it may be applied to a range of systems.

8.2 Future work

The model described in this work is an initial attempt to model off specular reflectivity in θ/λ space, and as such there is much room for improvement and development. There is considerable scope for improving the computational time required by the model. Development of more

efficient ways of solving the integral expression is the main way of speeding it up, as this is by far the most time consuming step. Development of the fitting algorithm for the fitting of specular and off specular results together is also required, so that fitting of the specular region does not dominate the off specular completely. Making the model more user friendly would be useful. It could be used by people not versed in the theory behind it to analyse experimental data, in the same way that specular models are.

Theoretical work should be carried out in order to find where the model is valid and if necessary then higher order terms should be derived and included.

In terms of the samples analysed it would be interesting to probe the F8/dPMMA interface at smaller lengthscales, possibly using spin echo neutron scattering, to see if the height to height correlation function required to fit the data is dependent on the length scale probed. It would also be good to measure an amorphous/amorphous polymer interface to see if off specular reflectivity from this type of interface can be fitted in the regions where the reflectivity from the F8/dPMMA samples is not well fitted. Though this was attempted in this work the samples used did not give good results.

The author believes it would be beneficial to build on the model at a neutron source. Many aspects of experiments that have been fairly insignificant in the collection of specular reflectivity now become important when collecting off specular reflectivity data. An example of this is knowing the solid angle of the detector pixels. by precisely defining instrumental geometry. Ideally the instrument and the analysis software should be developed together.

Appendix A

Derivation of BA and DWBA expressions

A.1 Solving for the Wave functions

The scattering cross section for a particle scattered from a point potential is given by (see section 2.5)

$$\frac{d\sigma}{d\Omega} = \frac{|f(\theta,\phi)|^2}{(4\pi)^2} \tag{A.1}$$

where the $(4\pi)^2$ denominator is given by the solid angle of the sphere which surrounds the scattering centre squared and the normalisation constant is disregarded. We are now solving to find an expression for $f(\theta,\phi)$. The time independent Schrödinger equation (TISE) is given by

$$\left(\frac{\hbar^2}{2m}\nabla^2 + E\right)\psi_k(\mathbf{r}) = V(\mathbf{r})\psi_k(\mathbf{r}) \tag{A.2}$$

and $E = \frac{\hbar^2 k^2}{2m}$

Equation A.2 can be solved by the method of Green's functions. The Green's function of the differential operator is essentially the inverse of the differential operator. Therefore the Green's function of the differential operator $G(\mathbf{r})$ acted on by the differential operator gives

$$\left(\frac{\hbar^2}{2m}\nabla^2 + E\right) G(\mathbf{r}) = \delta(\mathbf{r})' \tag{A.3}$$

The general solution to equation A.2 is

$$\psi_k(\mathbf{r}) = \phi_k(\mathbf{r}) + \int G(\mathbf{r},\mathbf{r}')V((r')\psi_k(\mathbf{r}')d^3r' \tag{A.4}$$

Because $\left(\frac{\hbar^2}{2m}\nabla^2 + E\right)\phi_k(\mathbf{r}) = 0$, $\phi_k(\mathbf{r})$ can be added to the inhomogeneous equation $\psi_k(\mathbf{r}) = \int G(\mathbf{r},\mathbf{r}')V((r')\psi_k(\mathbf{r}')d^3r'$. It is chosen to represent the incoming wave $\phi_k(\mathbf{r}) = e^{i\mathbf{kr}}$. The integral represents the outgoing scattered waves. Care must be taken in defining the Greens function so that it represents the physical problem, a single incoming wave and a spectrum of scattered waves. An equally valid but unphysical solution could define a spectrum of incoming waves. The Greens function for outgoing waves G_+ is given by

$$G_+ = -\frac{m}{2\pi\hbar^2}\frac{e^{ik|(\mathbf{r}-\mathbf{r}')}}{|\mathbf{r}-\mathbf{r}'|} \tag{A.5}$$

for information on how to derive the Greens function the reader is referred to reference [72]. This results in the following equation

$$\psi_k(\mathbf{r}) = e^{i\mathbf{kr}} - \frac{m}{2\pi\hbar^2}\int \frac{e^{ik|(\mathbf{r}-\mathbf{r}')}}{|\mathbf{r}-\mathbf{r}'|}V((r')\psi_k(\mathbf{r}')d^3r' \tag{A.6}$$

This is known as the Lippmann Schwinger equation. Far from the scattering centre it is reasonable to approximate $|\mathbf{r}-\mathbf{r}'| \cong r$ in the denominator as $r' \to \infty$. In the exponential $|\mathbf{r}-\mathbf{r}'| = r' - rcos\theta' + \frac{r^2}{r'}$. In the limit $r' \to \infty$, $|\mathbf{r}-\mathbf{r}'| = r' - rcos\theta'$. A vector $\mathbf{k_f}$ can be defined with magnitude k and direction r' so that $krcos\theta' = \mathbf{k_f}\cdot\mathbf{r}'$, which results in the following expression for the exponential and its coefficient.

$$\frac{e^{ikr}}{r}e^{-i\mathbf{k_f}\cdot\mathbf{r}'} \tag{A.7}$$

This vector $\mathbf{k_f}$ gives the amplitude component of the outgoing scattered circular wave with magnitude k_f and direction (θ,ϕ). The intensity of these components in all directions relative to each other give the probability that an incoming wave $\mathbf{k}$ is scattered in direction (θ,ϕ), as $\mathbf{k_f}$ is a function of magnitude and direction. This is shown graphically in figure A.1.

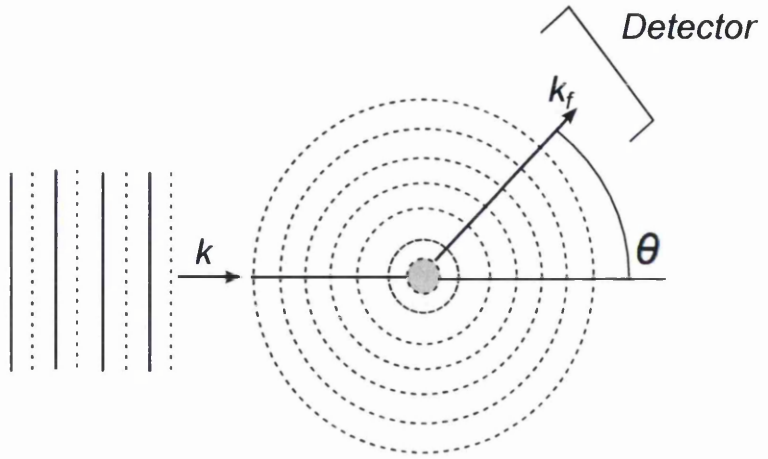

Figure A.1: Scattering into $\mathbf{k_f}$

Comparison between equation A.6 and 2.19 reveal that

$$f(\theta,\phi) \cong -\frac{m}{2\pi\hbar^2}\int e^{-i\mathbf{k}'\cdot\mathbf{r}'}V(r')\psi_k(\mathbf{r}')d^3r' \equiv \frac{m}{2\pi\hbar^2}\left\langle \phi_{k_f}\right| V\left|\psi_k\right\rangle \tag{A.8}$$

The differential scattering cross section is given by

$$\frac{d\sigma}{d\Omega} = C\frac{m^2}{(2\pi)^2\hbar^4}|\left\langle \phi_{k_f}\right| V\left|\psi_k\right\rangle|^2 \tag{A.9}$$

Where C is a constant. The wave function ψ_k can be expanded into a perturbation series. The zero order term corresponds to the unperturbed incident plane wave

$$\psi_{\mathbf{k}}^{(0)}(\mathbf{r}) = \phi_{\mathbf{k}}(\mathbf{r}) = e^{i\mathbf{k}\cdot\mathbf{r}} \tag{A.10}$$

The first and second order terms are given respectively by

$$\psi_{\mathbf{k}}^{(1)}(\mathbf{r}) = \phi_{\mathbf{k}}(\mathbf{r}) + \frac{m}{2\pi\hbar^2}\int d^3r' G_+(\mathbf{r},\mathbf{r}')V(\mathbf{r}')\psi_{\mathbf{k}}^{(0)}(\mathbf{r}') \tag{A.11a}$$

$$\psi_{\mathbf{k}}^{(2)}(\mathbf{r}) = \phi_{\mathbf{k}}(\mathbf{r}) + \frac{m}{2\pi\hbar^2}\int d^3r' G_+(\mathbf{r},\mathbf{r}')V(\mathbf{r}')\psi_{\mathbf{k}}^{(1)}(\mathbf{r}') \tag{A.11b}$$

The complete expression for $\psi_{\mathbf{k}}$ independent of coordinates is

$$|\psi_k\rangle = |\phi_k\rangle + \frac{m}{2\pi\hbar^2}(\hat{G_+}\hat{V}|\phi_k\rangle + \hat{G_+}\hat{V}\hat{G_+}\hat{V}|\phi_k\rangle)... = \frac{m}{2\pi\hbar^2}\sum_{n=0}^{\infty}(\hat{G_+}\hat{V})^n|\phi_{\mathbf{k}}\rangle = T|\mathbf{k}\rangle \quad \text{(A.12)}$$

where T is known as the transition matrix, and represents all the potential terms of the perturbation expansion. Using $f(\theta,\phi) = -\frac{m}{2\hbar}\langle\phi_{k_f}|V|\psi_k\rangle$

$$f = -\frac{m}{2\hbar^2}\langle\phi_{\mathbf{k_f}}|V + VG_+ + VG_+VG_+...|\phi_{\mathbf{k}}\rangle = -\frac{m}{2\pi\hbar^2}\langle\mathbf{k_f}|T|\mathbf{k}\rangle \quad \text{(A.13)}$$

$\langle\mathbf{k_f}|T|\mathbf{k}\rangle$ is the transition matrix element, allowing f to be defined in terms of T and plane waves with incoming and outgoing vectors $\mathbf{k}$ and $\mathbf{k_f}$ respectively.

A.1.1 Born Approximation

Taking the first order approximation of f gives

$$f_{Born} = -\frac{m}{2\pi\hbar^2}\langle\phi_{\mathbf{k_f}}|V|\phi_{\mathbf{k}}\rangle \quad \text{(A.14)}$$

This is the first Born approximation. The wavefunction $\psi_{\mathbf{k}}$ in equation A.8 is replaced by $\phi_{\mathbf{k}}$. It is equivalent to Fermi's Golden rule, which maps the probability of a system in one state acted on by an operator transforming into any of a continuum of states.

A.2 Incoming Waves

The solution to the Schrödingers equation $\psi_{\mathbf{k}}$ can be defined in a unphysical time reversed state, with an incoming circular wave and a outgoing plane wave where i is replaced with $-i$ (see Schiff chapter 9 [78]). In this situation the time reversed wavefunction $\psi_{\mathbf{k}}^-$ is

$$\psi_k^-(\mathbf{r}) \cong e^{i\mathbf{kr}} + f^-(\theta,\phi)\frac{e^{-ikr}}{r} \quad \text{(A.15)}$$

where f^- is the inverse scattering amplitude. The Greens function in this situation becomes

$$G_- = -\frac{m}{2\pi\hbar^2}\frac{e^{-ik|(\mathbf{r}-\mathbf{r}')}}{|\mathbf{r}-\mathbf{r}'|} \tag{A.16}$$

It is the complex conjugate of G_+. It follows that if V is real then the solution $\psi^+_{\mathbf{k}}(\mathbf{r}) = \psi^-_{-\mathbf{k}}(\mathbf{r})$ and $f = f^{-*}$ where $\psi^-_{-\mathbf{k}}(\mathbf{r})$ is the time reversed state to $\psi^+_{\mathbf{k}}(\mathbf{r})$ (where $\psi^+_{\mathbf{k}}(\mathbf{r}) = \psi_{\mathbf{k}}(\mathbf{r})$ defined above) and has the opposite momentum $-k$. Solving for the T matrix element in the same way as in the previous section using these time reversed functions the result is the same ie

$$\langle \mathbf{k_f}|T|\mathbf{k}\rangle = \langle \phi_{\mathbf{k_f}}|V|\psi_{\mathbf{k}}\rangle = \langle \psi^-_{\mathbf{k}}|V|\phi_{\mathbf{k_f}}\rangle \tag{A.17}$$

If V is complex then new wave functions must be defined, but this is not required in any model in this work.

A.3 Separating the Scattering Potential in two parts

In order to derive the Distorted Wave Born approximation the scattering potential V is divided into two parts V_1 and V_2, $V = V_1 + V_2$. The T matrix element is the sum of the wave function acted on by V_1 and a correcting term V_2. This procedure is useful when the wave equation V_1 term is exactly solvable and V_2 is small enough to be described as a perturbation. The T matrix element for two potentials is defined in the following way.

Following the procedure to define a scattering amplitude f, the time reversed wave function, $\psi^-_{1\mathbf{k_f}}(\mathbf{r})$, for scattering from V_1 alone with wave vector $\mathbf{k_f}$ is described as

$$\psi^-_{1\mathbf{k_f}}(\mathbf{r}) = \phi_{1\mathbf{k_f}}(\mathbf{r}') - \frac{m}{2\pi\hbar}\int G_-(\mathbf{r},\mathbf{r}')V_1(\mathbf{r}')\psi^-_{1\mathbf{k_f}}(\mathbf{r}')d^3r \tag{A.18}$$

The T matrix element for $V_1 + V_2$ is

$$\langle \mathbf{k_f}|T|\mathbf{k}\rangle = -\frac{m}{2\pi\hbar}\int \phi^*_{\mathbf{k_f}}(\mathbf{r})(V_1+V_2)(\mathbf{r})\psi^+_{\mathbf{k}}(\mathbf{r})d^3r \tag{A.19}$$

Substituting for $\phi_{1\mathbf{k_f}}(\mathbf{r}')$ from equation A.18 into equation A.19 gives for the left hand side

$$= -\frac{m}{2\pi\hbar}\int d^3r(\psi^{-*}_{1\mathbf{k_f}}(\mathbf{r})(V_1(\mathbf{r})+V_2(\mathbf{r}))\psi^{+}_{\mathbf{k}}(\mathbf{r}) - G_-(\mathbf{r},\mathbf{r}')V_1(\mathbf{r}')\psi^{-}_{1\mathbf{k_f}}(\mathbf{r}')(V_1(\mathbf{r})+V_2(\mathbf{r}))\psi^{+}_{\mathbf{k}}(\mathbf{r})) \tag{A.20}$$

Because of Hermitian conditions ($\int u^* \hat{A} u d^3r = \int (\hat{A}u)^* u d^3r$) equation A.20 can be rewritten as

$$= -\frac{m}{2\pi\hbar}\int d^3r(\psi^{-*}_{1\mathbf{k_f}}(\mathbf{r})(V_1+V_2)(\mathbf{r})\psi^{+}_{\mathbf{k}}(\mathbf{r}) - \psi^{-}_{1\mathbf{k_f}}(\mathbf{r}'))V_1(\mathbf{r}')G_+(\mathbf{r},\mathbf{r}')(V_1(\mathbf{r})+V_2(\mathbf{r}))\psi^{+}_{\mathbf{k}}(\mathbf{r})) \tag{A.21}$$

as G_+ is the complex conjugate of G_-. Noting that $G_+(\mathbf{r},\mathbf{r}')(V_1(\mathbf{r})+V_2(\mathbf{r}))\psi^{+}_{\mathbf{k}}(\mathbf{r}) = \psi^{+}_{\mathbf{k}}(\mathbf{r}) - \phi_{\mathbf{k}}(\mathbf{r})$ finally the T matrix element can be written

$$\langle \mathbf{k_f}|T|\mathbf{k}\rangle = -\frac{m}{2\pi\hbar}\left(\int d^3r\psi^{-*}_{1\mathbf{k_f}}(\mathbf{r})V_1(\mathbf{r})\phi_{\mathbf{k}}(\mathbf{r}) - \int d^3r\psi^{-*}_{1\mathbf{k_f}}(\mathbf{r})V_2(\mathbf{r})\psi^{+}_{\mathbf{k}}(\mathbf{r})\right) \tag{A.22}$$

which written in Dirac notation is

$$\langle \mathbf{k_f}|T|\mathbf{k}\rangle = \langle \psi^{-}_{\mathbf{k_f}}|V_1|\phi_{\mathbf{k}}\rangle + \langle \psi^{-}_{\mathbf{k_f}}|V2|\psi^{+}_{\mathbf{k}}\rangle \tag{A.23}$$

A.3.1 Distorted Wave Born Approximation

To approximate the second integral to first order in equation A.22 replace $\psi^{+}_{\mathbf{k}}(\mathbf{r})$ with $\psi^{+}_{1\mathbf{k}}(\mathbf{r})$ the first order term of the perturbation expansion. This is appropriate if V_2 is small. This result is the first order Distorted Wave Born Approximation. The expression in the ket of the first term of equation A.23 is simply a plane wave. The expressions in the bras in both terms are time reversed. The expression for the first order DWBA is

$$\langle \mathbf{k_f}|T|\mathbf{k}\rangle \approx \langle \psi^{-}_{\mathbf{k_f}}|V_1|\phi_{\mathbf{k}}\rangle + \langle \psi^{-}_{\mathbf{k_f}}|V_2|\psi^{+}_{1\mathbf{k}}\rangle \tag{A.24}$$

Appendix B

Neutron and Matter Interactions

B.1 Scattering from an assembly of atoms

The scattering amplitude f of a neutron scattered by a potential V is described by the Born approximation (see section A.1.1, equation 2.21). It can be written as an integral equation in terms of q the momentum transfer as $\mathbf{q} = \mathbf{k_i} - \mathbf{k_f}$ where $\mathbf{k_i}$ and $\mathbf{k_f}$ are the wave numbers of the incoming and outgoing waves respectively.

$$f = -\frac{m}{2\pi\hbar}\int e^{-i\mathbf{k_f}\cdot\mathbf{r}}V(\mathbf{r})e^{-i\mathbf{k_f}\cdot\mathbf{r}}d^3r = -\frac{m}{2\pi\hbar}\int e^{-i\mathbf{q}\cdot\mathbf{r}}V(\mathbf{r})d\mathbf{r} \tag{B.1}$$

The interaction between neutrons and nuclei (within a scattering medium) are only important at very small distances. The potential $V(\mathbf{r})$ can be replaced by the Fermi puesdo potential

$$V(\mathbf{r}) = \frac{2\pi\hbar}{m}b\delta(\mathbf{r} - \mathbf{r}') \tag{B.2}$$

so there is only any interaction at the point $(r - r') = 0$. Substituting into equation B.1 is a constant multiplied by the Fourier transform of a delta function, which is equal to unity. f is therefore equal to b which has units of length and is known as the scattering length of the nucleus. Different atoms and isotopes have different scattering lengths, dependent on the strength of scattering from them. From a single nucleus the differential cross section (see section 2.5.1) $\frac{d\sigma}{d\Omega} = b^2$. For an assembly of nuclei the potential is the sum of the potentials from each

individual nucleus.

$$V(\mathbf{r}) = \frac{2\pi\hbar}{m}\sum_j b_j\delta(\mathbf{r}-\mathbf{r_j}) \tag{B.3}$$

where j is an index over all atoms. Substituting this expression into $\psi_k(\mathbf{r})$ (equation 2.19, remembering $f_j = b_j$, taking the absolute squared and averaging leads to the expression for $\frac{d\sigma}{d\Omega}$

$$\frac{d\sigma}{d\Omega} = \left\langle \sum_{j,k}^{N} b_j b_k e^{i\mathbf{q}\cdot(\mathbf{r_k}-\mathbf{r_j})} \right\rangle \tag{B.4}$$

where the $\langle\rangle$ denote an average and N is the total number of atoms. Separating B.4 into two parts for terms where $j = k$ and terms where $j \neq k$ gives

$$\frac{d\sigma}{d\Omega} = N\langle b^2\rangle + \langle b\rangle^2 \sum_{j\neq k}^{N} \langle e^{i\mathbf{q}\cdot(\mathbf{r_k}-\mathbf{r_j})}\rangle \tag{B.5}$$

The first term on the right hand is simply N times the average value of the scattering length b^2. The second term comes from putting $b_j b_k = \langle b_j b_k\rangle = \langle b\rangle^2$. By defining $\Delta\bar{b}^2 = \langle b^2\rangle - \langle b\rangle^2$ B.5 can be written

$$\frac{d\sigma}{d\Omega} = N\overline{\Delta b^2} + \langle b\rangle^2 \sum_{j,k}^{N} \langle e^{i\mathbf{q}\cdot(\mathbf{r_k}-\mathbf{r_j})}\rangle \tag{B.6}$$

The first term is dependent only on the scattering length and has no dependence on atomic position. This corresponds to the incoherent scattering. The second term when $j \neq k$ is the coherent scattering. The coherent and incoherent cross sections are defined as $\sigma_{coh} = 4\pi\langle b\rangle^2$ and $\sigma_{coh} = 4\pi\Delta\bar{b}^2$ respectively. If there is no variation in the scattering length of the atoms in a sample, ie if a sample contains a single isotope of a single type of atoms, then no incoherent scattering will occur.

B.1.1 Neutron Spin

Neutrons have an intrinsic property known as spin, which can have either of two values $\frac{1}{2}$ or $-\frac{1}{2}$. This results into a nuclei having two different scattering lengths b^+ and b^- which are

dependent on the spin of the interacting neutron. The nuclei also have a fixed spin state i. There are $2(2i+1)$ possible states from the interaction between the nucleus and the neutron, $2(i+1)$ states for neutron spin of $\frac{1}{2}$ and $2(i)$ states for neutron spin of $-\frac{1}{2}$. The probability of b^+ occurring and b^- occurring are $\frac{i+1}{2i+1}$ and $\frac{i}{2i+1}$ respectively. Averaging for $\langle b \rangle$ gives [41]

$$\langle b \rangle = \frac{i+1}{2i+1} b^+ + \frac{i}{2i+1} b^- \tag{B.7a}$$

$$\langle b^2 \rangle = \frac{i+1}{2i+1} b^{+2} + \frac{i}{2i+1} b^{-2} \tag{B.7b}$$

The different spin states will cause incoherent scattering as the scattering lengths are different.

Appendix C

Self Consistent Field theory

A polmer chain with t segments can be described by the function $q(\mathbf{r}, \mathbf{r}', t)$ where $\mathbf{q}$ and $\mathbf{q}'$ are the beginning and end points of the chain respectively. An ideal isolated chain is a random walk and can be modelled by the diffusion equation

$$\frac{\partial q}{\partial t} = \frac{a^2}{6}\nabla^2 q(\mathbf{r}, \mathbf{r}', t) \tag{C.1}$$

where $a/6$ is the diffusion coefficient and a is the segment length of an individual monomer. A chain that is not in free space can be modeled by adding the potential $V(\mathbf{r})$ so equation C.1 becomes

$$\frac{\partial q}{\partial t} = \frac{a^2}{6}\nabla^2 q(\mathbf{r}, \mathbf{r}', t) - V(\mathbf{r})q(\mathbf{r}, \mathbf{r}', t) \tag{C.2}$$

If a polymer is in a melt with other polymers the potential it experiences will depend on the position of all chains interacting with it. In order to solve equation C.2 for a single chain, the location of every other chain must be known. As this cannot be known, a mean field potential is introduced. It can be assumed that each polymer chain of the same chemical type experiences a average potential $U(\mathbf{r})$. A system with of two highly immiscible polymers A and B will be considered. If the interface between the two has planar symmetry then only the z direction needs to be considered as the interactions will average out in the other dimensions. The mean field equations for U_A and U_B, the potentials experienced by A and B respectively are

$$\frac{U_A(z)}{kT} = \chi\Phi_B(z) + w(z) \tag{C.3a}$$

$$\frac{U_B(z)}{kT} = \chi\Phi_A(z) + w(z) \tag{C.3b}$$

The potentials in equations C.3 are composed of two parts. The first part depends on the chemical attraction or repulsion between monomers in the mix and contains the Flory Huggins interaction parameter χ. This first part is proportional to the average voulme fraction of each species in the mix. The second part is the hard core potential which prevents two polymer monomers occupying the same volume. The function $w(z)$ must be chosen to enusre that the mixture is incompressible, satisfying the condition

$$\Phi_A + \Phi_B = 1 \tag{C.4}$$

The distribution function equations for A and B are

$$\frac{\partial q_A}{\partial t} = \frac{a^2}{6}\nabla^2 q_A(\mathbf{r},\mathbf{r}',t) - U_A(\mathbf{r})q_A(\mathbf{r},\mathbf{r}',t) \tag{C.5a}$$

$$\frac{\partial q_B}{\partial t} = \frac{a^2}{6}\nabla^2 q_B(\mathbf{r},\mathbf{r}',t) - U_B(\mathbf{r})q_B(\mathbf{r},\mathbf{r}',t) \tag{C.5b}$$

In order to determine the mixing at the interface profile the volume fractions $\Phi_A(z)$ and $\Phi_B(z)$ across the interface must be determined. $\Phi_A(z)$ and $\Phi_B(z)$ are related to the distribution functions $q_A(z,t)$ and $q_B(z,t)$ by the equations

$$\Phi_A(z) = \frac{1}{N}\int_0^N dt q_A(z,N-t)q_A(z,t) \tag{C.6a}$$

$$\Phi_B(z) = \frac{1}{N}\int_0^N dt q_B(z,N-t)q_B(z,t) \tag{C.6b}$$

where the expressions are integrated over t the number of segments along a polymer chain, up til N the total number of steps. For each z the number of segments of polymer A relative to the

total number of segments A and B give the volume fraction $\Phi_A(z)$. This is shown graphically in figure C.1.

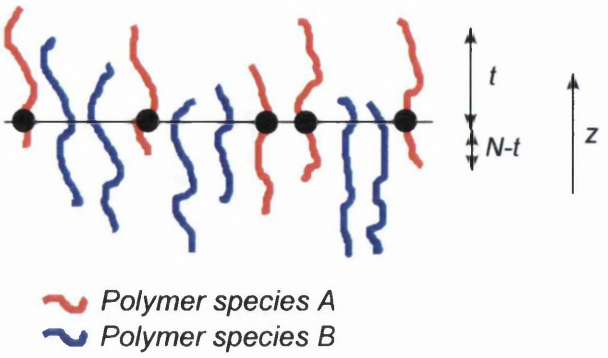

Figure C.1: Polymer chain contribution to volume fraction Φ_A, leading to equation C.6

In general iterative techniques must be used to solve for the volume fractions to obtain values for $q_A(z,t)$ and $q_B(z,t)$ and using them to refine the volume fraction profiles. However there is one situation when equations C.6 can be solved analytically, when two highly immiscible polymers have infinite molecular mass (infinite chain lengths). This is known as the Helfand theory [36]. In this case all chain segments are equivalent within equation C.6 since they are not affected by their position relative to the end of the chain. Equations C.6 are replaced by

$$\Phi_A(z) = q_A(z,t)^2 \tag{C.7a}$$

$$\Phi_B(z) = q_B(z,t)^2 \tag{C.7b}$$

the diffusion equations C.5 become

$$\frac{a^2}{6}\frac{d^2 q_A}{dz^2} = \chi q_B^2 q_A + w(z) q_A \tag{C.8a}$$

$$\frac{a^2}{6}\frac{d^2 q_B}{dz^2} = \chi q_B^2 q_B + w(z) q_B \tag{C.8b}$$

In the limits $\Phi_A(z \to \infty) = 0$ and $\Phi_A(z \to -\infty) = 1$ then the following solution can be found

$$\Phi_A(z) = \frac{1}{2}\left[1 + \tanh\frac{z}{w_1}\right] \tag{C.9}$$

where w is the interfacial width, the width across which mixing occurs, and is given by

$$w = \frac{b}{(6\chi)^{1/2}} \tag{C.10}$$

.

where b is now the average statistical segment length . The interfacial tension can be evaluted as

$$\gamma = k_B T \rho b \sqrt{\frac{\chi}{6}} \tag{C.11}$$

Bibliography

[1] http://www.chemistry.sc.chula.ac.th/bsac/gen%2030%20-%20synth%20polymers.pdf.

[2] B. Akgun, D. R. Lee, H. Kim, H. Zhang, O. Prucker, J. Wang, J. Rhe, and M. D. Foster. Self-affine surfaces of polymer brushes. *Macromolecules*, 40(17):6361–6369, 2007.

[3] M. Alcoutlabi and G. B. McKenna. Effects of confinement on material behaviour at the nanometre size scale. *Journal of Physics: Condensed Matter*, 17(15):R461, 2005.

[4] S. H. Anastasiadis1, T. P Russell, S. K. Satija, and C. F. Majkrzak. The morphology of symmetric diblock copolymers as revealed by neutron reflectivity. *J. Chem. Phys.*, 92(9):5677–5692, 1990.

[5] M. J. Banach, R. H. Friend. and H. Sirringhaus. Influence of the molecular weight on the thermotropic alignment of thin liquid crystalline polyfluorene copolymer films. *Macromolecules*, 36(8):2838–2844, 2003.

[6] G. Binnig, C. F. Quate, and Ch. Gerber. Atomic force microscope. *Phys. Rev. Lett.*, 56(9):930–933, 1986.

[7] E. Born, M. Wolf. *Principles of Optics.* Cambridge University Press, 7th edition, 1999.

[8] D.K. Bowen, M. Wormington, and P.A. McKeown. Measurement of surface roughnesses and topography at nanometer levels by diffuse x-ray scattering. *CIRP Annals - Manufacturing Technology*, 43(1):497 – 500, 1994.

[9] U. Dyakonov V. Brabec, C. Scherf. *Organic Photovoltaics; Materials, Device Physics, and Manufacturing Technologies.* Wiley, 3rd edition, 2008.

[10] D. Broseta, G. H. Fredrickson, E. Helfand, and L. Leibler. Molecular weight and polydispersity effects at polymer-polymer interfaces. *Macromolecules*, 23(1):132–139, 1990.

[11] R. A Buff, F. P. Lovett and F. H. Stillinger. Interfacial density profile for fluids in the critical region. *Phys. Rev. Lett*, 15(15):621–623, 1965.

[12] Braun. C. *Parratt 32 version 1.5.2, build 211.* HMI Berlin, 1997-1999.

[13] W. D. Callister. *Materials Science and Engineering: An Introduction.* Wiley, 3rd edition, 2003.

[14] S. S. Chang, A. B. Rodriguez, A. M. Higgins, C. Liu, M. Geoghegan, H. Sirringhaus, F. Cousin, R. M. Dalgleish, and Y. Deng. Control of roughness at interfaces and the impact on charge mobility in all-polymer field-effect transistors. *Soft Matter*, 4:2220–2224, 2008.

[15] D. Chen, F. Liu, C. Wang, A. Nakahara, and T. P. Russell. Bulk heterojunction photovoltaic active layers via bilayer interdiffusion. *Nano Letters*, 11(5):2071–2078, 2011.

[16] S. Langridge C.J. Kinane, R.M. Dalgliesh and D.G. Bucknall. Crisp instrument manual. November 2010.

[17] P. J. Collings. *Introduction to liquid crystals.* CRC Press, 3rd edition, 1997.

[18] P. Névot L Croce. étude des couches minces et des surfaces par rflexion rasante, spculaire ou diffuse, de rayons x. *Revue de Physique Applique*, 11(12):113–125, 1976.

[19] R. Cubitt and G. Fragneto. D17: the new reflectometer at the ill. *Applied Physics A: Materials Science amp; Processing*, 74:329–331, 2002.

[20] A. Daillant, J. Gibaud. *Xray and Neutron reflectivity: Principles and applications.* Springer, 2nd edition, 2008.

[21] J. Daillant. X-ray scattering at liquid surfaces and interfaces. *Current Science*, 78(12):1496–1506, 2000.

[22] R. Dalgliesh. Offspec data sheet, http://www.isis.stfc.ac.uk/instruments/offspec/technical/offspec-technical-information7145.html.

[23] D. K. G. de Boer. Influence of the roughness profile on the specular reflectivity of x rays and neutrons. *Phys. Rev. B.*, 49(9):5817–5821, 1994.

[24] J. P. de Silva, S. J. Martin, R. Cubitt, and M. Geoghegan. Observation of the complete rupture of a buried polymer layer by off-specular neutron reflectometry. *EPL (Europhysics Letters)*, 86(3):36005, 2009.

[25] Cambridge display technologies. Private communication.

[26] A. K. Doerr, M. Tolan, W. Prange, J.-P. Schlomka, T. Seydel, W. Press, D. Smilgies, and B. Struth. Observation of capillary waves on liquid thin films from mesoscopic to atomic length scales. *Phys. Rev. Lett.*, 83(17):3470–3473, 1999.

[27] S. F. Edwards. The statistical mechanics of polymers with excluded volume. *Proceedings of the Physical Society*, 85(4):613, 1965.

[28] M.L Fernandeza, J.S Higgins, J. Penfold, R.C Ward, C. Shackleton, and D. J. Walsh. Neutron reflection investigation of the interface between an immiscible polymer pair.

[29] P. Flory. *Statistical Mechanics of Chain Molecules.* Interscience, 2nd edition, 1969.

[30] J. A. Franz. http://www.icsi.berkeley.edu/ storn/code.html. 2011.

[31] G. H. Fredrickson, A. Ajdari, L. Leibler, and J. P. Carton. Surface modes and deformation energy of a molten polymer brush. *Macromolecules*, 25(11):2882–2889, 1992.

[32] M. P. Gelfand and M. E. Fisher. Finite-size effects in fluid interfaces. *Physica A: Statistical and Theoretical Physics*, 166(1):1 – 74, 1990.

[33] M. Grell, D. D. C. Bradley, M. Inbasekaran, and E. P. Woo. A glass-forming conjugated main-chain liquid crystal polymer for polarized electroluminescence applications. *Advanced Materials*, 9(10):798–802, 1997.

[34] M. Grell, D.D.C. Bradley, X. Long, T. Chamberlain, M. Inbasekaran, E.P. Woo, and M. Soliman. Chain geometry, solution aggregation and enhanced dichroism in the liquid-crystalline conjugated polymer poly(9,9-dioctylfluorene). *Acta Polymerica*, 49(8):439–444, 1998.

[35] H. C. Hamaker. The londonvan der waals attraction between spherical particles. *Physica*, 4(10):1058–1072, 1937.

[36] E. Helfand and Y. Tagami. Theory of the interface between immiscible polymers. *Journal of Polymer Science Part B: Polymer Letters*, 9(10):741–746, 1971.

[37] A. M. Higgins, A. Cadby, D. G. Lidzey, R. M. Dalgliesh, M. Geoghegan, R. A. L. Jones, S. J. Martin, and S. Y. Heriot. The impact of interfacial mixing on frster transfer at conjugated polymer heterojunctions. *Advanced Functional Materials*, 19(1):157–163, 2009.

[38] A. M. Higgins, P.C. Jukes, S.J. Martin, M. Geoghegan, R. A. L. Jones, and R. Cubitt. A neutron reflectometry study of the interface between poly(9,9-dioctylfluorene) and poly(methyl methacrylate). *Applied Physics Letters*, 81:4949, 2002.

[39] A. M. Higgins, S. J. Martin, P. C. Jukes, M. Geoghegan, R. A. L. Jones, S. Langridge, R. Cubitt, S. Kirchmeyer, A. Wehrum, and I. Grizzi. Interfacial structure in semiconducting polymer devices. *J. Mater. Chem.*, 13:2814–2818, 2003.

[40] Anthony M. Higgins, Simon J. Martin, Mark Geoghegan, Sasha Y. Heriot, Richard L. Thompson, Robert Cubitt, Robert M. Dalgliesh, Ilaria Grizzi, and Richard A. L. Jones. Interfacial structure in conjugated polymers: Characterization and control of the interface between poly(9,9-dioctylfluorene) and poly(9,9-dioctylfluorene-alt-benzothiadiazole). *Macromolecules*, 39(19):6699–6707, 2006.

[41] H. C. Higgins, J. S. Benoit. *Polymers and neutron scattering.* Oxford university press, 1st edition, 1997.

[42] V. Holy and T. Baumbach. Nonspecular x-ray reflection from rough multilayers. *Phys. Rev. B*, 49(15):10668–10676, 1994.

[43] V. Holy, J. Kubena, I. Ohlidal, K. Lischka, and W. Plotz. X-ray reflection from rough layered systems. *Phys. Rev. B*, 47(23):15896–15903, 1993.

[44] A. Ikram. http://centrin.net.id/ nslbatan/.

[45] The Mathworks Inc. http://www.mathworks.com/help/techdoc/ref/quadl.html. 2011.

[46] K. Israelachvili. *Intermolecular and surface forces.* Academic Press, 2nd edition, 1997.

[47] M. Jaiswal and R. Menon. Polymer electronic materials: a review of charge transport. *Polymer International*, 55(12):1371–1384, 2006.

[48] R. A. L. Jones. *Soft condensed matter.* Oxford university press, 1st edition, 2002.

[49] W. R Jones, R. A. L. Richards. *Polymers at surfaces and interfaces.* Cambridge university press, 1st edition, 1999.

[50] R. F. Kayser. Effect of capillary waves on surface tension. *Phys. Rev. A*, 33(3):1948–1956, 1986.

[51] I. Geoghegan M. Kesall, R. Hamley. *Nanoscale science and technology.* Wiley, 1st edition, 2005.

[52] K. H. Lee, P. E. Schwenn, A. R. G. Smith, H. Cavaye, P. E. Shaw, M. James, K. B. Krueger, I. R. Gentle, P. Meredith, and P. L. Burn. Morphology of all-solution-processed bilayer organic solar cells. *Advanced Materials*, 23(6):766–770, 2011.

[53] L. Li, G. Lu, S. Li, H. Tang, and X. Yang. Epitaxy-assisted creation of pcbm nanocrystals and its application in constructing optimized morphology for bulk-heterojunction polymer solar cells. *The Journal of Physical Chemistry B*, 112(49):15651–15658, 2008.

[54] L. C. Ludeman. *Fundamentals of digital signal processing.* John Wiley and Sons, 2nd edition, 1986.

[55] B. Mandelbrot. *The fractal geometry of nature.* WH Freeman, 1st edition, 1982.

[56] B. B Mandelbrot. Self-affine fractals and fractal dimension. *Physica scripta*, 32(1):257–260, 1985.

[57] R. A. Marsh, J. M. Hodgkiss, S. Albert-Seifried, and R. H. Friend. Effect of annealing on p3ht:pcbm charge transfer and nanoscale morphology probed by ultrafast spectroscopy. *Nano Letters*, 10(3):923–930, 2010. PMID: 20121212.

[58] B.R. McClain, M. Yoon, J.D. Litster, and S.G.J. Mochrie. Interfacial roughness in a near-critical binary fluid mixture: X-ray reflectivity and near-specular diffuse scattering. *The European Physical Journal B - Condensed Matter and Complex Systems*, 10:45–52.

[59] J. Menuir. Liquid interfaces: role of the fluctuations and analysis of ellipsometry and reflectivity measurements. *J. Physique*, 48:1819–1831, 1987.

[60] A. Messiah. *Quantum mechaics.* Dover Publications, 1999.

[61] P. mikulik. *X-ray Reflectivity from Planar and Structured Multilayers.* Masaryk University, 1997.

[62] D. C. Morse and G. H. Fredrickson. Semiflexible polymers near interfaces. *Phys. Rev. Lett.*, 73(24):3235–3238, 1994.

[63] A. C. Morteani, P.K.H. Ho, R.H. Friend, and C. Silva. Electric field-induced transition from heterojunction to bulk charge recombination in bilayer polymer light-emitting diodes. 86(16):163501, 2005.

[64] Petr. Necas, David. Klapetek. *http://gwyddion.net/.*

[65] Névot, L. and Croce, P. Caractérisation des surfaces par réflexion rasante de rayons x. application à l'étude du polissage de quelques verres silicates. *Rev. Phys. Appl. (Paris)*, 15(3):761–779, 1980.

[66] L. G. Parratt. Surface studies of solids by total reflection of x-rays. *Phys. Rev.*, 95(2):359–369, 1954.

[67] M. S. Lampinen J. A. Price, V. P. Rainer. *Differential evolution; a practical guide to global optimization.* Springer, 1st edition, 2005.

[68] A. Pynn, R. Skjeltorp. *Scaling phenomena in disordered systems.* Springer, 1st edition, 1986.

[69] R. Pynn. *Neutron Scattering: A primer.* Los Alamos Science, 1990.

[70] R. Pynn. Neutron scattering by rough surfaces at grazing incidence. *Phys. Rev. B*, 45(2):602–612, 1992.

[71] R. Pynn, M. B. Baker, G. Snith, and M. Fitzsimmons. Off specular scattering in neutron reflectometry. *J. Neutron research*, 7(1):139–158, 1998.

[72] G. F. Roach. *Green's functions.* Cambridge university press, 2nd edition, 1999.

[73] J.S. Rowlinson and B. Widom. *Molecular Theory of Capilliarity.* Dover Publications, 3rd edition, 1989.

[74] R. H. Rubenstein, M. Colby. *Polymer Physics.* Oxford, 3rd edition, 2003.

[75] T.P. Russell. X-ray and neutron reflectivity for the investigation of polymers. *Materials Science Reports*, 5(4):171 – 271, 1990.

[76] J. J Sakurai. *Modern quantum mechanics.* Addison Wesley, 1st edition, 1993.

[77] M. K. Sanyal, S. K. Sinha, K. G. Huang, and B. M. Ocko. X-ray-scattering study of capillary-wave fluctuations at a liquid surface. *Phys. Rev. Lett.*, 66(5):628–631, 1991.

[78] L. I Schiff. *Quantum mechaics.* Mcgraw Hill, 3rd edition, 1968.

[79] J.-P. Schlomka, M. Tolan, L. Schwalowsky, O. H. Seeck, J. Stettner, and W. Press. X-ray diffraction from si/ge layers: Diffuse scattering in the region of total external reflection. *Phys. Rev. B*, 51(4):2311–2321, 1995.

[80] D. W. Schubert and M. Stamm. Influence of chain length on the interface width of an incompatible polymer blend. *EPL (Europhysics Letters)*, 35(6):419, 1996.

[81] L. E. Scriven and C. V. Sternling. The marangoni effects. *Nature*, 187(2):186–188, 1960.

[82] Young-Soo Seo, T. Koga, J. Sokolov, M. H. Rafailovich, M. Tolan, and S. Sinha. Deviations from liquidlike behavior in molten polymer films at interfaces. *Phys. Rev. Lett.*, 94(15):157802, 2005.

[83] M. Sferrazza. *The study of polymer interfaces by specular and off-specular neutron reflection.* Cambridge University, 1998.

[84] M. Sferrazza, M. Heppenstall-Butler, R. Cubitt, D. Bucknall, J. Webster, and R. A. L. Jones. Interfacial instability driven by dispersive forces: The early stages of spinodal dewetting of a thin polymer film on a polymer substrate. *Phys. Rev. Lett.*, 81(23):5173–5176, 1998.

[85] Paul E. Shaw, Arvydas Ruseckas, and Ifor D. W. Samuel. Exciton diffusion measurements in poly(3-hexylthiophene). *Advanced Materials*, 20(18):3516–3520, 2008.

[86] M. Shipton. Ohttp://level1.physics.dur.ac.uk/skills/randomerrors.php, 2011.

[87] A.M. Shull, K.R. Mayes and T.P. Russell. Segment distributions in lamellar diblock copolymers. *Macromolecules*, 26(1):3929, 1993.

[88] S. K. Sinha, E. B. Sirota, S. Garoff, and H. B. Stanley. X-ray and neutron scattering from rough surfaces. *Phys. Rev. B*, 38(4):2297–2311, 1988.

[89] S.K. Sinha. X-ray diffuse scattering as a probe for thin film and interface structure. *J. Phys. III France*, 4(9):1543–1557, 1994.

[90] K. Stoev, K. Sakurai. Recent theoretical models in grazing incidence x-ray reflectometry. *The Rigahu Journal*, 14(2):22–37, 1997.

[91] V. W. Stone, X. Arys, R. Legras, and A. M. Jonas. An attempt to separate roughness from interdiffusion in the interfacial broadening between two immiscible polymers. *Macromolecules*, 33(8):3031–3041, 2000.

[92] V. W. Stone, A. M. Jonas, B. Nysten, and R. Legras. Roughness of free surfaces of bulk amorphous polymers as studied by x-ray surface scattering and atomic force microscopy. *Phys. Rev. B*, 60(8):5883–5894, 1999.

[93] H. Tang and K. F. Freed. Interfacial studies of incompressible binary blends. *J. Chem. Phys*, 94(9), 1991.

[94] C. Teichert, J. F. MacKay, D. E. Savage, M. G. Lagally, M. Brohl, and P. Wagner. Comparison of surface roughness of polished silicon wafers measured by light scattering topography, soft xray scattering, and atomic force microscopy. *Applied Physics Letters*, 66(18):2346 –2348, 1995.

[95] I. M. Tidswell, T. A. Rabedeau, P. S. Pershan, and S. D. Kosowsky. Complete wetting of a rough surface: An x-ray study. *Phys. Rev. Lett.*, 66(16):2108–2111, Apr 1991.

[96] M. Tolan, O. H. Seeck, J. Wang, S. K. Sinha, M. H. Rafailovich, and J. Sokolov. X-ray scattering from polymer films. *Physica B: Condensed Matter*, 28(1-3):22 – 26, 2000.

[97] B. Toperverg, V. Lauter-Pasyuk, H. Lauter, O. Nikonov, D. Ausserr, and Y. Gallot. Morphology of off-specular neutron scattering pattern from islands on a lamellar film. *Physica B: Condensed Matter*, 283(1-3):60 – 64, 2000.

[98] H. Tostmann, E. Dimasi, P. S. Pershan, B. M. Ocko, O. G. Shprko, and M. Deutsch. Surface structure of liquid metals and the effect of capillary waves: X-ray studies on liquid indium. *Phys. Rev. B*, 59(2):783–790, 1999.

[99] J.K.J. van Duren, X. Yang, J. Loos, C.W.T. Bulle-Lieuwma, A.B. Sieval, J.C. Hummelen, and R.A.J. Janssen. Relating the morphology of poly(p-phenylene vinylene)/methanofullerene blends to solar-cell performance. *Advanced Functional Materials*, 14(5):425–434, 2004.

[100] L. Van Hove. Correlations in space and time and born approximation scattering in systems of interacting particles. *Phys. Rev.*, 95(1):249–262, 1954.

[101] J. Wang, M. Tolan, O. H. Seeck, S. K. Sinha, O. Bahr, M. H. Rafailovich, and J. Sokolov. Surfaces of strongly confined polymer thin films studied by x-ray scattering. *Phys. Rev. Lett.*, 83(3):564–567, Jul 1999.

[102] M. Wormington, C. Panaccione, K. M. Matney, and D. K. Bowen. Characterization of structures from x-ray scattering data using genetic algorithms. *Philosophical Transactions of the Royal Society of London. Series A: Mathematical, Physical and Engineering Sciences*, 357(1761):2827–2848, 1999.

[103] H. Yan, S. Swaraj, C. Wang, N. C. Hwang, In.and Greenham, C. Groves, H. Ade, and C. R. McNeill. Influence of annealing and interfacial roughness on the performance of bilayer donor/acceptor polymer photovoltaic devices. *Advanced Functional Materials*, 20(24):4329–4337, 2010.

[104] G. C. Lu T. M. Yang, H. N. Wang. *Diffraction from rough surfaces and dynamic growth fronts, p63.* World scientific publishing, 1st edition, 1993.

[105] Y. Yoneda. Anomalous surface reflection of x rays. *Phys. Rev.*, 131(5):2010–2013, 1963.